University of Nottingham
UK | CHINA | MALAYSIA

Self-assembling Peptide-based Materials For 3D-printed Tissue Engineering Constructs

Thesis submitted to the University of Nottingham for the degree of Doctor of Philosophy

January 2025

Jordan Oliver Hill

Student ID: 20314420

Supervisors: Prof. Ricky Wildman & Prof. Alvaro Mata

Department of Chemical and Environmental Engineering, Faculty of Engineering

University of Nottingham

Abstract

There is a growing unmet global need for the transplant and repair of tissues and organs in humans. In some cases, such as those for traumatic spinal cord injury, current therapies focus on relieving pain and improving quality of life, and the chance of a full recovery of motor function is slim. Beyond personal impact, the inability to repair or replace tissues and organs has a profound economic impact. In this thesis, biological self-assembly is presented as a pathway towards future biomedical innovation in tissue engineering, regenerative medicine, and tissue modelling. The growth and development of biological systems is guided and underpinned by non-covalent interactions, yielding shapes, forms, and functions which combine to facilitate life. By exploiting the fundamentals of biological self-assembly, it is possible to create materials which closely recreate cellular milieus, mimicking the components and properties of the ECM. Here, peptide-based supramolecules are adapted for use in 3D printing systems, yielding precision control from the molecular to macroscopic scale. A heparin-mimetic peptide amphiphile is used to exploit the paracrine effect and is demonstrated to have the potential to improve neurite outgrowth in damaged neural cells. This system is then integrated into additive manufacturing by means of two-photon polymerisation, being combined with a photopolymerisable gelatin. Additive manufacturing is then used to aid the fabrication of peptide-based co-assembled supramolecular tubular membranes with a thickness in the range of native basement membranes. These membranes are demonstrated to support endothelial cell adhesion for up to 7 days post-seeding. By demonstrating the incorporation of additive manufacturing with molecular self-assembly in this manner, it is hoped that this work contributes to the growing body of research for tissue engineering and regenerative medicine which utilise peptide-based supramolecules as their foundation.

Acknowledgements

The journey to the preparation of a body of work which may be submitted as a doctoral thesis is not possible without the assistance and support of others. There are, therefore, many people deserving of recognition of their contribution – scientific and otherwise – to the completion of this manuscript.

Non-scientific Acknowledgements

Firstly, I would like to extend my unending gratitude to my parents – Robert and Adele – without whom I would not have developed an attitude of curiosity towards the world and an affinity for science from an early age. Their unwavering support and reassurance over the years helped me to determine this path for myself, and I have never looked back. Thank you, both.

To my partner, Alice, who has offered her unwavering support over the past 12 years of our lives, who moved to Nottingham with me to help me follow my goals and aspirations, I am forever grateful. No one outside of science should have to endure as many discussions about the way supramolecules can be manipulated and printed as you have. Thank you for everything.

To my long-time friends Georgie, Jonny, Josh, Juliette, Kamil, Nick, Nol, Sam, and Tissa, for continuing to visit and host from all over the country despite spiralling rail fares and petrol prices. Thank you, all.

I would also like to thank all the educators, teachers, and supervisors prior to my PhD programme who all helped to provide support, tuition, and guidance at all stages of my education.

Scientific Acknowledgements

Primarily, I would like to recognise the enormous contribution of my supervisors, Prof. Ricky Wildman and Prof. Alvaro Mata. Without their dedication to research and innovation, this project would never have existed. Their constant support, direction, and guidance helped this project to develop and achieve what it did. To both of you, thank you.

I would also like to recognise the contribution of external collaborators on this project. Namely, the material contributions of the group of Prof. Sandra van Vlierberghe of the University of Ghent, Belgium, for contributing gelatin norbornene for additive manufacturing. To the group of Prof. António Salgado at the University of Minho, Portugal for the donation of stem cell secretome and adipose-derived stem cells, and to Dr. Tiffany Pinho for her hard work and guidance in conducting neuron-based studies. Thirdly, to the groups of Prof. Jürgen Groll and Prof. Tomasz Jungst for the donation of melt-electrowritten PCL scaffolds for thin membrane formation. Without these collaborators, this project would not have branched and explored the avenues it did. Thank you, all, for your contribution.

To all members of the Mata research group who helped to make my time in Nottingham as memorable as it was. For discussing and debating new ideas and for their guidance on this project. Chiefly, to Dr. Yuanhao Wu, Dr. Cosimo Ligorio, and Dr. Helena Rouco for their scientific contributions to this project, and to all other members who have come and gone during my time in the group. Thank you, everyone.

To all members of the Centre for Additive Manufacturing and the A64 AddFabLab team for their support in additive manufacturing, and for their company during the preparation of this thesis. Thank you, all.

To the team at the nanoscale and microscale research centre for all their assistance with electron microscopy, confocal imaging, XPS, and ellipsometry. Credit and thanks are also given to Dr. Richard Cousins for performing sample measurements on the ellipsometer, and to Dr. Marion Limo for all her help in setting up, optimising, and performing SPR measurements.

To the proteomics team – Dr. Daniel Wilkinson and Dr. Kenneth Smith – at the Royal Derby Hospital, for all their assistance in the design and performing of proteomics measurements on stem cell secretome. Thank you, both.

Finally, I would like to thank the funding bodies, ERC PoC (NOVACHIP) and UKRMP2 for their support of this project.

Table of Contents

List of Figures

List of Abbreviations

2PP	Two-photon polymerisation	**HMPA**	Heparin mimetic peptide amphiphile
AM	Additive manufacturing	**hUVEC**	Human umbilical vein endothelial cells
BBB	Blood-brain barrier	**IDR/IDP**	Intrinsically disordered region / protein
BDNF	Brain-derived neurotrophic factor	**LMWG**	Low molecular weight gelator
CAD	Computer assisted design	**MEW**	Melt electrowriting
CD	Circular dichroism	**MTS**	(3-(4,5-demethylthiazol-2-yl)-5-(3-carboxymethoxyphenyl)-2-(4(sulfophenyl)-2H-tetrazolium)
CNS	Central nervous system	**NGF**	Neurotrophic growth factor
CMC	Critical micelle concentration	**PA**	Peptide amphiphile
DLP	Digital light processing	**PAG**	Photoacid generator
DLS	Dynamic light scattering	**PBS**	Phosphate-buffered saline
DPIN	Diphenyl iodonium nitrate	**PCL**	Poly(caprolactone)
ECM	Extracellular matrix	**PDMS**	Polydimethylsiloxane
ELP	Elastin-like polypeptide	**pI**	Isoelectric point
FITC	Fluorescein isothiocyanate	**PI**	Photoinitiator
GelMA	Gelatin methacrylate	**RA**	Retinoic acid
GelNB	Gelatin norbornene	**SCS**	Stem cell secretome
GelSH	Thiolated gelatin	**SDS**	Sodium dodecyl sulfate
GO	Graphene oxide	**SEM**	Scanning electron microscopy
HA	Hyaluronic acid	**SLA**	Stereolithography
(h)ADSCs	(Human) adipose derived stem cells	**SPPS**	Solid-phase peptide synthesis
HBPA	Heparin binding peptide amphiphile	**SPR**	Surface plasmon resonance
HEPES	4-(2-Hydroxyethyl)piperazine-1-ethane-sulfonic acid	**VAM**	Volumetric additive manufacturing

1. Introduction

1.1 Supramolecules and Molecular Self-assembly

1.1.1 Non-covalent Interactions – A Brief History

The behaviour of atoms and molecules is governed by electrons. The movement of electrons to a more energetically favourable state dictates the breaking and forming of bonds and the distribution of charges within a molecule, such as through the formation of tautomers or partial charges. These principles consequently determine the properties of molecules such as their solubilities, reactivities, and colour. Beyond this, the distribution of electrons also guides the way molecules are arranged in space and how they interact with each other, yielding multiple emergent properties such as surface tension of liquids, melting point of solids, and the secondary structure of proteins. These properties are typically dictated by weak, reversible, non-covalent interactions. Water, for example, is a liquid at room temperature because of the presence of hydrogen bonds between individual molecules. Other interactions which fall into this category include van der Waals forces, metal coordination, electrostatic interactions, hydrophobic forces, and π-π interactions.

The existence of interactions between molecules was first suggested by Johannes van der Waals in 1873,[1] after it was observed that real gasses did not adhere to the ideal gas law. These interactions are brought about by unequal electron densities about an atom or molecule, creating a partial charge. This charge, while incredibly weak and present only over short distances, may attract or repel nearby molecules. In larger systems, the sheer number of van der Waals forces present may lead to immediately observable effects. For example, it is currently understood that the transient and attractive forces between a surface and the foot of a gecko allow it to adhere to and walk on walls and ceilings.[2]

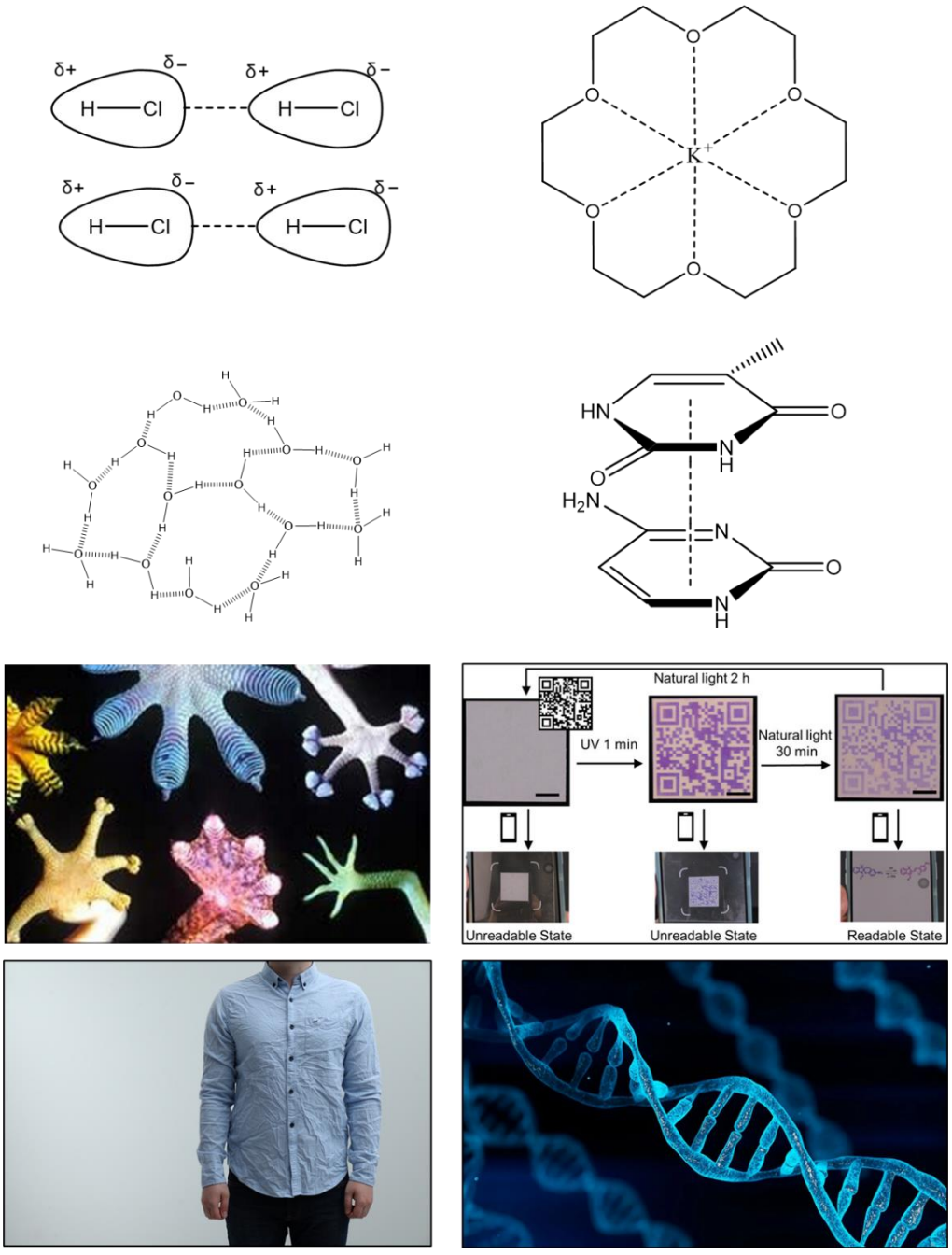

Figure 1: *Basic Intermolecular Interactions and Real-Life Examples.* ***Row 1 Left:*** *van der Waals forces between two molecules of hydrogen chloride. The electron distribution is denoted using partial positive and negative charges.* ***Row 1 Right:*** *a crown ether coordinating a potassium ion.* ***Row 2 Left:*** *hydrogen bonding between water molecules. Hydrogen bonds are denoted by dashed lines.* ***Row 2 Right:*** *π-π interactions between overlapping aromatic centres in cytosine and thymine.* ***Row 3 Left:*** *Images of the underside of arthropod feet. The electrostatic interaction between fine hairs allows a gecko to adhere to surfaces.* ***Row 3 Right:*** *The use of a host-guest system for time-dependent encryption. Reproduced from ref. 5.* ***Row 4 Left:*** *Creases in fabric are the result of hydrogen bonding between cellulose molecules. The water molecules of steam disrupt these bonds during ironing, allowing the fabric to be smoothed.* ***Row 4 Right:*** *The structure of DNA is held together by supramolecular interactions such as hydrogen bonding and π-π stacking.*

Following the description of van der Waals forces, host-guest interactions began to be understood following the 'lock-and-key' model of enzyme-substrate interactions presented by Emil Fischer in 1894.[3] Here, it was proposed that the enzyme acts as a 'lock', while the substrate or competitive inhibitor acts as the 'key', which may only fit into the lock if it is of the correct size, shape, and conformation. This understanding of host-guest complexes has since led to the synthesis of a vast range of host molecules, such as cyclodextrin, pillar[*n*]enes, crown ethers, or a family termed 'cucurbiturils', which have been used for drug delivery, environmental remediation, and encryption owing to their ability to selectively encapsulate a desired host molecule.[4, 5] Beyond host-guest chemistry, the lock-and-key model also provided the foundation for understanding molecular recognition, wherein molecules may 'recognise' other molecules owing to their spatial arrangement and distribution of charges. One example of this is the glycopeptide-based antibiotic vancomycin – used to treat methicillin-resistant meningitis – which inhibits bacterial cell wall formation by hydrogen bonding to an alanine-alanine dipeptide, resulting in cell death.[6] This is similar to the action of β-lactam antibiotics, which instead mimic the structure of the AA dipeptide and irreversibly inhibit the enzyme responsible for a final step of bacterial cell wall synthesis.[7]

After van der Waals' and Fischer's description of key fundamentals of supramolecular chemistry, Latimer and Rodebush published in 1920 their proposal of hydrogen bonding in liquids,[8] using Lewis theory to suggest that a free pair of electrons on the oxygen in a water molecule may exert force on the hydrogen atom of another in such a way that it may be considered a bond. Indeed, the strength of a hydrogen bond lies between that of van der Waals interactions and covalent bonds, although the exact strength depends on the nature of the donor and acceptor groups. The importance of hydrogen bonding was further compounded by Creeth, Gulland, and Jordan's proposal in 1947 that hydrogen bonding was present the structure of DNA.[9] Through these experiments, it was proposed that DNA consists of two chains of a sugar-phosphate backbone connected by hydrogen bonding between the two chains. 3 years after this proposal, Pauling and Corey reported in 1950 the presence of hydrogen bonding in polypeptides in relation to α-helices and β-sheets,[10] laying

the foundations for the understanding of protein secondary, tertiary, and quaternary structures. It has since come to be understood that a vast number of biological systems are underpinned by non-covalent interactions guiding molecular self-assembly and self-organization.

1.1.2 Non-covalent Interactions in Biological Systems

Biological systems are the product of molecular self-assembly. From the structure of biomolecules to the circadian rhythm, all that is biological is guided by the self-assembly and self-organization of hierarchical systems. The processes necessary for a biological system to be successful may be broken down into two broad classes: development and regeneration. Development encompasses processes which occur following egg fertilisation and the growth of a foetus, such as the formation of organs, limbs, and a heartbeat. Regeneration refers to that which happens, for example, after a wound or injury – the processes which allow the body to heal itself. Guiding these two broad classes are a set of principles of self-assembly, into which all processes may fall. These principles of biological self-assembly are: molecular self-assembly, compartmentalisation, diffusion-reaction, disorder-to-order transitions, and out-of-equilibrium processes.[11]

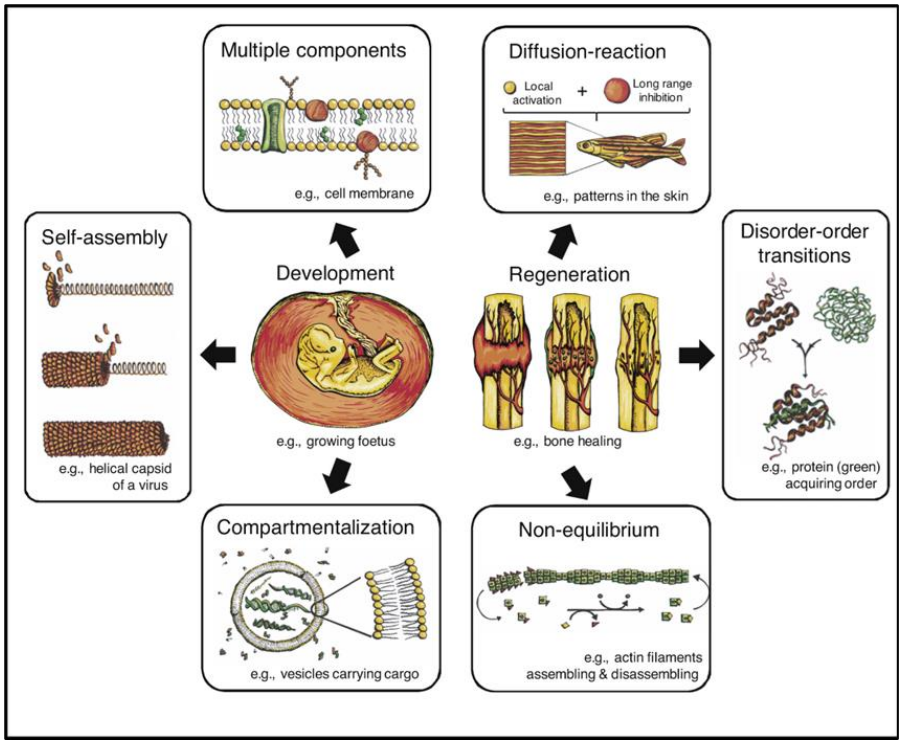

Figure 2: Self-assembly processes in development and regeneration. The key processes which underpin development and regeneration are: molecular self-assembly, biological complexity/multiple components, diffusion-reaction processes, disorder-order transitions in proteins, non-equilibrium thermodynamics (self-organisation), and compartmentalisation/coacervation. Together, these fundamentals of biology underpin a vast array of biological processes and may be exploited in an experimental manner to aid regenerative medicine. Reproduced from Ref. 11.

Self-assembly in biology is the driving force behind the formation of a wide array of structures, such as the capsid of a virus or collagen bundles in muscles. These processes occur near, or at, thermodynamic equilibrium, minimising the free energy of the system. Self-assembly occurs through non-covalent interactions such as van der Waals forces, π-π interactions, host-guest interactions, hydrogen bonding, and hydrophobic forces. Beyond this, self-assembly may refer to, for example, the self-assembly of cells to form tissues and organs with defined structures and functions.

The motion of components in biological systems may also result in the formation of distinct patterns. These patterns, some commonly called Turing Patterns after Alan Turing's mathematical description,[12] are ubiquitous in biology, such as the scales of a Zebrafish,[13] the spacing of hair follicles,[14] or the patterning of skin denticles in sharks.[15] A reaction-diffusion mechanism drives the autonomous formation of patterns and is crucial in deriving structure and

function in some systems.[12] Turing described six possible final states which may arise from the diffusion and reaction of two theoretical molecules – or morphogens in a biological sense – which may be imagined as two waveforms.[16] In case 1, the two waveforms converge and nullify to yield a stationary state of morphogen concentrations. Case 2 describes a uniform oscillation of morphogen oscillation, describing behaviours such as the beating of the heart through the contraction of muscle cells.[17] In Case 3 and 4, waves of a short wavelength are formed. In Case 3 these waves are stationary whereas in Case 4 they are oscillatory. Case 5 describes the formation of a travelling wave, while Case 6 describes the formation of stationary patterns – Turing patterns. It is possible, by tuning the initial parameters and boundary conditions, to precisely control the final state which is achieved and the ultimate pattern observed. The ability to control pattern formation may yield a degree of success in controlling the culture of tissues and organs.

Not all patterns and irregular shapes observed in biological systems are formed through Turing-like processes. The scales which cover the face and jaw of crocodilian species, for example, are formed through the cracking and breaking of skin during embryonic development.[18] These cracks are stochastic in nature and are minimally affected by genetic parameters. Interestingly, however, the scales covering the remaining body of crocodilians are patterned through a Turing-like reaction-diffusion mechanism. This difference has been speculatively attributed to the difference in embryonic growth rates of the jaw compared to the rest of the body of crocodilians. Nonetheless, this serves to highlight that, beyond Turing-like patterns, there remain other self-organisational systems in developmental biology which are yet to be modelled and fully understood.

On a larger scale, the self-assembled systems in biology may begin to form separate environments through phase separation, in a process termed compartmentalisation. Within eukaryotic cells, these compartments may be membrane-bound (organelles) or membraneless, with the membraneless compartments being termed biomolecular condensates.[19] Within these distinct environments, the environmental conditions may differ from the external conditions, such as differences in hydrophobicity or chemical makeup. Indeed,

many biomolecular condensates consist of multivalent molecules which may assemble into polymers, which decreases their solubility and results in entropically-driven phase separation.[20] One example of a biomolecular condensate is Cajal bodies, which exist as spherical artefacts within the nucleus of eukaryotic cells and are implicated in the post-translational modification of RNA.[21] Interestingly, these condensates may also contain further sub-compartments which act as solids with as-yet undeciphered function.[22]

Beyond multivalent molecules, condensates are also rich in proteins which contain an intrinsically disordered region (IDR). IDRs do not adopt a fixed 3-dimensional structure, instead existing as a random coil or globular aggregates. IDR-containing proteins may exhibit dynamic stiffnesses, transitioning from liquid-like behaviours to solid-like over time. This hardening may be driven by the formation of β-strand-like aggregations, leading to the growth of amyloid fibres and subsequent hardening. The transition between more and less-ordered states in IDRs affects their interactions with proteins and regulation of cellular processes.[23] As the phase separation behaviours of IDRs is characteristic to their peptide sequence, it is possible to rationally design amino acid sequences with encoded behaviours and modulate their interactions with other molecules.[24] In doing this, it may be possible to rationally design biomaterials following the same principles.

Function in biology may also be yielded from the specific structure of individual biomolecules. Within these molecules, there are certain degrees of order and disorder. Protein order may be achieved through the presence of, for example, α-helices and β-sheets, whereas disorder is present in the random coils. Some intrinsically disordered proteins and intrinsically disordered regions play crucial roles in achieving the function of different proteins. Upon protein-protein binding, there is often an associated change in the degree of order or disorder in one or both reactant(s), yielding a complex with characteristic folding. It may be the case that, upon binding of two ordered proteins, there is an increase in disorder in one protein.[25] Interestingly, two IDRs may bind to yield an ordered complex.[26, 27] In the case of the binding of Arf to Hdm2, the association of these proteins leads to the formation of amyloid-like oligomers. This structural transition may also be induced by recapitulating the amino acid sequence of the

binding motifs[28] – indicating the potential for the development of peptide-based materials which specifically interact with different proteins for, for example, cancer therapies.

Disorder-to-order transitions may also be examples of non-equilibrium thermodynamics, as the second law of thermodynamics indicates that living systems tend towards an increase in entropy (disorder). In 1944, Schrödinger proposed that living systems constantly stave off entropy through the intake of energy in the form of food. Similarly, this translates to the cellular level, where non-equilibrium dynamics drive, for example, the transcription of genes,[29] the fabrication of the actin cytoskeleton within cells,[30] and molecular motors such as kinesin.[31] Typically, it is the excess in chemical potential ($\delta\mu$) which drives these non-equilibrium processes. Concepts of non-equilibrium thermodynamics in biological systems have also developed from fluctuation relations and stochastic thermodynamics,[32, 33] which apply macroscopic thermodynamics to single particle systems, such as the Brownian motion of a particle in suspension. These non-equilibrium thermodynamics have since been applied to the behaviours and organisation of biological systems, such as the movement of cells through flagellar motion or the flocking of European starlings.[34, 35] Recently, non-equilibrium thermodynamics have been used to describe the self-organisation of small cell aggregates, such as those observed during embryogenesis or in organoids.[36]

As these biological systems grow, their increase in complexity – here referring to the number of different components – facilitates a greater diversity of biomolecular pathways and cellular functions. This complexity develops into a hierarchical system, wherein emergent functions occur as a result of the vast array of building blocks which are available. Muscles, for example, emerge from the self-organisation and hierarchical positioning of myofibrils into fibres, fibres into fascicles, and fascicles into tendons.[37] Similarly, biological pathways such as the clotting of blood are a cascade of molecular activations and signalling, and the lack of one component can interrupt the entire process.[38] It is possible, therefore, that future therapies would do well to incorporate complexity into their design, in order to increase their biological effects and mimic the native complexity observed in biological systems.

At this point, the principles of biological organisation have been defined as self-assembly, compartmentalisation, pattern formation, order-to-disorder transitions, and self-organisation, all of which are demonstrated to be ubiquitous in biological systems. These organisation principles, except for self-organisation which requires an energy input and occurs away from thermodynamic equilibrium, are all driven by supramolecular interactions and molecular self-assembly. Having determined the importance of these interactions in the survival of biological systems, it follows that exploiting these principles may be a useful line of research in tissue engineering and regenerative medicine, where artificial materials aim to act as a scaffold to support and direct cell growth. Indeed, many there are many biomedical applications which have taken inspiration from biology in their design.

1.2 Supramolecules in Biomedicine

It has already been mentioned that some antibiotics, such as vancomycin, utilise supramolecular interactions in their mechanism of action to disrupt the formation of bacterial cell walls, ultimately halting infection. Beyond antibiotics, a great deal of biomedical devices and materials have taken inspiration from nature, such as soft robotic actuators, organ-on-chip devices, and hydrogel tissue scaffolds. Many of these also utilise non-covalent interactions to improve their function and closer mimic the chemical milieu in biological systems, such as by recreating peptide sequences for molecular recognition or by fabricating materials soft enough to mimic native tissues. Some of these materials also display unique advantages over covalent systems, such as a greater ability to control materials at the molecular level or more biocompatible gelation mechanisms. In recent years, there has been great focus on the integration of self-assembly with biomedicine, in areas such as film coatings of biomedical devices, stimuli-responsive drug delivery systems, and self-assembling hydrogels.

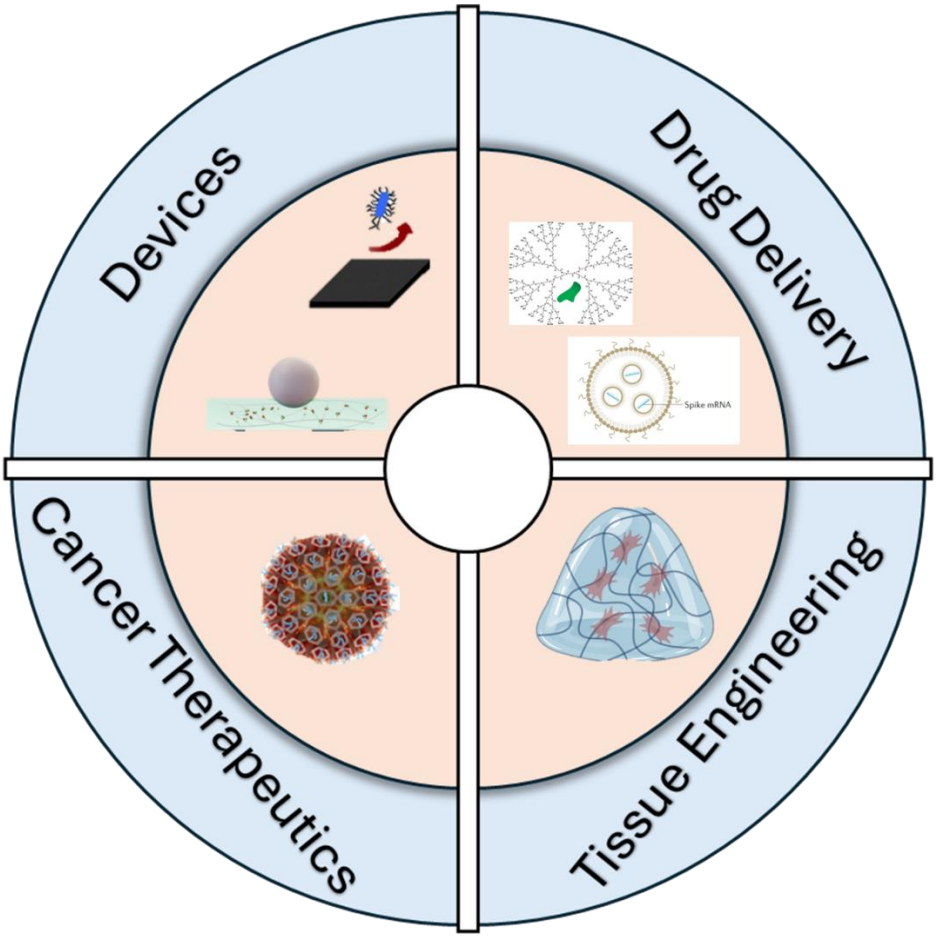

Figure 3: Applications of Supramolecular Systems in Biomedicine. ***Top Left:*** *Supramolecular coatings in devices such as catheters or bone implants may yield anti-biofilm or lubricant properties.* ***Top Right:*** *Supramolecular drug-delivery systems dendrimers and lipid nanoparticles.* ***Bottom Left:*** *Supramolecular anti-cancer therapeutics combining host-guest interactions and photodynamic therapy.* ***Bottom Right:*** *Supramolecular hydrogels may be used for cell encapsulation and tissue engineering. Anti-biofilm image credit: Ref 43. Lubricant surface image credit: Ref 45. Dendrimer image credit: Ref 48. Lipid nanoparticles image credit: Ref 49. Supramolecular pillar[6]arene image credit: Ref 52.*

Biomedical implants such as shunts, catheters, and pacemakers all benefit from surface modifications to prevent bacterial infection and immune rejection.[39, 40] Bacterial infections may arise from the formation of antibiotic-resistant biofilms, such as *Staphylococcus aureus* where penicillin resistance may be observed in over 90% of cases.[41] These infections and rejections typically result in the surgery needing to be redone (revision surgery), with the cost of revision surgery for just hip and knee implants in the US alone expected to rise to over $1.5bn by 2030.[42] One promising method to overcome these issues is the use of rationally-designed supramolecular coatings. A supramolecular system utilising the non-covalent attractive forces between polydopamine (PDA) and low

molecular weight poly(*N*-vinyl caprolactam) (PVCL) was demonstrated to inhibit biofilm formation for up to 28 days in both gram positive and gram negative bacteria.[43] This was the maximum time for which the device was tested. The surface also demonstrated tuneable hydrophilicity, thickness, and surface roughness by altering the ratio of PDA and PVCL. By tuning the hydrophilicity, it is possible to reduce the adhesion of lipophilic proteins, improving the anti-fouling capabilities of the device.

PDA self-assembly has also been used with poly(*N,N*-dimethylacrylamide) (PDMA) as a catheter coating with similar outcomes to the PDA/PVCL system,[44] indicating good applicability of this supramolecular system. Beyond anti-biofilm and anti-fouling properties, the dynamic nature of non-covalent boron-nitrogen (B-N) interactions has also been exploited in the development of low-friction coatings for, for example, hip joint implants.[45] The reversible nature of these dative bonds in a polymer network generates favourable bulk properties, including a low coefficient of friction and wear rate, improving their suitability for dynamic environments such as the hip joint.

Beyond surgical implants, supramolecular formulations have also been used for drug delivery systems. By exploiting the π-π interactions between the hydrophobic drug doxorubicin and a guanidinium-containing hydrophilic polymer, it has been shown to be possible to form a conjugated system with improved cellular uptake compared to free doxorubicin.[46] However, in vivo studies did not report a significant difference in tumour size reduction when treated with free doxorubicin and the conjugated doxorubicin, although a significant decrease in cardiotoxicity was observed. Other methods of supramolecular drug delivery include the use of dendrimers – large, branched structures with an architecture defined at the molecular level. These large macromolecules typically act as the host in a host-guest supramolecular system, entrapping a desired molecule within for slow and sustained release.[47, 48] In this case, where a poly(glycerol succinic acid) dendrimer was used to encapsulate the anti-cancer drug 10-hydroxycamptothecin, a significant decrease in the viability of human MCF-7 breast cancer cells was observed after just two hours, compared to application of the free drug, indicating the potential of these systems as supramolecular drug delivery systems.

Exploiting the hydrophobic effect, lipid nanoparticles (liposomes) have also seen a degree of clinical success in drug delivery systems. These structures typically form spherical bilayers through an emulsion process, entrapping an aqueous phase on the inner of the hollow sphere. A payload may be present either within this aqueous phase or in the lipid bilayer itself. A prominent example of lipid nanoparticles is their use in mRNA vaccines.[49] The lipid used in Moderna's mRNA-based SARS-CoV-2 vaccine carries a neutral charge at physiological pH, but the amino group presented on the inside of the liposome is positively charged, facilitating electrostatic interactions with the negatively charged mRNA phosphate backbone, stabilising it.[50] This mechanism of interaction and stabilisation is also preserved in the lipid used in the SARS-CoV-2 vaccine prepared by BioNTech and Pfizer.

Thirdly, supramolecular systems have been employed in anti-cancer therapeutics. These systems typically exploit host-guest interactions between a drug or prodrug and a large macrocycle, or mimic cell signalling and molecular recognition in carcinogenic cells. By introducing stimuli-responsive activation of therapies, supramolecular cancer therapeutics aim to reduce off-target effects, instead increasing their action at the tumour site. One such class of molecules, cucurbit[*n*]urils, act as a macrocyclic host, with their self-assembly driven by hydrophobic and electrostatic interactions. These materials have been demonstrated to encapsulate doxorubicin and camptothecin without negatively impacting the efficacy of these drugs.[51] Another class of molecules, pillar[*n*]arenes, have been developed to generate a "triple therapeutic" effect of photodynamic, photothermic, and chemotherapeutic action.[52] Here, a biphenyl-extended pillar[6]arene forms host guest interactions with a chlorambucil prodrug, yielding a spherical nanoparticle. This nanoparticle disassembles in the acidic tumour microenvironment, which simultaneously cleaves the prodrug for a chemotherapeutic effect.

A fourth area in which self-assembling systems have received attention is in the realm of tissue engineering and regenerative medicine. The ability of non-covalent interactions to recapitulate and mimic biological environments makes them prime candidates for incorporation into materials which interact with living organisms to support and actively direct their growth, proliferation, and

differentiation. Typically, these supramolecules are employed because of their ability to spontaneously self-assemble into ordered structures and fibres, forming gels. These gels may act as scaffolds to support cell growth. Supramolecular gels are typically formed by synthetic molecules, as opposed to molecules which are recovered from biomass such as alginic acid or chitosan. Alginates, for example, require further purification steps to remove endotoxins before they may be considered for use in a cell culture environment.[53] In addition, the synthetic nature of supramolecular gels results in the ability to control their biological effects, mechanical properties, and chemical reactivities on an atomic scale, yielding an unprecedented degree of control over the final gel.

1.3 Self-assembling Hydrogels in Tissue Engineering

A gel may be defined as a polymeric or colloidal non-fluid suspension with solvent entrapped within its pores.[54] This solvent may be an organic solvent in the case of an organogel or water in the case of a hydrogel. A gel in which all solvent has been removed and replaced with air may be termed a xerogel. In the context of tissue engineering and cell culture, hydrogels are commonly used, owing to the ubiquity of water in biological systems. Gels are useful in tissue culture as they provide a softer 3D environment in which to culture and study cell behaviour, more closely mimicking the native cellular environment as opposed to 2D cell culture which typically provides cells with a single, hard surface upon which to grow. Within the class of gels, there are two broad sub-divisions: polymer gels and supramolecular gels. Polymer gels are formed through covalent bonding, such as gelatin methacrylate (GelMA) or calcium alginate. On the other hand, supramolecular gels form networks through non-covalent interactions, exploiting the principles presented in 1.1 to fabricate a functional material.

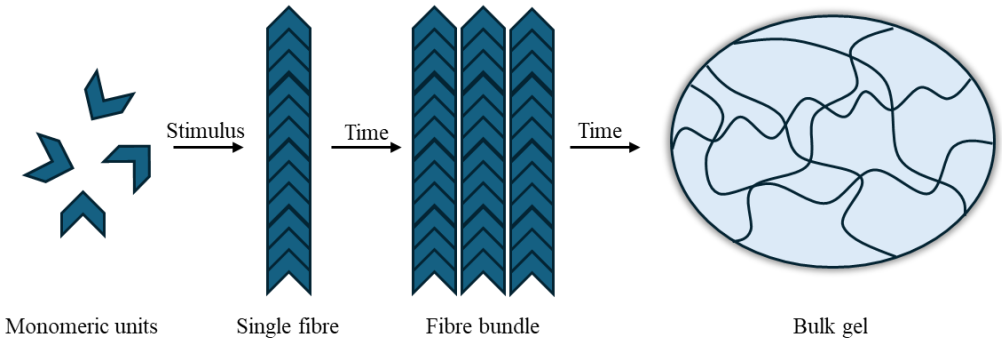

Figure 4: Schematic of Molecular Self-assembly for gel formation. Monomeric units may be triggered by the imposition of an external stimulus to self-assemble into higher-ordered structures such as fibres. As these fibres grow, they may bundle hierarchically, spanning the surrounding solvent and entrapping it within pores to form a bulk gel.

The use of hydrogels for biomedical purposes was first proposed by Wichterle and Lím in 1960,[55] using a copolymer of glycolmonomethacrylate and glycoldimethacrylate for use as a contact lens structure. In a tissue engineering and regenerative medicine sense, Yannis and Burke reported in 1980 the use of a collagen-glycosaminoglycan (GAG) co-precipitate for use as a skin graft in a full-thickness burn model.[56] In this system, it was reported that the co-assembly of collagen and a GAG led to control over the porosity of the resultant scaffold. This system was subsequently used in 10 human patients, with "good to excellent" results reported in all cases.[57] In the following two decades, interest in tissue engineering grew and, by 1998, artificial constructs for heart valves, skin grafts, blood vessels, cartilage, the liver, the gastrointestinal tract, bone, and tendons had been reported.[58]

Polymeric hydrogels, however, were not without limitations. Some, while mechanically robust, have a stiffness which may cause mechanical irritation, while others leach toxic degradation products or may be tumourigenic.[59] As a result, there began to be growing interest in the use of synthetic, small molecule hydrogelators as possible cell scaffolds, as well as how these molecules may be designed to precisely impact the material properties.[60-63] It was known in 2005 that the biological and physical properties of a hydrogel may be used to directly control the growth of cells.[64, 65] Self-assembling materials offered an unmatched ease of modulating these properties.

The ability to synthesise molecules with the capacity to self-assemble into higher-ordered structures allows for their properties to be controlled on an atomic scale. However, there are still some design rules which should be followed to facilitate molecular self-assembly into a hydrogel. Typically, supramolecular gelators contain groups which form complementary hydrogen bonding pairs, such as amides and nucleobases. Long hydrocarbon chains may be incorporated to exploit hydrophobic clustering. Aromatic structures may also facilitate self-assembly through π-π interactions. Chirality, too, is common in these molecules and specific enantiomers of the same molecule may self-assemble in a different manner, or not self-assemble at all.[66] Owing to the relative weakness and reversibility of non-covalent interactions compared to covalent bonds, supramolecular gels typically display a lower stiffness and stability than polymer gels. While a lowered stiffness may be desired in some tissue engineering scenarios, the poor stability presents itself as a problem. On the other hand, the dynamic nature of non-covalent interactions imparts a degree of self-healing ability to supramolecular hydrogels, allowing them to reform and recover after the application of shear, facilitating their injection into a target site.

Typically, supramolecular gelators exist as discrete monomeric units of a low molecular weight, termed low-molecular weight gelators (LMWGs). These gelators usually incorporate biological building blocks such as amino acids or carbohydrates into their structure. Very few examples of purely non-biological LMWGs used in cell culture exist. Carbohydrate-based gelators, such as the dibenzylidene-*D*-sorbitol (DBS) group of LMWGs developed by Smith and co-workers[67, 68] or *D*-glucosamine hydrogelator developed by Xu and co-workers[69] have shown some promise for tissue engineering applications, but may need to be combined with polymer gelators to overcome sub-optimal mechanical properties.[70, 71]

Purely supramolecular systems have been developed with nucleoside-based gelators. A cytidine-derivative was demonstrated to self-assemble into a self-healing gel which was tolerated by human fibroblast cells up to 72 hours post-contact,[72] indicating cell culture potential, although no further cell-based investigations were reported for this gel. An adenosine-based supramolecular system has been proposed as an injectable hydrogel for post-tooth-extraction

wound healing.[73] This system was found to completely degrade within 6 hours of application, with no adverse effects observed in multiple organs in a murine model. Furthermore, it was observed that the gel exhibited good antibacterial properties against both gram-positive and gram-negative bacteria and promoted bone healing in rat alveolar bone.

One interesting strategy to adapt nucleotides to tissue engineering applications is their conversion to an amphiphilic species.[74] In one case, an amphiphilic species with a thymidine head and hydrocarbon tail was demonstrated to be injectable, and could be 3D printed to scaffolds of a desired geometry. This hydrogelator was found to have good cytotoxicity with human gingival fibroblasts (>90% viability after 24 hours) but was significantly more cytotoxic to apical papilla stem cells (70% viability after 24 hours). While nucleoside-based gelators appear to have some potential in tissue engineering, they lack a high degree of customisation. They are typically limited to one or two nucleosides per molecule, and it is difficult to design bio-instructive molecules which interact with the cells with which they are cultured. To this end, peptide-based hydrogels have emerged as promising candidates for bioactive supramolecular scaffolds for cell culture.

1.4 Peptide-based Hydrogels in Tissue Engineering

1.4.1 Structural Considerations

Amino acids are the building blocks of proteins in biological systems. The presence or absence of different amino acids, and the order in which they are present, determines the secondary structure of proteins as hydrogen bonds are formed between residues. The two most observed secondary structures are the α-helix and the β-sheet, although others such as a π-helix or a β-turn may also be observed. The α-helix may occur in a single amino acid chain, with intramolecular hydrogen bonding occurring between carbonyl and amide groups of amino acid *n* and *n*+4. Proline is typically absent from α-helices as it lacks a free amide to act as a hydrogen bond donor, although is a favoured terminal amino acid in these structures.[75] Other helical structures, such as the 3_{10} helix, are possible, but are predicted to be energetically less favourable then the α-helix in longer peptides.[76]

Conversely to α-helices, β-sheets arise from hydrogen bonding between separate - or more separated within one molecule - peptide chains. As with α-helices, hydrogen bonding in β-sheets occurs between carbonyl and amide groups of neighbouring identical strands. These β-sheets may be either parallel or anti-parallel in orientation. In parallel β-sheets, hydrogen bonding occurs between adjacent amino acids of neighbouring peptides, whereas in the anti-parallel conformation hydrogen bonding occurs between the same amino acid in neighbouring strands.[77] Knowing how the spatial arrangement of hydrogen bonding motifs affects the secondary structure of proteins, it becomes possible to design synthetic peptide sequences with defined architectures.[78]

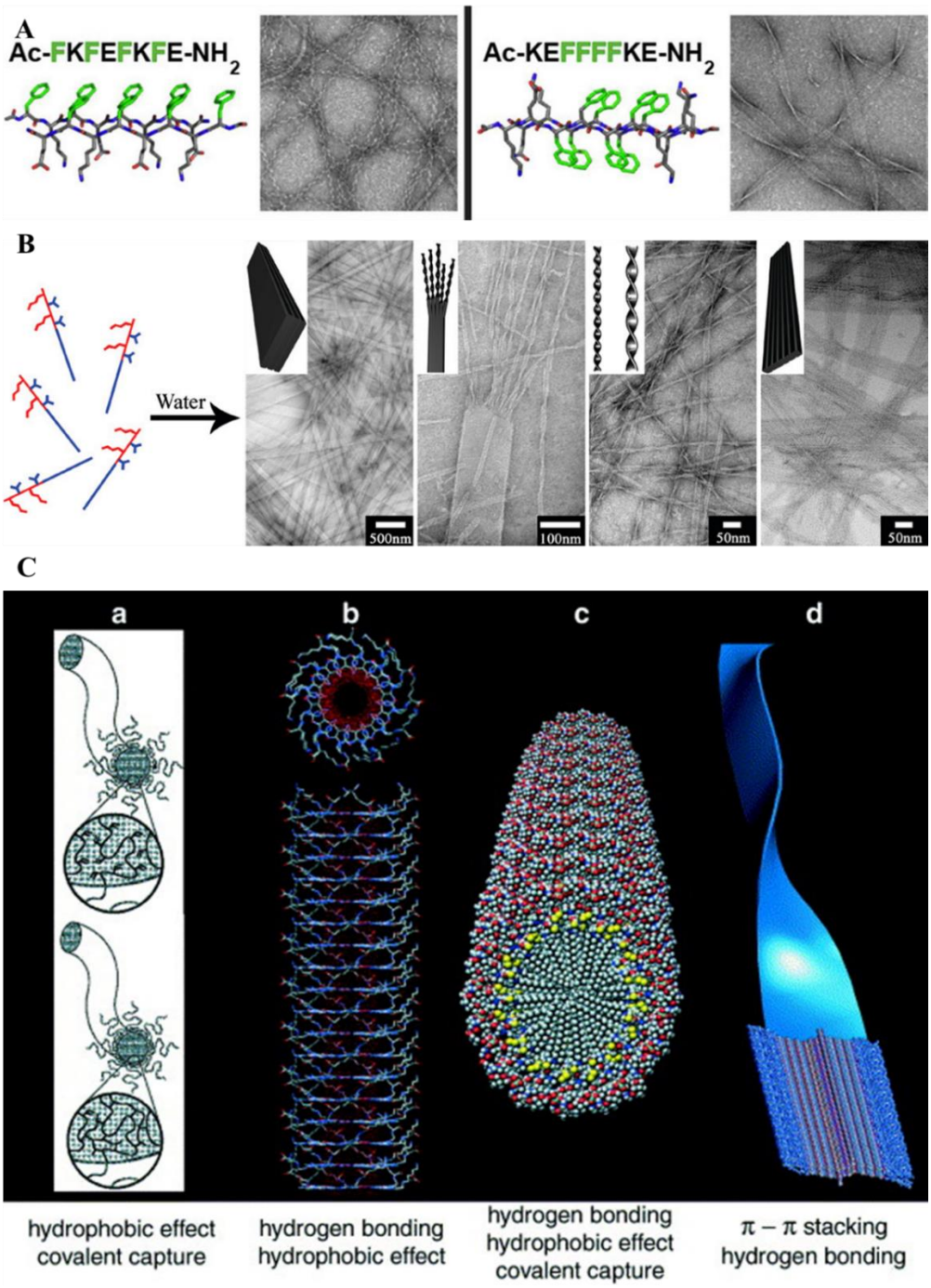

Figure 5: Examples of controlling nanostructure by tailoring supramolecular interactions. ***A)*** *Formation of fibres and ribbons in the Ac-(FKFE)$_2$-NH$_2$ sequence. Reproduced from Ref 80.* ***B)*** *Formation of ribbons, twists, and belts of the same molecule by altering the surrounding environment. Reproduced from Ref 81.* ***C)*** *Further examples of achievable structures including (from left to right) worm-like micelles, nanotubes, fibres, and ribbons. Reproduced from Ref 83.*

The ordering of the amino acid sequence can greatly impact the self-assembly behaviour of a peptide sequence. Amphipathic peptide sequences, where hydrophobic and hydrophilic amino acids are both present, display unique self-assembled morphologies depending on the sequence. The Ac-(FKFE)$_2$-NH$_2$

sequence, for example, forms ordered β-sheets with the alternated hydrophobic and hydrophilic residues on opposite faces of the sheet.[79] This facilitates hydrophobic clustering in the centre of a bilayer, enhancing the thermodynamic favourability of assembly. Clustering of the hydrophobic and hydrophilic domains in the sequences Ac-KEFFFFKE-NH_2, Ac-$(KFFE)_2$-NH_2, and Ac-FFKEKEFF-NH_2 results in a less favourable landscape for self-assembly, requiring greater concentrations for assembly to occur. It is also possible to alter hydrophobicity to impact the gelation rate of peptide hydrogelators, with increasing hydrophilicity increasing the thermodynamic unfavourability to self-assembly, ultimately delaying gelation.[80] By modulating the interactions between synthetic peptides, it has been possible to form, for example, ribbons, belts, rods, and twists.[81-83] Access to these shapes facilitates, among other benefits, the presentation of bioactive epitopes on the surface of assembled structures.

By ordering specific complementary peptide sequences, it is possible to organise the supramolecular interactions and direct their assembly into higher ordered structures. In the early 1990's, Zhang and co-workers developed a series of hydrogen-bonding peptides based on the EAKA and RADA repeat units.[84, 85] These units, up to 16 amino acids in length (RADA16 or EAKA16) form complementary hydrogen bonds, generating β-sheet structures and ultimately an ordered hydrogel. RADA16 has been demonstrated to have facilitate neural cell attachment and neurite outgrowth in vitro,[86] as well as haemostasis and wound healing in an in vivo ovine model.[87] Owing to the dynamic nature of the supramolecular bonds in RADA16, it has also found clinical use as an injectable hydrogel to prevent post-operative bleeding.[88]

The sequence of amino acids in EAK16 has also shed light on the effect of charge distribution in peptide-based hydrogels.[89] EAK16-I, EAK16-II, and EAK16-IV – where the numeral suffix indicates the number of charged groups clustered together, e.g., ++++---- for EAK16-IV – were observed to adopt different secondary structures. EAK16-IV was observed to have an increased level of β-turn, indicating the folding of the 16 amino acid sequence and generating a globular morphology, whereas EAK16-I and -II did not demonstrate any level of β-turn and generated a fibrillar morphology. Charge

distribution may also have a biological effect, with RAD16-I demonstrating greater protein adsorption and cell spreading compared to RAD16-II.[90] Therefore, when designing a peptide sequence for biomaterials use, it is important to consider the charge distribution along the peptide chain.

Beyond structural properties, peptides are involved in cell signalling, molecular recognition, and activation pathways. It therefore may be reasoned that mimicking the amino acid sequences responsible for activating certain pathways should lead to the recapitulation of biological effects. Beyond this, synthesising polypeptide sequences should also facilitate the recreation of the material and mechanical properties of proteins, such as collagen or elastin. Following this reasoning, many examples of peptide-based hydrogelators have been synthesised and their potential application in tissue engineering has been demonstrated.[91] These peptide sequences may take on cell adhesion, antimicrobial, or immunomodulatory functions, and may also mimic or bind to specific growth factors. Mimicked growth factors include osteonectin (GHK tripeptide), brain-derived neurotrophic factor (BDNF, RGIDKRHWNSQ sequence), and vascular endothelial growth factor (VEGF, KLTWQELYQLKYKGI sequence). Glycoproteins, such as laminin (IKVAK or YIGSR) or heparin (EDKS) may also be mimicked by peptide sequences, further reinforcing the idea that artificial peptide gels represent a unique class of bio-interactive materials. Synthetic techniques such as solid-phase peptide synthesis (SPPS) facilitates a straightforward method to the production of defined peptide sequences, allowing the growth of peptide libraries for biomaterials use. In addition to pure peptide gels, peptide sequences with structural modifications such as long alkyl tails have also been developed.

1.4.2 Peptide Amphiphiles

One distinct class of peptide-based hydrogelators is peptide amphiphiles (PAs), developed and first reported by Stupp and co-workers in 2001.[92] This class of molecule incorporates many of the self-assembly principles which drive biological systems, and contain rational design “building blocks" which may be modified to impart desired properties on the PA such as hydrogel stiffness, net charge, chemical crosslinking, or bioactivity. These building blocks exploit thermodynamic favourability, hydrophobic clustering, hydrogen bonding, and

electrostatic interactions to yield a molecule which gelates under mild stimuli and maintains a high degree of cytocompatibility. The supramolecular nature of peptide amphiphiles also allows reversible gelation, either by enzyme-mediated degradation or by counterion chelation, facilitating the recovery of entrapped cells for further analysis.[93, 94]

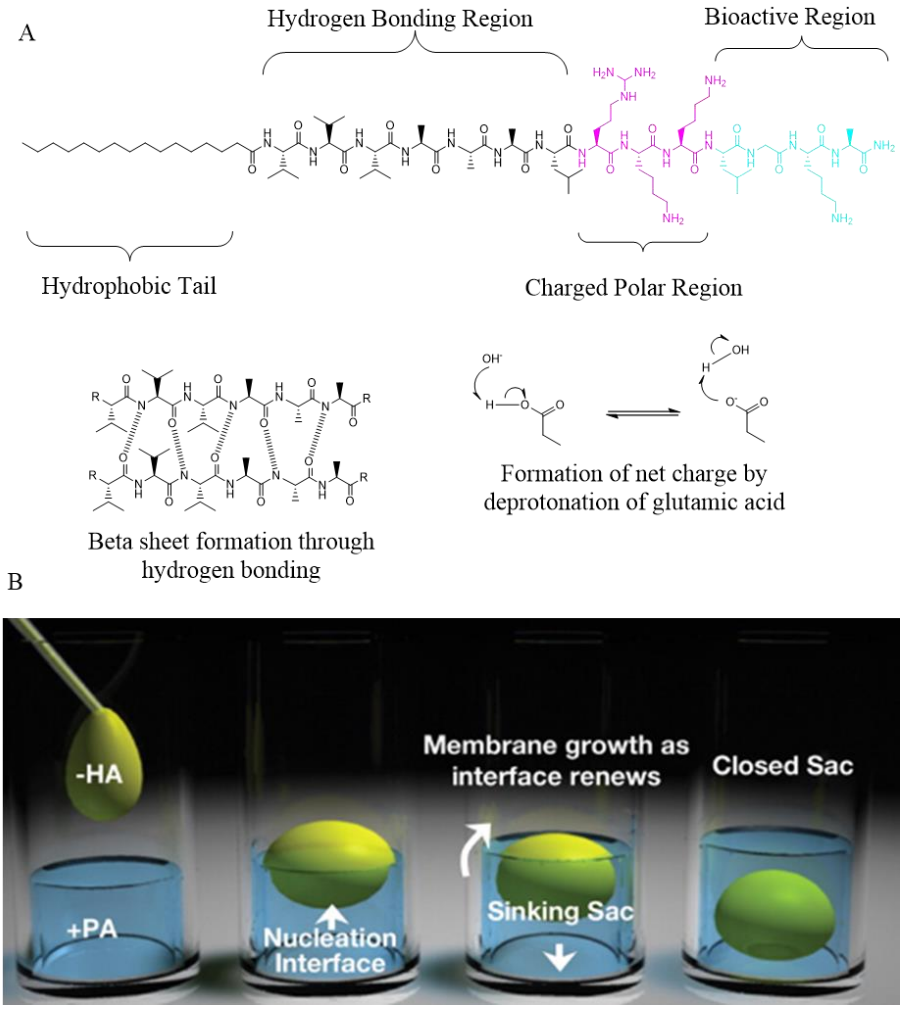

Figure 6: Structure and Use of Peptide Amphiphiles (PAs). ***A)*** *Basic structure of a PA and organising forces. Hydrogen bonding forms parallel β-sheets while the (de)protonation of a charged region aids with solubility and adds a trigger for gelation.* ***B)*** *Formation of hierarchical sacs by the dropwise addition of hyaluronic acid (HA) into a pool of cationic PA. Figure reproduced from Ref 105.*

An alkyl tail contributes greatly to hydrophobic clustering of these amphiphiles in aqueous media. This tail may be between 6 and 22 carbons in length,[95] although greater length contributes greatly to the thermodynamic favourability of self-assembly by increasing the hydrophobic forces at the centre of the cluster. At shorter chain lengths, a greater concentration of the PA is required to gelate. At sufficient length, these alkyl tails make cylindrical packing

thermodynamically favourable, leading to cylindrical micelle formation in solution. Several studies in different PA molecules have also observed such a trend, including more rapid gelation and improved pH stability.[96-98] Beyond gelation kinetics, controlling the hydrophobicity of the PA molecule in its micellar form also facilitates controlled release of hydrophobic drugs.[99]

In addition to length of alkyl chain, its position may either be at the N or C terminus of the peptide. Typically, as a terminal carboxylic acid is present on the alkyl chain, such as in palmitic or stearic acid, coupling is performed at the N terminus. However, as some peptide sequences may only be bioactive in the C-N direction,[100] coupling may need to be performed at the C terminus, typically by coupling to the ε-NH_2 group of a lysine. A more drastic alteration of the alkyl tail may include the introduction of crosslinked or crosslinkable moieties. In one example, a C_{12} alkyl tail of a PA was modified with either an aromatic dialdehyde or an aromatic diamine, which undergo a condensation reaction to form covalent imine bonds between monomers.[101] This system was able to form a hybrid covalent-supramolecular polymer with an unmodified PA in which covalent polymerisation was observed to be catalysed by the presence of the supramolecular PA.

The second segment of PA design is the presence of a β-sheet forming region. Learning from the fundamentals of protein secondary structure, complementary β-sheet forming amino acids are arranged to facilitate the formation of parallel β-sheets. These non-covalent interactions act as an organising and stabilising force, the absence of which from the core amino acids will inhibit the ability of the PA to form long-range fibres, instead resulting in the formation of spherical micelles.[102] The choice, number, and order of hydrogen bonding amino acids can have a direct impact on the resulting gel's mechanical and biological properties. In general, having more hydrogen bonding amino acids such as valine or alanine will result in a more stiff gel.[103] Having more strongly hydrogen bonding amino acids will also increase the stiffness, as will placing these closer to the core of the PA. The degree of hydrogen bonding can also have an impact on the cytotoxicity of the PA, with weak hydrogen bonding such as is observed in glycine being more likely to interact adversely with the cell membrane, resulting in cell death.[104]

Immediately following from the β-sheet forming region, a polar region is often added to PAs consisting of amino acids with chargeable side chains. These may include glutamic acid, lysine, or arginine and aid with the solubility of the PA in aqueous media. Owing to the repulsive electrostatic forces between PA molecules introduced by these charged domains, long-range ordering becomes less energetically favourable. Instead, it is now possible to induce gelation when desired by screening the charges, either by pH alteration or the addition of a counterion. In doing so, the repulsive forces are dampened, and the formation of long-range β-sheets becomes favourable resulting in bulk gel formation. This dampening may be induced by an oppositely-charged macromolecule, and this has been exploited through the self-assembly of a cationic PA with the anionic hyaluronic acid (HA) to form membranous sacs through hierarchical assembly.[105] A cationic PA/HA system has also been used to form a membrane with anti-cancer activity, possibly owing to the overexpression of anionic molecules on the membrane of cancer cells.[106] In a similar system, a cationic PA was triggered to self-assembly by amniotic fluid, fabricating a membrane that may aid in the repair of ruptured foetal membrane.[107]

While this charged region may have bioactive effects, it is possible to further control the biological properties of a PA in the fourth segment of the peptide sequence. This further segment typically contains a bioactive peptide sequence which may mimic or bind growth factors and proteins, be directly involved in cell signalling, or increase cell adhesion. A glycine linker may be present between the charged region and the bioactive epitope. These linkers increase the "exposure" of the bioactive epitope, increasing its efficacy, and stabilise the intermolecular β-sheet formation, improving gel formation. A linker of four glycine residues has been found to be optimal.[108] Regarding the bioactive epitope itself, a vast array of peptides have been conjugated to PA molecules, finding use in angiogenesis,[109, 110] chondrogenesis,[111] and neural tissue repair among other biomedical applications.[112] Among these bioactive epitopes, those which mimic or bind to heparin or heparan sulfate appear to have a broader range of applications than a single-purpose peptide sequence, perhaps owing to the ability of heparins to bind a broad range of active factors.[113]

1.4.3 Heparin-based Peptide Amphiphiles

Heparin is a glycosaminoglycan – a naturally-occurring linear polysaccharide containing carboxylic and sulfonic acid groups along its chain. It is expressed in a range of mammalian tissues, although has been observed to be absent in the brain of mammalian species.[114] Medically, heparin is mainly employed as an anticoagulant owing to its ability to bind to antithrombin and alter its conformation, increasing its activity against thrombin and other factors involved in the coagulation cascade.[115] Recently, there has been a growing body of work demonstrating a broader range of potential applications for heparin.[116] By enhancing blood flow and altering protein behaviour, heparin therapy has been demonstrated to improve the rates of live birth in IVF treatment,[117] repair of the glomerular basement membrane in patients demonstrating proteinuria,[118] and for treatment triglyceride-induced pancreatitis by binding lipoprotein lipases, which are subsequently released in the bloodstream and break down triglycerides.[119] The broad applicability of heparin in a biomedical setting has led to its incorporation into mimetic materials, including the design of heparin-mimetic peptide amphiphiles.

Key structural features of heparin are the presence of carboxylic and sulfonic acid moieties, which also act to impart a net-negative charge on the molecule. Knowing the principles of peptide amphiphile design, it is possible to design a PA with a net negative charge and carboxylic acid groups. This, however, is not sufficient to mimic the behaviours of heparin and sulfonation is required for this to be achieved.[120] For the introduction of a sulfonic acid, a moiety which is not naturally present in amino acids, the modification of a lysine side chain with 4-sulfobenzoic acid has been demonstrated to introduce a sulfonic acid group without inhibiting gelation.[110] This PA sequence, developed by Guler and co-workers, may bind multiple growth factors and release them in a temporally-controlled manner.[121] Heparin-based biomaterials may also aid to improve the half-life of bound proteins, indicating their promise as sustained delivery systems.[122]

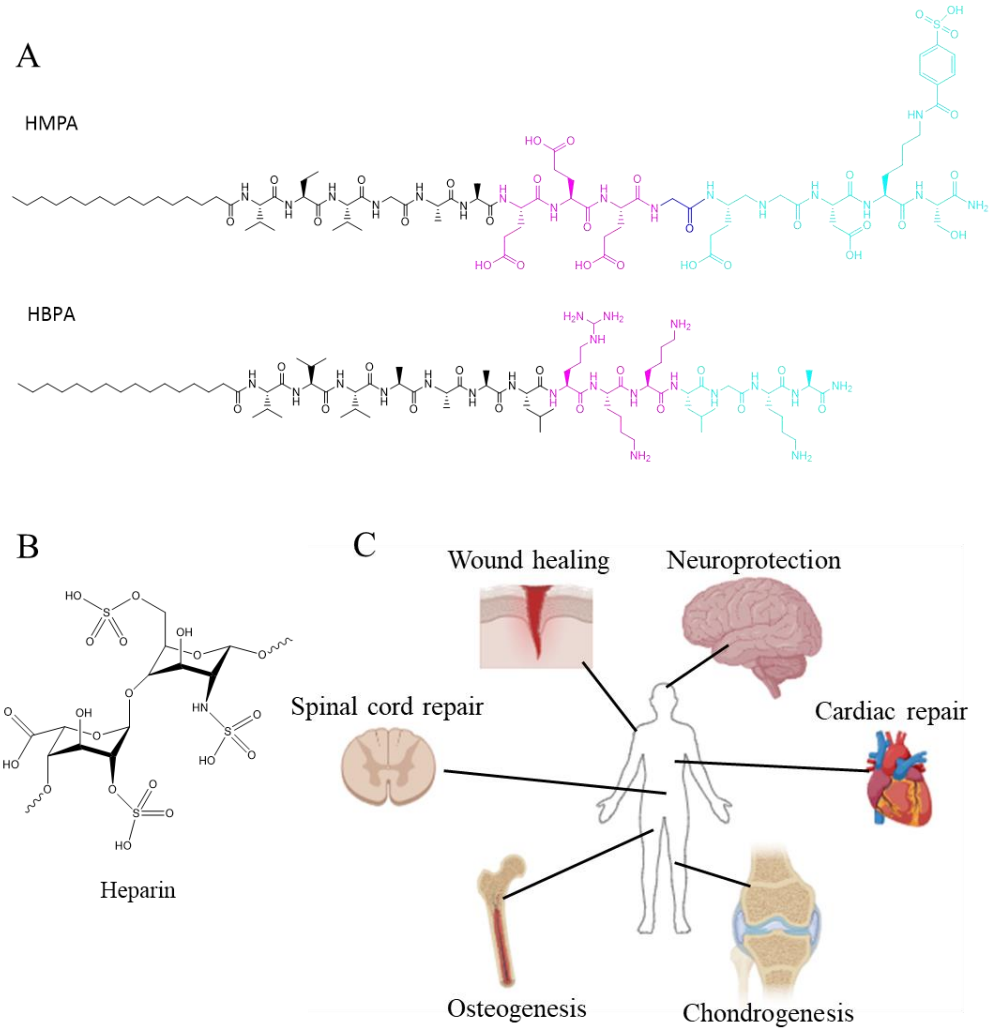

Figure 7: Heparin-based PAs and their Applications. ***A)*** *The structure of both the heparin mimetic (HMPA) and heparin binding (HMPA) PAs.* ***B)*** *The structure of heparin, demonstrating the presence of sulfate, carboxyl, and hydroxyl groups.* ***C)*** *Reported target tissues of heparin-based PA therapies.*

This heparin mimetic sequence has since been demonstrated to have broad range of potential applications. In angiogenesis, this PA has been demonstrated to significantly increase tube formation in endothelial cells compared to a non-sulfonated PA.[110] Such behaviour has been demonstrated to induce wound healing in a diabetic rat model and a full-thickness burn model.[123, 124] In chondrogenesis, this PA may closely mimic the native behaviour of heparin and trigger the chondrogenic differentiation in the ATDC5 cell line, mouse mesenchymal stem cells (mMSCs), and human MSCs.[125-127] By binding with bone morphogenetic protein-2 (BMP-2), the heparin mimetic PA is also able to demonstrate osteogenic behaviour and mineralisation.[128, 129] Here, the behaviour

of heparin regarding cell proliferation is also mimicked, with reduced cell proliferation on heparin-mimetic peptides resulting in increased mineralisation.

One area of research for the use of heparin-mimetic PAs is in the realm of neural tissue regeneration. Heparin is not believed to be present in the brain, so its application here is of particular interest. Indeed, this is perhaps reflected in the moderate binding affinity between heparins and neurotrophic factors.[130] Nonetheless, the protein affinity displayed by the heparin-mimetic PA has been used synergistically with a laminin-mimetic PA bearing the IKVAV sequence.[112] The presence of these two PAs together in the absence of external growth factors was demonstrated to significantly improve neurite outgrowth in rat PC-12 cells, with the effect being more pronounced than heparin-mimetic PA or laminin-mimetic PA used alone. Such an effect was also preserved in ex vivo and in vivo murine models of sciatic nerve injury.[131] Here, the use of the heparin and laminin-mimetic PAs together resulted in increased neurotrophic growth factor (NGF) expression from Schwann cells cultured atop the gels. This resulted in improved neuron repair in vivo, with improved sciatic function observed after injury. Similarly, this system also results in improved recovery following traumatic spinal cord injury in a murine system.[132] Outside of traumatic injuries, this synergistic system has also shown some promise in the treatment of Parkinson's disease (PD), preventing 6-hydroxydopamine (6-OHDA)-induced damage in human in vitro and murine in vivo models of PD. Here, the PA fibres are believed to impart an anti-apoptotic effect on the surrounding cells, protecting them from 6-OHDA damage.

In addition to heparin-mimetic PAs, heparin-binding PA sequences have also been developed. These PAs incorporate the consensus heparin-binding sequence XBBBXBX or XBBXBX, where X is any hydrophobic amino acid and B is any basic amino acid, termed Cardin-Weintraub sequences.[133] One sequence, LRKKLGKA, has been demonstrated to bind heparin with a high affinity.[134] This sequence has been demonstrated to incorporate heparin in a manner which induces angiogenesis in rat cornea.[135] In addition, this sequence, incorporating heparin, has been able to exploit the paracrine effect, recruiting factors secreted from mouse MSCs and being used as a gelled delivery vehicle for these factors in a mouse myocardial infarction model. Good recovery of left ventricular

contractility and relaxation was observed in mice treated with the factor-loaded gel, indicating the potential to further exploit this paracrine effect in heparin-based PA gels.[136]

Summarily, it has been presented so far that a vast array of supramolecular materials is available for use in biomedical settings from drug delivery to tissue repair. Among these, peptide-based materials provide a unique degree of personalisation for a desired application. As such, these materials have found use in the possible repair in a range of target tissues such as the brain, heart, skin, and pancreas. Within the class of peptide-based materials, peptide amphiphiles offer an excellent pathway to control over almost every aspect of a hydrogel. By altering the hydrophobicity, hydrogen bonding, electrostatic interactions, and in some cases π-π interactions, these molecules exploit a range of the fundamentals of biological self-assembly to fabricate functional, versatile materials. However, while it is possible to attain a great degree of bottom-up control in this manner, top-down control over the macroscopic structure of the hydrogel is limited. Therefore, the integration of automated top-down patterning into the fabrication of these hydrogels offers a solution to obtain both bottom-up and top-down control.

1.5 Additive Manufacturing and Biofabrication

1.5.1 Introduction to Additive Manufacturing

Additive manufacturing (AM) is the automated process of fabricating a structure by adding material or parts through deposition, curing, or sintering, as opposed to subtractive manufacturing which fabricates a structure through the removal of material by cutting, milling, or lathing. AM has attracted a great degree of attention due to its versatility and ease of use, facilitating the patterning of concrete for 3D-printed houses, metals for machine parts, and resins for hobbyists. Perhaps the most common method of 3D printing, stereolithography (SLA), was invented in 1984 by Charles Hull.[137] This method involves the layer-by-layer solidification of a photocurable resin by means of UV light projection in a predefined pattern. As the layers form, a 3D structure is created.

Other common methods of AM include layer-by-layer deposition of a quick-setting material through a nozzle (extrusion) or the rapid deposition of low-viscosity droplet onto a substrate (inkjet). Since Hull's SLA invention, other light-based methods of 3D printing have been developed. In 1997, Maruo et al. reported the first use of two-photon polymerisation (2PP) to print 3D dimensional structures with vastly improved spatial resolution.[138] In 2015, this method was used for the 3D printing of scaffolds for cartilage tissue engineering.[139] More recently, in 2019, Kelly et al. reported the use of volumetric additive manufacturing,[140] wherein a photocurable resin is irradiated with UV light while it is rotated within a bath. Such a method results in the printed structure curing at once, with improved surface finish and smoothness compared to layer-by-layer fabrication.

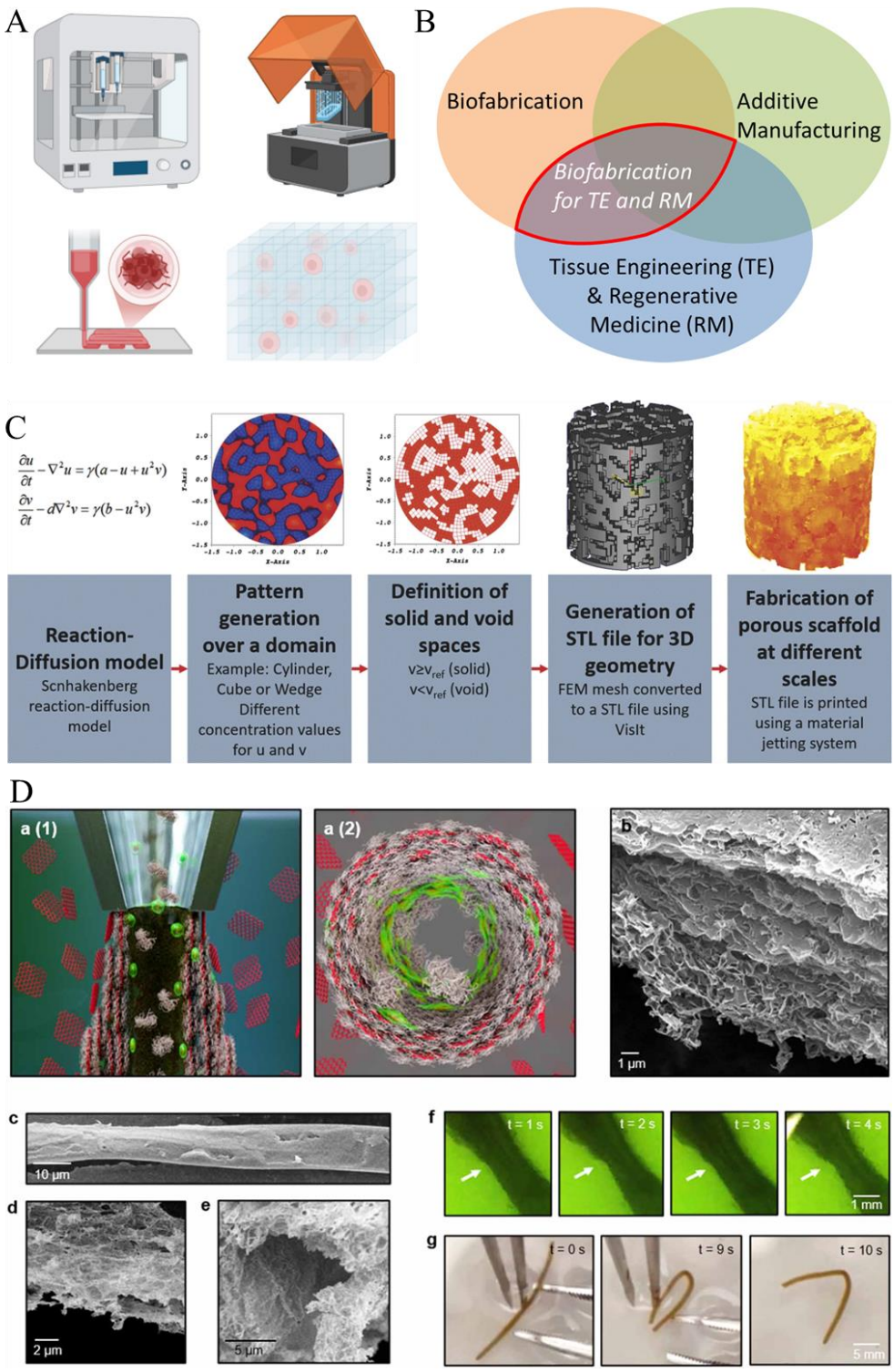

Figure 8: Biofabrication with self-assembly. ***A)*** *Diagrams of common methods of biofabrication: extrusion and digital light processing (DLP). Using these techniques, it is possible to fabricate structures with cells encapsulated.* ***B)*** *Venn diagram indicating the overlap and relation between additive manufacturing (AM), biofabrication, and tissue engineering (TE). Image reproduced from Ref 146.* ***C)*** *Use of reaction-diffusion pattern formation to design a 3D printed bone scaffold mimetic. Image reproduced from Ref 147.* ***D)*** *Extrusion printing of a co-assembled elastin like polypeptide (ELP) and graphene oxide (GO) tubular*

membrane. ELP is extruded into a bath of GO and a membrane is formed at the interface. The resulting tube may be perfused and manually manipulated. Image reproduced from Ref 151.

Given the versatility, reproducibility, and capacity to manufacture in high throughput of AM techniques, these have been integrated into a range of biomaterials for the purpose of precisely controlling the geometry and topology of a scaffold used for cell growth. This may be because a certain geometry is desired, such as a nose or ear for reconstructive surgery,[141] or to pattern spatial cues to actively guide and direct cell growth or differentiation.[142] It has been known since at least 1997 that the patterning of substrates for cell growth can directly impact the behaviour of cells.[143]

The use of AM in this manner falls under the definition of bioprinting, invented by Boland and co-workers in 2003,[144] defined in 2010 as "*the use of computer-aided transfer processes for patterning and assembling living and non-living materials with a prescribed* 2D *or* 3D *organization in order to produce bio-engineered structures serving in regenerative medicine, pharmacokinetic and basic cell biology studies.*".[145] Bioprinting, along with bioassembly, are one of two strategies which constitute "biofabrication", which itself was defined in 2016 as "*the automated generation of biologically functional products with structural organization from living cells, bioactive molecules, biomaterials, cell aggregates such as micro-tissues, or hybrid cell-material constructs, through Bioprinting or Bioassembly and subsequent tissue maturation processes.*".[146] The automated nature of biofabrication introduces both a high degree of control over the final structure and reproducibility, helping to manufacture replicate structures in a high throughput manner. Biofabrication may incorporate any method of AM, provided it fits within this definition, and indeed has been incorporated into inkjet, extrusion, and DLP/SLA technologies.

The capacity to integrate biofabrication with the fundamentals of biological self-assembly and self-organisation has previously been successfully demonstrated.[11] For example, a reaction-diffusion model has been used to generate computer-assisted design (CAD) designs for material jetting of bone scaffolds, recapitulating native bone architecture.[147] Reaction-diffusion patterns printed using DLP have also been demonstrated to impact the rate of growth of algae on surfaces, with different patterns achieving different immobilisation

capacities too.[148] Such an effect may be conserved in mammalian cell scaffolds, especially considering the impact scaffold geometry is known to have on cell adhesion, signalling, and differentiation.[49] Beyond biological principles for scaffold design, the use of supramolecular inks such as those containing self-assembling peptides has also been explored.[149]

One peptide-based example which integrates multiple principles of biological self-assembly is the co-assembly of an elastin-like polypeptide (ELP) with graphene oxide (GO), developed by Mata and co-workers and subsequently integrated into a biofabrication system.[150, 151] In this system an ELP, which exists as an intrinsically disordered peptide, is heated to its characteristic transition temperature. At this point, the ELP begins to undergo hydrophobic collapse, forming insoluble globular structures. When introduced to a dispersion of GO, an interfacial membrane is formed between the two materials, with co-assembly occurring because of the opposing net charges of the two molecules and a hydrophobic driving force. Over time, a reaction-diffusion mechanism drives the growth of the membrane, with the two components diffusing towards the interface. By extruding ELP into GO, it is possible to automate this process and fabricate a membrane which is capable of supporting endothelial cell growth, indicating potential use in vascular modelling and engineering.

Proper ink selection is one of the main challenges for successful biofabrication with supramolecules. Firstly, the ink should be non-toxic and biocompatible. Prior to gelation, the ink should be of an agreeable viscosity for the desired printing technique – if an ink does not flow it may not wet the surface of a DLP platform, or it may be difficult to extrude through a narrow nozzle in an extrusion setting. The gelation time should be fast, to prevent flow and loss of fidelity in extrusion/inkjet or layer distortion in DLP, and the gel should be of an agreeable stiffness for the desired tissue culture. Many popular inks, such as GelMA or sodium alginate, achieve these criteria which contributes to their widespread use. However, these materials do not yield control at the molecular level, limiting the degree to which the biological, physical, and chemical properties of the ink may be designed. These features are vital to mimicking natural extracellular matrix (ECM), and their control is critical in guiding cell signalling, proliferation, and differentiation.[152] To address this need molecules

which may be controlled at the molecular level, such as peptide-based inks, have started to be incorporated into biofabrication, yielding a new class of self-assembling bioinks.

1.5.2 Peptide Amphiphiles in Biofabrication

Peptide-based bioinks – including peptide amphiphiles – are one group of bioinks which are beginning to show promise in biofabrication. These materials may mimic the ECM, and their amino acid sequence may be modulated to impart control over gelation kinetics, gelation triggers, gel stiffness, and bioactivity. These materials, which may be used as single or multi-component inks, facilitate the integration of enhanced molecular complexity and hierarchical structures with emergent properties,[153] one of the key fundamentals of biological self-assembly. Without chemical modification, PAs lack a photo-crosslinkable moiety. Therefore, most reports of their use in biofabrication involve the use of extrusion or inkjet techniques.

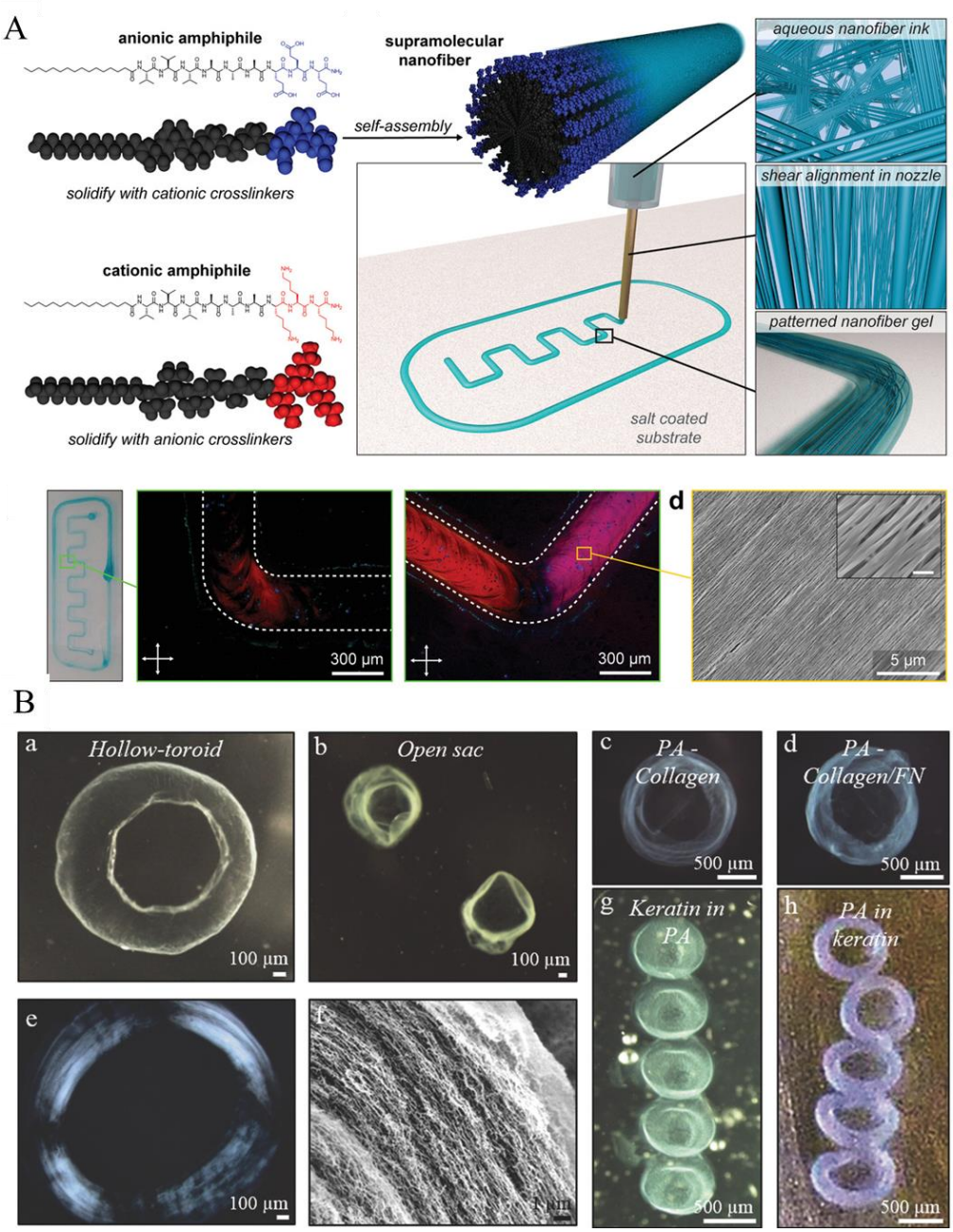

Figure 9: Extrusion and jetting of peptide amphiphile (PA) systems. ***A)*** *Extrusion printing of PAE_3, fabricating a gel with anisotropic alignment of fibres. The structure was beneficial for the culture of myoblasts. Image reproduced from Ref 156.* ***B)*** *Formation of toroidal structures by the jetting of PA solution into an oppositely charged biomolecule, with the alignment of PAK_2 fibres observed in this case (Be&f). Image reproduced from Ref 154.*

In an example of inkjet PA bioprinting, Mata and co-workers demonstrated a hierarchical co-assembly system by jetting a positively-charged PA into a solution of negatively-charged keratin and vice versa.[154] By altering the order of addition, it was possible to fabricate concave gel droplets (keratin into PA) and toroidal structures (PA into keratin). By modulating the jetting speed, it is

possible to achieve control over the diameter of the final printed structure, as well as the surface topology. Demonstrating broader applicability, it was also possible to co-assemble a negatively-charged PA with collagen and a collagen/fibronectin mixture and, by further exploring previous work on the formation of co-assembled PA/HA sacs,[105] it was possible to use jetting to form hollow toroidal gels. Incorporating cells, it was possible to bioprint primary human adipose-derived stem cells (hADSCs) in this system with a viability of 93% compared to a positive control.

Extrusion printing has also been used with PA inks. One PA, PAE_3, may have its fibres uniaxially aligned through thermal annealing.[155] Exploiting this characteristic in 2021, Stupp and co-workers demonstrated the ability to directly control this alignment of fibres through the control of shear in the nozzle of an extrusion 3D printer.[156] By spraying a gelling solution containing a counterion atop a previous layer, it was possible to develop a method fabricating 3D structures composed of multiple layers. In introducing alignment to 3D printed filaments, it was possible to culture myoblasts along the length of these fibres, with decreased electrochemical impedance along the direction of alignment. In contrast, gels with less or non-aligned fibres exhibited poor or no cellular alignment, indicating the importance of this control over fibre structure.

Similarly, Hartgerink and co-workers have also reported the successful extrusion printing of amphipathic peptide sequences in 2023.[157] Here, solutions above 3% w/v of gelator were required to achieve a stiffness capable of forming a self-supporting structure. The extrusion was also limited to a 25 G needle, with narrower gauges resulting in “flaring” of the extruded filament. Furthermore, layer height was therefore limited to 250 μm, and a deviation of 4.9% between CAD and actual print was observed in terms of the thickness of pores in a porous structure. While this study represents a good development in the biofabrication of supramolecular peptide hydrogels, there are still some limitations which may be overcome, such as the resolution and fidelity of prints. In addition, it was noted that, while both cationic and anionic species were observed to be non-toxic to C2C12 cells, proliferation was observed to be greatly increased on a cationic peptide sequence. Such an observation may help to instruct future ink selection in peptide biofabrication.

1.6 Summary

The role of molecular self-assembly in the development and regeneration of biological systems cannot be understated. These non-covalent interactions underpin processes such as cell membrane formation, protein folding, wound healing, cellular organisation, and organ shape, all of which are vital to the continuation of life. In tissue growth and regeneration, these interactions may take the form of physical and biochemical cues, which trigger cell signalling pathways to induce a cascade of cellular behaviours, such as cell recruitment or factor secretion, resulting in a bulk effect such as the healing of a cut.

By mimicking these interactions in synthetic molecules, it is possible to control almost all material, chemical, and biological properties. One class of material, peptide amphiphiles, provides almost unmatched control over its properties. By modulating different sections of the molecule, it is possible to control its 1D formation in solution, the rate of gelation, thickness of fibres, gel stiffness, gelation trigger, overall net charge, and bioactivity. PAs may be used in a self-assembled system alone, may co-assemble with other PAs, or co-assemble with other biomolecules to form a hierarchical structure with emergent properties. Owing to this, PAs have been used in a broad array of biomedical applications covering a range of different tissues.

By integrating PAs into AM techniques, it is possible to achieve control over its bulk structure with high precision and reproducibility. In doing so, 3D printed structures with defined geometries, topologies, and fibre alignments may be fabricated, with potential in, for example, myogenesis or neurogenesis. These purely supramolecular systems typically lack cytotoxic moieties and, owing to their synthetic nature, are typically free of contaminants or endotoxins which may be present in naturally sourced bioinks such as alginates.

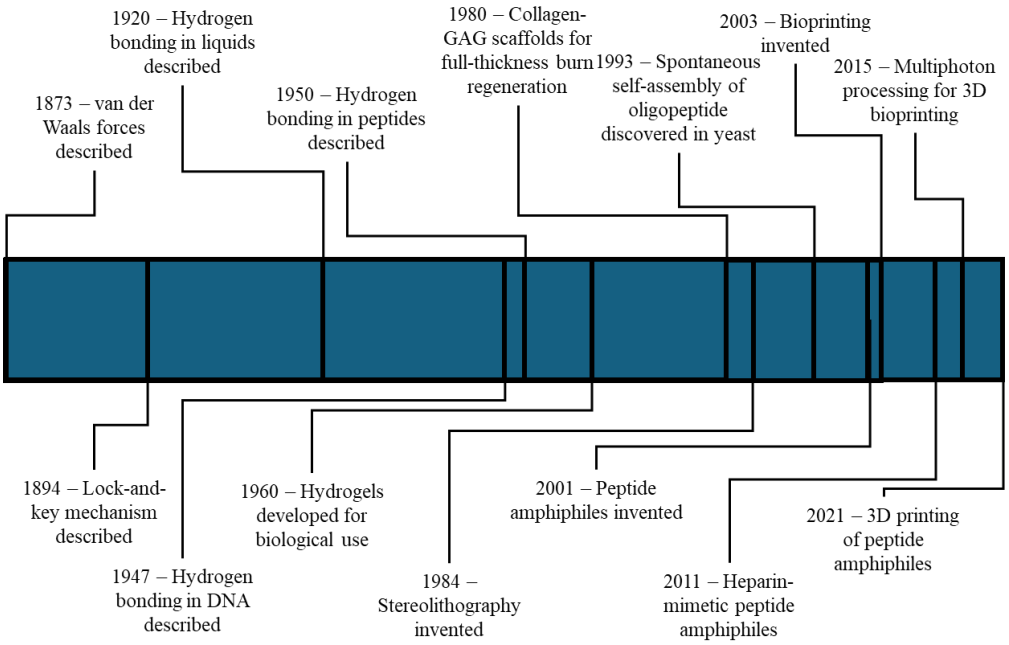

Figure 10: Timeline of key milestones in the additive manufacturing of self-assembling materials for biomedical applications.

In this thesis, it will be demonstrated that the use of PAs in additive manufacturing, although still perhaps in its infancy, holds good potential for the development of active bioinks. The heparin mimetic PA developed by Guler and co-workers,[110] demonstrated to bind and release different active factors, will be fully utilised through the introduction of adipose-derived stem cell secretome (SCS), a highly complex mixture of active factors, cytokines, and extracellular vesicles with known neurogenic properties. This purely supramolecular system will be demonstrated to have a beneficial effect on the outgrowth of neurites, and its incorporation into AM will be explored.

1.7 Aims and Objectives

This thesis aims to deliver a 3D-printable supramolecular system which improves the recovery of motor function in an in vivo spinal cord injury model. In order to do this, several core objectives will be targeted:

- Successfully integrate several additive manufacturing techniques with self-assembling peptides, such as extrusion, SLA, and 2PP. Utilising light-based printing will improve upon current literature which demonstrates only extrusion-based methods.

- Demonstrate that any bioactivity and material properties are conserved when or if successful integration is achieved, such as increased neurite outgrowth compared to an untreated control.
- Show that such materials are non-toxic and biocompatible through the use of cell viability measurements.
- Demonstrate the benefits of using supramolecular materials in biomedical applications compared to covalently crosslinked polymer gels, such as gelatin.
- Use ex vivo models, such as spinal cord slices, to demonstrate neurotrophic benefits of these supramolecular printed materials.

Achieving these objectives, given the few papers which have demonstrated successful integration of self-assembling peptide amphiphiles into additive manufacturing, would demonstrate a contribution to the growing body of work in this area.

1.8 Bibliography

1. van der Waals, J. D. Universiteit Leiden, 1873.
2. Autumn, K.; Sitti, M.; Liang, Y. A.; Peattie, A. M.; Hansen, W. R.; Sponberg, S.; Kenny, T. W.; Fearing, R.; Israelachvili, J. N.; Full, R. J., *Proc. Natl. Acad. Sci.* **2002,** *99* (19), 12252-12256.
3. Fischer, E., *Ber. Dtsch. Chem. Ges.* **1894,** *27* (3), 2985-2993.
4. Park, K. M.; Suh, K.; Jung, H.; Lee, D.-W.; Ahn, Y.; Kim, J.; Baek, K.; Kim, K., *Chem. Commun.* **2009,** (1), 71-73.
5. Ju, H.; Zhu, C. N.; Wang, H.; Page, Z. A.; Wu, Z. L.; Sessler, J. L.; Huang, F., *Adv. Mater.* **2022,** *34* (6), 2108163.
6. Watanakunakorn, C., *J. Antimicrob. Chemother* **1984,** *14* (suppl_D), 7-18.
7. Tipper, D. J.; Strominger, J. L., *Proc Natl Acad Sci U S A* **1965,** *54* (4), 1133-41.
8. Latimer, W. M.; Rodebush, W. H., *J. Am. Chem. Soc.* **1920,** *42* (7), 1419-1433.
9. Creeth, J. M.; Gulland, J. M.; Jordan, D. O., *J. Chem. Soc.* **1947,** (0), 1141-1145.
10. Pauling, L.; Corey, R. B.; Branson, H. R., *Proc. Natl. Acad. Sci.* **1951,** *37* (4), 205-211.
11. Hill, J.; Wildman, R.; Mata, A., *Curr Opin Biotechnol* **2022,** *74*, 42-54.
12. Turing, A. M., *Philos. Trans. R. Soc. B* **1952,** *237* (641), 37-72.
13. Watanabe, M.; Kondo, S., *Trends Genet* **2015,** *31* (2), 88-96.
14. Sick, S.; Reinker, S.; Timmer, J.; Schlake, T., *Science* **2006,** *314* (5804), 1447-1450.
15. Cooper, R. L.; Thiery, A. P.; Fletcher, A. G.; Delbarre, D. J.; Rasch, L. J.; Fraser, G. J., *Sci. Adv.* **2018,** *4* (11), eaau5484.

16. Kondo, S.; Miura, T., *Science* **2010,** *329* (5999), 1616-1620.
17. Berenfeld, O.; Abboud, S., *Med. Eng. Phys.* **1996,** *18* (8), 615-625.
18. Milinkovitch, M. C.; Manukyan, L.; Debry, A.; Di-Poï, N.; Martin, S.; Singh, D.; Lambert, D.; Zwicker, M., *Science* **2013,** *339* (6115), 78-81.
19. Banani, S. F.; Lee, H. O.; Hyman, A. A.; Rosen, M. K., *Nat. Rev. Mol. Cell Biol.* **2017,** *18* (5), 285-298.
20. Li, P.; Banjade, S.; Cheng, H.-C.; Kim, S.; Chen, B.; Guo, L.; Llaguno, M.; Hollingsworth, J. V.; King, D. S.; Banani, S. F.; Russo, P. S.; Jiang, Q.-X.; Nixon, B. T.; Rosen, M. K., *Nature* **2012,** *483* (7389), 336-340.
21. Nizami, Z.; Deryusheva, S.; Gall, J. G., *Cold Spring Harb Perspect Biol* **2010,** *2* (7), a000653.
22. Lang, M.; Jegou, T.; Chung, I.; Richter, K.; Münch, S.; Udvarhelyi, A.; Cremer, C.; Hemmerich, P.; Engelhardt, J.; Hell, S. W.; Rippe, K., *J. Cell Sci.* **2010,** *123* (3), 392-400.
23. Kulkarni, P.; Leite, V. B. P.; Roy, S.; Bhattacharyya, S.; Mohanty, A.; Achuthan, S.; Singh, D.; Appadurai, R.; Rangarajan, G.; Weninger, K.; Orban, J.; Srivastava, A.; Jolly, M. K.; Onuchic, J. N.; Uversky, V. N.; Salgia, R., *Biophys Rev (Melville)* **2022,** *3* (1), 011306.
24. Tang, N. C.; Su, J. C.; Shmidov, Y.; Kelly, G.; Deshpande, S.; Sirohi, P.; Peterson, N.; Chilkoti, A., *Nat. Commun.* **2024,** *15* (1), 3727.
25. Rosenzweig, R.; Sekhar, A.; Nagesh, J.; Kay, L. E., *eLife* **2017,** *6*, e28030.
26. Demarest, S. J.; Martinez-Yamout, M.; Chung, J.; Chen, H.; Xu, W.; Dyson, H. J.; Evans, R. M.; Wright, P. E., *Nature* **2002,** *415* (6871), 549-553.
27. Sivakolundu, S. G.; Nourse, A.; Moshiach, S.; Bothner, B.; Ashley, C.; Satumba, J.; Lahti, J.; Kriwacki, R. W., *J. Mol. Biol.* **2008,** *384* (1), 240-254.
28. Bothner, B.; Lewis, W. S.; DiGiammarino, E. L.; Weber, J. D.; Bothner, S. J.; Kriwacki, R. W., *J. Mol. Biol.* **2001,** *314* (2), 263-277.
29. Ahsendorf, T.; Wong, F.; Eils, R.; Gunawardena, J., *BMC Biol* **2014,** *12*, 102.
30. Foffano, G.; Levernier, N.; Lenz, M., *Nat. Commun.* **2016,** *7* (1), 13827.
31. Ariga, T.; Tomishige, M.; Mizuno, D., *Phys. Rev. Lett.* **2018,** *121* (21), 218101.
32. Genthon, A.; Lacoste, D., *Sci. Rep.* **2020,** *10* (1), 11889.
33. Seifert, U., *Eur. Phys. J. B* **2008,** *64* (3), 423-431.
34. Jou, D.; Perez-Garcia, C.; Llebot, J. E., *J. Theor. Biol.* **1986,** *122* (4), 453-458.
35. Castellana, M.; Bialek, W.; Cavagna, A.; Giardina, I., *Phys. Rev. E.* **2016,** *93* (5), 052416.
36. Vagne, Q.; Salbreux, G., *Phys. Rev. E.* **2025,** *111* (1), 014423.
37. Gillies, A. R.; Lieber, R. L., *Muscle Nerve* **2011,** *44* (3), 318-31.
38. Davie, E. W.; Fujikawa, K.; Kisiel, W., *Biochemistry* **1991,** *30* (43), 10363-70.
39. Ahmadabadi, H. Y.; Yu, K.; Kizhakkedathu, J. N., *Colloids Surf. B Biointerfaces* **2020,** *193*, 111116.
40. Amani, H.; Alipour, M.; Shahriari, E.; Taboas, J. M., *Adv. Healthc. Mater.* **2024,** *13* (29), 2401253.
41. Chambers, H. F., *Emerg Infect Dis* **2001,** *7* (2), 178-82.

42. Kurtz, S.; Ong, K.; Lau, E.; Mowat, F.; Halpern, M., *JBJS* **2007,** *89* (4), 780-785.
43. Yazdani-Ahmadabadi, H.; Yu, K.; Gonzalez, K.; Luo, H. D.; Lange, D.; Kizhakkedathu, J. N., *ACS Appl. Mater. Interfaces* **2024,** *16* (29), 38631-38644.
44. Yu, K.; Alzahrani, A.; Khoddami, S.; Ferreira, D.; Scotland, K. B.; Cheng, J. T. J.; Yazdani-Ahmadabadi, H.; Mei, Y.; Gill, A.; Takeuchi, L. E.; Yeung, E.; Grecov, D.; Hancock, R. E. W.; Chew, B. H.; Lange, D.; Kizhakkedathu, J. N., *Adv. Healthc. Mater.* **2021,** *10* (6), 2001573.
45. Wang, C.; Wang, R.; Li, Y.; Hou, X.; Han, S.; Zhao, X., *J. Colloid Interface Sci.* **2025,** *683*, 521-530.
46. Cui, P.-F.; Zhuang, W.-R.; Hu, X.; Xing, L.; Yu, R.-Y.; Qiao, J.-B.; He, Y.-J.; Li, F.; Ling, D.; Jiang, H.-L., *Chem. Commun.* **2018,** *54* (59), 8218-8221.
47. Morgan, M. T.; Carnahan, M. A.; Immoos, C. E.; Ribeiro, A. A.; Finkelstein, S.; Lee, S. J.; Grinstaff, M. W., *J. Am. Chem. Soc.* **2003,** *125* (50), 15485-15489.
48. Jansen, J. F. G. A.; de Brabander-van den Berg, E. M. M.; Meijer, E. W., *Science* **1994,** *266* (5188), 1226-1229.
49. Martínez-Moreno, D.; Jiménez, G.; Chocarro-Wrona, C.; Carrillo, E.; Montañez, E.; Galocha-León, C.; Clares-Naveros, B.; Gálvez-Martín, P.; Rus, G.; de Vicente, J.; Marchal, J. A., *Mater. Sci. Eng. C* **2021,** *122*, 111933.
50. Buschmann, M. D.; Carrasco, M. J.; Alishetty, S.; Paige, M.; Alameh, M. G.; Weissman, D., *Vaccines* **2021,** *9* (1), 65.
51. Chen, M.; Hu, C.; Zhang, S.; Wu, D.; Mao, Z.; Zheng, X., *Front. Chem.* **2022,** *10*.
52. Ding, Y.; Yu, W.; Wang, J.; Ma, Y.; Wang, C.; Wang, Y.; Lu, B.; Yao, Y., *ACS Macro Lett.* **2022,** *11* (7), 830-834.
53. Dusseault, J.; Tam, S. K.; Ménard, M.; Polizu, S.; Jourdan, G.; Yahia, L. H.; Hallé, J.-P., *J. Biomed. Mater. Res. A* **2006,** *76A* (2), 243-251.
54. Hou, X.; Zaks, T.; Langer, R.; Dong, Y., *Nat. Rev. Mater.* **2021,** *6* (12), 1078-1094.
55. Wichterle, O.; LÍM, D., *Nature* **1960,** *185* (4706), 117-118.
56. Yannas, I. V.; Burke, J. F., *J Biomed Mater Res* **1980,** *14* (1), 65-81.
57. Burke, J. F.; Yannas, I. V.; Quinby, W. C., Jr.; Bondoc, C. C.; Jung, W. K., *Ann Surg* **1981,** *194* (4), 413-28.
58. Bonassar, L. J.; Vacanti, C. A., *J. Cell. Biochem.* **1998,** *72* (S30-31), 297-303.
59. Mondino, B. J.; Salamon, S. M.; Zaidman, G. W., *Surv. Ophthalmol.* **1982,** *26* (6), 337-344.
60. Estroff, L. A.; Hamilton, A. D., *Chem. Rev.* **2004,** *104* (3), 1201-1218.
61. Zhang, S., *Biotechnol. Adv.* **2002,** *20* (5), 321-339.
62. Jeong, B.; Gutowska, A., *Trends Biotechnol.* **2002,** *20* (7), 305-311.
63. Ratner, B. D.; Bryant, S. J., *Annu Rev Biomed Eng* **2004,** *6*, 41-75.
64. Stevens, M. M.; George, J. H., *Science* **2005,** *310* (5751), 1135-1138.
65. Discher, D. E.; Janmey, P.; Wang, Y.-l., *Science* **2005,** *310* (5751), 1139-1143.
66. Jokić, M.; Makarević, J.; Žinić, M., *J. Chem. Soc., Chem. Commun.* **1995,** (17), 1723-1724.

67. Cornwell, D. J.; Okesola, B. O.; Smith, D. K., *Soft Matter* **2013,** *9* (36), 8730-8736.
68. Okesola, B. O.; Smith, D. K., *Chem. Commun.* **2013,** *49* (95), 11164-11166.
69. Yang, Z.; Liang, G.; Ma, M.; Abbah, A. S.; Lu, W. W.; Xu, B., *Chem. Commun.* **2007,** (8), 843-845.
70. López-Acosta, Á.; Chivers, P. R. A.; Piras, C. C.; Kay, A. G.; Genever, P. G.; Smith, D. K., *ChemNanoMat* **2024,** *10* (8), e202400183.
71. Piras, C. C.; Genever, P. G.; Smith, D. K., *Mater. Adv.* **2022,** *3* (21), 7966-7975.
72. Skilling, K. J.; Kellam, B.; Ashford, M.; Bradshaw, T. D.; Marlow, M., *Soft Matter* **2016,** *12* (43), 8950-8957.
73. Wang, Z.; Zhang, Y.; Yin, Y.; Liu, J.; Li, P.; Zhao, Y.; Bai, D.; Zhao, H.; Han, X.; Chen, Q., *Adv. Mater.* **2022,** *34* (13), 2108300.
74. Latxague, L.; Patwa, A.; Amigues, E.; Barthélémy, P., *Molecules* **2013,** *18* (10), 12241-12263.
75. Kumar, S.; Bansal, M., *Proteins:Struct., Funct., Bioinf.* **1998,** *31* (4), 460-476.
76. Wu, Y.-D.; Zhao, Y.-L., *J. Am. Chem. Soc.* **2001,** *123* (22), 5313-5319.
77. Bour, P.; Keiderling, T. A., *Comput. Theor. Chem.* **2004,** *675* (1), 95-105.
78. Ulijn, R. V.; Smith, A. M., *Chem. Soc. Rev.* **2008,** *37* (4), 664-675.
79. Lee, N. R.; Bowerman, C. J.; Nilsson, B. L., *Biomacromolecules* **2013,** *14* (9), 3267-3277.
80. Niece, K. L.; Czeisler, C.; Sahni, V.; Tysseling-Mattiace, V.; Pashuck, E. T.; Kessler, J. A.; Stupp, S. I., *Biomaterials* **2008,** *29* (34), 4501-4509.
81. Cui, H.; Muraoka, T.; Cheetham, A. G.; Stupp, S. I., *Nano Lett.* **2009,** *9* (3), 945-951.
82. Hartgerink, J. D.; Zubarev, E. R.; Stupp, S. I., *Curr. Opin. Solid State Mater. Sci.* **2001,** *5* (4), 355-361.
83. Marini, D. M.; Hwang, W.; Lauffenburger, D. A.; Zhang, S.; Kamm, R. D., *Nano Lett.* **2002,** *2* (4), 295-299.
84. Zhang, S.; Holmes, T.; Lockshin, C.; Rich, A., *Proc Natl Acad Sci U S A* **1993,** *90* (8), 3334-8.
85. Zhang, S.; Holmes, T. C.; DiPersio, C. M.; Hynes, R. O.; Su, X.; Rich, A., *Biomaterials* **1995,** *16* (18), 1385-1393.
86. Holmes, T. C.; de Lacalle, S.; Su, X.; Liu, G.; Rich, A.; Zhang, S., *Proc Natl Acad Sci U S A* **2000,** *97* (12), 6728-33.
87. Lee, M. F.-H.; Ananda, A., *Auris Nasus Larynx* **2023,** *50* (3), 365-373.
88. Sankar, S.; O'Neill, K.; Bagot D'Arc, M.; Rebeca, F.; Buffier, M.; Aleksi, E.; Fan, M.; Matsuda, N.; Gil, E. S.; Spirio, L., *Front. bioeng. biotechnol.* **2021,** *9*.
89. Jun, S.; Hong, Y.; Imamura, H.; Ha, B. Y.; Bechhoefer, J.; Chen, P., *Biophys J* **2004,** *87* (2), 1249-59.
90. Sieminski, A. L.; Semino, C. E.; Gong, H.; Kamm, R. D., *J. Biomed. Mater. Res. A* **2008,** *87A* (2), 494-504.
91. Ligorio, C.; Mata, A., *Nat. Rev. Bioeng.* **2023,** *1* (7), 518-536.
92. Hartgerink, J. D.; Beniash, E.; Stupp, S. I., *Science* **2001,** *294* (5547), 1684-1688.
93. Jun, H.-W.; Yuwono, V.; Paramonov, S. E.; Hartgerink, J. D., *Adv. Mater.* **2005,** *17* (21), 2612-2617.

94. Ligorio, C.; Martinez-Espuga, M.; Laurenza, D.; Hartley, A.; Rodgers, C. B.; Kotowska, A. M.; Scurr, D. J.; Dalby, M. J.; Ordóñez-Morán, P.; Mata, A., *J. Mater. Chem. B* **2024,** *12* (46), 11939-11952.
95. Hartgerink, J. D.; Beniash, E.; Stupp, S. I., *Proc. Natl. Acad. Sci. U.S.A.* **2002,** *99* (8), 5133-5138.
96. Fry, H. C.; Peters, B. L.; Ferguson, A. L., *J. Phys. Chem. B.* **2021,** *125* (5), 1317-1330.
97. Xu, X.-D.; Jin, Y.; Liu, Y.; Zhang, X.-Z.; Zhuo, R.-X., *Colloids Surf. B Biointerfaces* **2010,** *81* (1), 329-335.
98. Castelletto, V.; Kaur, A.; Kowalczyk, R. M.; Hamley, I. W.; Reza, M.; Ruokolainen, J., *Biomacromolecules* **2017,** *18* (7), 2013-2023.
99. Dube, N.; Seo, J. W.; Dong, H.; Shu, J. Y.; Lund, R.; Mahakian, L. M.; Ferrara, K. W.; Xu, T., *Biomacromolecules* **2014,** *15* (8), 2963-2970.
100. Okur, Z.; Senturk, O. I.; Yilmaz, C.; Gulseren, G.; Mammadov, B.; Guler, M. O.; Tekinay, A. B., *Biomater. Sci.* **2018,** *6* (7), 1777-1790.
101. Yu, Z.; Tantakitti, F.; Yu, T.; Palmer, L. C.; Schatz, G. C.; Stupp, S. I., *Science* **2016,** *351* (6272), 497-502.
102. Paramonov, S. E.; Jun, H.-W.; Hartgerink, J. D., *J. Am. Chem. Soc.* **2006,** *128* (22), 7291-7298.
103. Pashuck, E. T.; Cui, H.; Stupp, S. I., *J Am Chem Soc* **2010,** *132* (17), 6041-6.
104. Newcomb, C. J.; Sur, S.; Ortony, J. H.; Lee, O.-S.; Matson, J. B.; Boekhoven, J.; Yu, J. M.; Schatz, G. C.; Stupp, S. I., *Nat. Commun.* **2014,** *5* (1), 3321.
105. Capito, R. M.; Azevedo, H. S.; Velichko, Y. S.; Mata, A.; Stupp, S. I., *Science* **2008,** *319* (5871), 1812-1816.
106. Utsugi, T.; Schroit, A. J.; Connor, J.; Bucana, C. D.; Fidler, I. J., *Cancer Res.* **1991,** *51* (11), 3062-3066.
107. Barrett, D. W.; Okesola, B. O.; Costa, E.; Thrasivoulou, C.; Becker, D. L.; Mata, A.; Deprest, J. A.; David, A. L.; Chowdhury, T. T., *Prenat. Diagn.* **2021,** *41* (1), 89-99.
108. Taraballi, F.; Natalello, A.; Campione, M.; Villa, O.; Doglia, S. M.; Paleari, A.; Gelain, F., *Front Neuroeng* **2010,** *3*, 1.
109. Ghanaati, S.; Webber, M. J.; Unger, R. E.; Orth, C.; Hulvat, J. F.; Kiehna, S. E.; Barbeck, M.; Rasic, A.; Stupp, S. I.; Kirkpatrick, C. J., *Biomaterials* **2009,** *30* (31), 6202-12.
110. Mammadov, R.; Mammadov, B.; Toksoz, S.; Aydin, B.; Yagci, R.; Tekinay, A. B.; Guler, M. O., *Biomacromolecules* **2011,** *12* (10), 3508-3519.
111. Yaylaci, S.; Guler, M. O.; Tekinay, A. B., *Regen. Biomater.* **2022,** *10*.
112. Mammadov, B.; Mammadov, R.; Guler, M. O.; Tekinay, A. B., *Acta Biomater.* **2012,** *8* (6), 2077-2086.
113. Forsten, K. E.; Fannon, M.; Nugent, M. A., *J. Theor. Biol.* **2000,** *205* (2), 215-230.
114. Nader, H. B.; Takahashi, H. K.; Straus, A. H.; Dietrich, C. P., *Biochim. Biophys. Acta, Gen. Subj.* **1980,** *627* (1), 40-48.
115. Gray, E.; Hogwood, J.; Mulloy, B., *Handb Exp Pharmacol* **2012,** (207), 43-61.
116. Chen, D., *Curr. Res. Transl. Med.* **2021,** *69* (4), 103300.
117. Dentali, F.; Grandone, E.; Rezoagli, E.; Ageno, W., *J. Thromb. Haemost* **2011,** *9* (12), 2503-2506.

118. Lewis, E. J.; Xu, X., *Diabetes Care* **2008,** *31* (Supplement_2), S202-S207.
119. Hammond, D. A.; Finlay, L., *Hosp. Pharm.* **2017,** *52* (10), 675-678.
120. Tamada, Y.; Murata, M.; Makino, K.; Yoshida, Y.; Yoshida, T.; Hayashi, T., *Biomaterials* **1998,** *19* (7), 745-750.
121. Mammadov, R.; Mammadov, B.; Guler, M. O.; Tekinay, A. B., *Biomacromolecules* **2012,** *13* (10), 3311-3319.
122. Chopra, P.; Logun, M. T.; White, E. M.; Lu, W.; Locklin, J.; Karumbaiah, L.; Boons, G. J., *ACS Chem Biol* **2019,** *14* (9), 1921-1929.
123. Senturk, B.; Mercan, S.; Delibasi, T.; Guler, M. O.; Tekinay, A. B., *ACS Biomater. Sci. Eng.* **2016,** *2* (7), 1180-1189.
124. Yergoz, F.; Hastar, N.; Cimenci, C. E.; Ozkan, A. D.; Tekinay, T.; Guler, M. O.; Tekinay, A. B., *Biomaterials* **2017,** *134*, 117-127.
125. Ustun, S.; Tombuloglu, A.; Kilinc, M.; Guler, M. O.; Tekinay, A. B., *Biomacromolecules* **2013,** *14* (1), 17-26.
126. Ustun Yaylaci, S.; Sardan Ekiz, M.; Arslan, E.; Can, N.; Kilic, E.; Ozkan, H.; Orujalipoor, I.; Ide, S.; Tekinay, A. B.; Guler, M. O., *Biomacromolecules* **2016,** *17* (2), 679-689.
127. Yaylaci, S. U.; Sen, M.; Bulut, O.; Arslan, E.; Guler, M. O.; Tekinay, A. B., *ACS Biomater. Sci. Eng.* **2016,** *2* (5), 871-878.
128. Kocabey, S.; Ceylan, H.; Tekinay, A. B.; Guler, M. O., *Acta Biomater.* **2013,** *9* (11), 9075-9085.
129. Tansik, G.; Kilic, E.; Beter, M.; Demiralp, B.; Kiziltas Sendur, G.; Can, N.; Ozkan, H.; Ergul, E.; Guler, M. O.; Tekinay, A. B., *Biomater. Sci.* **2016,** *4* (9), 1328-1339.
130. Chu, H.; Johnson, N. R.; Mason, N. S.; Wang, Y., *J. Control. Release.* **2011,** *150* (2), 157-163.
131. Mammadov, B.; Sever, M.; Gecer, M.; Zor, F.; Ozturk, S.; Akgun, H.; Ulas, U. H.; Orhan, Z.; Guler, M. O.; Tekinay, A. B., *RSC Adv.* **2016,** *6* (112), 110535-110547.
132. Sever-Bahcekapili, M.; Yilmaz, C.; Demirel, A.; Kilinc, M. C.; Dogan, I.; Caglar, Y. S.; Guler, M. O.; Tekinay, A. B., *Macromol. Biosci.* **2021,** *21* (1), 2000234.
133. Cardin, A. D.; Weintraub, H. J., *Arteriosclerosis* **1989,** *9* (1), 21-32.
134. Rajangam, K.; Arnold, M. S.; Rocco, M. A.; Stupp, S. I., *Biomaterials* **2008,** *29* (23), 3298-3305.
135. Rajangam, K.; Behanna, H. A.; Hui, M. J.; Han, X.; Hulvat, J. F.; Lomasney, J. W.; Stupp, S. I., *Nano Lett.* **2006,** *6* (9), 2086-2090.
136. Webber, M. J.; Han, X.; Prasanna Murthy, S. N.; Rajangam, K.; Stupp, S. I.; Lomasney, J. W., *J Tissue Eng Regen Med.* **2010,** *4* (8), 600-610.
137. Hull, C. W. Apparatus for production of three-dimensional objects by stereolithography. 1984.
138. Maruo, S.; Nakamura, O.; Kawata, S., *Opt. Lett.* **1997,** *22* (2), 132-134.
139. Mačiulaitis, J.; Deveikytė, M.; Rekštytė, S.; Bratchikov, M.; Darinskas, A.; Šimbelytė, A.; Daunoras, G.; Laurinavičienė, A.; Laurinavičius, A.; Gudas, R.; Malinauskas, M.; Mačiulaitis, R., *Biofabrication* **2015,** *7* (1), 015015.
140. Kelly, B. E.; Bhattacharya, I.; Heidari, H.; Shusteff, M.; Spadaccini, C. M.; Taylor, H. K., *Science* **2019,** *363* (6431), 1075-1079.

141. Yang, P.; Ju, Y.; Hu, Y.; Xie, X.; Fang, B.; Lei, L., *Biomater. Res.* **2023,** *27* (1), 1.
142. Lai, H.; Gong, B.; Yin, J.; Qian, J., *Mater. Des.* **2022,** *218*, 110663.
143. Chen, C. S.; Mrksich, M.; Huang, S.; Whitesides, G. M.; Ingber, D. E., *Science* **1997,** *276* (5317), 1425-1428.
144. Mironov, V.; Boland, T.; Trusk, T.; Forgacs, G.; Markwald, R. R., *Trends Biotechnol.* **2003,** *21* (4), 157-161.
145. Guillemot, F.; Mironov, V.; Nakamura, M., *Biofabrication* **2010,** *2* (1), 010201.
146. Groll, J.; Boland, T.; Blunk, T.; Burdick, J. A.; Cho, D.-W.; Dalton, P. D.; Derby, B.; Forgacs, G.; Li, Q.; Mironov, V. A.; Moroni, L.; Nakamura, M.; Shu, W.; Takeuchi, S.; Vozzi, G.; Woodfield, T. B. F.; Xu, T.; Yoo, J. J.; Malda, J., *Biofabrication* **2016,** *8* (1), 013001.
147. Velasco, M. A.; Lancheros, Y.; Garzón-Alvarado, D. A., *J. Comput. Des. Eng.* **2016,** *3* (4), 385-397.
148. Abdallah, Y. K.; Estévez, A. T., *Buildings* **2023,** *13* (8), 1972.
149. Khan, Z.; Kahin, K.; Rauf, S.; Ramirez-Calderon, G.; Papagiannis, N.; Abdulmajid, M.; Hauser, C. A. E., *Int J Bioprint* **2019,** *5* (1), 173.
150. Wu, Y.; Okesola, B. O.; Xu, J.; Korotkin, I.; Berardo, A.; Corridori, I.; di Brocchetti, F. L. P.; Kanczler, J.; Feng, J.; Li, W.; Shi, Y.; Farafonov, V.; Wang, Y.; Thompson, R. F.; Titirici, M.-M.; Nerukh, D.; Karabasov, S.; Oreffo, R. O. C.; Carlos Rodriguez-Cabello, J.; Vozzi, G.; Azevedo, H. S.; Pugno, N. M.; Wang, W.; Mata, A., *Nat. Commun.* **2020,** *11* (1), 1182.
151. Wu, Y.; Fortunato, G. M.; Okesola, B. O.; Brocchetti, F. L. P. D.; Suntornnond, R.; Connelly, J.; De Maria, C.; Rodriguez-Cabello, J. C.; Vozzi, G.; Wang, W.; Mata, A., *Biofabrication* **2021,** *13* (3), 035027.
152. Lutolf, M. P.; Hubbell, J. A., *Nat. Biotechnol.* **2005,** *23* (1), 47-55.
153. Hedegaard, C. L.; Mata, A., *Biofabrication* **2020,** *12* (3), 032002.
154. Hedegaard, C. L.; Collin, E. C.; Redondo-Gómez, C.; Nguyen, L. T. H.; Ng, K. W.; Castrejón-Pita, A. A.; Castrejón-Pita, J. R.; Mata, A., *Adv. Funct. Mater* **2018,** *28* (16), 1703716.
155. Zhang, S.; Greenfield, M. A.; Mata, A.; Palmer, L. C.; Bitton, R.; Mantei, J. R.; Aparicio, C.; de la Cruz, M. O.; Stupp, S. I., *Nat. Mater.* **2010,** *9* (7), 594-601.
156. Sather, N. A.; Sai, H.; Sasselli, I. R.; Sato, K.; Ji, W.; Synatschke, C. V.; Zambrotta, R. T.; Edelbrock, J. F.; Kohlmeyer, R. R.; Hardin, J. O.; Berrigan, J. D.; Durstock, M. F.; Mirau, P.; Stupp, S. I., *Small* **2021,** *17* (5), 2005743.
157. Farsheed, A. C.; Thomas, A. J.; Pogostin, B. H.; Hartgerink, J. D., *Adv. Mater.* **2023,** *35* (11), 2210378.

2. Self-assembling Hydrogels for Neural Tissue Engineering

2.1 Introduction

Biological complexity was used as a key fundamental to underpin this study. Treating biology as a complex system allows us to begin to understand why physiological systems function as they do.[1] Emergent functions may only exist with a sufficient degree of complexity.[2] Hydrogen bonding, for example, may only occur in the presence of an H-bond donor and H-bond acceptor. Single proteins may not be active alone, but together they may form vital cell-membrane structures or signalling cascades which are vital to life. Blood clotting, too, is an emergent function which only occurs if all necessary steps in the blood clotting cascade are achieved.[3] It can therefore be seen that biological complexity underpins a great deal of physiological function, and that it is not unreasonable to want to exploit it in tissue engineering. However, complexity on a biological scale is something which is difficult, time-consuming, and expensive to engineer synthetically. Therefore, we turned to the complexity exhibited in nature, exploiting the factors which are secreted by adipose-derived stem cells as they proliferate as a material termed the stem cell secretome (SCS).

As stem cells proliferate in culture, they secrete a vast number of soluble factors and extracellular vesicles, including growth factors, cytokines, mRNAs, and bioactive lipids. These factors activate paracrine signalling pathways,[4] and it is this paracrine signalling theory which is currently believed to be the primary mechanism for the efficacy of stem cell therapy.[5] Stem cell therapy, however, has significant shortcomings in that implanted cells are liable to immune rejection or teratocarcinoma formation. In the case of therapy using only paracrine factors, these limitations are removed.

Factors in SCS have, across studies, been found to be significantly upregulated in comparison to a random population.[6] This upregulation contributes greatly to an increased bioactivity, resulting in antiapoptotic,[7] osteogenic,[8] angiogenic,[9] and neurogenic properties.[10] Additionally, SCS therapy has been found to

improve outcomes in dermal wound healing,[11] retinal ischemia,[12] and even hair loss.[13] Across multiple studies, however, neurological applications of SCS appear to be its most effective application, with over 17% of factors in adipose-derived stem cell secretome being reported to be involved in neuronal outgrowth or neural communication.[14] Indeed, meta-analysis of SCS for the treatment of traumatic brain injury found statistically significant improvement in recovery across 31 studies of murine and porcine treatment.[15] SCS therapy has also been found to significantly improve outcomes in murine models of ischemic brain injury, Alzheimer's disease, spinal cord injury, multiple sclerosis, and sciatic nerve transection.[16] This neurological activity appears preserved across SCS from multiple tissue sources, and does not deviate significantly based on the source.

However, despite clinical potential and promising in vivo data, SCS still encounters some limitations in its use. Chiefly, SCS injected into target tissue is typically subject to a rapid clearance time and may be washed away from the site of administration. Such an event would likely reduce any beneficial effect. Furthermore, factors which are free floating in media are subject to the same half-lives as all proteins, and their efficacy may reduce over time. To overcome both these limitations, it may be beneficial to encapsulate the SCS within a biomaterial and allow factors to diffuse outwards over time at the site of implantation. Multiple polymeric hydrogels, such as collagen or silk fibroin, have been used to encapsulate and release secretome over time.[17] Across these studies, the slow-release was observed to increase the rate at which tissue regenerated, indicating a benefit to biomaterial-secretome materials. However, no examples were found of using a supramolecular hydrogel to bind the factors in the secretome, rather than simply encapsulate factors within the pores of a gel. Binding factors may increase their half-life,[18] and therefore it is hoped that by using supramolecular materials, the therapeutic effect of the SCS may be further increased.

2.2 Aims and Objectives

Here, it was aimed that a functional material was developed which incorporated many or all the SCS into it for controlled release. This gel would ideally be peptide-based to be completely biological in nature and reduce possible toxicity.

This gel should form under biological conditions and not require toxic crosslinkers, extreme temperatures or pH levels to form. Finally, the gel should be of a stiffness which is biologically relevant to the tissue in which it will be implanted. In this case, this would be spinal cord matter.

Once such a gel is developed, it should demonstrate the ability to bind multiple proteins and release these in a controlled manner, so that any possible implantation would require only one operation to implant the gel for sustained release. On top of this, the gel should degrade in a reasonable timeframe to allow for full tissue regeneration in its place.

Finally, the developed gel – loaded with SCS – should demonstrate a degree of neurotrophy. This may come in the form of improved neurite outgrowth in neuronal cells, or improve survival of mature neurons, or increased gene expressions associated with neuron recovery and growth. Such an experiment would indicate the potential for this gel to restore motor function in a spinal cord injury model.

2.3 The Stem Cell Secretome

The stem cell secretome was provided by members of the Salgado Group at the University of Minho, Portugal. Briefly, adipose-derived stem cells (ASCs) were cultured until passage 5, at which point the growth media was collected and transferred to a centrifugal concentrator (Figure 11A). The solution was centrifuged to yield a roughly 100x concentrated SCS containing 200 μg/mL of proteins as determined by Bradford Assay (data not shown). Upon receipt, SCS was stored at -20 °C until use in a sterile environment. Before use, it was determined that it was necessary to attempt to understand the nature of the SCS. Therefore, proteomics was chosen for qualitative analysis and prediction of proteins present. Samples for proteomics were analysed by liquid chromatography with tandem mass spectrometry (LC/MS-MS) (see section 2.9.12 for methodology).

LC/MS-MS revealed a great deal of detail regarding the composition of the SCS. It was observed that 537 proteins were detected (Figure 11B), a number similar to those which have been reported for stem cell secretomes.[19] It may also be possible that other factors are present, but at a concentration below the

limit of detection. Most factors were predicted to possess a molecular weight of <100 kDa, a measure which was supported by SDS analysis (Figure 11G inset). The broad range of proteins across a range of mWs is also supported by the weak signal provided by staining with a sensitivity of 5 ng protein. As the concentration of protein in the SCS had been measured at 200 µg mL^{-1}, a total of 1,300 ng of protein was present for SDS-PAGE. This results in an average of 2.42 ng per protein, nearing the lower detection limit of the stain. A silver staining procedure would have been more suited to this low concentration.

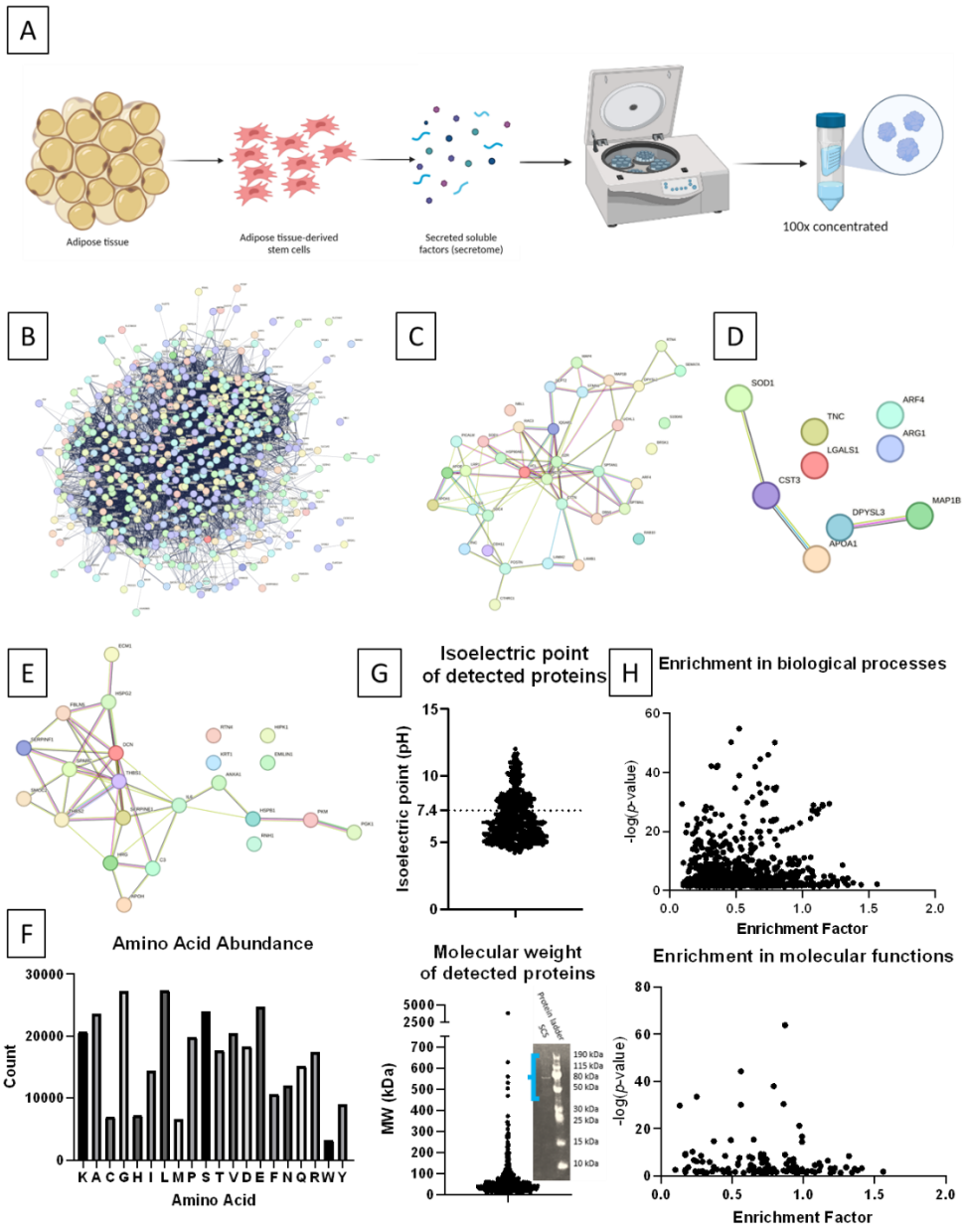

Figure 11: Secretome collection and characterisation. A: Schematic of secretome preparation. B: Protein-protein interaction map of entire secretome. Nodes represent individual proteins while edges represent known interactions. Generated using StringDB. C-E: Protein-protein interaction maps of proteins detected

in the secretome which are involved in (C) neuron projection development, (D) response to axon injury, and (E) regulation of angiogenesis. F: Breakdown of the abundance of each amino acid within the secretome. G: Plots of the (upper) isoelectric points and (lower) molecular weights of the detected proteins. (Inset lower) SDS-PAGE of the entire secretome. H: Ontological analysis of enriched processes and functions in the secretome. Enrichment factor is plotted on the x axis, with a greater value indicating greater enrichment, while the $-\log_{10}$(p-value) is plotted on the y axis, with a greater value indicating lower false discovery probability.

STRING (https://string-db.org/) ontological analysis indicated that, between these factors, there are 10,840 known interactions governing a total of 883 different biological processes, with each protein having an average of 40.3 interactions. For comparison, a random population of 537 proteins would be expected to possess just 4,194 interactions, so we observe here a 158.5% increase in biological activity (PPI enrichment p-value $<1\text{x}10^{-16}$). Of the detected factors, 93 are implicated in nervous system development, 33 are implicated in neuron projection development, and 9 are involved in the response to axon injury. Gene ontology (GeO) enrichment analysis of biological processes (Figure 11H) indicated enrichment of factors involved in axon regeneration of the peripheral nervous system (1.26), response to axon injury (0.81), and neuron projection development (0.28). Heparin binding was also enriched (0.63), indicating that SCS contains more heparin binding factors than a random population and is thus suited to heparin-based materials. Here, enrichment is calculated using:

$$log_{10} \frac{observed\ no.\ associated\ proteins}{expected\ no.\ associated\ proteins}.$$

Equation 1: Calculation of the enrichment of biological processes in the stem cell secretome.

Therefore, any value above 0 indicates enrichment. In total, significant (p<0.05) enrichment was observed in 873 biological processes and 121 molecular functions. From this ontological analysis, we can predict that this batch of secretome should possess a degree of biological activity in a wide range of functions. The upregulation of factors involved in neurological processes indicate its potential in central nervous system (CNS) therapeutics.

Beyond neurological properties, 49 of the predicted proteins are known to be involved in wound healing, an enrichment of 0.61. Proteins involved in endothelial cell development were upregulated with an enrichment of 0.66.

Endochondral bone growth (0.76), angiogenesis (0.33), and muscle cell differentiation (0.46) were all significantly enriched. This diverse array of biological activity predicted to be present in the SCS indicates that it may also find use beyond neurological applications, and that its efficacy is derived from the abundance of upregulated proteins.

It was also observed that most of the proteins present in the SCS exhibit an isoelectric point (pI) below a pH of 7.4 (Figure 11G), indicating that many proteins in this solution will carry a net negative charge under physiological conditions. This is not unexpected but helps in guiding biomaterial design. Materials which hope to bind large numbers and varieties of proteins for increased complexity should either carry a net positive charge to maximise electrostatic interactions or should aim to mimic bioactive molecules which are known to effect multiple binding.

The most abundant proteins present in the secretome were found to be keratins, collagens, fibronectin, albumin, vimentin, and periostin (Figure 12). Keratins are typically expressed by mammalian epithelial cells, although there is evidence that adipose tissue – from which the stem cells which produced this secretome are derived – also expresses keratins.[20] Keratin itself may act as a scaffold for cell adhesion and proliferation, and there is some evidence that it may play an active role in wound healing.[21] Here, however, it may also be possible that keratin is present from the handling of the secretome.

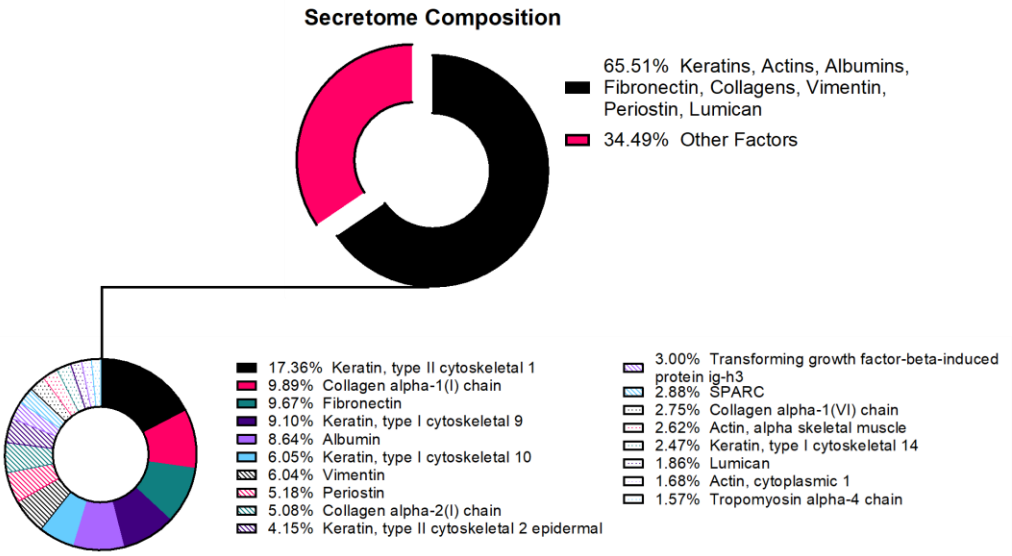

Figure 12: Breakdown of the most abundant proteins present in the secretome as predicted by LC-MS/MS.

The proteins predicted which are known to have, or may have, neuroactive properties include MAP1B, tenascin, CTTN, IL-6, drebrin-1, and stathmin. In total, of proteins implicated in neuron projection development (36 total), there are also 82 reported interactions between these proteins. This highly interactive network further supports the idea that SCS will act as an effective treatment for neural tissue damage. Beyond this, 64 proteins present are involved in aiding cell adhesion, indicating that the presence of secretome in a hydrogel which lacks adhesion motifs may help to overcome issues associated with this.

It should be noted, however, that secretome in literature displays a degree of variation between batches. Different proteomic profiles may be observed, as has been reported in previous studies.[19] Therefore, while the data here are useful for this study and may be indicative of the possible proteomic profile of adipose-derived stem cell secretome elsewhere, they should not be applied to other batches. Conversely, it may also be noted that there are proteins which are regularly conserved and are observed in multiple studies. It would be interesting, in future work, to explore the impact of batch-to-batch variability by comparing the biological effects of SCS from different labs and countries.

Having determined the composition of the secretome and identified key neurotrophic factors, it now remains to design a material which may yield a functional material capable of both controlled release and supporting tissue

growth. Here, peptide amphiphiles were used as a biocompatible, customisable class of material.

2.4 Hydrogel Design

2.4.1 Introduction and Rationale

The physiochemical properties of peptide amphiphiles may be directly controlled on a molecular scale. Here, PAs with the generic sequence $C_{16}V_3A_3$ were used as a base. A C_{16} tail yields optimal fibre formation and stability owing to the ideal hydrophobicity and size. A V_3A_3 β-sheet forming region typically yields gels of agreeable stiffness for 3D cell culture at around 10 kPa. Modification of the β-sheet forming region, such as V_2A_2, may have allowed further modulation of the stiffness of the gel, but the initial scope focussed on achieving gelation incorporating secretome components. Therefore, it was determined that PAs would be investigated systematically to ascertain useful sequences (Table 1).

Table 1: List of PAs used in Section 2.3. "PA" in each sequence refers to "Peptide Amphiphile", while subsequent letters are single letter amino acid codes. "NH_2" denotes amine-terminated sequences.

PA Name	*Full Sequence*	*Purpose*
PAE_2	$C_{16}V_3A_3E_2$-NH_2	Filler
PAE_3	$C_{16}V_3A_3E_3$-NH_2	Filler
PAE_3RGDS	$C_{16}V_3A_3E_3G_2RGDS$-NH_2	Cell adhesion
PAK_2	$C_{16}V_3A_3K_2$-NH_2	Filler
PAK_3	$C_{16}V_3A_3K_3$-NH_2	Filler
PAK_4	$C_{16}V_3A_3K_4$-NH_2	Filler
PAK_3AGD	$C_{16}V_3A_3K_3AGD$-NH_2	Cell adhesion
PAK_3GHK	$C_{16}V_3A_3K_3GHK$-NH_2	Wound healing

Initial testing with the chosen PAs indicated that they would be suitable for further study. All the PAs can form gels when their charges are suitably screened using a counterion (Experimental 2.9.2). At 2% w/v, these gels typically possess a stiffness of around 10 kPa except for thermally treated PAE_3, which was observed to be around 1 order of magnitude stiffer (Figure 13). The lower stiffnesses observed here are within the ranges which have previously been

reported for cerebral tissues, but far greater than that reported for spinal cord segments.[22] It is therefore possible that neurons may be able to proliferate within this gel, but perhaps only those harvested from a cerebral source would be optimally cultured. Nonetheless, it is hoped that any secretome released from an implanted gel would trigger neural growth in the spinal cord around the implant. The implant would, ideally, degrade over time and allow for cell growth in its place. It may also be possible to reduce the stiffness of these PA hydrogels by reducing the weight percentage, bringing the stiffness more in line with that of spinal cord tissue.

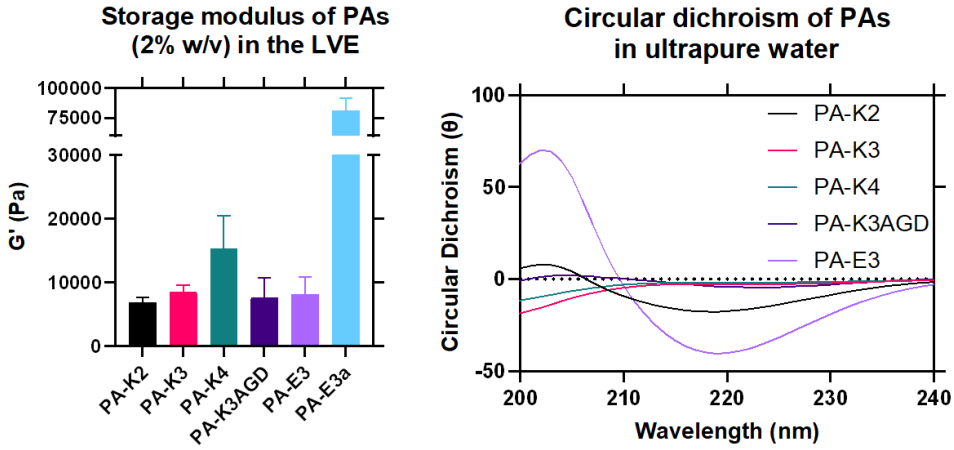

Figure 13: Initial characterisation of selected PAs. Left: Storage modulus (G') as measured by frequency sweeps of 2% w/v PA hydrogels formed in ultrapure water. Values are taken as an average of the reported G' between 0.1 and 10 Hz for triplicate measurements. A greater G' value indicates a higher stiffness. Right: Circular dichroism of PAs in solution state in ultrapure water. Values at each wavelength are presented as an average of 3 measurements of 3 separate samples – 9 measurements total. PAE_3 demonstrates the greatest β-sheet character.

Circular dichroism (CD) reveals more about the molecular ordering of these PAs and may be useful in predicting their properties (Figure 13). Here, PAE_3 was observed to have the strongest β-sheet character, followed by PAK_2 and PAK_3AGD. Interestingly, PAK_3 and PAK_4 both exhibited a more random coil structure, with complete lack of β-sheets, although both were able to form hydrogels in the same solvent. This weaker β-sheet character may indicate greater difficulty in achieving hydrogels with weaker charge dampening, as a greater energy input may be needed to achieve molecular ordering and long-range fibre formation.

2.4.2 Initial Gelation Screening

Firstly, it was investigated whether PAs can form gels in the presence of SCS. Proteins and soluble factors are charged species which may contain hydrophobic domains and β-sheet forming regions. It is therefore not unreasonable to predict that there may be some disruptive interaction between PAs and factors which may prevent or somewhat inhibit gelation. Selected PAs were therefore screened in different buffers with the SCS, and the order of addition (PA injected into secretome against secretome injected into PA) was also investigated (Figure 14). For this experiment, only the gelation with SCS was investigated and no counterions were added.

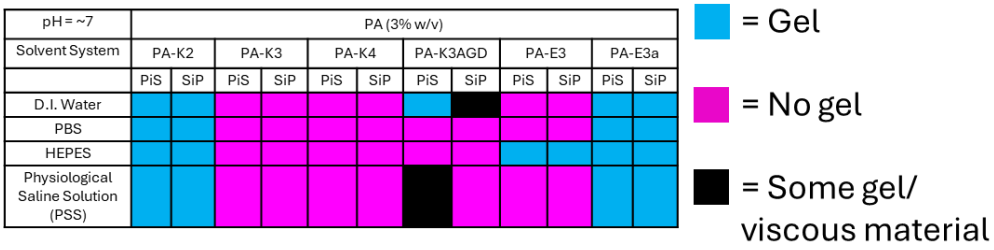

Figure 14: Gelation screening of PAs with SCS in different buffers. PiS = PA injected into SCS. SiP = SCS injected into PA. The presence of a gel was determined visually and by the use of forceps to probe for gel formation. "Some gel" denotes that some aggregation/precipitation of gelled or gel-like material was observed, but did not gel the entire droplet.

It was observed that, just through the addition of SCS, PAK_2 and PAE_3a were able to form a gel after 1 hour of incubation at 37 °C in all buffer systems tested. The order of addition did not affect the gelation. In the case of PAK_3 and PAK_4, no gelation was observed in any system. It may be the case that any gel formed was of too low of a stiffness to handle manually and was destroyed when an attempt was made to check for a gel. However, the volume used was not sufficient for rheological testing. A microrheological test, such as by atomic force microscopy (AFM) may reveal whether a gel was formed or not. Interestingly, PAE_3 was observed to form a gel with the SCS in HEPES buffer only, where the order of addition did not affect gelation.

For PAK_3AGD, a gel was only observed when the PA was dissolved in pure water and injected into SCS. Injecting SCS into the PA resulted in the formation of gelled species, but these were broken pieces as opposed to a whole gel. It

may be the case that PAK_3AGD exhibits faster gelation kinetics with the SCS than PAK_2 or PAE_3a, and that the injection of SCS into the PA disrupts and breaks the already gelled material. Secondly, the introduction of buffers to the PA solution further disrupts gelation, indicating that this system may not be suitable for biological applications where a maintenance of constant pH using a buffer is required. However, it may also be possible to form the gel in water and subsequently exchange the solvent with a buffered solution for effective biological work.

From this screening, it may be concluded that HEPES may be the most suitable solvent for further work. It also indicates that PAK_2 and PAE_3 exhibit slower gelation kinetics with the SCS than PAK_3AGD, owing to the ability to inject SCS into the PA without breaking the gel. It was also noted that PAK_2, PAE_3, PAE_3a, and PAK_3AGD may be the most suitable PAs to carry into further work.

2.4.3 Effect of Net Charge

Following the identification of some target PA systems, the impact of net charge of the PA on secretome gelation was investigated. Lysine-based (PAK_2, PAK_3, PAK_4) and glutamic acid-based (PAE_2, PAE_3) were chosen as starting points. It was predicted that, owing to the average pI of proteins in the secretome, PA molecules which carry a net positive charge at physiological conditions would exhibit greater electrostatic interactions, greater charge dampening, and therefore readily form a gel. Theoretically, the addition of an extra lysine or glutamic acid should result in an increase or decrease in net charge at pH 7.4, and PAK_3 would most readily form a gel when introduced to the SCS.

Determination of the ζ-potential of each PA revealed that the overall electrical potential remained roughly constant between K_2 to K_3 and E_2 to E_3 (Figure 15A). The absolute values of the ζ-potential indicate good stability in solution of these colloids. Their relative values may indicate that, at physiological pH, the pKb or pKa of the third amino acid may not be reached, resulting in protonation or deprotonation at only two of the three amino acids and thus a similar ζ-potential.

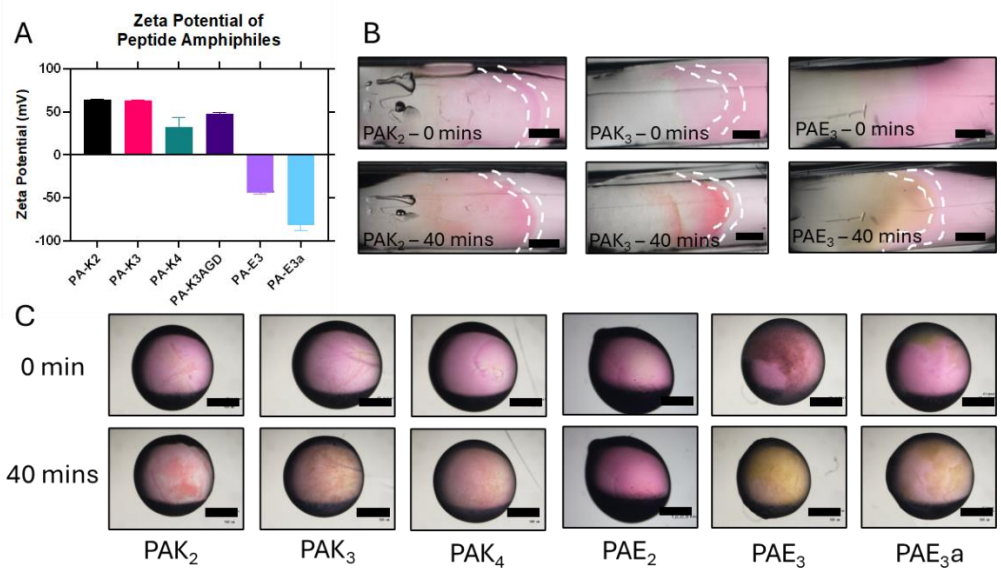

Figure 15: The effect of charged groups on gel formation with SCS. A: ζ potential of selected PAs measured in ultrapure water. B: Interfacial experiments determining gel formation and diffusion of constituents. PA begins on the left-hand side of each image while SCS is observed with a pink colouration on the right-hand side of each image. Interfaces are highlighted with dashed lines. Scale = 500 µm. C: Bulk gel formation in selected PAs. PA solutions were injected into a droplet of secretome. Scale = 1 mm.

Interestingly, despite the similar ζ-potentials, PAK_2 was observed to immediately form a gel upon contact with the SCS whereas PAK_3 exhibited slightly slower gelation kinetics (Figure 15B). An immediate interface is observed when both PAK_2 and PAK_3 encounter the SCS, across which the red colouration of the SCS diffuses, eventually crossing this interface entirely against a diffusion gradient. While this red colouration may simply be the phenol red dye of the media in which the secretome is collected, its movement along the diffusion gradient indicates a degree of affinity and electrostatic interaction between the secretome and PA. The formation of the gel indicates that the electrostatic repulsion between PA monomers is decreased, allowing the self-assembly into long-range fibres. A slight difference in kinetics of the diffusion of SCS into the PA is observed between 1% w/v PAK_2 and PAK_3, with PAK_2 exhibiting faster uptake than PAK_3. This may be due to the slightly less negative ζ-potential of PAK_3, meaning a lower electrical potential and therefore slightly weaker electrostatic interactions. Indeed, the gel formed by PAK_3-SCS more readily disintegrates upon agitation than PAK_2-SCS. Rheological measurements would have been preferred for characterisation but were not performed due to the precious nature of SCS. Despite its tendency to

disintegrate and slower gelation kinetics, a PAK_3-SCS gel may still prove to be desirable should it exhibit lower stiffness compared to PAK_2-SCS, a trait more favourable in neural tissue scaffolds.

This apparent 'series' in tendency to gel in the presence of SCS, with PAK_2 more easily forming a gel with SCS, followed by PAK_3 and then PAK_4, is in line with the β-sheet character of these molecules revealed by CD (Figure 13). It may be the case, therefore, that β-sheet character of PAs in solution may be used to predict the ease with which a PA may form a gel, as there is less of an energy input required to achieve order and form a gel.

In the case of PAE_2 and PAE_3, a gel was observed to form slowly over time in both cases. PAE_2 appeared to exhibit faster gelation than PAE_3, with a gel being observed almost immediately upon introduction to SCS. However, no diffusion of the SCS was observed across the interface (Figure 15B). The lack of diffusion was not unexpected – far fewer proteins in the SCS are expected to carry a net positive charge at physiological pH, therefore any charge dampening effects would be much weaker in the negatively charged PAE_x gels. The observed gelation may be explained through the presence of multivalent cations in the media used to collect the secretome. Neurobasal-A media contains calcium chloride at a concentration of 1.8 mM, which is sufficient to trigger the gelation of PAE_x materials. Additionally, magnesium chloride is present at 0.8 mM, which may also contribute to charge dampening. Despite the lack of protein-induced gelation, the slower gelation kinetics of PAE_x with SCS indicate the possibility of mixing the proteins with the PA solution prior to gelation and subsequent physical entrapment within the porous structure.

When PAE_3 is thermally treated with an 80 °C heat-cool cycle, it appears to be more susceptible to gelation upon introduction to the SCS. A gel is more readily observed, although this is perhaps in contradiction to the ζ potential measurement that indicates PAE_3a is more stable in solution than PAE_3 and should require a greater energy input to gelate. It may be the case that the greater ζ potential on the surface of PAE_3a fibres exhibit a greater affinity to cationic species, and therefore Ca^{2+} may diffuse from the SCS into the gel at a greater

rate, increasing the rate of gelation. A similar effect is also observed with PAE_2 and PAE_2a.

From investigation into the effect of charge, it was determined that both positively and negatively charged PAs may be of use in fabricating a secretome gel. PAK_x gels form gels upon contact with the SCS, after which diffusion into the PA is observed. Conversely, PAE_x gels display little to no diffusion from SCS into PA and do not form gels immediately upon contact. Understanding this is important as it informs subsequent formulation of gels. For example, PAE_x solutions may be mixed with proteins and gelled in situ (i.e., within a spinal cord injury site), allowing for easier injection and application. PAK_x gels, on the other hand, may find more use as a moulded implant, perhaps with the SCS gel being formed ex situ before being implanted. Nonetheless, neither class of PAs may be discounted from this set of experiments.

2.4.4 Effect of Bioactive Epitopes

Having determined that both PAK_x and PAE_x molecules may be suitable for the fabrication of SCS gels, attention was now turned to the possibility of adding bioactive epitopes to these monomers. Currently, the PAK_x and PAE_x sequences lack any degree of bioactivity. This may be overcome through the addition of SCS, but it was also deemed necessary to attempt to imbue these sequences with their own bioactivity which may remain after the release of SCS proteins. Two tripeptide sequences, one inspired by the RGD sequence and the other being GHK were used as a base for this purpose. The RGD sequence is implicated in aiding cell adhesion whereas GHK may contribute to wound healing. Both, therefore, are relevant in attempting to trigger the proliferation of neural stem cells and recovery in a spinal cord injury. Three separate PA sequences were selected – PAK_3AGD, PAK_3GHK, and PAE_3RGDS.

In the case where an RGD-inspired sequence was added to PAK_3, gelation kinetics were accelerated and the resulting gel was more stable, being able to be handled unlike an SCS gel formed with PAK_3 alone (Figure 16). It is unlikely that this is due to the bioactivity of the AGD sequence itself, as integrin-binding sequences are present in proteins which are already abundant within the SCS. This change in gelation kinetics may be due to the presence of aspartic acid, the

deprotonation in solution of which may aid the charge-dampening between monomers and make gelation more energetically favourable than with PAK_3. Indeed, PAK_3AGD possesses a less positive ζ-potential than PAK_3, indicating that it is slightly less stable in its micellar form.

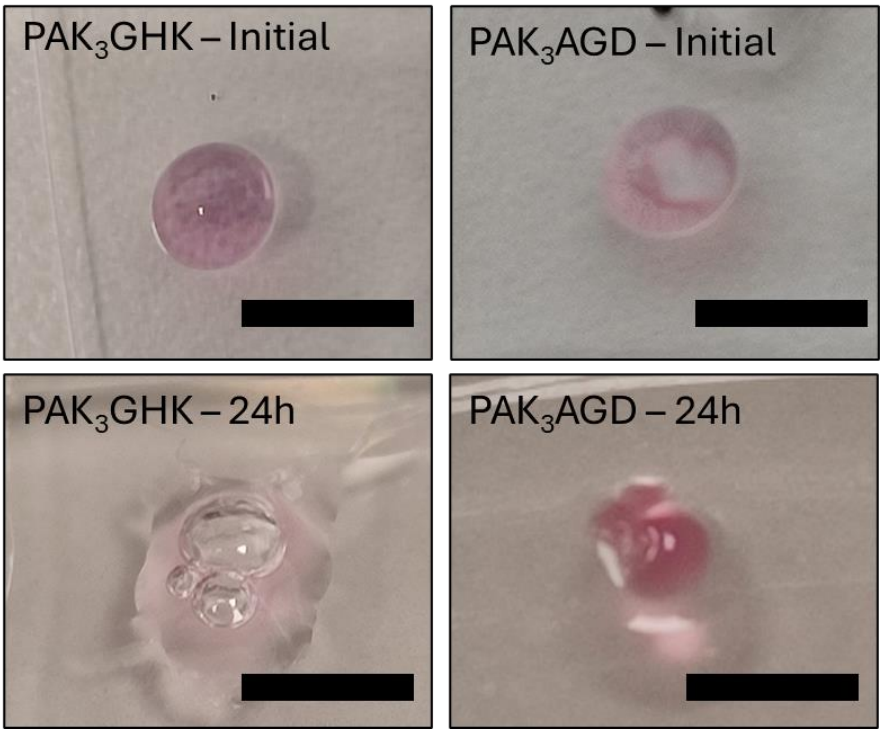

Figure 16: Camera images of the gelation of bioactive PAK_x solutions in SCS over the period of 24 hours. Gelation was only observed with PAK_3AGD, whereas PAK_3GHK remained as a liquid. Scale = 2 mm. Pink colouration is due to phenol red in the secretome.

In the case of PAK_3GHK, no gelation at all was observed upon introduction to the SCS (Figure 16). This may be a result of the additional lysine increasing electrostatic repulsion between monomers, making gel formation less energetically favourable and resulting in the failure to form a gel. Indeed, PAK_4 also fails to form a gel in the presence of SCS, indicating that PAs above a certain net charge are less likely to form gels upon charge dampening by proteins alone. It may be possible to form gels at a more basic pH, at which the lysine side chains may be less protonated, resulting in less repulsion between monomers and more energetically favourable gel formation. Importantly, it was also noticed that, once mixed with the SCS, PAK_3GHK could no longer be gelated using a counterion solution, indicating that there may be some disruptive interactions between the factors in the SCS and PA molecules.

Adding an RGDS domain to PAE_3 drastically reduced solubility in buffered solution. It was not possible to form a gel using 2% w/v PAE_3RGDS. However, when present at 5% w/w and below in a mixture of PAE_3 (meaning 0.1% w/v total in solution), it is possible to achieve complete dissolution and subsequent gelation. It was observed, however, that the RGDS domain may act as a nucleation site for calcium phosphate crystals when the PA is dissolved in PBS and subsequently gelated with calcium chloride (Figure 17). Indeed, arginine-phosphate interactions have been reported as being highly stable, indicating an energetic favourability.[23] It has previously been reported that arginine may act as a nucleation site for mineralisation in hydrogels.[24] This may have unforeseen adverse effects in terms of gel stiffness, cell adhesion, and subsequent cell survival within the gel. Additionally, the secretome may itself introduce a multitude of proteins into PAE_x hydrogels which bear cell adhesion domains, rendering the RGDS domain obsolete. In the case where HEPES or water are used as solvents for PAE_3RGDS, no crystal formation is observed under scanning electron microscopy (SEM) (Figure 17). Therefore, it is recommended that future studies avoid the use of phosphate buffers when an arginine residue is present.

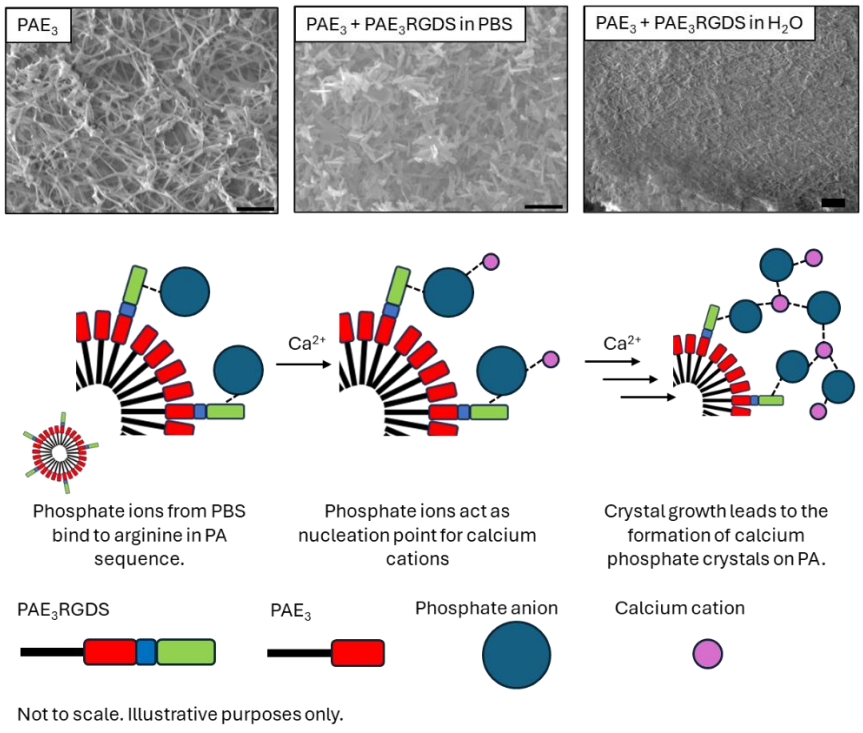

Figure 17: Upper: SEM micrographs of (left) PAE_3 fibres and crystal formation observed on (middle) PAE_3RGDS formed in PBS. Needle-like crystals cover the gel fibres. Scale = 300 nm. (Right) Micrograph

of PAE_3RGDS formed in ultrapure water Scale = 300 nm. Lower: Proposed mechanism of crystal formation on PA fibres. Phosphate anions, present from the PBS buffer, coordinate with the arginine of the PA to form a stable complex. This then acts as a nucleation site for the formation of calcium phosphate crystals upon the addition of Ca^{2+} cations.

Calcium phosphate crystals are likely not observed in other systems containing Ca^{2+} and PBS, such as PAE_3 because, in these systems, the valency of calcium is satisfied when dampening the charges of two glutamic acid side chains between PAE_3 molecules. It is therefore unable to form a compound with the phosphate ions, and there are no nucleation sites for crystal growth. The PO_4^{3-} anion, conversely, may donate two electrons to two arginine side chains in PAE_3RGDS, and maintain a single valent electron which may complex with Ca^{2+}, acting as a nucleation site and facilitating crystal growth.

2.4.5 Alignment of Fibres in SCS Gels

It has previously been reported that PA sequences which contain glutamic acid blocks in their charged region may have their fibres aligned through thermal treatment.[25] Doing so creates a unique scaffold for anisotropic cell growth and may aid directional proliferation such as that seen in myoblasts or neurons. Therefore, it was deemed appropriate to investigate whether such alignment may be observed in SCS gels. Here, PAE_3 solution was heated to 80 °C for 30 minutes before being allowed to cool to room temperature (19 °C). Following this, the solution was mixed 1:1 with the SCS and gelled with a $CaCl_2$ injection.

It was observed that alignment of the PA fibres was retained with the addition of the SCS (Figure 18), indicating the potential for creating an anisotropic milieu for cell growth and proliferation. It is good to note that the presence of factors from the SCS does not appear to disrupt the formation of aligned fibres – further evidence of PAE_3 lacking any bioactivity. Conversely, no alignment was observed in any of the PAK_x gels, with or without the SCS. This was expected, as no previous reports exist of alignment in PAK_x gels.

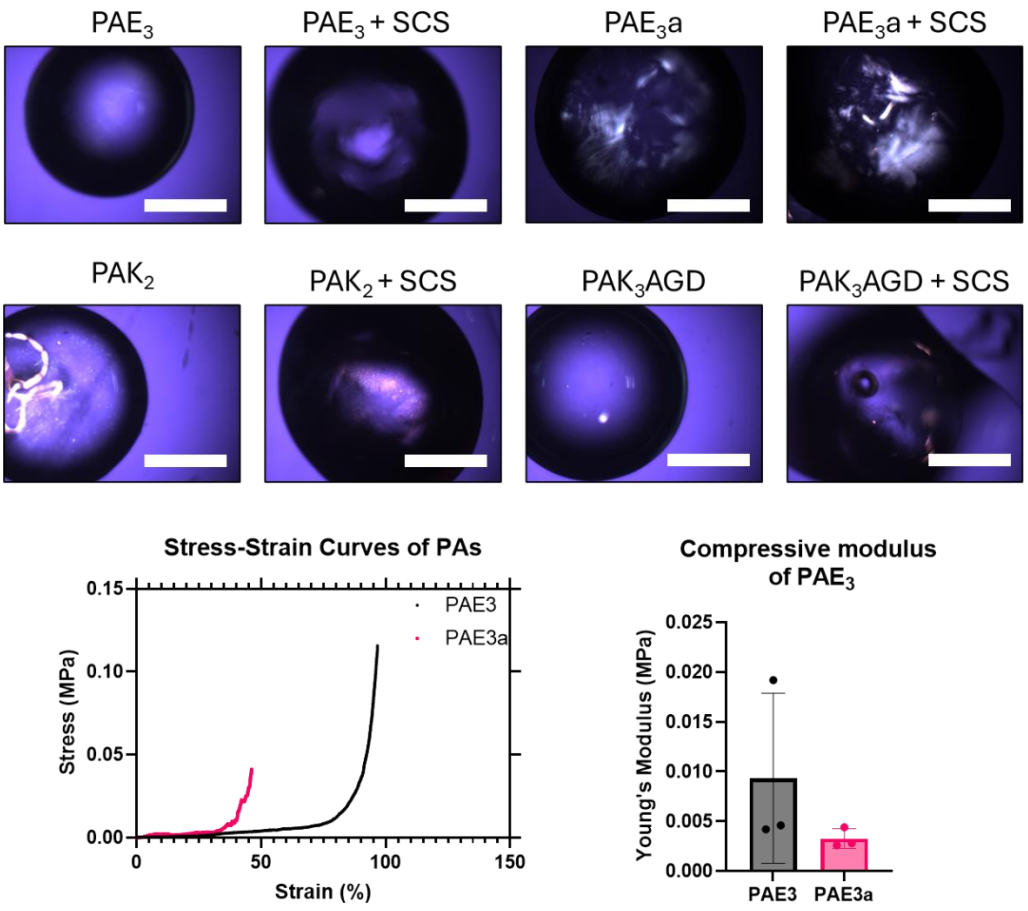

Figure 18: Upper: Polarised light microscopy images of PAs. Alignment of fibres in PAE_{3a} is indicated by the presence of bright regions within the gel droplet. Scale = 1 mm. Lower left: Representative stress-strain curves for PAE_3 and PAE_{3a}. PAE_{3a} was found to have a lower modulus, strain at break, and stress at break than PAE_3. Lower right: Compressive modulus of PAs.

As a further material characterisation to determine the suitability of PAE_3 for neural tissue engineering, the compressive modulus was determined through uniaxial compression testing (Figure 18). This was due, in part, to the forces which are likely to be experienced within the spinal cord, which may both be oscillatory and uniaxial. It was observed that both 1% PAE_3 and PAE_{3a} possess a compressive modulus (0.01-0.003 MPa) roughly one order of magnitude lower than previously reported values for combined white and grey matter of the cervical spinal cord, also measured under uniaxial compressive loading.[10] Other reports have determined the spinal cord parenchyma in the absence of pia mater – a meningeal membrane in the CNS – to be as low as 5 kPa,[26] the same value as observed for PAE_3 and PAE_{3a}. These data suggest that PAE_3 formulations are likely to be suitable candidates for neural tissue engineering for spinal cord injuries.

2.5 Heparin-based Hydrogels

2.5.1 Rationale

Having determined that PAE_x sequences may be mixed with secretome prior to gelation and be aligned to create what may be a more advantageous scaffold for directed neural outgrowth, it was decided that PAE_x sequences were to be used for further study in this case. Furthermore, it was decided that a sequence with the potential for binding multiple proteins was needed, as PAE_x sequences did not appear to have any affinity to the proteins in the SCS. Therefore, a heparin-inspired sequence was decided upon, as heparin is known to display an affinity to multiple proteins.[27] A previously reported sequence,[28] DK(4-sulfobenzoic acid)S, wherein the lysine side chain is functionalised with 4-sulfobenzoic acid to mimic the sulfonic acid groups found in heparin, was used in this case. A second previously reported sequence designed to bind heparin and form a gel was also used to compare the properties of the heparin-mimetic PA (HMPA) with heparin (Table 2).

Table 2: List of PA sequences used in heparin-based investigations. The following abbreviations are used: HM = Heparin-mimetic, HB = Heparin-binding, ns = non-sulfonated, sc = scrambled.

PA Name	*Full Sequence*	*Purpose*
HMPA	$C_{16}V_3A_3E_3GEGDK(4\text{-sulfobenzoic acid})S\text{-}NH_2$	Heparin-mimetic sequence
HMPAns	$C_{16}V_3A_3E_3GEGDKS\text{-}NH_2$	Non-sulfonated heparin mimetic control
HMPAsc	$C_{16}V_3A_3E_3GGSDEK(4\text{-sulfobenzoic acid})\text{-}NH_2$	Scrambled heparin-mimetic control
HBPA	$C_{16}V_3A_3LRKKLGKA\text{-}NH_2$	Heparin-binding sequence
HBPAsc	$C_{16}V_3A_3LRKKKLAG\text{-}NH_2$	Scrambled heparin-binding control

2.5.2 Material Design and Characterisation

Firstly, the ζ potential of the HMPA and HBPA sequences was determined (Figure 19A). HMPA was observed to have a similar ζ potential to the sodium salt of heparin indicating that, at the very least, it would have similar electrostatic interactions with proteins as heparin. The HBPA sequence was observed to have a positive ζ potential owing to the arginine and lysine charged groups, so was expected to electrostatically interact with heparin. An interaction was observed through the increase in optical absorbance at 600 nm when dilute solutions of HBPA and heparin were mixed, indicating the formation of a HBPA-heparin complex (Figure 19C). It was also not possible to form a material with HBPAsc, confirming the bioactivity of the HBPA sequence.

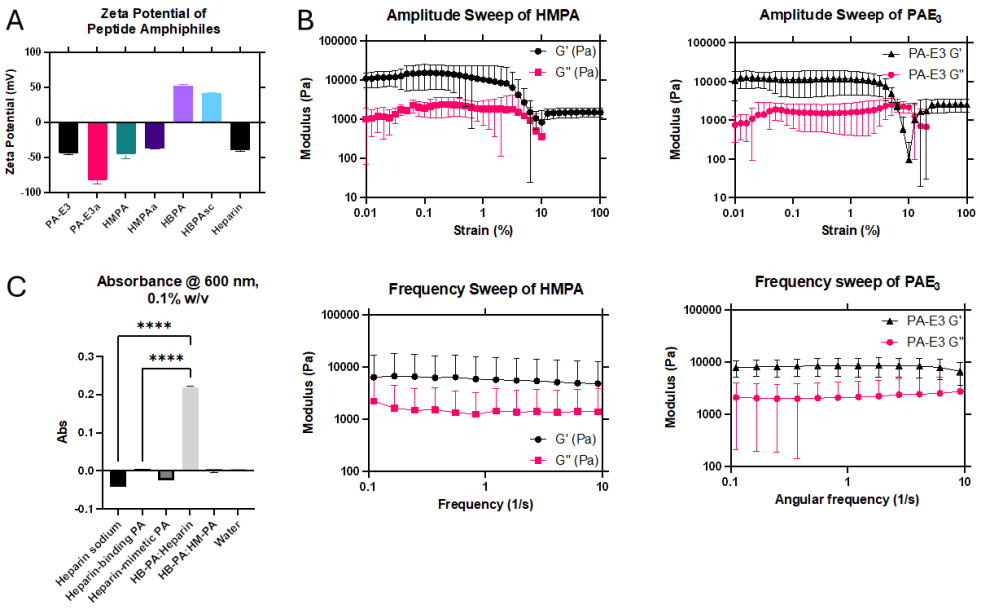

Figure 19: Characterisation of HMPA and HBPA. A) ζ-potential measurements of PA sequences conducted in ultrapure water. HMPA carries a similar net charge to PAE₃, indicating the suitability of mixing these two sequences. B) Rheological measurements of HMPA compared to PAE₃. A frequency sweep reveals that HMPA forms a gel and is of a similar stiffness to PAE₃. C) Turbidity measurements of HBPA when mixed with heparin in solution performed by measuring absorbance at 600 nm. An increase in turbidity indicates the formation of a precipitous complex. Statistical significance determined by ordinary one-way ANOVA ($p<0.0001$).

Rheological measurements revealed that HMPA and PAE_3 possess similar mechanical properties with both the average G' and the crossover region being very similar in both gels (Figure 19B). This was not unexpected as, typically, mechanical properties of PAs are determined by the β-sheet forming region as opposed to the charged and bioactive groups. However, it should be noted that, in some replicates for HMPA, the crossover region was observed at a lower strain than PAE_3, indicating some degree of unpredictability with this system and the potential of forming a more brittle gel. The frequency sweeps of both PAE_3 and HMPA appear to be indicating that G' and G'' will converge towards a crossover point at a lower frequency, indicating some self-healing ability of these gels. This indicates that the supramolecular nature of the PA is maintained in HMPA and that the introduction of the 4-sulfobenzoic acid modification of the lysine side chain does not introduce covalent crosslinking. Owing to the

length of time required to investigate behaviours at frequencies below 0.1 Hz, it was not possible to do so before dehydration of the gel occurred.

2.5.3 Stability and Release

The stability of these hydrogels in solution was investigated to determine their suitability for implantation. Ideally, gels should be stable for several days-weeks to allow for a cell scaffold to form which may self-support after loss of the gel. Furthermore, rapid degradation of a gel which is designed for sustained release may simply release all proteins within the gel in a very short time period. However, a gel which does not degrade may also cause issues, preventing full tissue regeneration and potentially causing mechanical damage due to swelling over time.

A stability study reveals that HMPA is significantly less stable in PBS than PAE_3, with an average of 18.1% of mass remaining after 7 days compared to 67.8% of PAE_3 mass remaining (Figure 20C&D). This may be due to the rheological properties observed in HMPA, where some gels may be more brittle and liable to break under strain compared to PAE_3. For this experiment, PBS was exchanged daily, and gels were constantly handled to perform weighing. It may be the case that such strain causes the degradation of the HMPA gels. Indeed, all HMPA:PAE_3 mixtures were observed to have a lower average mass remaining after 7 days compared to PAE_3, although a statistically significant difference is only observed once the mass percentage of HMPA is greater than 50. Interestingly, PAE_3 mixed with the scrambled HMPA sequence, HMPAsc, was observed to be the most stable gel, more stable than PAE_3 alone. It may be possible, therefore, to alter the HMPA sequence to achieve optimal stability while also maintaining protein binding ability.

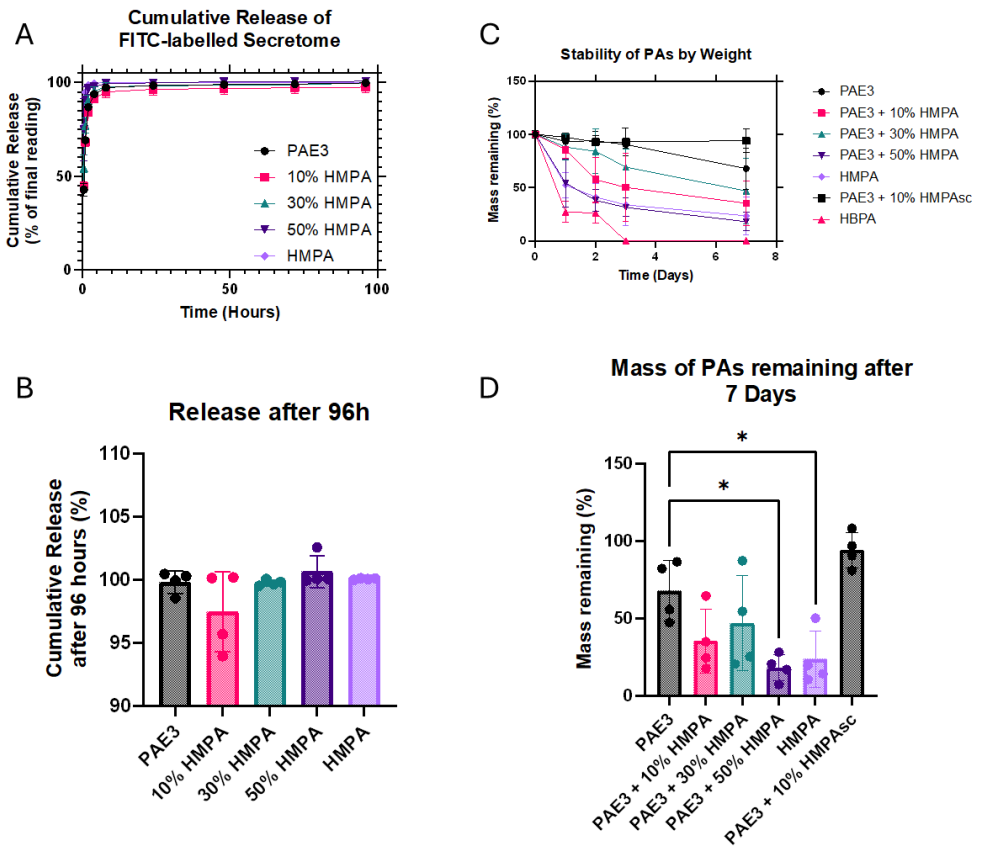

Figure 20: Secretome release profiles and stability of PAs in buffered solution. A) Cumulative release of FITC-labelled secretome from PA hydrogels as determined by plate reader measurements ex/em 495/530 nm. B) Total protein released from PAs after 96 hours. C) Stability of PA hydrogels in PBS solution over 7 days. D) Total mass remaining in PAs after 7 days. Statistical significance determined using ordinary one-way ANOVA.

In conjunction with stability measurements, the release of secretome from PA formulations was monitored by labelling proteins with fluorescein isothiocyanate (FITC), a fluorescent tag which binds to free amine groups (Figure 20A&B). Proteins were labelled before being mixed with the PA, and unbound dye was removed through dialysis to minimise any staining of PA fibres. Initially, a burst release is observed in all formulations with roughly 98% of proteins released within the first 48 hours in PAE_3, HMPA, and the 30% and 50% w/w mixtures. However, it is possible that the dialysis was incomplete, and that unbound dye was also present in the SCS which would have diffused out rapidly. After 96 hours, roughly all the total protein had been released from these formulations. In the case of PAE_3 containing 10% HMPA by weight, however, an average of 97.4% of proteins had been released. Although not statistically significant, this indicates the potential of this formulation to act as a controlled

release system. Further replicates would be required to confirm this hypothesis. Importantly, this release data must be contextualised with the stability data, where it is observed that the 10% HMPA formulation degrades roughly twice as fast as PAE_3, and therefore, if no affinity to proteins were present, would be expected to release proteins twice as fast.

It was also observed that the fluorescence equipment used here was unable to detect protein concentrations of 1 ng mL^{-1}, yielding similar fluorescence intensities as a PBS blank. This, combined with possible cumulative error of up to 2% on the equipment, may result in masking any release of proteins after several days. It may, however, be stated that a large majority of the proteins are probably released within the first 48 hours. However, a more sensitive technique, such as ELISA, is required to determine whether further proteins are released after this time.

It may also be the case that the current ratio of SCS:PA means the PA is overloaded with proteins, leading to what appears to be a near-complete loss of loading within the first 48 hours. However, it was not possible to perform the experiment with a lower SCS loading and still detect SCS at lower concentrations. A more sensitive measurement technique, such as ELISA, is needed for this study. Indeed, it has previously been determined by ELISA that the release of factors such as vascular endothelial growth factor (VEGF) is greatly controlled from gels which contain the HMPA sequence, with less than 5% released over the course of 7 days.[28] Similarly, nerve growth factor (NGF) release from a heparin-mimetic PA has also been observed to be less than 10% release over 10 days.[29]

2.5.4 Binding Affinity

It now remained to determine the affinity of HMPA to factors found within the SCS. While the DKS sequence has previously been investigated using ELISA and isothermal titration calorimetry (ITC) and the presence of a binding affinity to proteins has been confirmed, examples could not be found using surface plasmon resonance (SPR) to fully characterise binding kinetics (K_a and K_d) and an affinity constant, K_D. This characterisation would allow a further understanding of the binding behaviour of this PA beyond that which has already

been reported. Furthermore, it would further validate the use of SPR for the characterisation of PAs, an application which has only been seldom reported. SPR was chosen to quantify the binding affinity between PAs and growth factors due to its low volume requirement and high sensitivity. Ideally, this technique may be paired with ITC experiments to yield complementary data, especially owing to the minimal literature precedent for PA use in SPR.

In SPR, a ligand is immobilised upon the surface of a sensor chip (Figure 21A). Here, proteins were covalently bonded to a dextran-coated gold sensor chip using amine coupling. This is a standard method of ligand immobilisation and was chosen due to its ease and efficiency at successfully immobilising proteins with minimal loss of conformation or activity. The analyte – PAs in this case – in solution is then passed over the immobilised proteins at a set flow rate. Simultaneously, a single-wavelength light source is directed at the gold sensor at a fixed angle. This light source, at this fixed angle, excites electrons within the gold layer, which then travel as a plasmon wave parallel to the gold layer. This plasmon wave may be detected as absorbed light. As this plasmon wave travels at the interface of gold the outside medium, it is incredibly sensitive to any adsorbed material on the sensor chip. Any alteration in the refractive index of the adsorbed material will shift the angle of incidence required to achieve the plasmon wave. The degree to which this angle shifts may be plotted as a response on the SPR sensorgram. As the refractive index of the ligand-analyte complex is crucial in measuring SPR, the analyte should be as homogenous as possible.

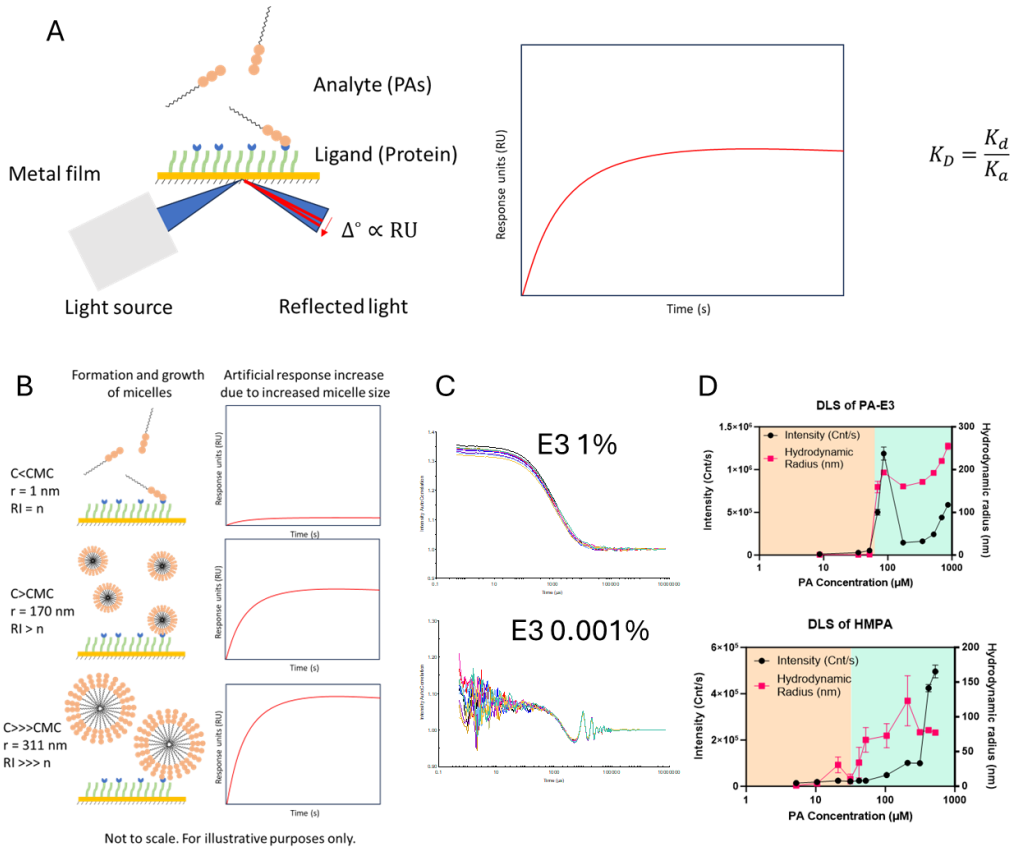

Figure 21: Application of critical micelle concentration (CMC) measurements for surface plasmon resonance (SPR). A) Diagram of the working of SPR and determination of K_D. B) Proposed effect of micelles and fibres on SPR sensorgrams. Larger particles may induce a greater SPR response. C) Dynamic light scattering (DLS) correlograms for PAE_3 in ultrapure water above and below a CMC. D) Determination of CMC using DLS measurements at a fixed laser intensity. CMC is determined by the loss of scattering intensity and lack of particle detection.

Therefore, prior to conducting SPR using PAs, the critical micelle concentration (CMC) must be determined. Micelles have far greater hydrodynamic radii, masses, and polydispersity indices than individual monomers in solution. Micelles of different sizes may have different refractive indices than individual monomers and may possess multiple binding sites (Figure 21B). Both refractive index and number of binding sites are key parameters for accurate and reliable SPR measurements. Therefore, owing to the innate heterogeneity of micellar dispersions, it was theorised that SPR should be performed below the CMC of a PA. As the CMC varies by PA sequence, this must be determined for each PA individually. Using fixed laser intensity DLS, the CMC of PAE_3 and HMPA was measured (Experimental 2.9.9).

It was observed that HMPA has a slightly lower CMC than PAE_3, although both were observed to be micellar above 50 μM concentration (Figure 21C&D). Therefore, it was determined that concentrations above 50 μM would not be useful for affinity measurements in SPR. However, the association (K_a) and dissociation (K_d) constants may not be affected by particle size, as this is a measure of the rate of binding and is not necessarily impacted by the magnitude of the SPR response. This is useful as, if signals below the CMC are too small to be detected by SPR and unable to be used in K_D determination by affinity, larger signals above the CMC may be used for K_D determination by kinetics.

Having determined the CMC of the PAs of interest, SPR was then performed the measure their affinities to growth factors identified in our secretome or reported elsewhere. Interleukin-6 (IL-6) was chosen as a model protein to measure affinity. IL-6 was detected as present in the SCS and is a key modulator of inflammation following spinal cord injury and its presence activates the JAK/STAT3 transcription pathway which stimulates the regeneration of neurons.[30] Therefore, the ability to bind this factor is relevant to the efficacy of the HMPA sequence.

IL-6 was successfully immobilised on a CM5 dextran-coated gold sensor chip using amine coupling (Experimental 2.9.10). A solution of ethanolamine was used to 'cap' unreacted surface and prevent unwanted coupling to the NHS ester. A second flow cell was used as a control and contained only the ethanolamine-capped NHS ester. As analytes, heparin, HMPA, PAE_3, scrambled HMPA (HMPAsc), and non-sulfonated HMPA (HMPAns) were used. Flow rates, contact time, and flow cell regeneration methods were all kept constant for each experiment.

A reliable affinity curve could not be generated for the PAs below the CMC. While a response was observed which increased with concentration, indicating binding to the ligand, the magnitude and variation of this response below the CMC was too low to generate any data. Above the CMC, however, reasonable responses were observed (Figure 22). This has been reported previously with micellar materials in SPR, both with carbohydrates and PAs.[31, 32] However, unlike reported in these papers, here it is not believed that these molecules only

begin to bind once in their micellar form. Instead, the large increase in the magnitude of the response is believed to be due to the size of these micelles, which trends towards a greater hydrodynamic radius with increasing concentration. Therefore, a larger response is obtained compared to monomeric binding. Due to the heterogeneity of PA micelles, it is not possible here to obtain an affinity curve above the CMC as this requires saturation of the magnitude of the response. If micelle size increases with concentration, the magnitude of the response will continue to be artificially increased. Estimation of K_D by kinetics, however, relies on the rates of association and dissociation, which are independent of response magnitude. Therefore, kinetic evaluation of the data was performed.

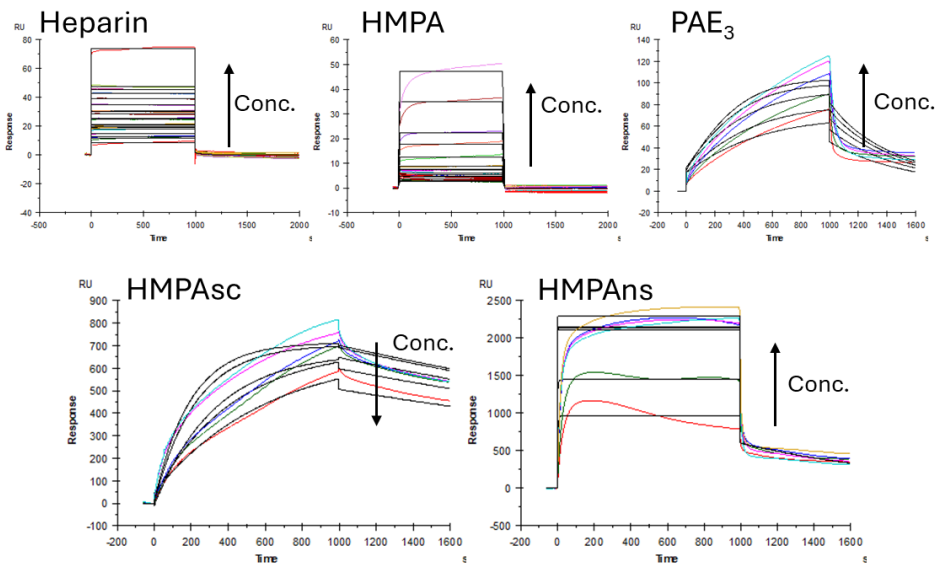

Bivalent Analysis

Analyte	K_a^1 (M^{-1} s^{-1})	K_d^1 (s^{-1})	K_a^2 (RU^{-1} s^{-1})	K_d^2 (s^{-1})	K_D^1 (M)	K_D^2 (RU)	χ^2
Heparin	1.45×10^{6}	9.70×10^{-3}	4.40×10^{-3}	5.35×10^{-2}	6.71×10^{-9}	1.22×10^{1}	0.853
HMPA	1.65×10^{6}	2.64×10^{-3}	3.72×10^{-3}	2.89×10^{-5}	1.59×10^{-9}	7.76×10^{-3}	1.045
PAE_3	1.09×10^{0}	2.57×10^{-2}	1.24×10^{-3}	3.21×10^{-2}	2.36×10^{-2}	2.60×10^{1}	92.300
HMPAsc	3.43×10^{5}	5.60×10^{-3}	5.69×10^{-3}	1.12×10^{-2}	1.63×10^{-8}	0.20×10^{1}	732
HMPAns	2.12×10^{1}	1.40×10^{-3}	8.24×10^{-5}	8.34×10^{-3}	6.62×10^{-5}	1.08×10^{2}	18640.345

1:1 Binding

Analyte	K_a (M^{-1} s^{-1})	K_d (s^{-1})	K_D (M)	χ^2
Heparin	2.62×10^{5}	8.39×10^{-3}	3.20×10^{-8}	0.853
HMPA	7.05×10^{6}	6.21×10^{-2}	8.81×10^{-9}	1.040
PAE_3	1.45×10^{1}	2.11×10^{-3}	1.45×10^{-4}	79.5
HMPAsc	2.79×10^{1}	2.66×10^{-4}	9.50×10^{-6}	1045
HMPAns	3.80×10^{3}	9.77×10^{-4}	2.57×10^{-7}	32000

Figure 22: SPR Analysis of binding to IL-6. Top: Sensorgrams (coloured) with fitted overlays (black) for 1:1 binding models of heparin, HMPA, PAE_3, HMPAsc, and HMPAns to IL-6. Middle: Table of kinetics values for a bivalent fit. Lower: Table of kinetics values for 1:1 binding.

Achieving a good theoretical fit to describe the binding behaviour of the control PAs (PAE_3, HMPAsc, and HMPAns) proved to be difficult. For these samples, χ^2 values of 79.5, 1045, and 32,000 were obtained using a 1:1 binding fit. Typically, χ^2 values of <10 are required to indicate a good fit and reliable K_a and K_d values. Therefore, the absolute values of these control sequences cannot be said to be reliable. However, visual observation of the sensorgrams indicate that

the K_a value for PAE_3 may be lower than that provided by the theoretical fit, indicating the true K_D may be lower than provided. In the case of HMPAsc, the response was observed to decrease in magnitude with increasing analyte concentration, indicating increased binding to the control channel. The K_a is also visually lower than the provided theoretical fit. The values obtained for HMPAns come with the caveat that the χ^2 value is 32,000, indicating unreliable values. Visually, it appears that the K_a of HMPAns may be similar to HMPA, but a decrease in response is observed over time, indicating dissociation and weaker binding.

HMPA exhibited a K_D value in the same order of magnitude as heparin, as well as similar association and dissociation rates. The χ^2 values for HMPA and heparin were 1.04 and 0.85, respectively, indicating that the K_a and K_d values are reliable. The suggested increase in affinity from PAE_3 to HMPA indicates that the bioactive sequence works as desired and that there is minimal affinity resulting from the hydrophobic effect (i.e., the hydrocarbon tail of the PA to any hydrophobic residues in the protein) or from self-organisation of the β-sheet forming region of the PA to β-sheet regions of the protein. The reduced affinity displayed by HMPAns indicates the importance of the sulfate groups if one wishes to mimic heparin in protein-binding biomaterials, while the lack of affinity from HMPAsc highlights the importance of the order of amino acids in a PA. From this data, it can be concluded that the HMPA possesses similar binding kinetics and affinities to IL-6 as heparin itself. However, due to the χ^2 values obtained, there is reduced reliability of the values obtained for the control PAs. A secondary measure of affinity, such as isothermal titration calorimetry, is likely needed.

With EGF, a low response was observed in the case of both heparin and HMPA. However, it was observed that the response became more negative over time, eventually leading to a negative response. While this may be indicative of instrument error, it may also be the case that binding to PAs may cause the conformation of the bound ligand to change, altering its refractive index and thus leading to a negative signal. Such an effect has been previously reported in the SPR analysis of small molecules.[33] This is an important consideration, as a change in protein conformation following binding to the PA may result in a loss

of efficacy of the secretome. Owing to the nature of the data obtained for binding to EGF, a reliable value for K_D could not be obtained.

Having now determined through SPR that the HMPA may display similar binding affinity and kinetics when compared to heparin, it now remained to be shown that a functional material may be fabricated with the potential for neurotrophy and neurological applications.

2.6 Engineering of Neural Cells

2.6.1 Rationale

Having now demonstrated the stability, biocompatibility, and binding affinity of the heparin mimetic PA, along with the ability to form a secretome-loaded PA hydrogel, it now remained to be seen whether this design could translate to an in vitro application. It was hypothesised that sustained, multi-factor release from the secretome-loaded PA could induce neurotrophic effects.

2.6.2 The SH-SY5Y Cell Line

Here, the SH-SY5Y cell line was used as an in vitro model of neural stem cells in the human spinal cord. This cell line has been subcloned from a bone marrow metastasis biopsy of a human neuroblastoma, with the original cell line called the SK-N-SH line. The SH-SY5Y cell line typically proliferates as both neuroblast-like and epithelial-like phenotypes and may spontaneously interconvert between both morphologies. It is the neuroblast-like morphology which holds relevance, as they may be forced to undergo differentiation by a combination of retinoic acid (RA) and neurotrophic growth factors to achieve a neuron-like phenotype, characterised by long neurite outgrowths and expression of neuronal markers. This model may therefore be similar to induced differentiation of neural stem cells in the human spinal cord, and potential subsequent motor function recovery by the outgrowth of neurites. Therefore, it was theorised that stem cell secretome, released from PA hydrogels, may induce this differentiation and be relevant for the desired application.

2.6.3 Cell Culture

The SH-SY5Y cell line was cultured as per standard protocol (Experimental 2.9.13-2.9.17). Briefly, three separate media formulations were used: growth medium (10% heat-inactivated FBS, 1% Glutamax, 1% antibiotic/antimycotic), differentiation medium 1 (2.5% hi-FBS, 1% Glutamax, 1% antibiotic/antimycotic, 10 μM RA), and differentiation medium 2 (1% hi-FBS, 1% Glutamax, 1% antibiotic/antimycotic). Cells were cultured in growth medium until 80% confluency, at which point they were seeded in Matrigel-coated wells of a 96 well plate at a density of 5,000 live cells per well. 24 hours after seeding, growth medium was replaced with differentiation medium 1, and cells were allowed to proliferate for 5 days. Differentiation medium 1 was then replaced with differentiation medium 2, supplemented with 10 ng mL^{-1} NGF and 50 ng mL^{-1} BDNF. After 5 further days of culture, cells are considered fully differentiated and assessed phenotypically.

2.6.4 Cell Viability with PA Hydrogels

Firstly, it was demonstrated that the PAs to be used are not cytotoxic. A cell viability assay of (3-(4,5-demethylthiazol-2-yl)-5-(3-carboxymethoxyphenyl)-2-(4(sulfophenyl)-2H-tetrazolium) (MTS) was performed to quantify cell survival both when seeded atop PA hydrogels and when brought into contact with PA molecules in solution (Figure 23). MTS is reduced to its insoluble formazan product by the presence of oxidoreductase enzymes. The degree of reduction, which may be measured colorimetrically, may be indicative of the number of cells which are alive in a population.

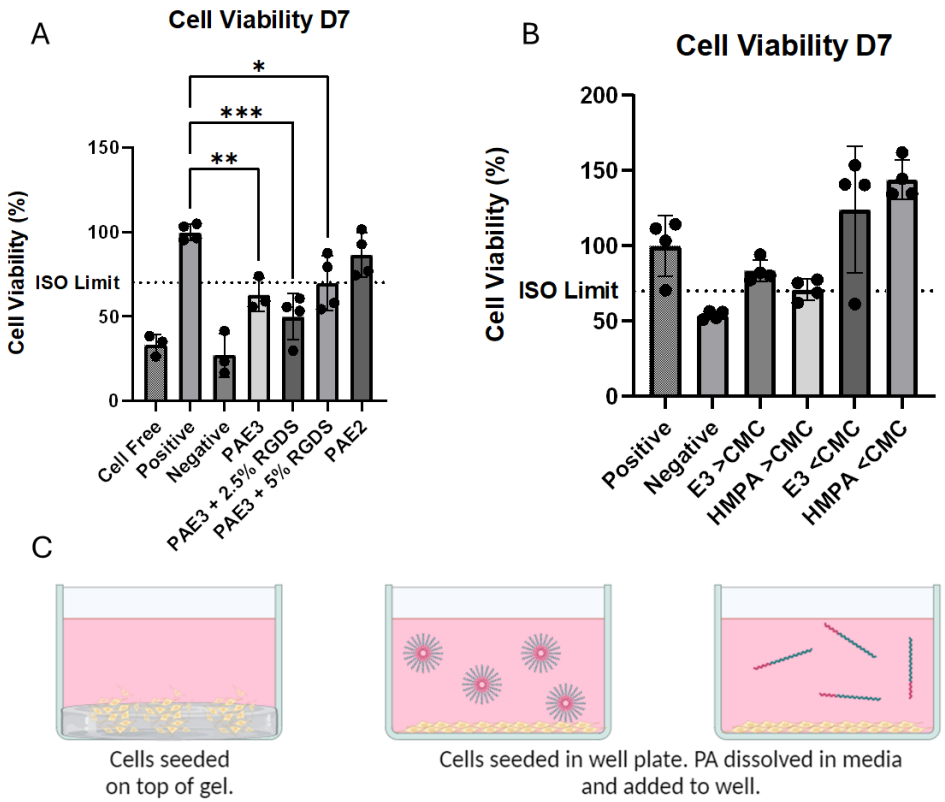

Figure 23: Viability of undifferentiated SH-SY5Y cells with PA gels and monomers. A: Viability 7 days after being seeded atop preformed gels. Viability was measured using an MTS assay. Negative control: DMSO for 10 minutes. Statistical significance measured using ordinary one-way ANOVA ($p<0.05$). B: Viability after being cultured in media containing PA monomers or micelles. C: Schematic of experimental setup.

When seeded atop PA hydrogels, cells are observed to significantly decrease in viability after 7 days, except in the case of PAE_2 (Figure 23). However, it is unlikely that the PA hydrogel itself is cytotoxic. Rather, it may be the lack of adhesion motifs present resulting in cell death. Cell death may not occur as quickly as expected in the floating cells as the SH-SY5Y cell line can consist of both an adherent and non-adherent population. Therefore, these non-adherent cells can survive several days in an environment which lacks adhesion motifs. Indeed, observing the morphology of the cells seeded upon these gels reveals that cells maintain a rounded shape from the point of seeding, further supporting the idea that a lack of adhesion is the main reason for the lack of long-term survival. Interestingly, no significant difference was observed in the survival of cells seeded onto PAE_3 and PAE_3 + PAE_3RGDS, indicating the crystallisation observed under SEM microscopy may indeed hinder the bioactivity of these epitopes.

Previously, it has been observed that some cells are less likely to adhere and proliferate on surfaces which contain a net negative charge. Fibroblasts and endothelial cells have both shown this characteristic.[34, 35] In the case of SH-SY5Y cells, it has previously been observed that increasing negative charge on a surface by plasma-enhanced vapour deposition results in reduced cell adhesion as a result of the carboxyl groups deposited on the surface.[36] Surfaces modified with net-positively charged allylamine were found to increase cell adhesion.[37] It may therefore not be that these PAs are toxic, rather that the lack of cell adhesion results in gradual cell death.

When cultured on an adherent plate in media containing dissolved PA, both above and below the CMC, no significant decrease in viability is observed over time. This indicates that the PA molecules themselves are not cytotoxic, and that any fibres or molecules that may break away as a gel implant degrades in vivo are unlikely to pose a risk to patient health. Having determined the biocompatibility of these gels in relation to the SH-SY5Y cell line, the ability of SCS-laden hydrogels to successfully differentiate this cell line was investigated.

2.6.5 Neurite Outgrowth with Secretome-loaded PA Hydrogels

Following RA treatment, it is possible to replace the regimented growth factor treatment with secretome treatment and maintain neurite outgrowth, provided the presence of the factors is sustained for the 5-day differentiation period. Here, several conditions were explored to investigate the neurite outgrowth in SH-SY5Y cells using secretome-loaded PA Hydrogels (Table 3).

Table 3: Table of experimental conditions for the differentiation of SH-SY5Y cells by secretome-loaded PA hydrogels.

Sample Group	Matrigel	1 Day	6 Days	11 Days
1	Undifferentiated	→	→	→
2	Undifferentiated	Retinoic Acid	→	→
3	Undifferentiated	Retinoic Acid	Growth Factors	→
4	Undifferentiated	Retinoic Acid	Secretome	→
5	Undifferentiated	Retinoic Acid	Secretome-PA	→
6	Undifferentiated	Retinoic Acid	PA only	→
7	Undifferentiated	Retinoic Acid	PBS	→

For this study, cells were seeded and cultured as per the protocol described in 2.6.3. One day prior to the addition of growth factors, secretome-loaded PA hydrogels were formulated and immersed in differentiation medium 2. Secretome was allowed to release from the hydrogel into the surrounding medium for 24 hours. At this point, differentiation medium 1 was removed from the cells and medium containing released factors from the gels was added. This media was refreshed every 24 hours until terminal differentiation was theoretically achieved.

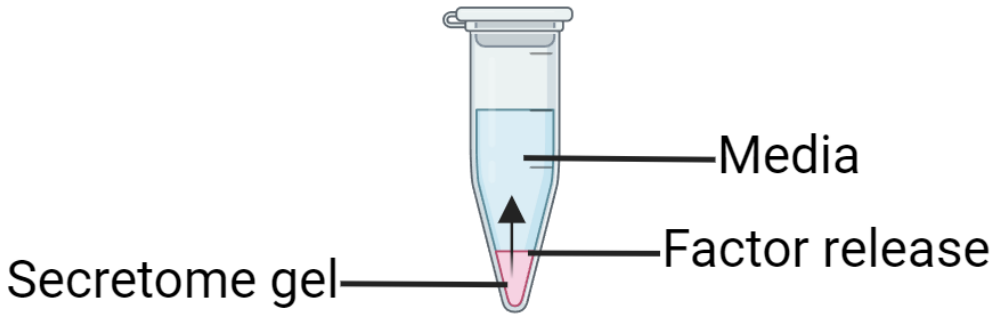

Figure 24: Schematic of experimental setup. Secretome is released from the PA gel into the surrounding media over time. Every 24 hours, this conditioned media is replaced on the differentiating cells.

A set of SH-SY5Y cells were left undifferentiated as controls. No changes in phenotype were observed, and large clusters were seen to form as cells became overconfluent (Figure 25A). This is typical of undifferentiated SH-SY5Y cells

and confirms that no differentiation takes place in the absence of RA and growth factors. Following treatment with RA (Figure 25B), morphological differences are observed in the cells, and neurite outgrowths are seen. In the case where cells are treated with just RA, these outgrowths are shorter than in cells treated with both RA and growth factors. This agrees with previous knowledge of the SH-SY5Y cell line that RA treatment may induce transcriptomic changes in the cells to initiate differentiation, but neurite outgrowth and terminal differentiation is only reliably achieved in the presence of the appropriate growth factors. Reduced proliferation in these differentiated cells is aided by reducing the concentration of foetal bovine serum (FBS) once RA is added to the media, pushing the cells towards a serum-starved state.

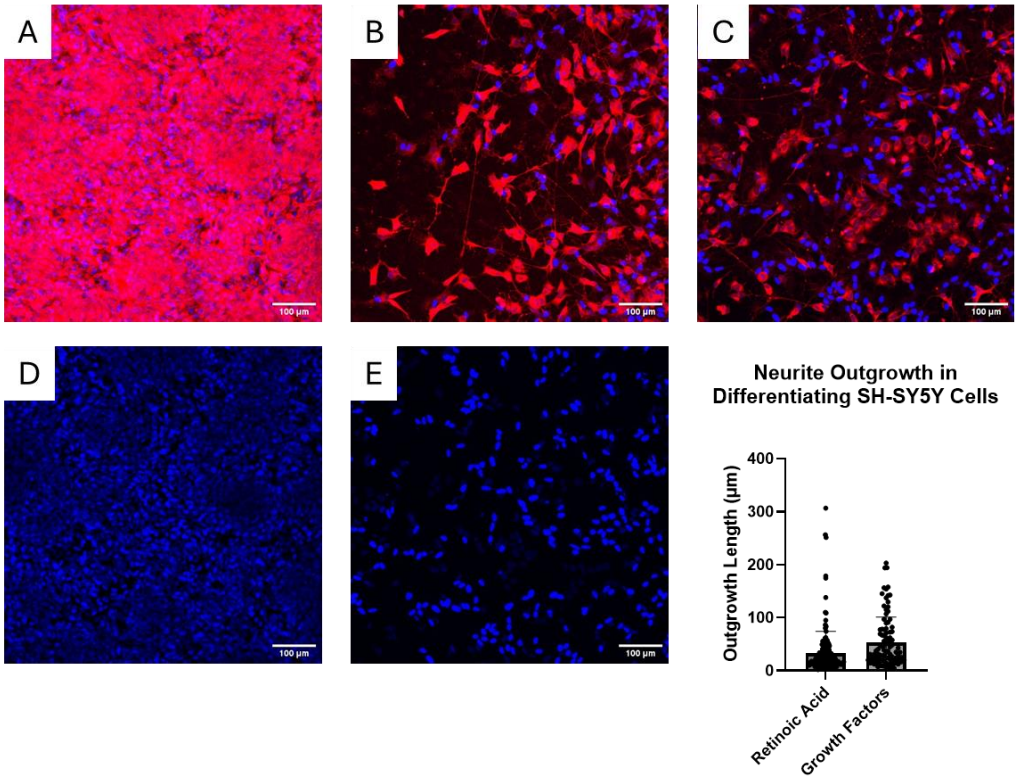

Sample	Average outgrowth length (µm)	Standard Deviation (s^2)	% Increase from Retinoic Acid
Retinoic Acid	32.4	41.6	N/A
Growth Factors	53.7	47.3	65.6

Figure 25: Characterisation of the SH-SY5Y cell line undergoing differentiation. A-C: Membrane and nucleus staining of SH-SY5Y cells after A) no treatment, B) Retinoic acid treatment, and C) Retinoic acid and growth factor treatment. All images taken after 10 days of culture. Scale = 100 µm. D, E: Nucleus

staining of SH-SY5Y cells D) before and E) after differentiation. All images taken after 10 days of culture. Scale = 100 µm. Bottom right: Measurement of neurite outgrowth with and without growth factor treatment. Measured using the SNT plugin for ImageJ.

The introduction of a gel-based delivery system for SCS was observed to induce an increase neurite outgrowth in all cases where the HMPA was present, compared to the administration of a single dose of liquid secretome (Figure 26). In the case of using PAE_3 with SCS, minimal increase was observed, and neurite outgrowth appears to be lower than when using growth factors alone. This agrees with the SPR data that the HMPA has a greater affinity to some proteins compared to PAE_3, therefore PAE_3 may release all factors at once and a sustained effect may not be observed. There is some previous literature that proteins bound to biomaterials experience a greater half-life than those unbound in solution,[38] and it may therefore be that more proteins maintain activity over time when HMPA is present in the formulation.

The greatest increase was observed with a 30% w/w HMPA mixture with PAE_3, followed by 10% w/w. Above 30% HMPA, this effect is less pronounced. This may be due to a crowding effect on the surface of the fibres, in which the increased number of bioactive epitopes will sterically block the binding of proteins, resulting in reduced binding and possibly reduced protein activity. Previously, epitope weight percentages ranging between 10-30 have been observed to be the most effective, such as in promoting cell adhesion.[39] In addition to the potential for increased half-lives due to increased protein binding, it is possible that the release of proteins over time is indeed sustained in the HMPA formulations, although more accurate measures of this are needed, such as ELISA quantification, due to the uncertainty in readings introduced by the plate reading equipment used in Section 2.4.3. If there is sustained release, this would result in the differentiating cells receiving a lower dosage of SCS at each time point compared to the liquid SCS, which may indicate a degree of dosage-dependent neurite outgrowth. Indeed, there is evidence that secreted factors from stem cells, such as the secretome, are only bioactive at low doses and lose their efficacy at higher doses.[40]

An increase in neurite outgrowth was also observed in 30% w/w HMPA when compared with the standard growth factor treatment of NGF and BDNF (Figure

26). Here, each gel formulation was prepared in a manner which meant each well would receive active factors at a similar concentration to the growth factors used in the control. Therefore, it is unlikely that a concentration effect has led to this difference. It may be that the inherent complexity of the SCS, as demonstrated by LC-MS/MS analysis (Figure 11B), results in a greater neurotrophic effect. It may be that a greater number of pathways related to neurite outgrowth are activated by the increased number of different factors, resulting in greater neurite outgrowth. Indeed, LC-MS/MS analysis did reveal a significant upregulation of factors related to multiple neurological processes.

Minimal difference was observed between cells exposed to exposed only to RA and cells exposed to RA and PAs (Figure 26). While not unexpected, this is important to confirm that any differentiation observed in secretome-treated cells would be a result of the secretome only. Additionally, it indicates that PAs released as the hydrogel degrades do not appear to induce transcriptomic changes, although further physiological investigation would be required to confirm this. It also indicates that any potential fragments containing glutamic acid, a neurotransmitter, may not alter cell behaviour.

The impact of the use of SCS is also indicated by comparing the neurite outgrowth in cells treated by gels containing SCS with PA gels alone (Figure 26). An increase in outgrowth length was observed when the SCS was added to the PA formulation in every case that HMPA was present. The change was most pronounced 10% HMPA, which saw a 97.62% increase in outgrowth length, followed by 30% HMPA at 78.24% increase. Conversely, minimal increase was observed when secretome was used with PAE_3 or with HBPA. When HMPAsc was used at 10% w/w with PAE_3, a decrease in neurite outgrowth was observed, further lending evidence to the efficacy of the HMPA sequence. Comparatively, outgrowth in 10% HMPA with SCS were, on average 133.17% longer than 10% HMPAsc with SCS. This data aligns with the SPR data previously obtained, which indicated that HMPAsc had a very low affinity to proteins in comparison to HMPA. Therefore, it is possible that the proteins released by HMPA have a higher efficacy than those released by HMPAsc, which is reflected in the increased neurite outgrowth.

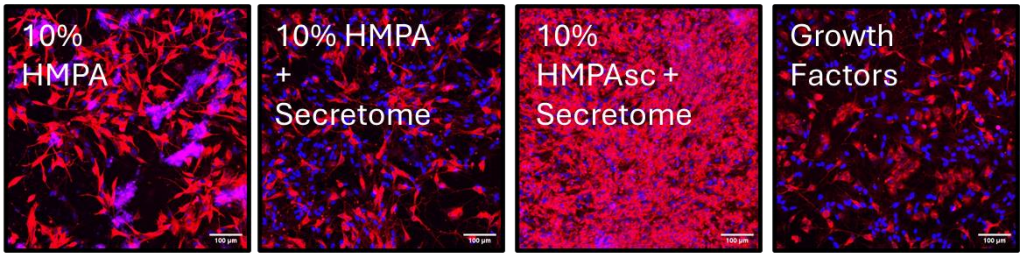

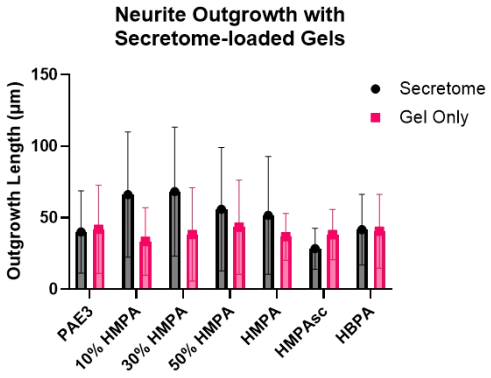

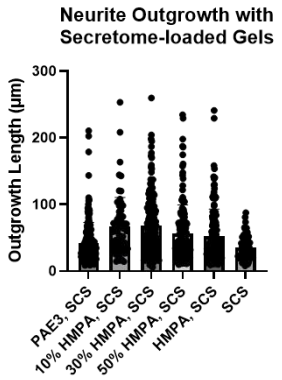

Sample	Average outgrowth length (µm)	Standard Deviation (s^2)	% Change from SCS	% Change from Growth Factors
SCS	34.9	17.5	N/A	-35.1
PAE3+SCS	42.0	30.9	+20.5	-21.8
10% HMPA+SCS	66.2	44.1	+89.9	+23.3
30% HMPA+SCS	68.3	45.3	+96.0	+27.3
50% HMPA+SCS	56.0	43.3	+60.7	+4.3
HMPA+SCS	51.7	41.4	+48.3	-3.7
Growth Factors	53.7	47.3	+54.0	N/A

Figure 26: Neurite outgrowth in SCS-treated SH-SY5Y cells. ***Top:*** *Representative images of SH-SY5Y cells after undergoing different treatments. Membrane staining = red. Nucleus staining = blue. Scale = 100 µm.* ***Middle Right:*** *Comparison of neurite outgrowth lengths in SH-SY5Y cells treated with liquid secretome and gel-released secretome.* ***Middle Left:*** *Comparison the effect of adding SCS to a PA gel on neurite outgrowth.* ***Bottom:*** *Tabulated comparisons of neurite outgrowth as a result of PA formulation.*

It is difficult to fully understand the mechanism of action of the SCS and how, on a molecular scale, it improves neurite outgrowth. LC-MS/MS did reveal a significant upregulation of neuroactive factors which likely contribute to neurite outgrowth (Figure 11B-E). However, nerve growth factor (NGF) was notably absent from the list of predicted proteins. In this study, the SH-SY5Y cells are differentiated into cholinergic neurons. Previously, a lack of NGF was observed

to impede the growth of cholinergic neurons and trigger their atrophy in an Alzheimer's model.[41] Here, however, such an effect was not observed and SCS treatment with an apparent lack of NGF was able to improve neurite outgrowth. It may therefore be possible that NGF was present below the limit of detection for proteomics here. Furthermore, it was observed to be possible to formulate the PA-SCS hydrogel in a manner which yields an increase in average neurite outgrowth length compared to NGF treatment. It is possible that the sheer number of neuroactive factors present can overcome the lack of NGF, potentially triggering signalling pathways that aid in neurogenesis. Tenascin, for example, was detected in the secretome and is known to regulate the activity of cholinergic neurons found in the human colon.[42] Overall, it is likely that the exploitation of biological complexity here has contributed to the neurotrophic effects of the SCS.

2.6.6 Survival and Neurite Outgrowth in Damaged Mature Neurons

Having gathered evidence that the release of proteins from SCS-loaded PA hydrogels may successfully lead to increased neurite outgrowth of the SH-SY5Y cell line, it may be inferred that these formulations are neurotrophic. To further probe the extent to which these formulations may be beneficial in a spinal cord model, it was deemed necessary to investigate whether they may prevent or delay cell death in mature neurons which have been mechanically damaged and increase neurite outgrowth following this damage. Any possible neuroprotective effect would be helpful in restoring motor function following spinal cord injury, wherein cells have been damaged mechanically.

Here, SH-SY5Y cells underwent the standard differentiation protocol as described in section 2.6.3. Following differentiation, cells were passaged using 0.05% w/v trypsin (as opposed to 0.25% w/v used in standard passaging) to minimise chemical damage to the cells. Successful detachment from the plate was observed. Cells were then replated at the same density as when detached from the plate. It was observed that all neurite outgrowths had been destroyed, and cells had adopted a rounded morphology immediately after seeding, indicating mechanical damage to the cells. Viability staining confirmed the cells were still alive immediately after seeding (Figure 27). In theory, as these

differentiated SH-SY5Y cells have achieved a post-mitotic state, damage to the neurite outgrowth and cells themselves will lead to cell death. This method may therefore be viewed as a simple model of a traumatic spinal cord injury, wherein damaged mature neurons are unable to reform connections or recover populations through mitosis, leading to a permanent loss of motor function.

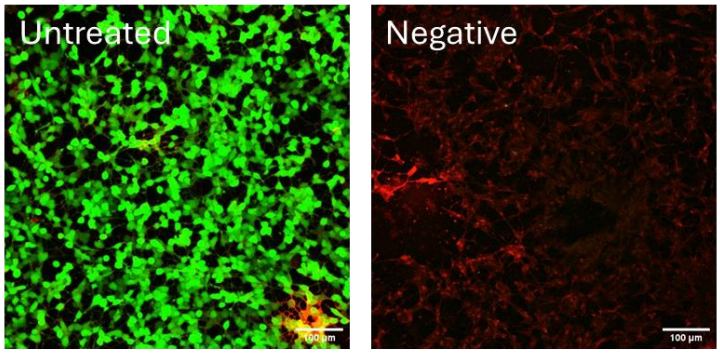

Sample	Average outgrowth length (µm)	Standard Deviation (s^2)	% Change from Negative
Untreated	28.5	14.7	-26.3
SCS	31.7	18.7	-5.9
Growth Factors	47.1	31.6	+58.7
Negative	33.1	19.9	N/A

Figure 27: Viability and outgrowth of replated SH-SY5Y cells. ***Top Left and Middle:*** *Representative images of SH-SY5Y cells stained for viability (green) and outgrowth (red). Scale = 100 µm.* ***Top Right:*** *Measurement of neurite outgrowth in replated control conditions.* ***Bottom****: Tabulated comparison of the effect of different treatments on neurite outgrowth.*

In the control conditions, it was observed that minimal difference in outgrowth length is achieved through the administration of liquid secretome, with this condition yielding lengths similar to replated cells which were left untreated and replated cells which were treated with DMSO to act as a negative control (Figure 27). The outgrowths present in the negative control – the cell death in which is confirmed by the lack of green staining – are likely from prior to replating and may serve as a baseline for neurite outgrowth in this replating experiment. It was not unexpected that an untreated sample would not exhibit greatly increased outgrowth lengths, as there are no growth factors in the media to induce this.

In the case of the liquid secretome, it may be that the 24-hour incubation before the media change is not sufficient to induce noticeable outgrowths over the following 96 hours. This agrees with the outgrowth observed before replating, where liquid SCS induced minimal increase in outgrowth length (Figure 26). Therefore, it is likely that a sustained presence of factors is required for increased outgrowth length. This argument is supported by the increase in outgrowth length when replated cells are introduced to a sustained presence of the growth factors NGF and BDNF. Therefore, it was believed that factors released from gels may also yield beneficial effects.

It was observed that, in all conditions except HMPA-SCS, cells were able to survive for the length of the experiment – 5 days. The reason for the apparent toxicity towards replated SH-SY5Y cells from HMPA is not known, although it was also observed that MTS assays were also toxic to the replated cells – cells would die during incubation with the MTS reagent, regardless of the experimental condition. Neither HMPA nor MTS are observed to be toxic to the SH-SY5Y cell line before replating. It may be that replating these cells introduces some changes in their biology which makes them more susceptible to certain changes in their environment. No previous studies have reported this, so it is difficult to make a claim as to the exact reason for toxicity. Previous studies looking at replated SH-SY5Y cells observed only their viability and did not report any transcriptomic experiments.

For the neurite outgrowth, 10% HMPA with secretome was found to increase the average length of measured neurites compared to all other conditions (Figure 28). This agrees with the neurite outgrowth data observed in differentiating SH-SY5Y cells, where 10% HMPA with secretome was observed to induce the greatest increase in average outgrowth length compared to a secretome-free control. This indicates that the 10% HMPA formulation is optimal for delivering proteins in a manner which maintains their neurotrophic abilities. On average, 10% HMPA is the formulation which sees the slowest release of proteins over time, and it may be this sustained release which consistently supplies developing neural cells with required growth factors for longer outgrowths.

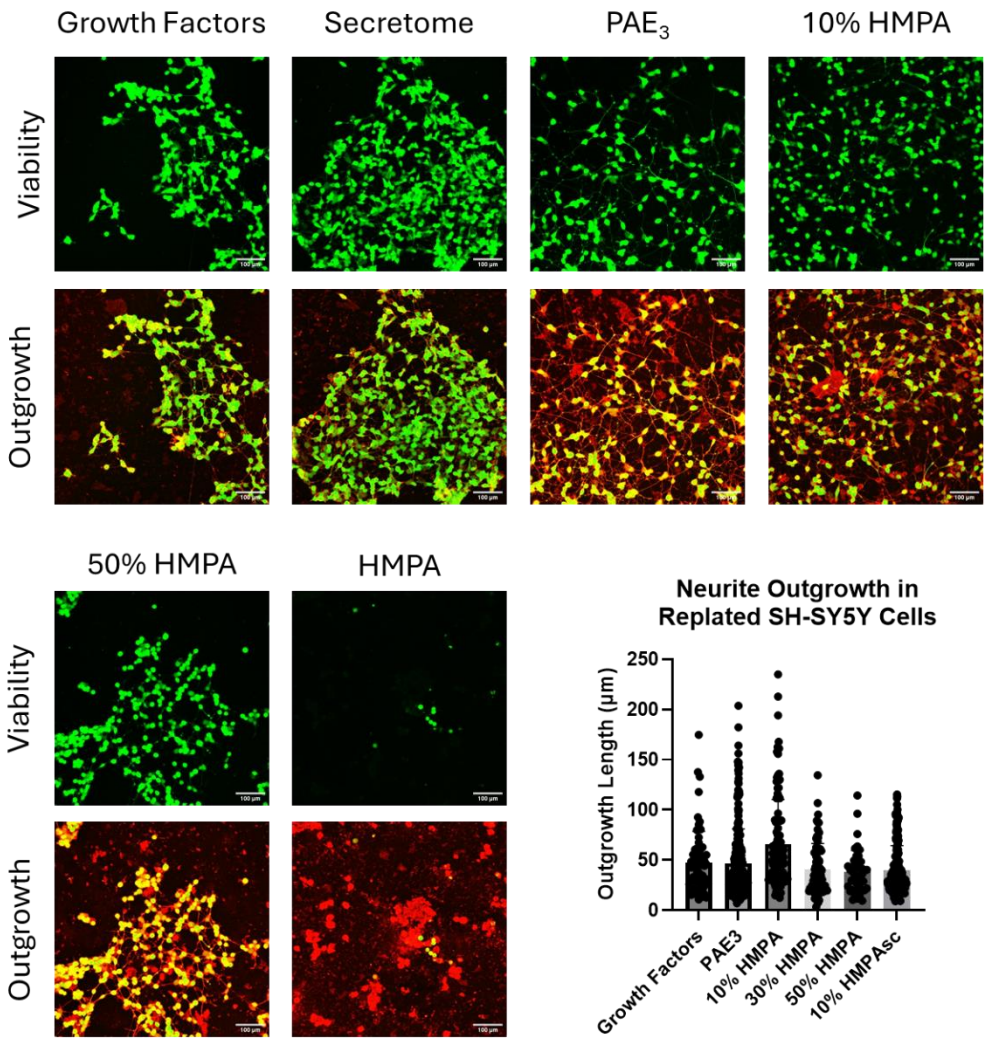

Sample	Average outgrowth length (µm)	Standard Deviation (s^2)	% Change from Growth Factors
Growth Factors	47.1	31.6	N/A
PAE3+SCS	46.7	34.5	+9.3
10% HMPA+SCS	66.1	44.2	+40.0
30% HMPA+SCS	40.7	25.9	-17.9
50% HMPA+SCS	38.0	21.6	-31.7
10% HMPAsc+SCS	40.1	24.4	-22.7

Figure 28: Neurite outgrowth in replated mature SH-SY5Y cells. Green = cell viability stain. Red = cell membrane stain. Both live and dead cells may be stained red, but only live cells may be stained green. ***Middle Right****: Graph of neurite outgrowth measurements after 5 days of treatment.* ***Bottom:*** *Tabulated comparisons of neurite outgrowth after replating.*

In the case of 30%, 50%, and 100% HMPA, a large amount of gel debris is observed with the cells, indicating rapid degradation of these gels in line with the stability data previously obtained (Figure 20). It may therefore be the case that proteins in these formulations were released at a much faster rate and were exhausted before the completion of the experiment, resulting in reduced neurite outgrowths. PAs for this experiment were handled delicately to minimise degradation, but it appears to be impossible to avoid above certain weight percentages of HMPA. It would therefore seem necessary to either adjust the sequence of the HMPA to make it more stable and robust in response to mechanical forces or incorporate a polymer gel for improve mechanical properties.

However, while it is promising that average neurite outgrowth length may be increased using PA-SCS formulations, it must be mentioned that the SH-SY5Y cell line is derived from a bone-metastasis of a neuroblastoma. While they are cells derived from the central nervous system (CNS), they are not entirely representative of the entire network of cells which constitute the spinal cord. Future work must focus on examining more complex models of the spinal cord, such as ex vivo slices or in vivo administration, to fully explore the efficacy of the PA-SCS formulations. It must be stated that, in this body of work, only a single replicate of each condition was performed for neurite outgrowth studies. This was done to cover a greater number of conditions and identify possible leads for future works. Therefore, while the data appear to follow a trend predicted by the test hypothesis, replicate values would be needed for increased confidence in beneficial effects and disprove the null hypothesis.

2.7 Conclusions

Here, it has been described how a conscientiously designed peptide sequence may be used to form a hydrogel for the binding and controlled release of multiple proteins in a complex fluid. This functionality was applied to neural tissue engineering, chiefly the differentiation of the SH-SY5Y cell line – a broadly used model in neuroscience – owing to the neuroactive properties of adipose-derived stem cell secretome as described in previous literature and as predicted by gene ontology from LC-MS/MS data.

It was determined through LC-MS/MS and ontological analysis that the secretome is a highly bioactive protein mixture, with a significantly greater population of proteins involved in biological processes than would be expected to be observed in a random population. Within this, neurologically relevant biological processes are also significantly upregulated, indicating the potential for neural tissue engineering applications. However, single-dose application of liquid secretome was not found to be sufficient to induce neural differentiation in the SH-SY5Y cell line. A controlled release system would therefore represent a significant improvement upon liquid injection.

In this vein, PA molecules were screened for their suitability for use in a system with the SCS. It was observed that PAK_2 and PAE_3 presented as the most likely candidates. Other candidates, such as PAK_3, PAK_4, PAK_3AGD, and PAK_3GHK Owing to the slower gelation kinetics and the potential to align PAE_3 fibres and potentially create a more favourable environment for neuronal growth, it was selected as the sole PA of interest. This alignment was observed to be maintained when gelated with SCS. However, as PAE_3 is not bioactive and was not predicted to interact with a vast majority of proteins in the SCS, a bioactive sequence was designed.

Heparin was used as the inspiration for this sequence, and a previously reported heparin-mimetic sequence was conjugated to PAE_3 to yield HMPA. HMPA was observed to have binding kinetics to IL-6 similar to that of heparin, providing K_D estimations in the same order of magnitude as heparin. When mixed with PAE_3, a formulation of 10:1 PAE_3:HMPA weight ratio was found to yield, on average, a more controlled release of proteins, maintaining roughly 5% of protein on average after 96 hours. PAE_3 alone and formulations containing greater weight ratios of HMPA were not found to exhibit controlled release.

These formulations were then tested for their neurotrophic effects. An increase in neurite outgrowth was observed when the SCS was paired with a HMPA-containing formulation, indicating the effectiveness of this PA sequence. In the case of replated SH-SY5Y cells, only 10% w/w HMPA was observed to induce an increase in neurite outgrowth compared to growth factor treatment, therefore signalling that this may be the optimal formulation for growth factor release.

However, the stability of these PA gels was unpredictable, with HMPA-containing formulations degrading rapidly in solution. While this may not be an issue in a controlled experiment where mechanical forces applied to the PA are minimised, it would be cause for concern should these gels ever be used as an implant, as the desired release profile would be lost upon degradation. Therefore, it was decided to explore formulations to increase stability of these gels – opening the possibility to introduce 3D-printable moieties or polymer hydrogels into the formulation.

2.8 Future Work

The work presented here has demonstrated the ability of using a heparin-mimetic peptide amphiphile sequence to bind secretome proteins with a similar affinity and kinetic profile to native heparin and used this to fabricate a functional hydrogel capable of increasing the neurite outgrowth in the SH-SY5Y cell line, both in undifferentiated and mature phenotypes. However, while this represents a good in vitro study, further work should be conducted to further explore the potential of these formulations.

Firstly, work should be conducted to accurately quantify the rate of release of specific proteins from these hydrogels using ELISA. A range of different proteins should be used to confirm the ability to bind multiple factors in these gels. It is predicted that, owing to the binding affinity of the heparin-mimetic sequence, release from PAE_3-HMPA formulations will be more controlled with increasing HMPA. This would occur up to a point where a crowding effect is observed, possibly above 30% w/w, at which less binding would occur, and release would be faster.

Further to this, improving the stability of these PA formulations would also be of importance. It is demonstrated that the HMPAsc sequence is more stable than the HMPA sequence, despite not providing any binding affinities. It is possible, therefore, that there may be a sequence arrangement which offers both mechanical stability and binding affinity. Additionally, it would likely be possible to make these HMPA formulations less stiff by shifting towards a PAE_2 base sequence. This base sequence may still provide anisotropy by thermal

annealing, but would also trend towards a lower stiffness, perhaps opening the possibility for brain tissue engineering as well as spinal cord.

It would also be interesting to investigate whether these formulations work on other neuronal cell lines, such as human spinal cord astrocytes. Such an investigation would confirm that the molecular pathways activated by the released factors here are carried into a more relevant cell model. Following from this, ex vivo models, such as murine spinal cord slices, could be used prior to in vivo modelling in a rat spinal cord injury. The implanted hydrogel would need to display greater efficacy in restoring motor function in this case when compared to liquid secretome administration. From the SH-SY5Y neurite outgrowth data, it is possible that this may occur.

Should these gels be made less stiff and useable in brain tissue engineering, they may be used to aid recovery in brain injury models. Further to this, the SCS has also been shown to be effective in improving the symptoms of Alzheimer's disease.[10] As neurogenesis appears conserved, or even improved, when moving from liquid SCS to PA-SCS, it is possible that the beneficial effects in Alzheimer's models may also be conserved in these gels. Thirdly, the use of PA-SCS would possibly be beneficial in the treatment of amyotrophic lateral sclerosis (ALS), with pre-clinical evidence demonstrating the potential of SCS for treatment of this disease.[43]

It was also believed that these gels presented themselves as candidates for additive manufacturing. By introducing top-down control on the shape of the gel, it may be possible to further control the release profile by altering the surface area-to-volume ratio. In doing so, it is believed that a vast range of release profiles could be achieved, allowing for personalised delivery systems based on individual patient needs. Furthermore, precision shape control may allow for the fabrication of implants which specifically fit the shape of an individual spinal cord injury, filling a defect and possibly improving patient outcome. However, many additive manufacturing techniques which would offer the resolution required for this are light-based techniques, such as stereolithography (SLA) or two-photon polymerisation (2PP). Therefore, while extrusion and inkjet are likely the most natural applications for PA hydrogels, it

would be possible to combine PAs with a photopolymer to integrate this system with high-resolution techniques.

2.9 Experimental

2.9.1 SDS-PAGE

Samples for SDS-PAGE were prepared and run as per manufacturer's protocol. Briefly, SCS (6.5 µL), lithium dodecyl sulphate (LDS) buffer (4x, 2.5 µL) (NuPAGE), and reducing agent (10x, 1 µL) (NuPAGE) were mixed and incubated at 70 °C for 10 minutes. Meanwhile, running buffer was prepared by diluting 2-(*N*-morpholino)ethanesulfonic acid (MES) sodium dodecyl sulphate (SDS) (20x, 50 mL) to 1 L using deionised water. Samples were run in a 10% bis-tris polyacrylamide gel (NuPAGE) for 35 minutes at 200 V. PageRuler Plus prestained protein ladder was used as a control.

Following electrophoresis, gels were washed 3x with Milli-Q water (100 mL, 30 minutes) before staining overnight with PageBlue protein staining solution. Gels were then destained 2x with Milli-Q water (100 mL, 5 minutes) before a final wash (100 mL, 30 minutes). Stained gels were then imaged on an Odyssey XF Imager (Li-Cor) with an exposure time of 2 minutes.

2.9.2 Gel formation

PAs (2% or 4% w/v) were dissolved in HEPES buffer (10 mM, pH 7.4) in the absence of a vortex or mixing. For PA-E3, NaOH (1 M) was added in 0.5 µL graduations until complete dissolution was observed. PAs were used to form gels immediately after dissolution. For HMPA and PA-E3, gels were formed by injecting PA solution (2% w/v) into $CaCl_2$ (0.002-1 M) or secretome. For cell-based experiments, secretome was supplemented with additional $CaCl_2$ (20 mM). For HBPA gels, heparin solution (2.66% w/v) was injected into HBPA solution (4% w/v) in a 1:1 volume ratio, yielding a gel with a 3:2 HBPA:heparin weight ratio and final PA concentration of 2% w/v. Following introduction to the gelling solution, PAs were incubated (37 °C, 5% CO_2) for 24 hours before use.

2.9.3 Rheology

Rheological measurements were performed on an MCR 302 modular compact rheometer (Anton Paar, Austria) using an 8 mm diameter parallel plate (PP08, Anton Paar). All experiments were performed in triplicate and the gel was replaced after each experiment. Amplitude sweeps were performed from 0.001-100% strain, from which the linear viscoelastic (LVE) region of the gel was determined. Frequency sweeps were performed from 100-0.1 rad s^{-1} at a strain within the LVE region. Data were processed using the RheoCompass software (Anton Paar).

2.9.4 Uniaxial Compression Testing

Uniaxial compression testing for Young's Modulus determination was performed using a TA.HDPlus texture analyser (Stable Micro Systems) fitted with a 5 kg load cell and 32 mm diameter cylindrical probe. Gels of 100 µL volume were formed under the same conditions prior to loading on the base plate. Compression testing was performed at a movement speed of 1 mm s^{-1} and ceased upon sample break. All measurements were performed in a lab controlled at 19 °C. Data were exported using the Exponent software and plotted using GraphPad Prism.

2.9.5 Zeta Potential

Zeta potentials of solutions were measured on a Zetasizer Nano Series system (Malvern Panalytical). PAs (0.1% w/v) were dissolved in ultrapure water immediately prior to measurement. Each measurement was performed in triplicate. Data were processed using the Zetasizer Software (Malvern Panalytical).

2.9.6 Polarised Light Microscopy

Birefringence images were obtained on a Zeiss Axioplan brightfield microscope with an optical polariser. Samples were formed on a polydimethylsiloxane (PDMS) substrate before being transferred to a glass slide for imaging. Samples were imaged no longer than 24 hours after formation.

2.9.7 Circular Dichroism

Samples for CD were prepared in ultrapure water to a concentration of 0.001% w/v. Samples were injected into a clean quartz cuvette with a 1 mm light path. Measurements were performed on a Chirascan Plus CD (Applied Photophysics) in triplicate. Data is presented as an average of all scans.

2.9.8 Scanning Electron Microscopy

Samples were prepared for SEM through serial dehydration. Initially, samples are fixated by immersion in paraformaldehyde (4% w/v) for 20 minutes, followed by immersion in ethanol at a series of concentrations (20, 50, 70, 80, 90, 96, 100% v/v). Following this, samples are subjected to critical point drying and subsequent iridium coating (10 nm). Scanning electron microscopy was performed on a 7000F SEM (JEOL, Japan) with an accelerating voltage not exceeding 15 kV.

2.9.9 Dynamic Light Scattering

DLS measurements were performed using a DynaPro Plate Reader II (Wyatt, USA) at a fixed attenuation level of 95% and laser power of 20%. Three measurements were taken for each sample, with each measurement consisting of ten attenuations. PAs were reconstituted in Milli-Q water and diluted to the desired concentrations in a black, glass bottom 96 well sensoplate (Greiner Bio-one, Austria) immediately before measurement. Data were processed using DYNAMICS V7 software (Wyatt, USA).

2.9.10 Surface Plasmon Resonance

Surface plasmon resonance measurements were performed on a Biacore T200 sensor (Cytiva, USA). Recombinant human IL6 (Peprotech, USA) was dissolved in PBS at a stock solution of 1 mg mL^{-1}, before being diluted to 10 µg mL^{-1} in acetate buffer (pH 4.0) prior to immobilisation. Immobilisation was performed via amine coupling to an EDC/NHS complex on a dextran-coated gold sensor CM5 chip (Cytiva, USA) at flow rate of 10 µL min^{-1} for 1200 s. Unreacted EDC/NHS was capped with ethanolamine. A blank immobilisation was performed on a reference flow cell.

HEPES-buffered saline (HBS-P) was prepared as a 10x stock solution containing HEPES (0.1 M), NaCl (1.5 M), and P20 surfactant (0.5% 2v/v) in

Milli-Q water and pH adjusted to 7.4 using NaOH. The buffer was filtered with 0.22 µm filters, degassed, and stored at 4 °C in the absence of light. The buffer was diluted to 1x concentration using Milli-Q water immediately before sample preparation.

All samples were prepared using HBS-P buffer immediately before measurement. Samples were injected at a flow rate of 5 µL min^{-1} for a contact time of 1000 s, followed by a dissociation time of 1000 s. A regeneration step of glycine-HCl (pH 2.5) was performed after every injection at a flow rate of 30 µL min^{-1} and a contact time of 30 s. All sample measurements were performed at 25 °C. Data were processed using Biacore T200 evaluation software.

2.9.11 FITC Fluorescence Measurements

SCS was labelled with a FluoReporter FITC labelling kit (ThermoFisher, Cat. No. F6434). Labelling was performed as directed by the supplier, with the exception that a Pur-A-Lyzer mini dialysis kit (Merck, USA) was used to purify labelled protein and remove unbound dye.

2.9.12 Liquid Chromatography Tandem Mass Spectrometry (LC/MS-MS)

Samples were precipitated using trichloroacetic acid (TCA)–acetone. TCA was added to 20 % (v/v), followed by 30 min incubation at −80 °C and centrifugation at 20,000 *g* for 20 min. Protein pellets were then washed with ice-cold (−20 °C) acetone, briefly the pellets were solubilised in acetone, aided by ultrasonication, followed by a centrifugation at 20,000 *g* for 20 min. The washed pellets were resuspended in 1.0 M triethylammonium bicarbonate buffer (TEAB) followed by centrifugation at 20,000 *g* for 5.0 min to remove insoluble material.

Samples were quantified using the BCA kit or nanodrop and 100 µg of each sample were subjected to liquid digestion. 4 µL of 50 mM tris (2-carboxyethyl)phosphine (TCEP)/DTT was added to 45 µL of sample to reduce samples, followed by an ultrasonication step for 2 min. Samples were then alkylated with addition of iodoacetamide for 30mins at RT. Precipitation was performed with acetone and samples were then resuspended in ammonium bicarbonate and digested overnight with LC grade trypsin at 37 °C overnight

Before performing the tandem mass spectrometry (MS/MS) analysis the peptide mixtures were cleaned/desalted C18 stationary phase tips.

Credit is given to Dr. Daniel Wilkinson and Dr. Kenneth Smith for the preparation and running of samples.

2.9.13 Cell Culture

SH-SY5Y cells were sourced from the ATCC at passage 11 and not used beyond passage 20. Cells were cultured in DMEM/F-12 1:1 media (Gibco 11320074) supplemented with 10% heat-inactivated FBS (HI-FBS), 1% Glutamax (Gibco 35050038), and 1% antibiotic-antimycotic (AA). Heat inactivation of FBS was achieved by heating to 56 °C for 30 minutes. Media changes were performed every 3 days. Cells were passaged upon reaching 80% confluency, split 1:5 at each passage.

Three separate media were used during cell culture: Growth Media (GM) containing 10% HI-FBS, 1% Glutamax, 1% AA; Differentiation Media 1 (DM1) containing 2.5% HI-FBS, 1% Glutamax, 1% AA, 10 μM all-trans retinoic acid (RA) (Stemgent 004-0021); Differentiation Media 2 (DM2) containing 1% HI-FBS, 1% Glutamax, 1% AA, 10 ng/mL BDNF (450-02 Peprotech), 50 ng/mL NGF (450-01 Peprotech).

Retinoic acid was stored in the absence of light at -20 °C as a 10 mM stock solution in DMSO, prepared by dissolving 5 mg RA in 1.66 mL DMSO.

Growth factors BDNF and NGF were stored at 25 μg/mL in a 0.1% BSA-buffered PBS solution at -20 °C.

Both RA, BDNF, and NGF were added to their respective media immediately prior to use, and this supplemented media was not used more than 24 hours after preparation.

For differentiation, Matrigel-coated plates were prepared for cell seeding. 1 day prior to plate preparation, Matrigel stock solution was transferred from -20 °C storage to 4 °C storage. On the day of preparation, an aliquot of PBS was placed in an ice bath and allowed to cool for 30 minutes. Matrigel was then added to ice cold PBS at a 1:50 Matrigel:PBS volume ratio and mixed via vortex. 100 μL

of Matrigel solution was then added to every well in a 96-well plate and incubated at 37 °C for 1 hour. After this, all fluid was aspirated from every well, and the plate was irradiated with UV for 30 minutes. Plates were stored at 4 °C for no more than 1 week before use.

Cells were differentiated following a slightly adapted version of a previous protocol. Here, cells at 80% confluency were passaged and resuspended in growth media (Day 0). These cells were then seeded atop Matrigel-coated plates at a density of 2,500 cells per well containing 200 µL GM. Immediately after seeding, cells were left to rest at room temperature for 1 hour before transfer to a 37 °C incubator.

The following day (Day 1), GM was replaced with DM1 in all but one condition, which was left as an undifferentiated control. On day 3, a media change was performed, with DM1 being replaced with fresh DM1. On day 5, PA gels were prepared and immersed in DM2 media without BDNF and NGF. On day 6, DM1 was replaced with DM2, or the DM2 from the PA samples. Media was then changed every 24 hours in all samples until day 11, at which point cells were stained using the Neurite Outgrowth Staining Kit (ThermoFisher A15001) for further imaging.

2.9.14 Replating Differentiated Cells

Cells for replating were differentiated following the above protocol but not stained on day 11. At this point, cells were detached from the Matrigel-coated plate using 0.05% Trypsin-EDTA for 3 minutes. These cells were then replated at a density of 10,000 cells per well in a Matrigel-coated 96-well plate containing 200 µL GM2 without BDNF and NGF. Replated cells were then treated with either growth factors or the released factors from PA gels for 5 days, with media being changed every 24 hours.

2.9.15 Staining Procedure

Immediately prior to imaging, cells were stained using the Neurite Outgrowth Staining Kit (ThermoFisher A15001) as per supplier's protocol. Briefly, media was removed from the cultured cells. Then, both the viability and membrane stain were diluted 1:1000 in PBS and added to each well. Samples were

incubated for 30 minutes at 37 °C. After this, staining solution was replaced with background suppression dye diluted 1:100 in PBS. At this point, samples were imaged.

2.9.16 Confocal Imaging

Confocal imaging was performed on a Leica SPE point scanning confocal microscope. Viability was visualised using a 488 nm laser, while outgrowth staining was visualised using a 532 nm laser. Samples were imaged immediately after staining.

2.9.17 Neurite Outgrowth Measurements

Neurite outgrowth was quantified using ImageJ with the SNT analysis plugin. Outgrowths were measured manually using the images obtained from the 532 nm laser in confocal imaging.

2.10 Bibliography

1. Bruggeman, F. J.; Westerhoff, H. V., *Trends Microbiol.* **2007,** *15* (1), 45-50.
2. Aderem, A., *Cell* **2005,** *121* (4), 511-513.
3. Smith, S. A.; Travers, R. J.; Morrissey, J. H., *Crit Rev Biochem Mol Biol* **2015,** *50* (4), 326-36.
4. Chang, C.; Yan, J.; Yao, Z.; Zhang, C.; Li, X.; Mao, H.-Q., *Adv. Healthc. Mater.* **2021,** *10* (7), 2001689.
5. Gnecchi, M.; Zhang, Z.; Ni, A.; Dzau, V. J., *Circ Res* **2008,** *103* (11), 1204-19.
6. Kapur, S. K.; Katz, A. J., *Biochimie* **2013,** *95* (12), 2222-2228.
7. Rehman, J.; Traktuev, D.; Li, J.; Merfeld-Clauss, S.; Temm-Grove, C. J.; Bovenkerk, J. E.; Pell, C. L.; Johnstone, B. H.; Considine, R. V.; March, K. L., *Circulation* **2004,** *109* (10), 1292-1298.
8. Linero, I.; Chaparro, O., *PLOS ONE* **2014,** *9* (9), e107001.
9. Hsiao, S. T.; Lokmic, Z.; Peshavariya, H.; Abberton, K. M.; Dusting, G. J.; Lim, S. Y.; Dilley, R. J., *Stem Cells Dev.* **2013,** *22* (10), 1614-1623.
10. Hijroudi, F.; Rahbarghazi, R.; Sadigh-Eteghad, S.; Bahlakeh, G.; Hassanpour, M.; Shimia, M.; Karimipour, M., *Neuromolecular Med.* **2022,** *24* (4), 424-436.
11. Lee, E. Y.; Xia, Y.; Kim, W. S.; Kim, M. H.; Kim, T. H.; Kim, K. J.; Park, B. S.; Sung, J. H., *Wound Repair Regen.* **2009,** *17* (4), 540-547.
12. Roth, S.; Dreixler, J. C.; Mathew, B.; Balyasnikova, I.; Mann, J. R.; Boddapati, V.; Xue, L.; Lesniak, M. S., *Investig. Ophthalmol. Vis. Sci.* **2016,** *57* (7), 3522-3532.
13. Park, B.-S.; Kim, W.-S.; Choi, J.-S.; Kim, H.-K.; Won, J.-H.; Ohkubo, F.; Fukuoka, H., *Biomed. Res.* **2010,** *31* (1), 27-34.
14. Gomes, E. D.; Mendes, S. S.; Assunção-Silva, R. C.; Teixeira, F. G.; Pires, A. O.; Anjo, S. I.; Manadas, B.; Leite-Almeida, H.; Gimble, J. M.;

Sousa, N.; Lepore, A. C.; Silva, N. A.; Salgado, A. J., *Stem Cells* **2018,** *36* (5), 696-708.
15. Muhammad, S. A.; Abbas, A. Y.; Imam, M. U.; Saidu, Y.; Bilbis, L. S., *Mol. Neurobiol.* **2022,** *59* (5), 2894-2909.
16. Muhammad, S. A.; Nordin, N.; Fakurazi, S., *Rev. Neurosci.* **2018,** *29* (3), 321-332.
17. Arifka, M.; Wilar, G.; Elamin, K. M.; Wathoni, N., *Polymers (Basel)* **2022,** *14* (6).
18. AlQahtani, A. D.; O'Connor, D.; Domling, A.; Goda, S. K., *Biomed. Pharmacother.* **2019,** *113*, 108750.
19. Kehl, D.; Generali, M.; Mallone, A.; Heller, M.; Uldry, A.-C.; Cheng, P.; Gantenbein, B.; Hoerstrup, S. P.; Weber, B., *NPJ Regen. Med.* **2019,** *4* (1), 8.
20. Ho, M.; Thompson, B.; Fisk, J. N.; Nebert, D. W.; Bruford, E. A.; Vasiliou, V.; Bunick, C. G., *Hum. Genomics* **2022,** *16* (1), 1.
21. Burnett, L. R.; Rahmany, M. B.; Richter, J. R.; Aboushwareb, T. A.; Eberli, D.; Ward, C. L.; Orlando, G.; Hantgan, R. R.; Van Dyke, M. E., *Biomaterials* **2013,** *34* (11), 2632-2640.
22. Cheng, S.; Clarke, E. C.; Bilston, L. E., *Med. Eng. Phys.* **2008,** *30* (10), 1318-1337.
23. Woods, A. S.; Ferré, S., *J. Proteome Res.* **2005,** *4* (4), 1397-1402.
24. Ghosh, M.; Halperin-Sternfeld, M.; Grigoriants, I.; Lee, J.; Nam, K. T.; Adler-Abramovich, L., *Biomacromolecules* **2017,** *18* (11), 3541-3550.
25. Zhang, S.; Greenfield, M. A.; Mata, A.; Palmer, L. C.; Bitton, R.; Mantei, J. R.; Aparicio, C.; de la Cruz, M. O.; Stupp, S. I., *Nat. Mater.* **2010,** *9* (7), 594-601.
26. Ozawa, H.; Matsumoto, T.; Ohashi, T.; Sato, M.; Kokubun, S., *J. Neurosurg. Spine* **2004,** *1* (1), 122-127.
27. Peysselon, F.; Ricard-Blum, S., *Matrix Biol* **2014,** *35*, 73-81.
28. Mammadov, R.; Mammadov, B.; Toksoz, S.; Aydin, B.; Yagci, R.; Tekinay, A. B.; Guler, M. O., *Biomacromolecules* **2011,** *12* (10), 3508-3519.
29. Mammadov, R.; Mammadov, B.; Guler, M. O.; Tekinay, A. B., *Biomacromolecules* **2012,** *13* (10), 3311-3319.
30. Leibinger, M.; Andreadaki, A.; Diekmann, H.; Fischer, D., *Cell Death Dis.* **2013,** *4* (9), e805-e805.
31. Murthy, B. N.; Voelcker, N. H.; Jayaraman, N., *Glycobiology* **2006,** *16* (9), 822-832.
32. Hüttl, C.; Hettrich, C.; Miller, R.; Paulke, B.-R.; Henklein, P.; Rawel, H.; Bier, F. F., *BMC Biotechnol.* **2013,** *13* (1), 51.
33. Bonnet, H.; Coche-Guérente, L.; Defrancq, E.; Spinelli, N.; Van der Heyden, A.; Dejeu, J., *Anal. Chem.* **2021,** *93* (8), 4134-4140.
34. Tan, F.; Xu, X.; Deng, T.; Yin, M.; Zhang, X.; Wang, J., *Biomed. Mater.* **2012,** *7* (5), 055009.
35. van Wachem, P. B.; Hogt, A. H.; Beugeling, T.; Feijen, J.; Bantjes, A.; Detmers, J. P.; van Aken, W. G., *Biomaterials* **1987,** *8* (5), 323-328.
36. Buttiglione, M.; Vitiello, F.; Sardella, E.; Petrone, L.; Nardulli, M.; Favia, P.; d'Agostino, R.; Gristina, R., *Biomaterials* **2007,** *28* (19), 2932-2945.
37. Harsch, A.; Calderon, J.; Timmons, R. B.; Gross, G. W., *J. Neurosci. Methods* **2000,** *98* (2), 135-144.

38. Mester, S.; Evers, M.; Meyer, S.; Nilsen, J.; Greiff, V.; Sandlie, I.; Leusen, J.; Andersen, J. T., *MAbs* **2021,** *13* (1), 1893888.
39. Webber, M. J.; Tongers, J.; Renault, M. A.; Roncalli, J. G.; Losordo, D. W.; Stupp, S. I., *Acta Biomater* **2010,** *6* (1), 3-11.
40. Kesidou, D.; Bennett, M.; Monteiro, J. P.; McCracken, I. R.; Klimi, E.; Rodor, J.; Condie, A.; Cowan, S.; Caporali, A.; Wit, J. B. M.; Mountford, J. C.; Brittan, M.; Beqqali, A.; Baker, A. H., *Mol. Ther.* **2024,** *32* (1), 185-203.
41. Cuello, A. C.; Bruno, M. A., *Neurochem. Res.* **2007,** *32* (6), 1041-1045.
42. Aktar, R.; Peiris, M.; Fikree, A.; Cibert-Goton, V.; Walmsley, M.; Tough, I. R.; Watanabe, P.; Araujo, E. J. A.; Mohammed, S. D.; Delalande, J.-M.; Bulmer, D. C.; Scott, S. M.; Cox, H. M.; Voermans, N. C.; Aziz, Q.; Blackshaw, L. A., *J. Physiol.* **2018,** *596* (17), 4237-4251.
43. Walker, C. L., *Neural Regen Res* **2019,** *14* (9), 1522-1524.

3. The Additive Manufacturing of Self-assembling Hydrogels

3.1 Introduction

Having determined that a PA formulation exists which may be beneficial for the controlled release of multiple factors and therefore useful in secretome-based treatment of traumatic spinal cord injury, it was now decided that attempts should be made to integrate these systems with additive manufacturing for 'top-down' control of structures. Spinal cord damage or defects may adopt different topologies or sizes depending on the nature of the injury. Therefore, the ability to fabricate an implant which accurately recreates the geometry of the injury would be useful in possibly increasing efficacy by reducing 'dead space' (gaps between the gel and tissue) and preventing damage which may be caused by swelling of the gel. Here, several methods of additive manufacturing were tried to build a range of novel methodologies. Extrusion and light-based systems were initially adopted, owing to their ease of use and accessibility. Inkjet systems were considered, as the viscosity of PA solutions is typically within the range required for inkjet printing. However, in current inkjet systems there is a volume requirement of roughly 5 mL to sufficiently fill a cartridge, which would not be feasible with PA systems and therefore inkjet printing was not explored here. Successful top-down fabrication was observed in both extrusion and two-photon systems.

3.2 Aims and Objectives

The SCS-PA system developed in the previous chapter demonstrated good potential for nerve regeneration applications, having indicated that the released factors from a HMPA-PAE_3 hydrogel may lead to greater neurite outgrowth compared with growth factor treatment. However, these gels lacked mechanical stability – the gels were observed to degrade and lose high weight percentages in under 1 week, which may reduce their efficacy in an in vivo model. Furthermore, there remains the inability to precisely shape and pattern these gels. Doing so may facilitate the development of personalised hydrogel implants

for the sustained release of multiple soluble factors, with the potential existing to generate CAD structures from injury scans, so that an exact implant for a single patient may be printed.

Here, it was planned to integrate the PA-SCS formulation with AM to facilitate the top-down patterning of these gels and produce complex geometries on-demand. To demonstrate this, there are several objectives which must be achieved.

The principle aim here is to demonstrate that PA formulations may be integrated with a range of AM techniques, such as extrusion, inkjet, and light-based instruments. For extrusion, it must be demonstrated that the PA may be extruded through a nozzle in a controlled manner without the gelation being disrupted. The low viscosity of PA solutions appears to indicate that they may be suited to inkjet printing. However, inkjet printers require larger volumes of ink (~5 mL), which would not be feasible with PA solutions.

For light-based techniques, it should be demonstrated that the PA formulation may be made to gelate either directly or indirectly using light – ideally around 365-405 nm, as this is the working range of most light-based 3D printers. Failing this, the PA should be mixed with a photopolymerisable material and demonstrated to gelate in a two-gelator system.

Should successful integration with AM be achieved with these PAs, it should then be demonstrated that the biological effects observed in the previous chapter are preserved here. SCS-PA formulations should be successfully integrated into AM, and the release of the SCS from the PA should show improved neurite outgrowth compared to a non-treated and growth factor-treated control group. Cells should be treated the same as previously, undergoing retinoic acid treatment to induce transcriptional changes before SCS-PA treatment to trigger neurite outgrowth.

Secondary goals should also be defined. Here, it is hoped that a more stable PA formulation may be achieved through AM, such as through the inclusion of a polymer gelator. It would also be interesting to aim for gels with different regions of stiffness, achieved through AM patterning or different light exposures in the case of light-based techniques. In the case that any interesting mechanical

properties are observed in PA AM formulations, these should also be characterised to investigate any novel molecular behaviours. This may include different molecular packing, both before and after self-assembly, such as the lamellar plaques observed in annealed PAE_3.

3.3 Extrusion Printing

3.3.1 Extrusion Printing with Aqueous PA Solutions

Extrusion printing is one method which may be used to pattern peptide amphiphile systems. The slight self-healing ability of PA gels, predicted by the slope of a logarithmic plot of G' against ω in a rheological frequency sweep, indicates that shear-induced damage during extrusion printing may be recovered from, allowing the gels themselves to be extruded. Furthermore, the rapid gelation kinetics of a PA hydrogel observed in a plot of G' against time indicate that a liquid-in-liquid system would also be possible with minimal loss of print fidelity. Indeed, a liquid-in-liquid system would completely remove any concerns about shear-induced damage by only initiating gelation after the PA has extruded from the nozzle. Therefore, a liquid-in-liquid system was pursued.

Initially, a proof-of-concept experiment was performed to demonstrate that the PAE_3 used here may be extruded into a bath of $CaCl_2$ to produce a single, continuous gel (Figure 29A&B). The PA solution was extruded via manual pipetting into the gelling solution. It was observed that, when Ca^{2+} is present at 20 mM, PAE_3 gelates instantly upon contact, creating a defined structure at it exits the pipette tip. Here, a heterogenous thickness was observed in the extruded structure as lateral movement was performed manually, so could not be performed at a constant speed and flow rate, highlighting the need for translation with automated 3D printing systems for good reproducibility and homogeneity.

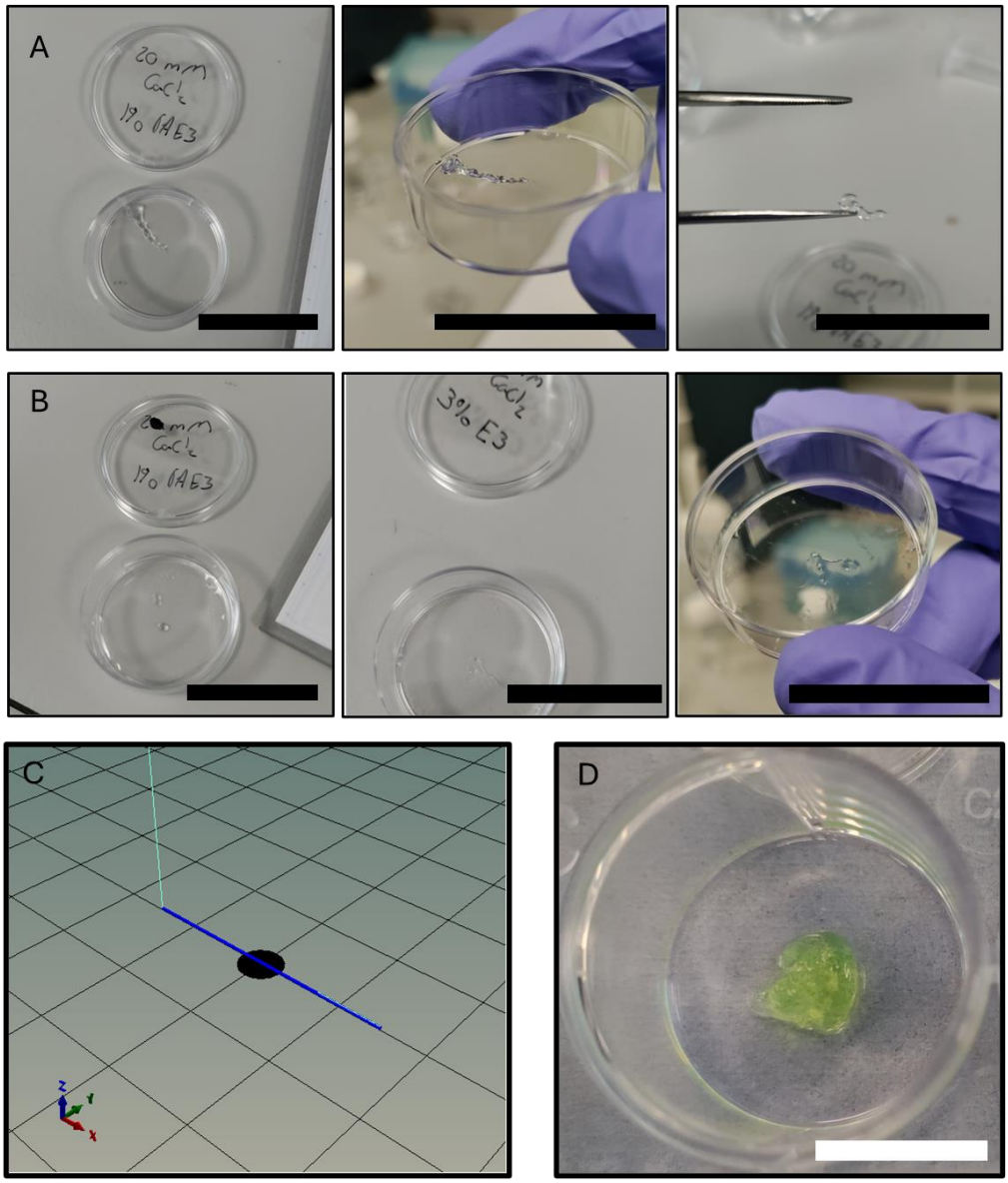

Material	Nozzle	Pressure	Speed	Temp	Gelling medium
PAE_3 (1%)	30 G	1 kPa	10 mm s^{-1}	20 °C	$CaCl_2$ (1 M)

Figure 29: Simple extrusion testing of PAE_3. ***A:*** *Manual extrusion via pipette of PAE_3 into 20 mM $CaCl_2$ solution and resulting gel. Scale = 32 mm.* ***B:*** *Manual extrusion of 1% and 3% PAE_3 into 2 mM $CaCl_2$ and ultimate failure of gelling. Scale = 32 mm.* ***C:*** *CAD image of desired structure (dark blue line).* ***D:*** *Actual printed structure. The extrusion of the PA solution could not be controlled accurately, and the resulting print lost all fidelity. Green colouration results from the use of thioflavin T dye. Scale = 5 mm. Table: Print parameters. Speed refers to the velocity at which the printhead moved in the XY directions.*

Upon reducing the Ca^{2+} concentration to 2 mM, the gelation rate was observed to decrease to the point where no defined structure was observed with 1% or 3% PAE_3 (Figure 29B). It is believed that here, the reduction in Ca^{2+} concentration

reduced the charge-dampening effect of these ions, inhibiting the rate of gelation and allowing PAE_3 micelles to diffuse away from the tip of the pipette, resulting in an effective reduction in PA concentration and thus preventing gelation. Some gelled material is observed with 3% PAE_3, and this may be due to the higher concentration facilitating gelation. This is not unexpected, as it was observed in the previous chapter that 2 mM Ca^{2+} may gelate a 1% PAE_3 solution by injection into the PA solution. Here, however, the order of addition is reversed, resulting in gelation failure.

This manual extrusion experiment served to highlight several useful fundamentals for the extrusion printing of PAE_3. Firstly, it was demonstrated that it is indeed possible to pattern the PA by extruding it in a defined direction in a bath containing counterions to trigger gelation. This confirms eligibility for extrusion 3D printing. Secondly, a lower limit of Ca^{2+} concentration of 20 mM was defined, a useful parameter for future printing. Thirdly, it appears that increasing the PA concentration does not appear to increase the gelation kinetics to a point which compensates for weak counterion concentrations, ruling out the possibility of printing PAE_3 directly into, for example, cell culture media which contains divalent cations as part of standard formulation. Following from this proof-of-concept, attempts were made to extrude PA solutions using an automated extrusion 3D printing system.

A 1% w/v solution of PAE_3 was observed to have a viscosity close to that of water, which is not ideal for extrusion printing and would be more suited to inkjet applications. Nonetheless, printing was attempted using the parameters shown in Figure 29. It was observed that, even at the absolute minimum possible pressure applied by the printer (1 kPa), all print fidelity was lost and even the printing of a straight line was not possible. The low viscosity of the ink, even within such a narrow nozzle, meant it was not possible to reduce the rate of flow any further. A range of printhead movement speeds were attempted, but no difference was observed in the results. It was ensured that the Z height – the distance between the substrate and the tip of the nozzle – was equal to the inner diameter of the nozzle. This would have, ideally, introduced a drag to the PA as it was extruded an improved print success. No such improvement was observed. Moving to a higher gauge needle may have been a possible line of investigation

and, if successful, may have facilitated greater print resolution owing to the lower inner diameter. It may also be the case that a syringe pump-based system may offer greater control over the flow rate, as this would rely less on a minimum ink viscosity.

By increasing the concentration of PA in solution, it is possible to increase the viscosity and thus the printability in an extrusion setup. Here, 2% PAK_3AGD was extruded in a liquid-in-liquid system, allowing for the fabrication of basic shapes containing acute angles and sharp turns without breaking or snapping the printed structure (Figure 30). Printing was possible using a 22 G nozzle. A simple multi-layer shape was also constructed, although the density and lack of adhesion to the substrate of the PA results in detachment and floating in the gelling solution. This ultimately makes multi-layer printing more difficult and less reliable. Furthermore, the need to use higher concentrations of PA to increase the viscosity ultimately limits control of macroscopic properties, such as stiffness and porosity, to a specific window. Higher concentrations of PA may increase any cytotoxic effects present and will also greatly increase the cost of PA printing. Previous studies have demonstrated good printability with 4% w/v PA solutions, but this would vastly increase the cost of larger prints. A simpler, more economic method of increasing PA solution viscosity should be sought.

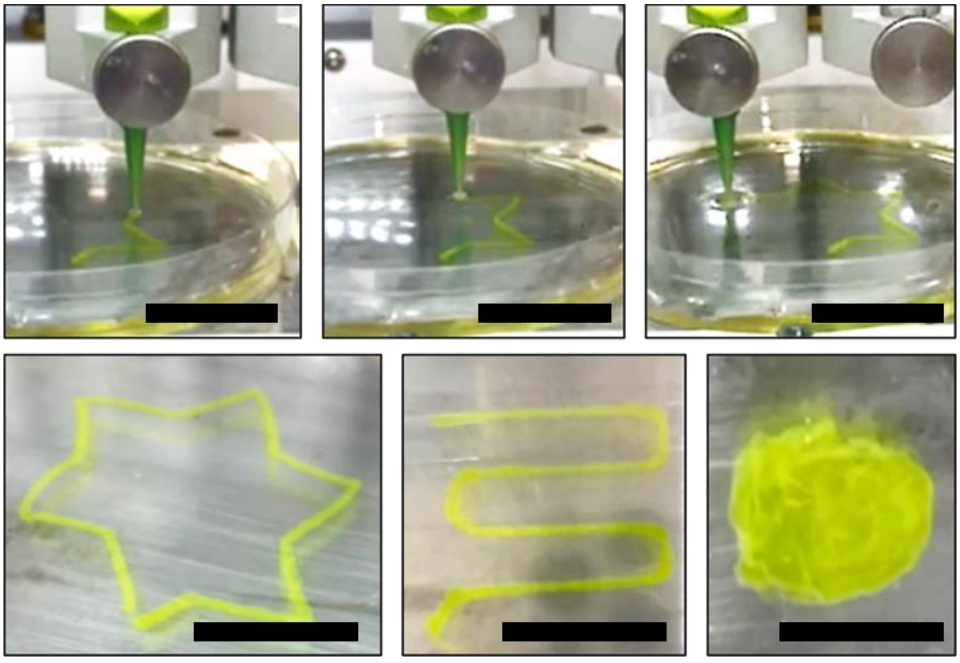

Figure 30: Liquid-in-liquid extrusion printing of PAK_3AGD (2% w/v) into a gelling solution using a Cellink INKredible+ extrusion bioprinter.. Simple shapes (lower left, lower middle) and a multi-layer shape (lower

right) were attempted. Scale = 3 mm. Green colouration was achieved through the addition of thioflavin T dye and was used for visualisation purposes only.

3.3.2 Extrusion Printing with Nonaqueous PA Solutions

3.3.2.1 Material Characterisation

To achieve an increase in viscosity of lower concentration PA solutions, glycerol was tried as an additive. Glycerol is a non-toxic, biocompatible, economic, and highly viscous compound which may introduce the desired fluid properties to our PA solutions. It is miscible with water, allowing for mixtures of varying concentration ratios and viscosities to be prepared. However, while glycerol is capable of hydrogen bonding, the exact nature of hydrogen bonding in glycerol may alter the molecular packing and self-assembly of the PA in solution. Previous studies using sodium dodecyl sulfate (SDS) have demonstrated that dissolution in glycerol results in the formation of lamellar structures as opposed to spherical micelles.[1] These lamellar structures may self-assemble into cylindrical micelles and thus a gel upon completion of a heat-cool cycle. Such behaviour is not observed in aqueous solutions of SDS. Similarly, dispersions of graphene oxide in glycerol exhibit different crystalline ordering compared to aqueous dispersions, resulting in improved long-term stability and increased electrical conductivity, as well as an inversion of the correlation between graphene oxide concentration and dispersion viscosity.[2] Therefore, it is likely that the introduction of glycerol into PA solutions will alter the molecular behaviour, perhaps introducing some interesting properties. Further study on the effect of glycerol is recommended.

Here, the introduction of glycerol was not found to prevent the gelation of PAE_3 in a $CaCl_2$ solution, up to a solution of 90% v/v glycerol. At higher concentrations, no gelation was observed. This may be due to difficulties in fully dissolving the PA in high viscosity solutions, or it may be due to a disruption in the molecular arrangement of PA molecules in nonaqueous solution, which would subsequently inhibit gelation. Some evidence for the disruption of PA gelation may be observed through rheological studies of the gels. Firstly, an amplitude sweep reveals a significant increase in the brittleness of the gel formed in nonaqueous solution. While aqueous PAE_3 typically begins to exit the linear viscoelastic region at around 5% shear strain, nonaqueous PAE_3 shows a

breakdown of the gel network at just below 0.1% shear strain. This is an important consideration as it indicates that any printed constructs may be far less resilient to, for example, fluid flow when changing media in a 3D cell culture setting.

Gelation is also far slower when a formulation containing glycerol (80% v/v) is used. Here, rheological measurements were performed within the linear viscoelastic region of the gel, determined by a prior amplitude sweep (Figure 31B&C). Gelling solution ($CaCl_2$, 1 M) was injected into PA solution 10 seconds after moving the upper geometry – a parallel plate – to the measuring distance. In the case of aqueous PA solution, gelation is observed almost immediately, after which there is a short period of stiffening as the Ca^{2+} ions diffuse through the solution. The final stiffness is achieved within 20 minutes. In the case of a formulation containing glycerol (80% v/v), however, there is a significant lag time from the injection of gelling solution until the detection of the gel by the rheometer. This lag time was observed to fluctuate when performed in triplicate but was not observed to be greater than 25 minutes. A slope of stiffness was still observed at the completion of the time sweep, indicating that the PA in glycerol had not fully gelated after 60 minutes.

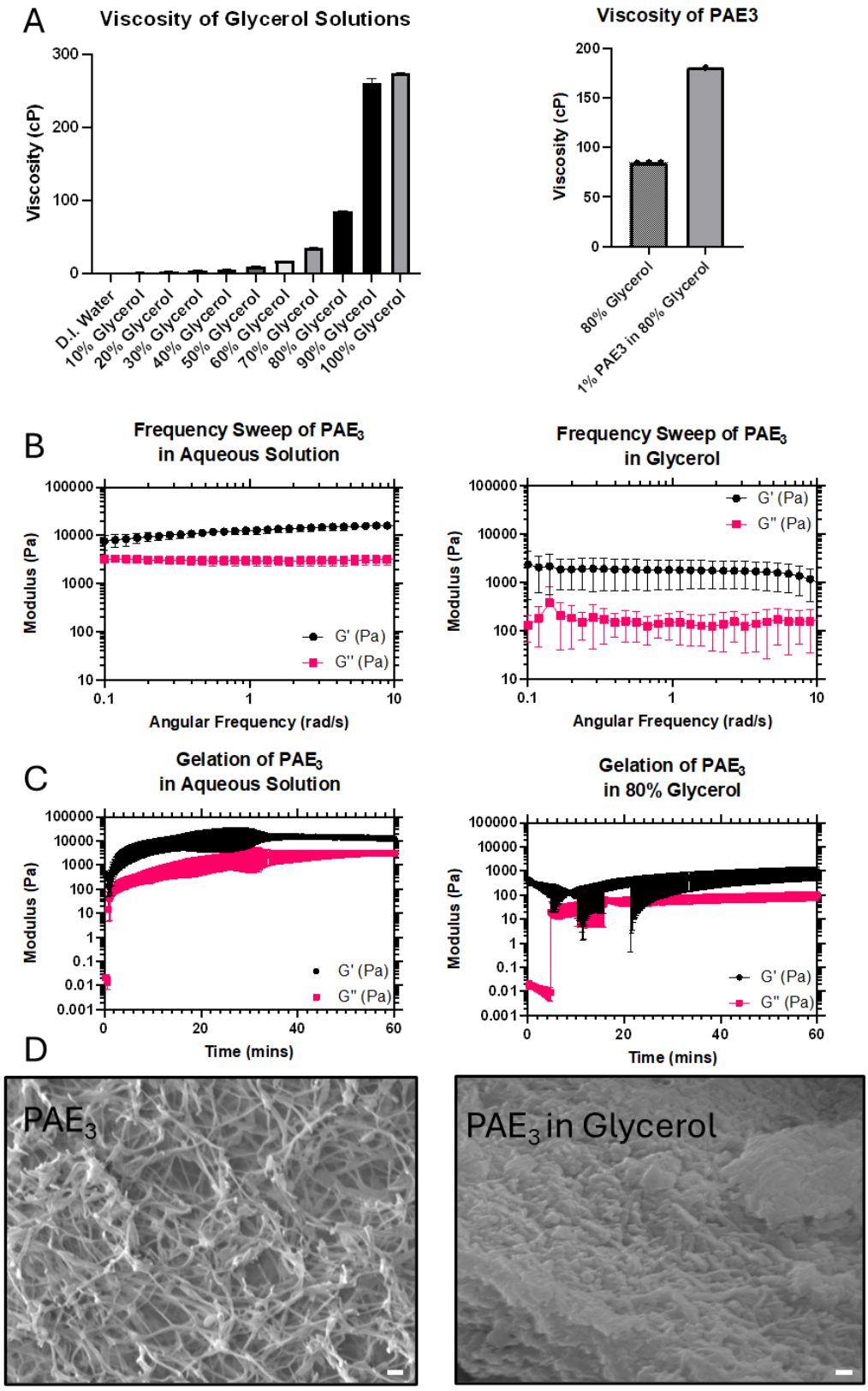

Figure 31: Characterisation of a glycerol-PA gel formulation. A) Viscosity of formulations and effect of PA addition determined using an automated liquid handling system (Experimental 3.7.3). B) Frequency sweeps for PA hydrogels in both aqueous and nonaqueous solvent. C) Time sweeps of PA gelation in both

aqueous and nonaqueous solvent. D) SEM micrographs of PA hydrogels in both aqueous and nonaqueous solvent. Scale = 100 nm.

The slower gelation kinetics may be due to different factors. Firstly, glycerol is a far more viscous fluid than water (Figure 31A). This will reduce the diffusivity of any species dissolved within it, such as calcium ions or PA molecules undergoing gelation, and subsequently slow the gelation. Secondly, as glycerol is a more strongly hydrogen-bonding species than water, there may be a greater energetic barrier to overcome for the PA molecules to self-assemble into fibres, requiring a greater molarity of calcium to occur.

Alterations in the molecular arrangement of PAs in glycerol are also indicated by the changes in the magnitude of the storage modulus, G', and the slope of the frequency sweep observed between 10 and 0.1 rad s^{-1} (Figure 31B). After being allowed to fully gelate, a PAE_3 (1% w/v) aqueous gel exhibits a stiffness significantly greater than is observed in a PAE_3 (1% w/v) nonaqueous gel. The stiffness of a PA gel is driven in part by the nature of hydrogen bonding in the β-sheet forming region. Disruption or alteration of this region may have an impact on the stiffness of a PA gel. It may be the case that solvated glycerol molecules may form H-bonds with this β-sheet region. Indeed, previous literature has observed that glycerol may insert into the β-sheet region of soy protein isolate, altering the secondary conformation and giving rise to β-turns in the place of some β-sheets.[3] If such a transformation is also present in nonaqueous PA systems, this loss of order may be responsible for the decrease in stiffness.

In addition to the change in magnitude of G', a slight slope with increasing angular frequency is observed only in aqueous PAE_3 (1% w/v) gels. This is important as this slope is indicative of an eventual crossover point and therefore points to self-healing abilities of a hydrogel. The absence of this slope in the nonaqueous PA gel indicates that its behaviour is closer to that of a chemically crosslinked hydrogel, as opposed to a supramolecular system. This indicates that extrusion of a nonaqueous gel may irreversibly damage the gel. A liquid-in-liquid system would likely be preferred.

SEM micrographs of PA gels formed in glycerol indicate a possible loss of porosity when glycerol is used, although it may also be the case that standard SEM sample preparation is not currently sufficient to remove glycerol from the gel structure. A similar situation was observed in published reports of SDS hydrogels formed in glycerol.[1] This potential loss of porosity, coupled with the increased viscosity of the fluid trapped within the hydrogel network, may limit cell migration in the gel in a bioprinting setting. Solvent exchange, or simply soaking the printed structure in aqueous solution, may help to mitigate this issue.

Interestingly, these micrographs also indicate morphological changes in the PA network. Whilst aqueous PAE_3 is observed to be a porous network of intertwined fibres, nonaqueous PAE_3 appears to adopt a layered lamellar structure – similar to that reported of SDS in glycerol or in heated PAE_3 prior to cooling. In the case of PAE_3, heating to 80 °C for 30 minutes results in the formation of lamellar structures. Subsequent cooling causes these structures to peel apart, forming long-range anisotropic fibres. It may, therefore, be possible to create aligned structures in the nonaqueous PAE_3 without the need for heating. However, to further investigate the molecular structure of PAE_3 in glycerol, techniques such as small angle neutron scattering (SANS) would likely be required.

3.3.2.2 Extrusion Printing

Having characterised the material properties of PAE_3 in nonaqueous solution, determining that it may be of a suitable viscosity for extrusion printing and is still capable of gelling, it was decided to attempt to extrusion print with this formulation. By increasing the viscosity of the PA solution using glycerol, it becomes more facile to integrate this system with extrusion printing (Figure 32). Using a 1% w/v PA solution, it is possible to print shapes containing acute angles and curved edges. It is also possible to return the nozzle to the gel and adjoin PA to previously printed areas. Furthermore, as glycerol has a greater density than water, there is no longer any issue with detachment or floating from the substrate, facilitating multi-layer printing. However, the increased viscosity reduced the viable nozzle diameters for extrusion printing. Above 25 G, it was

not possible to force the PA solution through the nozzle using the pneumatic printing system available, at pressures up to 200 kPa.

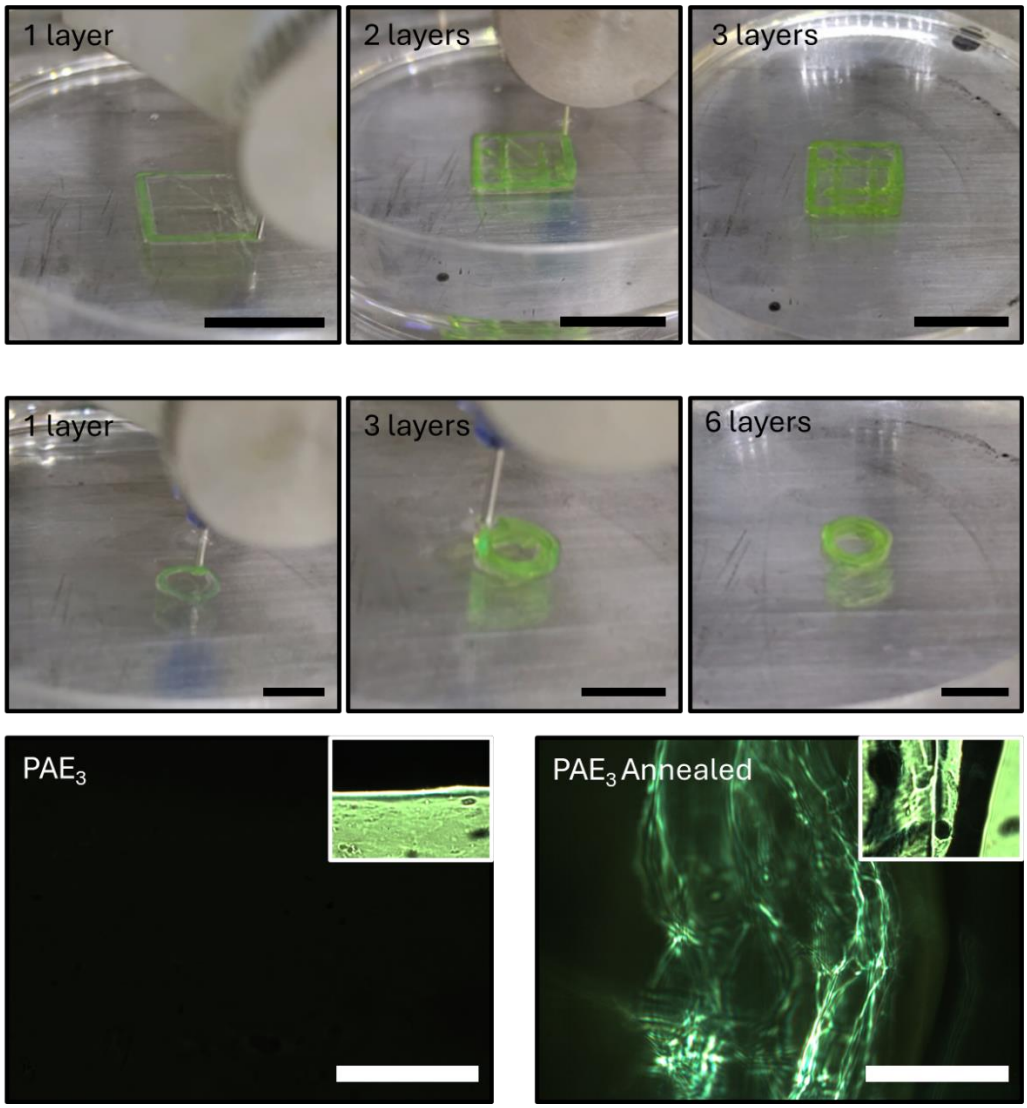

Figure 32: Liquid-in-liquid extrusion printing of PAE_3 nonaqueous formulations. Green colouration results from the use of thioflavin T dye. Upper: Extrusion printing of a 3-layer woodpile-like structure. Scale = 10 mm. Middle: Extrusion printing of a 6-layer tube-like structure. Gels stained with thioflavin T. Scale = 5 mm. Lower: (left) Polarised light microscopy image of extruded PAE_3 gel with (inset) light microscope image. (Right) Polarised light microscopy image of extruded PAE_3 after 80 °C heat-cool cycle with (inset) optical light image. The presence of bright regions indicate anisotropy/fibre alignment within the material. Scale = 500 µm.

The ability to print sharp corners with such a brittle PA indicates the benefits of using a liquid-in-liquid system for extrusion printing of PAs. By initiating gelation only at the point of extrusion, there should be minimal strain arising from printing corners. Printing a gelled PA, conversely, will introduce strain on the system as corners are printed, potentially resulting in broken filament and a

failed print. However, in the case of liquid-in-liquid printing, the height of the print (Z-dimension) is limited by the height of the liquid bath or the depth which may be reached by the nozzle – whichever is the shallowest. This may limit prints to a few centimetres high. Such a limitation would not be met in a successful gel extrusion system. One possible solution to this would be the introduction of a coaxial printing system, wherein the gelling solution is extruded as a "shell" around the gelator core. Such a system would remove the bath requirement, facilitating greater printing capacity in the Z-dimension. In addition, a coaxial system would reduce the volume of gelling solution required, which may be beneficial if the gelling solution is composed of a more precious material, such as growth factors or proteins. For example, given the data from Chapter 2 regarding the gelation kinetics of PAK_3AGD with SCS, it may be possible to coaxially print these two systems, while extruding PAK_3AGD into a bath of secretome would require too great of a volume of SCS.

Despite the slow gelation kinetics of PAE_3 in glycerol, it is possible to print multi-layer structures without the need for a pause between layers. The reason for this may be that, when extruded into a bath of Ca^{2+}, gelation occurs immediately at the interface between PAE_3 and divalent cations forming, in this case, a tubular filament capable of supporting its own weight. As the remainder of one layer is printed, the Ca^{2+} ions slowly diffuse into the PA, increasing the stiffness of the filament to a point where it can support the next layer deposited onto it, ultimately allowing multiple layers to be printed. Here, up to 6 layers were printed, resulting in a tube-like structure. Were this system not limited in the Z-dimension, such a tubular structure may be useful for vascular tissue engineering.

Importantly, polarised light microscopy reveals that the long-range alignment of fibres is possible in this extrusion system (Figure 32). Here, following thermal treatment of 80 °C for 30 minutes and subsequent cooling to room temperature, extruded filaments are observed to display birefringence characteristic of the alignment of fibres. This anisotropy is – currently – exclusive to PAs containing more than one consecutive glutamic acid in its charged region and is observed in PAE_2, PAE_3, and PAE_4. Recent literature has indicated the ability to create aligned fibres with other amphiphilic peptides

containing two sets of two lysine residues,[4] highlighting that this may be possible with PAK_x sequences. Translating these aligned structures to a printable system may be important for the fabrication of cell scaffolds with optimal milieus for directed cell growth, such as that observed in muscle fibres or nerve systems.

It was also observed that, following a period of extended heating (80 °C, >24 hours) and being allowed to cool to room temperature, the viscosity of PAE_3 solutions in 80% glycerol increased to the point where they were at almost a gel-like state, and could be handled. A reliable viscosity measurement could not be obtained using liquid handling equipment, indicating that the viscosity is greater than 300 cP, the current upper limit of this equipment. This material, however, was not a gel as it immediately dissipated upon immersion into a PFA solution to produce a sample for SEM imaging. Heating the PA-glycerol solution to 200 °C and allowing it to cool to room temperature results in the loss of flowability and a material which appears self-supporting (Figure 33). This material, however, was not a gel and was again observed to dissipate into an added aqueous solution. It may, however, still be possible to trigger a thermal gelation of the PA, as is observed in the heating of sodium dodecyl sulfate (SDS) in glycerol.[1] In this case, SDS forms a lamellar structure – as is observed in the thermal annealing of PAE_3 – which results in a self-assembled gel. It is not unreasonable, therefore, to believe a similar mechanism of gelation may be possible in PAs. Further or more extreme heating may be required. However, it does also appear that the extreme heating here is causing some damage to the system, indicated by the change in colour of the solution.

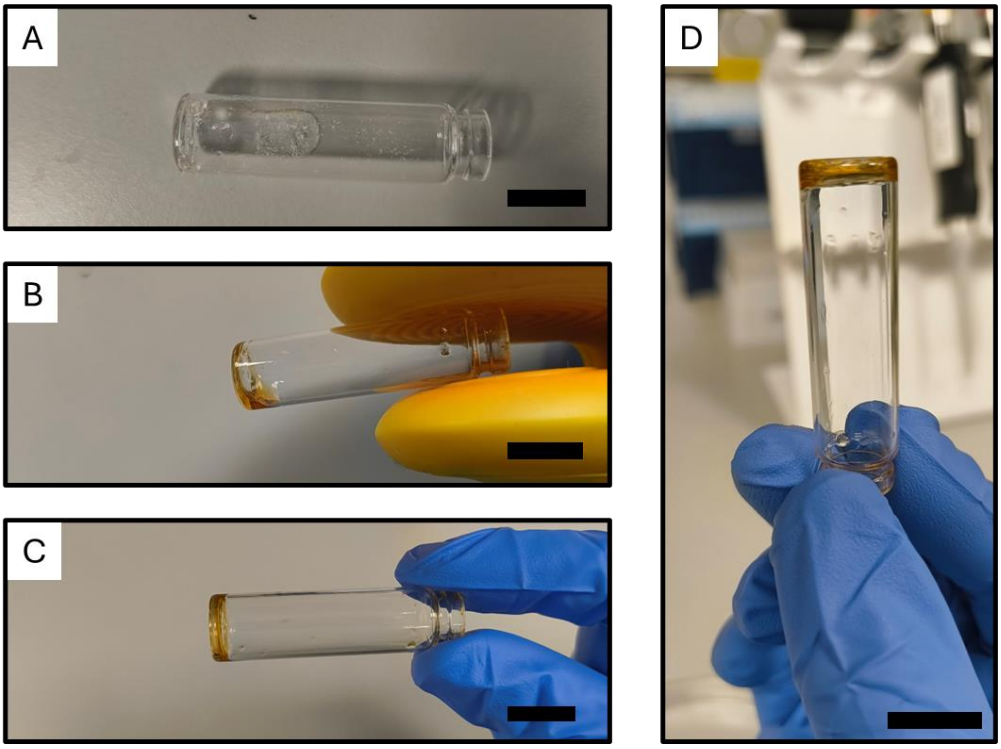

Figure 33: Thermal treatment of glycerol-PAE$_3$. ***A:*** *Flow of glycerol-PAE$_3$ solution in a horizontal glass vessel prior to thermal treatment.* ***B:*** *Flow of glycerol-PAE$_3$ immediately after 30 minutes at 200 °C. A colour change from colourless to brown is observed.* ***C&D:*** *Loss of flowability after cooling to room temperature following thermal treatment demonstrated by vial inversion test. Scale = 3 mm.*

Here, it has been demonstrated that glycerol represents a pathway to successful bioprinting of PA hydrogels by increasing their viscosity without entirely preventing gelation. The fact that glycerol does not mix with water without stirring allows the extruded filament to maintain its shape in a bath of gelling solution. As a result, good shape resolution and print fidelity is achieved. In addition, the thermal alignment of PAE$_3$ fibres appears to be maintained, suggesting the ability of these extruded materials to be used as aligned milieu for, for example, neural or muscular cells which typically display anisotropic morphologies. Owing to volume restrictions, this system was not attempted with the SCS/SH-SY5Y model.

3.4 Light-based Printing of PAs

The main limitation of extrusion-based printing with PAs is the volume requirement. Currently, PAs are far less economic than conventional cell scaffolds such as gelatin. Therefore, it was decided to attempt to move towards light-based printing systems which may require as little as 40 µL to successfully

print. Furthermore, these systems offer a resolution which is unmatched by the extrusion system attempted in Section 3.2, which would be an advantage when attempting to print structures for the planned application of spinal cord implants. Currently, light-based printing may be UV or two-photon based, typically requiring a photoinitiator to generate a radical species capable of initiating free radical polymerisation. However, PA molecules are not inherently capable of undergoing free radical polymerisation – they lack the typical functional groups, such as an acrylate group - which are normally used to crosslink monomers. Furthermore, many of the useful properties of PAs – tailored stiffness, self-healing, porosity – arise from the self-assembly properties. Interfering with these by introducing chemical crosslinks may limit the benefits of these supramolecular systems. Therefore, it was initially attempted to create a UV-triggered gel by use of a photoacid, as PAE_3 may be gelled by the introduction of a strong acid.

3.4.1 Photoacid-induced Gelation of PAE_3

Diphenyl iodonium nitrate (DPIN) is a photoacid which may rapidly generate nitric acid upon UV irradiation. Monitoring this reaction by measuring the pH at set time points indicates that the concentration of H^+ increases linearly over time at a set energy input (Figure 34). As pH is a $\log_{10}$ scale, it therefore takes 10 times longer each time a decrease of 1 is desired. Here, irradiation of PAE_3 (10 μL, 1% w/v) containing DPIN (1 M) did not result in a gel-like material until 30 minutes of exposure had been achieved. Not enough material was formed to perform rheological testing. Successful photoacid generation was indicated by the formation of an opaque solution, resulting from the presence of iodobenzene, a degradation product of DPIN. While this preliminary result indicates the potential for a PAE_3 photoacid system, it is far too slow to integrate into a 3D printing system, which may require hundreds of layers. Additionally, pH monitoring of this system showed a decrease in the rate at which acid was generated compared to irradiation of pure DPIN. It is not possible to increase further the concentration of DPIN, as it is already near its saturation limit, and decreasing the concentration of PAE_3 may result in the failure to form a gel.

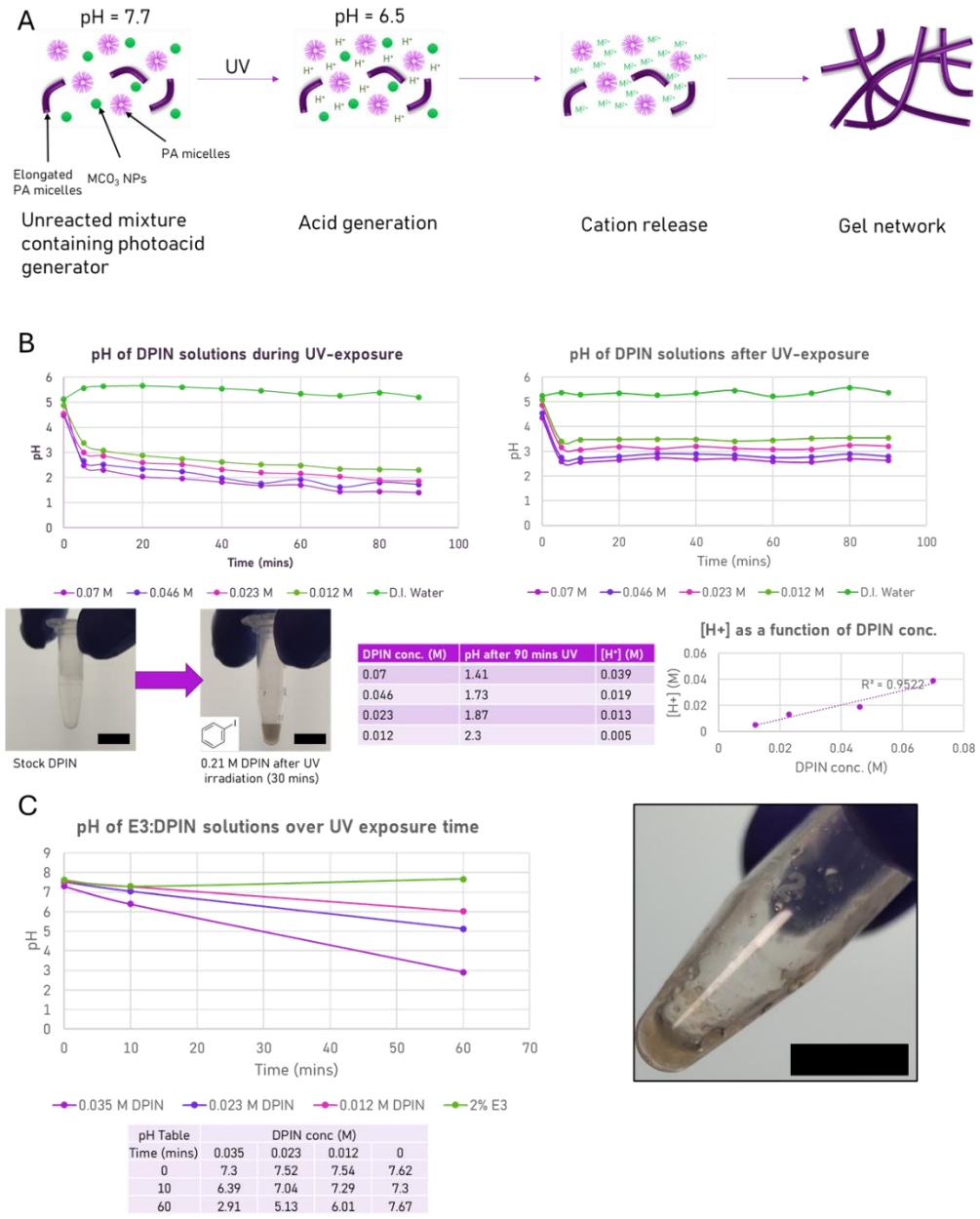

Figure 34: Photoacid gelation of PAE3. A: proposed reaction scheme. The UV irradiation of DPIN generates an acidic environment. At pH 6.5, $CaCO_3$ is solubilised, generating Ca^{2+} cations. The generation of these cations would lead to the gelation of PAE3. B: Behaviour of DPIN solutions and rate of acid generation, demonstrating the absence of "dark curing". A colour change is also observed in this time, further indicating successful acid generation. C: Behaviour of DPIN-PA solutions and presence of minimal gelled material on the inside of a 1.5 mL Eppendorf tube following irradiation. Scale = 5 mm

To attempt to remedy this, a suspension of nano sized $CaCO_3$ (nanocalcite) was introduced to the system. Nanocalcite is insoluble in water above pH 6.5. Below this pH, however, it dissolves to liberate Ca^{2+} ions, H_2O, and CO_2 gas. Using nano sized $CaCO_3$ is important as larger particles may sediment, causing uneven gelation. Nanoparticles are kept in suspension by Brownian motion. It was

believed that, by introducing a Ca^{2+}-donating component, gelation may be more easily achieved. However, it was observed that the rate of acidification slowed upon introducing $CaCO_3$, to the point where no dissolution was observed after 1 hour of irradiation. It may be the case that using a UV source of a wavelength closer to the λ_{max} of DPIN may be more successful. A different photoacid, with a λ_{max} closer to the wavelengths of traditional printers (365, 385, or 405 nm) may also hold potential, but currently many examples of these liberate more hazardous acids, such as perfluoroethanesulfonic acid ($C_2F_5SO_3H$),[5] which is classed as a suspected carcinogen and reproductive hazard. However, as DPIN was observed to generate an acid under irradiation at 365 nm, this is unlikely to be the main cause of failure in this system.

It is uncertain exactly why this system failed. DPIN is observed to produce an acid under irradiation at 365 nm. Upon the introduction $CaCO_3$, the decrease in pH is slowed, but this may be because the $CaCO_3$ acts as a buffer as it is solubilised, generating H_2O from the excess H^+. However, upon the introduction of PAE_3, both $CaCO_3$ solubilisation and pH decrease are inhibited. PAE_3 does not absorb strongly at 365 nm, so it is not likely to be acting as a photoabsorber. Previous systems have achieved pH-based gelation with a supramolecular gelator upon DPIN irradiation, therefore the concept is sound.[6] UV irradiation also does not disrupt PA structure or gel formation, as PAs have been UV sterilised for cell assays. There may, in this case, be a cumulative effect of the PA and $CaCO_3$ consuming H^+ as it is generated. As H^+ ions may also coordinate with PA molecules and trigger gelation, there may be fewer H^+ available to trigger the solubilisation of $CaCO_3$. However, from DPIN alone there may be insufficient H^+ to trigger PA gelation, resulting in a failed reaction with insoluble $CaCO_3$ and pre-gel PA.

A previous example in which a photoacid generator was used to gelate a PA was demonstrated by Stupp and co-workers.[7] Here, the sequence $C_{16}A_4G_3E_3$ (PAG_3E_3) formed a bulk gel after 1 minute of irradiation with 254 nm light in the presence of the non-commercial photoacid benzyldimethylsulfonium chloride. Compared to the PAE_3 used here, PAG_3E_3 contains a more-weakly hydrogen bonding section, so should display slower gelation kinetics. The hydrophobic driving force should also be the same in both cases, as well as the

charge-dampening requirement to induce gelation. It is, therefore, maintained that the light-induced gelation of PAE_3 using a photoacid is possible, but was not achieved here.

Despite the inability to form a gel reliably and efficiently in a photoacid system, it was still believed to be possible to integrate PAs with a light-based system. Pivoting from a single gel to a co-gel system was now pursued, with a secondary, photoactive gelator to be mixed with the PA.

3.4.2 Co-gelation of PAs and Gelatin Norbornene

3.4.2.1 Rationale

Here, a gelatin-based system utilising gelatin norbornene (GelNB) and gelatin thiol (GelSH) was used as a gelation system with PAE_3. Gelatin is a well-studied material in the context of tissue engineering, acting as a biocompatible scaffold for cell growth. It is relatively economic, able to be synthesised on a multi-gram scale, and the modification of its primary amines facilitates the modulation of chemical properties. Methacrylation of gelatin, for examples, yields gelatin methacrylate (GelMA), a molecule which may be crosslinked in the presence of a radical species to yield a chemically crosslinked polymer. Methacrylate groups, however, somewhat compromise the biocompatibility of GelMA, and incomplete curing may lead to a reduction in cell viability.

The norbornene group, conversely, appears to have comparatively little impact on the viability of biologics, indicating that it may be preferable to methacrylate groups in biomaterials such as gelatin. Additionally, GelNB materials have displayed greater reaction rates and subsequent cell spreading in hydrogels compared to GelMA, while requiring lower masses of photoinitiator.[8, 9] However, while gelatin biomaterials offer excellent support as scaffolds, they have limited bioactivity and offer limited ability to introduce bioactive moieties. It is therefore difficult to control properties such as protein binding. Therefore, to overcome this, the bioactive HMPA was introduced as a co-gel system with GelNB and GelSH to combine the beneficial properties of these materials.

GelSH was chosen as a crosslinker based on previous literature which compared a range of different thiol crosslinkers in GelNB-based systems.[10] It was observed that, compared to the likes of 4-arm poly(ethylene glycol)-SH-20k

(PEG4SH) and tetra(ethylene glycol) dithiol (TEGSH), GelSH yields gels with a lower storage modulus and swelling ratio, indicating improved suitability for neural tissue applications. The stiffness of these materials was observed to be around 10 kPa, similar to that of PAE_3, indicating that the gel should behave similarly to pure PAE_3, but perhaps degrade less rapidly due to the chemical crosslinking.

3.4.2.2 Volumetric Additive Manufacturing

Owing to the expensive nature of PA solutions, large volumes of PA-GelNB mixture (resin) could not be prepared. In light of this, traditional light-based printing techniques such as SLA and DLP could not be used as the commercial systems require greater than 20 mL of resin for a single print. An in-house setup for VAM had recently been prepared, requiring just 2 mL of resin for a single print. This system maintains the light-based fundamentals of SLA printing, but resins are instead placed in a glass vial in front of the projector. The vial is then rotated as images are projected into it, curing the entire print at once. The uncured material can then be removed from the vial to isolate the printed structure for further experiments.

Here, it was planned that a solution of GelNB, GelSH, and PA may be printed in this manner (Figure 35E). First, the resin is cured using VAM to produce a distinct geometry which is then isolated from the uncured resin. At this point, it is hypothesised that PA micelles are physically entrapped within the cured gelatin. By adding a solution of $CaCl_2$, it would then be possible to gelate the PA, creating two interwoven gel networks in one structure. Here, the gelatin would provide mechanical stability and the ability to pattern from the top-down, while the PA would provide bioactivity and protein binding.

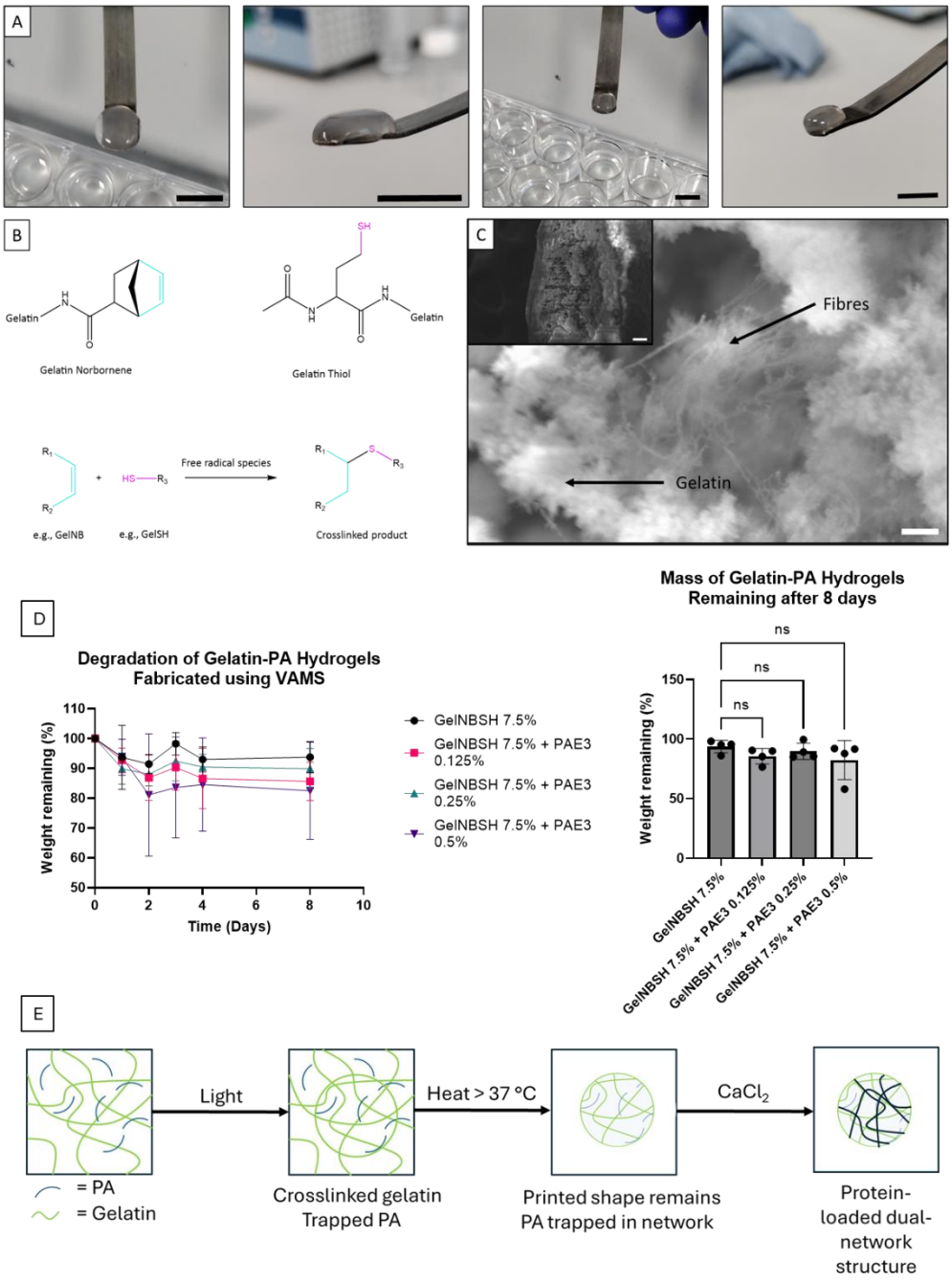

Figure 35: VAM printing of gelatin-PA two-component gels. ***A:*** *Disk-shaped print cured using VAM. Scale = 3 mm.* ***B:*** *Reaction scheme for GelNB-GelSH crosslinking.* ***C:*** *SEM micrographs of two-component gel structure with (inset) bulk gel also visible. The PA is present as fine fibres in the centre of the image, while gelatin has adopted a different morphology.* ***D****: Degradation of gelatin-based hydrogels over the course of 8 days, measured gravimetrically.* ***E:*** *Proposed two-component system composed of interlinked networks of GelNB and PAE₃. Chemically crosslinked GelNB and GelSH entrap PA micelles within the network. Excess fluid is then removed, and the remaining structure is introduced to $CaCl_2$ to initiate gelation of PAE₃.*

It was observed that the presence of the PA did not inhibit photocuring of the gelatin in the resin, and it was possible to produce a simple disc geometry

(Figure 35A) (Experimental 3.7.9). This disc could be manipulated and handled with ease and was not observed to degrade at the same rate observed for pure PAs, with the gelatin-PA prints observed to maintain greater than 80% of their initial mass after 8 days (Figure 35D). The degradation rate of these discs was not observed to significantly increase with increasing PA concentration, although there is a trend towards increased degradation rate with higher PA concentration, indicating the possibility that, at 1-2% PA, there may be some significant effect. Speculatively, the terminal carboxyl groups of the glutamic acids within PAE_3 may be interacting with the radical species formed upon irradiation of the photoinitiator. This would decrease the degree to which norbornene radicals are formed, somewhat inhibiting crosslinking and possibly reducing gel stability. It may be possible to measure the degree of consumption of the norbornene alkene group using, for example, Raman spectroscopy on crosslinked gels to support this speculation, as the alkene group would yield a signal at roughly 1600 cm^{-1}.

A cross-sectional SEM image revealed what appears to be dual network within the gel (Figure 35C). One of these networks appears to be individual fibres, such as is observed in PAs. The other network appears to be more dense or globular, which may be the crosslinked gelatin speculated based on the fact it does not appear to be PA. Importantly, the fibre-like network was not observed in a sample of gelatin alone, suggesting that these fibres are indeed PA. These data do appear to indicate that it is possible to form a gel which contains both gelatin and PA networks. However, even using 2 mL per print proved to be resource intensive. As GelNB has previously been used in 2PP systems, it was believed to be possible to translate the gelatin-PA system to 2PP, which would require less than 100 µL of resin per print.

3.4.2.3 Two-photon Polymerisation

Having determined that PA and GelNB may indeed form a co-gel in a UV-based additive manufacturing system, it now remained to demonstrate that millimetre-scale structures with sub-millimetre features may be printed, to fabricate with minimal volume as necessitated by both the small scale of spinal cord defects and the small volumes of secretome available. To achieve this, two-photon

polymerisation (2PP) was identified as an ideal additive manufacturing technique.

For this system, photoinitiator (PI) choice was important for successful printing. Traditional PIs absorb strongly around the UV region (~365-405 nm), and irradiation at this wavelength elevates the molecule to its excited state, cleaving a bond and generating a free radical species which triggers polymerisation of the alkenes present in the monomer, such as acrylate, methacrylamide, or vinyl species. 2PP systems, however, operate outside of the UV region, utilising a femtosecond pulsed laser at either 780 or 515 nm. The wavelength used in this case is 780 nm. The energies of two photons absorbed by one molecule add up, resulting in excitation of the molecule. For a 2PP initiator to function, it must be able to absorb two photons at once, and this excitation must result in bond cleavage and radical formation (Type I PIs) or proton abstraction (Type II PIs).

Recently, several classes of PI for use in 2PP systems have been synthesised.[11] The performance of these PIs is typically reported in terms of their Goeppert-Mayer (GM) value, which quantifies their absorbance by stating that 1 in 10^{50} photons is absorbed over a distance of 1 cm in a material with a density of 1 molecule per cm^3 when exposed to a photon flow of 1 photon per second per cm^2. Of these 2PP PIs, however, only very few are water-soluble.

One such class of water-soluble PIs is based on the 2PP dye 5-bis-[4-(diethylamino)-benzylidene]-cyclopentanone (BDEA). From this parent molecule, there now exists BSEA, P2CK, G2CK, and E2CK. P2CK, G2CK and E2CK were observed to be significantly cytotoxic to outgrowth endothelial cells within 30 minutes at a concentration of 1.82 mM,[12] although PC2K was far less cytotoxic than the other two PIs at this concentration and thus preferable in this case. In a direct comparison of BSEA and P2CK, P2CK has been observed to be significantly more cytotoxic to L929 mouse fibroblast cells in a concentration-dependent manner, down to 0.13 mM where cell viability was observed to be around 50% after 24 hours.[13] This difference is proposed to be due to the reduced hydrophilicity of P2CK allowing it to penetrate cell membranes and produce cytotoxic singlet oxygen upon irradiation. BSEA would therefore be recommended for 2PP bioprinting, where cells are present

during irradiation. Here, however, as cells were not present during printing, P2CK was deemed suitable for use in this case.

The overall formulation to be used was determined based upon previous knowledge. A gelatin hydrogel containing 7.5% w/v gelatin yields mechanical properties which are in the region of PAE_3, and therefore would not drastically change the stiffness compared to the PA system. The ratio of GelNB to GelSH was determined based on the reported degrees of substitution (DoS) of each component. The GelNB, donated by the Van Vlierberghe group of the University of Gent, was reported to have a DoS of roughly 90%, while the GelSH, sourced from a commercial supplier, was reported to have a DoS of roughly 72%. Therefore, a weight ratio of 4.45:5.55 NB:SH was determined to attempt to achieve as close to a 1:1 NB:SH functional group molar ratio as possible, as doing so ensures more favourable mechanical properties. PAE_3 was used at a final concentration of 2%, as it is known to form gels at this weight percentage. P2CK was used at 0.4% w/v, a concentration at which it sufficient to trigger polymerisation, but low enough to hopefully minimise cytotoxicity should this formulation be used for bioprinting in future. Finally, the secretome was present at 25% v/v – lower than in the previous chapter but, due to difficulties in solubilising GelSH due to some oxidation in storage, it was not possible to introduce a greater volume of secretome.

The optimised printing parameters for 2PP of a GelNB-GelSH system have previously been reported.[10] Using these as a starting point, printing of small-scale structures was successfully achieved (Figure 36) (Experimental 3.7.10). High print fidelity, including the fabrication of micrometre-scale features, was observed, confirming the suitability of this technique for the additive manufacturing of spinal cord implants on the desired scale. The good print fidelity of these structures, coupled with the maintenance of thermal responsiveness of non-printed regions indicates a certain degree of stability in the formulation. Here, type A gelatin was used in both GelNB and GelSH, which carries a net positive charge at physiological pH. PAE_3, HMPA, and most factors in the SCS carry a net negative charge at physiological pH. It is therefore not unreasonable to predict some interaction between the gelatin and other constituents, resulting in undesired gelation. Such an effect was not observed,

with no gelation prior to printing, indicating that the net positive charge of the gelatin is not sufficient to dampen the repulsion between PAE_3 molecules and trigger gelation.

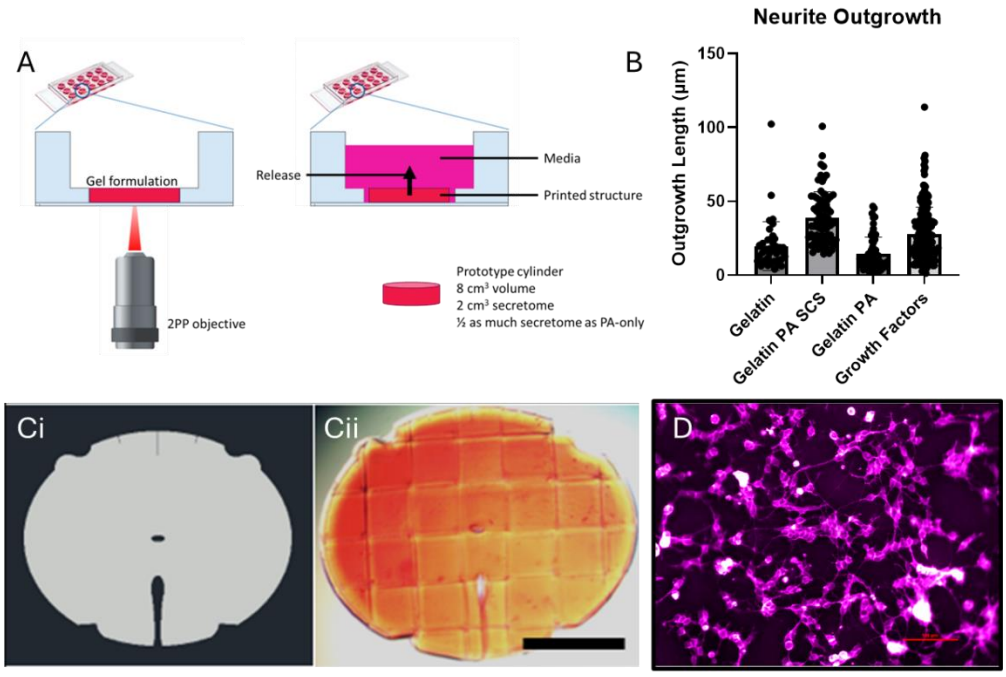

Sample	Average outgrowth length (µm)	Standard Deviation (s^2)	% Change from Growth Factors
Gelatin	19.6	16.5	-29.4
Gelatin+PA+SCS	38.8	17.6	+39.6
Gelatin+PA	14.4	11.4	-48.2
Growth Factors	27.8	18.2	N/A

Figure 36: 2PP of gelatin-PA hydrogels for improved neurite outgrowth. ***A:*** *Prints are formed in the base of a microwell, after which uncured material is removed and media added for release.* ***B:*** *Quantification of neurite outgrowths observed after treatment in different conditions.* ***C:*** *comparison between a CAD design (i) and printed structure (ii) viewed under optical microscopy. Scale = 1 mm.* ***D:*** *confocal microscopy image of mature SH-SY5Y cells following treatment with secretome released from gelatin-PA prints Scale = 100 µm. Lower: Tabulated comparison of neurite outgrowth in different conditions.*

However, it was not explored whether porous structures could be fabricated. More intricate topologies may require further washing steps to isolate the printed structure. In doing this with a protein-loaded print, burst release is likely to be more pronounced, owing to the greater surface area to volume ratio, and the total protein remaining after washing would likely be far lower. This may have an impact on the biological activity of the print. In the case of a co-gel

system where the PA itself is a mimetic of an active factor such as an IKVAV sequence, more intricate structures, such as gyroids, may find use.

A further limitation of 2PP may be the requirement for stitching together fields of view (FOV's). At the point of stitching, two FOV's will overlap. This overlap area will be irradiated for twice the amount of time as the rest of the print. This may create areas of varying mechanical properties, such as increased stiffness, which may in turn have some impact on the growth of cells, which may prefer one stiffness over another, leading to clusters of cells rather than a homogenous culture. Clusters, however, are likely to be only in the XY direction, as the Z dimension of the print is constructed as a single layer in this case. On the other hand, the ability to fabricate areas of different stiffness in XY using 2PP may make it possible to fabricate structures which more closely recreate the stiffness gradients in biological systems. The spinal cord, for example, consists of grey matter and white matter, which are of two different stiffnesses.[14] By irradiating an area of the printed structure for a different time or intensity to other areas in the XY plane, these gradients could be recreated.

Following confirmation that a PA-gelatin co-gel may be fabricated in a 2PP system, the retention of biological properties from the PA-only system explored in Chapter 2 was investigated. It was observed that neurite outgrowth of differentiated SH-SY5Y cells was increased when SCS was introduced to the printed structures compared to prints which lacked SCS (Figure 36). Furthermore, neurite outgrowth also increased in comparison to the standard protocol of differentiation, wherein cells are treated with NGF and BDNF, providing further evidence for the efficacy of the SCS in neurological applications. However, it must be stated that, in this case, a single replicate was performed for each condition, owing to a low volume of secretome available for screening. Therefore, while these results appear promising, further work should be performed before an effect is confirmed.

The retention of these biological effects in a light-based printing system is important, as it indicates that the generation of radical species from P2CK do not significantly impact the efficacy of soluble factors. Previously, it has been reported that free radical species may induce conformational changes and loss

of function in proteins. Here, that does not appear to have been the case. It may be that the self-terminating free-radical polymerisation and rapid rate of polymerisation limits the number and time of free radical species available to interact with the proteins. This indicates the possibility to further use of other secretomes or conditioned media being integrated into 3D printing for controlled release or directed cell growth.

This is an important consideration for the use of bioprinting with small biomolecules and soluble factors. Beyond simple loss of function because of oxidative stress induced by free radical species, possible misfolding may also result from this irradiation. The presence of free radicals, and subsequent protein misfolding, is implicated in Alzheimer's disease progression.[15] Therefore, future work should demonstrate that, for neurological applications, the use of free-radical polymerisation in the presence of proteins does not lead to misfolded or malignant protein species which may cause later disease.

Nonetheless, these data appear to indicate a good degree of protein survival following 2PP irradiation and free radical generation, as their biological effects appear to be conserved from the PA only gels presented in the previous chapter. There is, therefore, the possibility that these gels may find use as potential implants in spinal cord injury models to help trigger the recovery of motor function.

3.5 Conclusions

It has been determined in this chapter that there are several novel methods in which to integrate the self-assembly of PAs with additive manufacturing to achieve a material which is both bioactive and may be patterned with a high resolution. Such techniques may be used to develop structures with specific topologies to directly impact cell behaviour or factor release.

By increasing the viscosity of a PA solution with glycerol, it is possible to increase the range of viable extrusion pressures and nozzle gauges on a pneumatic extrusion printer, making this process more facile. In doing so, gelation is not completely prevented, and a printed gel may be formed. This gel is less stiff than its aqueous counterpart but demonstrates good stability and may continue to be aligned in the case of PAE_3 by thermal treatment. It may also be

possible to trigger the gelation of the glycerol-PA system by thermal treatment, but the correct conditions for this are not yet found.

In light-based systems, an attempted workaround for the intrinsic inertness of PAs in UV light using a photoacid system to release Ca^{2+} and trigger gelation was also found to have some potential, as some gelled material was observed after extended irradiation. However, these current conditions are not viable for 3D printing, as the gelation is far too slow and unreliable. However, it remains possible that the correct experimental conditions for this system may be found, and a UV-triggered self-assembly of PAs may still be possible.

By introducing a photo-crosslinkable polymer, namely GelNB and GelSH, it becomes possible to integrate PAs with light-based printing, namely 2PP. Here, it appears that a two-component gel system is formed, with the PA and gelatin networks entwined with each other in a single bulk gel. This gel demonstrates improved stability and may be printed with high fidelity. Furthermore, by loading these gels with SCS, the capacity to trigger improved neurite outgrowth of differentiating SH-SY5Y cells is carried over from pure PA gels. This experiment suggests that it may be possible to print these gels as implants for traumatic spinal cord injury, and that they may be able to trigger improved outgrowth of neurites in these injuries.

3.6 Future Work

While the work here has demonstrated some development in the use of supramolecular hydrogels in additive manufacturing, it represents mostly initial work consisting of in vitro studies. Although a successful formulation for printing and subsequent improved neurite outgrowth was identified and printed, further work should be done on the optimisation of this formulation and structure for neural tissue ingrowth.

Regarding extrusion printing with PAs, a shift towards a syringe pump-based printing system, as opposed to pneumatic printing, would likely represent an improvement in control of flow rate with low viscosity inks. This would open the possibility of printing with lower weight percentage PA solutions, facilitating the extrusion printing of softer PA gels, improving the range of stiffnesses which may be achieved. Furthermore, in improving control of flow

rate, it would become possible to achieve greater control over the alignment of PA fibres in PAE_3, as this alignment is dependent upon the flow rate and subsequent drag experienced by the PA filament as it is extruded. Achieving controlled, reproducible alignment of PA fibres through extrusion printing would facilitate the production of aligned environments for directed cell growth in muscular and neural cells, which may aid their differentiation into functional tissues. Beyond the neurological applications explored so far, aligned PA fibres may find use in the culture of muscular tissue in applications such as, for example, cultured artificial meats. Before this, however, high levels of control over fibre alignment must be demonstrated.

The integration of PAs into light-based printing techniques appears to demonstrate some potential. While it is possible to use a photoacid and UV irradiation to eventually trigger gelation of PAs, the process is currently far too slow for 3D printing. Optimisation of this system, either through altering the UV wavelength or the photoacid used, would likely result in the ability to trigger the self-assembly of PAs with a far lower UV dose, potentially facilitating their use in a 3D printing DLP or SLA system. If such a system were to be achieved, the resolution of printed PA gels may be greatly improved in comparison to extrusion printing.

It would be possible, using 2PP, to print a structure with defined pores as small as 200 nm in diameter, as this is the absolute maximum resolution of the printer in use. With this capability, it may be possible to print a structure which not only triggers neurite outgrowth with the release of SCS but also guides the growth of these neurites through the printed structure by providing a defined architecture. It has previously been demonstrated that neurites develop anisotropically along a concentration gradient of growth factor, and therefore it is possible that they would penetrate the SCS-loaded construct in this case, possibly improving the rate and efficacy of motor function recovery in a spinal cord injury model.

The use of the gelatin-PA gel system in VAM should also be explored further, as there are currently no other examples of a self-assembled/polymeric hybrid gel produced by VAM. It is believed that the promising data observed in 2PP samples should be translatable to VAM to produce larger-scale prints. At the

time of experimentation, the in-house VAM system had recently been developed, and it was possible only to make simple structures with the PA and gelatin available. With a greater volume of resin and a now more developed VAM system, it would be possible to make more complex geometries which may be able to direct cell growth.

Finally, it should be investigated whether other cell types or tissues could possibly be integrated into these systems. SH-SY5Y cells, and neural applications in general, were chosen here because of the reported neurotrophic capacity of the SCS and the ability to align PAE_3 to create an environment for directed cell growth. However other cell types, such as muscle cells, also develop with a degree of anisotropy, which may be aided by the present of an aligned scaffold on which to growth and differentiate.

3.7 Experimental

3.7.1 PA Formulation

PAs for extrusion printing were prepared in HEPES buffer between 1-2% w/v. PAE_3 was solubilised using 1.0 M NaOH solution, added in 1 µL steps until complete dissolution was observed.

For glycerol-PA solutions, glycerol mixtures with D.I. water were prepared at various volume fractions from 10-100% v/v. PA powder was then added directly to these mixtures, followed by addition of 1.0 M NaOH in 1 µL steps until complete dissolution. For 70% v/v and above glycerol, some gentle agitation of the mixture is required for complete PA dissolution.

For thermal annealing, PA solutions were placed inside an Eppendorf tube for 80 °C heating or a glass vial for 200 °C heating. These containers were placed inside an oven which had been preheated to the desired temperature. Solutions were heated for the desired amount of time before being removed from the oven and being allowed to cool to ambient temperature.

3.7.2 Extrusion Printing

Extrusion printing was performed on an INKredible+ extrusion bioprinter (Cellink, Sweden). CAD designs were generated using AutoCAD (Autodesk,

USA) and sliced using Slic3r on the Cellink HeartWare software to generate gcode.

For printing, PA solutions were withdrawn into a 1 mL syringe before being injected into a 3 mL printing cartridge (Cellink) using a female-female Leuer-Leuer connector, with all air bubbles being removed before printing. Printing was then performed using a variety of nozzle gauges (22-30 G), pressures (1 kPa – 30 kPa), and printhead movement speeds (. PA solutions were extruded directly into a bath of $CaCl_2$ (1.0 M) to trigger gelation immediately upon extrusion.

3.7.3 Viscosity Measurements

Viscosity measurements were performed on a Hamilton MicroLab Star Liquid Handling system at 25 °C. 300 µL of sample is deposited into the well of a 96-well plate. The sample is then aspirated by the liquid handler in four parallel channels using air displacement pipetting at a constant aspiration rate. The pressure change over time during aspiration is measured by pressure sensors in the pipetting heads. The pressure drop experienced as sample enters the pipette is then related to the viscosity by the Hagen-Poiseuille equation:

$$P = \int_0^H \frac{8\mu Q}{\pi(\frac{R_t + R_{(t-0.01)}}{2})^4} dH - \rho g(0.02 - H_t) - \frac{2\gamma cos\theta}{R_t}$$

Where ρ = density, g = gravity of Earth, µ = dynamic viscosity, γ = surface tension, and θ = contact angle between liquid and pipette. The curve of pressure over time is then fitted using MATLAB with a least-square method. Viscosity is then determined with the curve which fits best to the experimental data.[16]

3.7.4 Rheology Measurements

Rheology was performed on an Anton-Paar MCR 302 rheometer using an 8 mm diameter parallel plate. PA solutions (70 µL) were deposited on the lower plate of the rheometer and triggered to gelate by injecting counterion solution (1 M, 5 µL) into the PA droplet. PAs were allowed to gelate for 10 minutes in a sealed environment before testing, at which point excess fluid was blotted away.

Amplitude sweeps were performed from 0.01-100% strain at a frequency of 10 Hz.

Frequency sweeps were performed from 100-0.1 Hz at 0.1% strain, determined to be in the LVE of the gels by the amplitude sweep.

Time sweeps were performed at 0.1% strain and 10 Hz frequency. For time sweeps, measurement recording was initiated immediately after injection of counterion solution.

3.7.5 Scanning Electron Microscopy

Samples were prepared for SEM by sequential ethanol drying followed by critical point drying (CPD). First, samples were immersed in 4% paraformaldehyde (PFA) for 20 minutes. Following this, samples were sequentially dried in ethanol-water mixtures of increasing ethanol concentration (20%, 50%, 70%, 80%, 90%, 96%, 100%), with 2 washes of 3 minutes at each concentration. Samples were then subjected to critical point drying before being snapped to reveal the gel inner, followed by sputter coating with 10 nm of iridium.

Dried and coated samples were then imaged on a JEOL FEG-SEM 7000F. Accelerating voltage did not exceed 10 KeV to prevent sample damage.

3.7.6 Polarised Light Microscopy

Polarised light microscopy was performed on a Zeiss Axioplan using a polarised light filter. Samples were prepared on glass microscope slides immediately prior to imaging.

3.7.7 Photoacid-based Gelation

DPIN (Merck, catalogue no. 127396) was dissolved in D.I. water at the desired molar concentrations. This solution was then mixed either at a 1:1 volume ratio with a 4% PA solution or 1:1:1 with a 6% PA solution and a 3 M $CaCO_3$ nanoparticle (Nanografi, Türkiye) dispersion to yield a 2% PA solution with 1 M $CaCO_3$.

Solutions inside an Eppendorf were then irradiated using a 30 W 365 nm UV bulb at a distance of 5 cm for up to 90 minutes. The solubilisation of $CaCO_3$ was assessed visually.

pH measurements were taken on a MettlerToledo FiveEasy pH Meter with a micro pH probe. The pH meter was calibrated with a 3-point calibration immediately prior to each session, with the slope ensured to not be below 95%.

3.7.8 Gelatin-PA Solution Preparation

Gelatin-norbornene was provided by the Van Vlierberghe group of The University of Gent, Belgium. Thiolated gelatin was sourced from a commercial supplier (Merck, catalogue no. 904643). GelNB and GelSH were both solubilised in separate D.I. water solutions at 37 °C at 10% w/v. These solutions were then mixed at 4.45:5.55 volume ratios to prepare a 10% w/v GelNB-GelSH solution at a 1:1 NB-SH molar ratio. All thiol-containing solutions were purged with nitrogen for 5 minutes to minimise oxidation and disulfide formation, which would lead to undesired and irreversible gelation.

This stock gelatin solution was then mixed at a 3:1 volume ratio with an 8% w/v PA solution to yield a 7.5% w/v gelatin, 2% w/v PA mixture. In the case where secretome was present, this was first mixed with the PA solution, before mixing with gelatin.

P2CK was synthesised and provided by Dr Jonathan Moore at the University of Nottingham. LAP was obtained from a commercial source (Merck).

Samples were prepared and used on the day of printing, with the photoinitiator (either P2CK (0.04% w.v) or LAP (0.5% w/v)) added in the absence of light as the final component immediately before printing.

3.7.9 Volumetric Additive Manufacturing

VAM was performed on an in-house setup using a 405 nm light source. 2 mL of sample was deposited in a 3 mL glass vial, which was then mounted in a rotating holder. The vial was rotated a total of 720 ° at 24 ° s^{-1} for a total print time of 30 seconds. The vial was then warmed to 37 °C in a pre-heated water bath and the print was removed from the vial by pouring.

3.7.10 2 Photon Polymerisation

2PP was performed on an UpNano NanoOne system utilising a 90-femtosecond pulsed laser at 780 nm. Printing was performed in vat mode using a 10x air objective. Samples (20 μL) were deposited in the wells of an Ibidi μ-Slide 15 well chambered coverslip (Ibidi, catalogue no. 81506). Printing was performed at 37 °C using a heated stage, with temperature constantly monitored during the printing process.

Printing was performed with the following parameters: laser power = 80 mW, infill speed = 600 m s^{-1}, FOV = 50 μm, FOV overlap = 5 μm, block height = 25 μm. Following printing, unreacted sample was gently aspirated to leave behind the printed sample.

3.7.11 Cell Culture and Confocal Microscopy

Cells were cultured, differentiated, stained, and imaged following the same protocol as outlined in *2.9.13-2.9.17*.

3.8 Bibliography

1. Matthews, L.; Przybyłowicz, Ż.; Rogers, S. E.; Bartlett, P.; Johnson, A. J.; Sochon, R.; Briscoe, W. H., *J. Colloid Interface Sci.* **2020,** *572*, 384-395.
2. Singh, P.; Chamoli, P.; Sachdev, S.; Raina, K. K.; Shukla, R. K., *Appl. Surf. Sci.* **2020,** *509*, 144710.
3. Yan, Z.; Li, Q.; Zhang, P., *Appl. Spectrosc.* **2017,** *71* (11), 2437-2445.
4. Farsheed, A. C.; Zevallos-Delgado, C.; Yu, L. T.; Saeidifard, S.; Swain, J. W. R.; Makhoul, J. T.; Thomas, A. J.; Cole, C. C.; Garcia Huitron, E.; Grande-Allen, K. J.; Singh, M.; Larin, K. V.; Hartgerink, J. D., *ACS Nano* **2024,** *18* (19), 12477-12488.
5. Huang, L.; Liao, H.; Yang, J.; Zeng, Z., *J. Photochem. Photobiol. A* **2018,** *367*, 124-127.
6. Cornwell, D. J.; Daubney, O. J.; Smith, D. K., *J. Am. Chem. Soc.* **2015,** *137* (49), 15486-15492.
7. Lee, H.-K.; Soukasene, S.; Jiang, H.; Zhang, S.; Feng, W.; Stupp, S. I., *Soft Matter* **2008,** *4* (5), 962-964.
8. Mũnoz, Z.; Shih, H.; Lin, C.-C., *Biomater. Sci.* **2014,** *2* (8), 1063-1072.
9. Göckler, T.; Haase, S.; Kempter, X.; Pfister, R.; Maciel, B. R.; Grimm, A.; Molitor, T.; Willenbacher, N.; Schepers, U., *Adv. Healthc. Mater.* **2021,** *10* (14), e2100206.
10. Van Hoorick, J.; Dobos, A.; Markovic, M.; Gheysens, T.; Van Damme, L.; Gruber, P.; Tytgat, L.; Van Erps, J.; Thienpont, H.; Dubruel, P.; Ovsianikov, A.; Van Vlierberghe, S., *Biofabrication* **2021,** *13* (1), 015017.
11. Wloka, T.; Gottschaldt, M.; Schubert, U. S., *Chem. Eur. J.* **2022,** *28* (32), e202104191.

12. Li, Z.; Torgersen, J.; Ajami, A.; Mühleder, S.; Qin, X.; Husinsky, W.; Holnthoner, W.; Ovsianikov, A.; Stampfl, J.; Liska, R., *RSC Advances* **2013,** *3* (36), 15939-15946.
13. Huang, X.; Zhang, Y.; Shi, M.; Zhang, L.-P.; Zhang, Y.; Zhao, Y., *Eur. Polym. J.* **2021,** *153*, 110505.
14. Bailly, N.; Wagnac, E.; Petit, Y., *J Mech Behav Biomed Mater* **2025,** *163*, 106898.
15. Christen, Y., *Am J Clin Nutr* **2000,** *71* (2), 621S-629S.
16. Zhou, Z.; Ruiz Cantu, L.; Chen, X.; Alexander, M. R.; Roberts, C. J.; Hague, R.; Tuck, C.; Irvine, D.; Wildman, R., *Addit. Manuf.* **2019,** *29*, 100792.

4. Peptide-Based Co-assembling Materials

4.1 Introduction

It has now been determined that peptide amphiphiles may be used as a self-assembling component in additive manufacturing systems. The peptide sequence may be rationally designed to yield a specific function and may be possible to bind and release multiple proteins in complex fluid to produce a biological effect, such as the increased neurite outgrowth length indicated previously. This idea of complexity in biomaterials design may help to yield emergent functions, where the final material, such as a protein-loaded PA, possesses properties which are greater than the two individual components, such as a PA alone and proteins alone. Following from this, it was decided to investigate whether peptide-based materials could be further incorporated into complex, hierarchical materials through their co-assembly with another molecule.

Previous work has demonstrated that rationally designed peptide-based molecules may co-assemble through non-covalent interactions to yield a functional material.[1-3] Peptide amphiphiles, for example, may co-assemble with elastin-like polypeptides to yield bioactive tubular membranes via a diffusion-reaction mechanism.[4] By altering the charge and bioactive epitope, both the mechanical and biological properties of the resultant membrane may be tuned. Similarly, ELPs may be used in combination with organic materials to co-assemble into tubular membranes. ELPs have previously been co-assembled with graphene oxide to form a tubular membrane capable of supporting the growth of endothelial cells.[5, 6] As with the PA-ELP system, altering the peptide sequence here allows control over the ultimate properties of the membrane. The thickness and permeability of the membrane could also be tuned by exploiting the transition temperature of the ELP, to a point where the tubular structure could be manually handled and perfused, whereas the PA-ELP membranes had begun to degrade after 7 days. Knowing this, it was decided that the possibility

of further integrating graphene oxide within peptide-based co-assembling systems would be further explored.

4.2 Aims and Objectives

The principal aim of this chapter is to demonstrate that, through co-assembly with graphene oxide, a peptide-based material may be formed with novel material or biological characteristics. While this may be a novel material combination altogether, it may also be the case that current material combinations are explored and further developed to improve their properties. This may take the form of improved biomimicry, such as closer recreating native biological tissue, or improving cell response in terms of adhesion, proliferation, or differentiation.

This material should then be characterised as fully as possible, such as its mechanical properties and cytotoxicity. Should these be agreeable, the material should be used for in vitro cell culture, to attempt tissue growth atop or within the material. Achieving this goal, along with full characterisation, would represent a good step towards recreating biological tissue using only supramolecular interactions. The cells used for in vitro studies should be relevant to the desired application, such as endothelial cells for tubular membranes.

Secondly, it should be demonstrated that this material may be integrated within additive manufacturing techniques. Previous work has demonstrated that the GO-ELP co-assembly system may be integrated within an extrusion system to provide precise top-down control over the geometry of the tubular membrane, and it is predicted that a novel liquid-in-liquid co-assembly system may also be integrated within extrusion. Similarly with the gelatin-PA system presented previously, it may also be beneficial to integrate a photopolymerisable moiety within the co-assembled system, so that it may be patterned using DLP or SLA printing techniques. Such a move would represent a move away from a pure supramolecular system but may yield more precise geometry control by allowing the use of higher-resolution printing techniques.

4.3 Peptide Amphiphiles, Elastin-like Polypeptides, and Graphene Oxide

Building upon the previously reported systems of PA-ELP and ELP-GO, it was initially attempted to fabricate a co-assembled system between PA and GO. ELPs are examples of intrinsically disordered proteins, they do not adopt an ordered conformation and therefore undergo structural change with temperature. At and above a characteristic transition temperature, ELPs undergo hydrophobic collapse and transition from a hydrogel-like structure to insoluble hydrophobic coacervates. The hydrophobic region of these ELPs interacts and co-assembles with the basal plane of GO flakes, while the charged ELP regions co-assemble on the charged hydroxyl groups which adorn the edges of GO flakes. Knowing this, PAK_3AGD and PAK_3GHK were selected as candidate PAs, carrying both a net positive charge at neutral pH and a hydrophobic region, meaning it mimics well the structural characteristics of the IK24 ELP sequence. To compare the effect of charge, PAE_3 was used as a negatively charged comparison.

In all cases, it was observed that GO aggregation occurred upon contact with the PA solution, indicating potential membrane formation. This effect appeared most pronounced in structures formed with PAK_3AGD and PAK_3GHK, where a more notable phase separation between GO-based membrane and surrounding fluid was observed (Figure 37). This result was in line with what was expected, as positively charged PAs may co-assemble with GO both via hydrophobic and electrostatic interactions, whereas PAE_3 may assemble only through hydrophobic interactions. In the case of PAK_3GHK, it appeared that, similarly to ELP-GO membranes, dragging a pipette laterally while extruding the PA solution facilitated the fabrication of shaped membranes. These membranes, however, were incredibly weak to handle, and collapsed under their own weight when removed from the surrounding fluid.

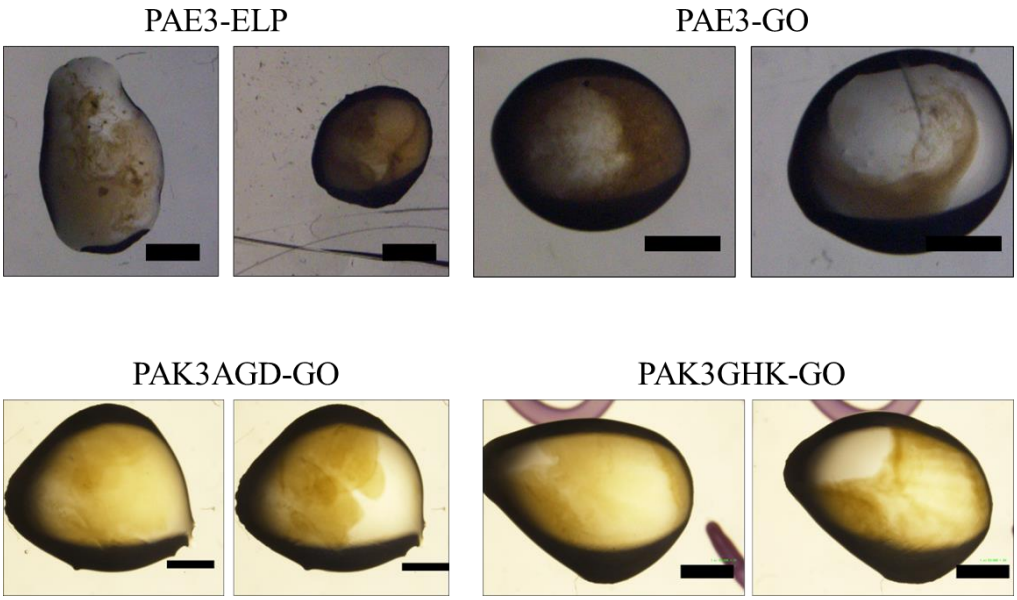

Figure 37: Optical microscope images of combinations of PAs with ELP and GO immediately and 10 minutes after introduction of one solution to the other. GO dispersions (0.1% w/v) were injected into droplets of PA atop a PDMS substrate using a manual pipette. Samples were covered and left to rest at room temperature for 10 minutes. No robust membrane formation was observed in any of the attempted combinations. Scale = 1mm.

It may be the case that the supramolecular interaction between individual PA molecules and GO flakes is too weak to form a robust membrane, or that it is energetically unfavourable for PA micelles to disassemble to simply adhere to the basal plane of the GO flakes. However, reducing the PA concentration to below the critical micelle concentration would also likely reduce the attractive forces which trigger GO to diffuse towards the interface, also limiting membrane formation.

It was also noted that the resultant material did not appear gel-like, indicating either insufficient charge-dampening by the charged hydroxyl groups of GO, or disruption of the ordered β-sheet region of the PA molecules. Both effects would ultimately disrupt gel formation. There is literature evidence that graphene oxide may disrupt β-sheet formation in adsorbed proteins, predicted using molecular dynamics simulations but not confirmed experimentally.[7] Speculatively, this effect may be preserved in adsorbed PAs, inhibiting gel formation. However, IK24-GO complexes exhibit a greater degree of β-sheet conformations at 30 °C (T_t of IK24) compared to IK24 alone, indicating that this may not necessarily be the case. Further study may be required to

understand the poor interaction between PA and GO. Isothermal titration calorimetry (ITC) or fluorescence emission titrations may reveal some information about the nature of this interaction, yielding binding affinities. However, as no material which could be handled could be formed, other systems were explored.

As the IK24 ELP carries a net positive charge at its T_t, it was theorised that it may be able to form a material with PAE_x sequences through electrostatic interactions. As both materials also contain β-sheet regions, it was also hypothesised that co-assembly may be possible. Introduction of a 2% w/v PAE_3 solution to a 2% IK24 suspension at 30 °C resulted in the formation of a coacervate species which appeared to have gel-like mechanical properties. However, as with the PA-GO mixtures, this material was also too fragile to be handled and disintegrated upon removal of surrounding fluid. The gel formed here may be a result of charge dampening by the oppositely charged IK24 ELP, and it is not possible to determine whether co-assembly occurred through simple observation under microscope. However, as this material could also not be handled, it was not investigated further.

Having been unable to form a mechanically robust material using PA-GO or PA-ELP combinations, it was determined that the IK24-GO system should be adopted and improved upon for additive manufacturing purposes. IK24 is more economic than any PA, so its inclusion in extrusion printing for larger-scale applications is more accessible than PAs. It was observed that the co-assembling IK24-GO system could be easily replicated here, and that the resulting tubes could be handled and manipulated using forceps without disintegrating. This system was therefore selected for further study.

4.4 Extrusion Printing of GO-ELP membranes

It has already been previously reported that the extrusion of IK24 ELP (2% w/v) into a pool of GO aqueous dispersion (0.05-0.4% w/v) facilitates the automated fabrication of tubular membranes on the centimetre length scale with precise geometric control.[5] Here, it was first determined whether this system could be recreated using available extrusion equipment, and which parameters produce reliable, replicable tubes. Should this be achieved, it would then be possible to

alter the experimental setup to control the ultimate properties of the membrane, such as its strength or thickness.

A range of print settings were first attempted to determine how best to produce a GO-ELP membrane (Figure 38). The concentrations of IK24 and GO were maintained at 2% w/v and 0.1% w/v, as these were reported to produce the most robust membranes. Several printing parameters were available to be altered: printhead movement speed, extrusion pressure (flow rate), printhead temperature, bed temperature, nozzle gauge, and z-lift. Nozzle gauge and z-lift are somewhat linked, as the distance between the tip of the nozzle and the printbed should be the same as the nozzle inner diameter. For printhead and bed temperature, these were set at 30 °C, as it has already been determined in previous work that this temperature results in the most robust membranes between IK24 and GO.[5] This therefore left the printhead movement speed, nozzle gauge, and extrusion pressure to be optimised. An .stl file containing simple straight lines was designed, and the resulting gcode edited to instruct the printer to extrude these lines at a range of printhead movement speeds to more rapidly screen the printing parameters.

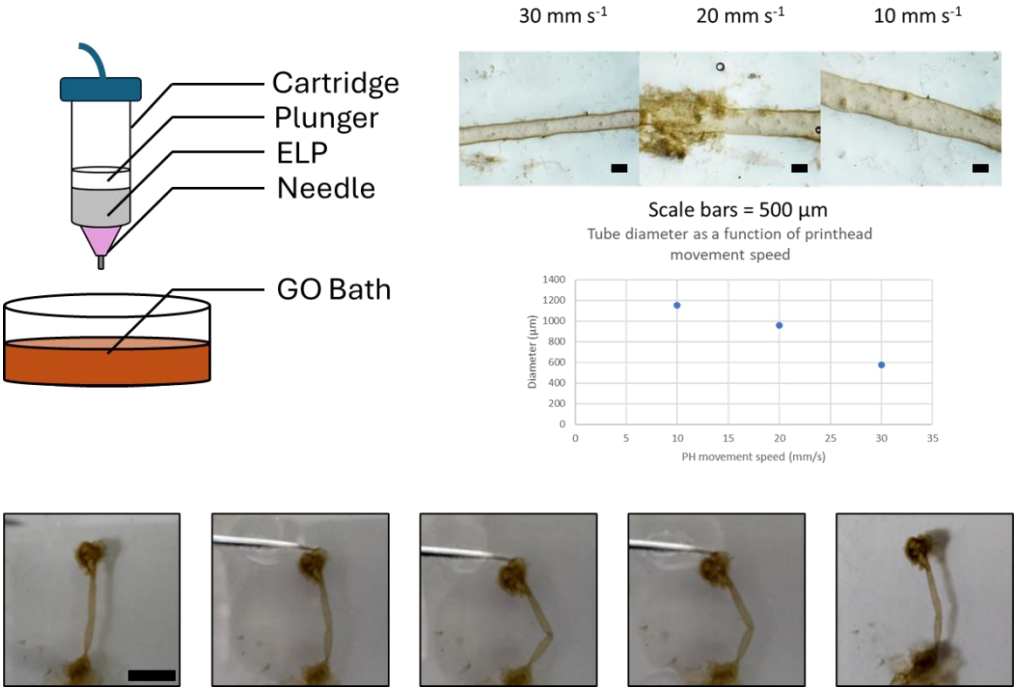

Figure 38: Extrusion printing of ELP-GO membranes using a liquid-in-liquid setup. Top left: Basic schematic of the experimental setup. ELP is loaded into a 3 cc cartridge mounted in the printer. A pressure is then applied by the printer, which extrudes the ELP into a GO bath. Top right: Effect of printing

parameters of the diameter of the final tube. Increasing the printhead movement speed results in a lower tube diameter. Lower: Stills from a camera video of the ability to manipulate printed tubular membranes, with the ability to return to original shape after deformation. Scale = 3 mm.

As a starting point, a 30 G nozzle (0.159 mm ID) was selected for extrusion of the ELP, as this was the closest available nozzle to the gauge which had been used in previous literature,[6] with printhead movement speeds varying from 10-30 mm s^{-1}. A set pressure of 24 kPa was applied, as it was at this point flow was observed from the nozzle. It was observed that, as opposed to a "perfect" parameter existing, varying the extrusion parameters facilitated good control over the dimensions of the resulting tube. From 10-30 mm s^{-1}, it was observed that the diameter of the tube reduced with increasing printhead movement speed at a constant pressure (Figure 38). Above 30 mm s^{-1}, however, it was noticed that the tube would begin to "pinch" and separate along the length of the tube, indicating an upper limit of movement speed. A similar effect was observed when altering the applied pressure at a constant movement speed, with a lower pressure, and thus lower flow rate, resulting in a lower diameter and a greater pressure increasing the diameter of the tube. This effect was not entirely unexpected and is due to the expansive forces of the ELP as it is extruded from the nozzle. At a greater flow rate or lower movement speed, a greater volume of ELP is being extruded in the same time frame, forcing the walls of the forming tube to be expanded, creating a tube with a greater diameter.

The extrusion of ELP into GO, at the tip of the nozzle, may be thought of as a sudden expansion problem, to which the Borda-Carnot equation may be applied:

$$\Delta E = \xi \frac{1}{2} \rho (v_1 - v_2)^2$$

Equation 2: The Borda-Carnot Equation. E = mechanical energy, ξ is the loss coefficient, ρ is the fluid density, and v_1 and v_2 are the flow velocities before and after the expansion.

Here, while there is a small resistive force from the GO dispersion, the ELP may be thought of as being extruded into a larger space with an infinite cross-sectional area, as an approximation. Here, because the printhead moves away from the point at which the ELP is extruded, it can be approximated that the flow rate after extrusion is close to - but not always exactly - 0, as there is

minimal pressure acting on already-extruded material. Therefore, the expansion of the ELP solution may be viewed as similar, but not exactly akin to:

$$A_1 v_1 = A_2 v_2$$

Equation 3: Approximation of change in cross-sectional area (A) and velocity (v) before (1) and after (2) extrusion.

Therefore, assuming A_1 and v_2 are constant in all cases, a greater v_1 (increased flow rate) would yield a greater A_2 (tube diameter). In the case of changing printhead movement speed, if v_1 is different to the printhead movement speed, there would then be a force acting on the already-extruded ELP, altering the value of v_2. For example, if a printhead moves along axis *y* at -10 mm s^{-1}, while the ELP is extruded at a velocity of 20 mm s^{-1}, a compressive force would act upon the already extruded droplet, forcing it to expand radially into the surrounding area, growing the tube diameter. Similarly, if a printhead moves along axis *y* at -20 mm s^{-1}, while ELP is extruded at 10 mm s^{-1}, relatively more drag is experienced by the extruded droplet and its velocity after extrusion may be thought of as negative along axis *y*. This results in "pinching" of the extruded fluid, reducing the tube diameter. It must also be assumed that there is an attractive force which maintains in place the initial material extruded, which forces the subsequent pinching.

At this point, however, it is where Equation 3 fails to successfully explain tube growth. In the case where printhead movement velocity is greater than extrusion velocity, the velocity after extrusion should be thought of as negative. For this to satisfy Equation 3, however, this would have to result in an increase in A_2, the cross-sectional area after extrusion. In effect, however, the opposite is observed. This is because Equation 3 assumes that A_2 is an applied constraint (e.g., a wall), rather than a variable result (tube diameter), and that v_2 is a uniaxial velocity as opposed to radial growth. For now, it is understood that the relationship between printhead movement speed or flow velocity and tube diameter appears fairly linear.

The problem may be simplified by describing the total length travelled by the printhead as a cylinder with length *L*, radius *r*, and a total volume $V_{cylinder}$. *L* is

a fixed variable and does not change. $V_{cylinder}$ must be equal to the volume of ELP extruded from the nozzle, V_{ELP}. As the volume of a cylinder is given as:

$$V = \pi r^2 L$$

Equation 4: Volume of a cylinder.

The radius, *r*, is given as:

$$r = \sqrt{\frac{V}{\pi L}}$$

Equation 5: Radius of a cylinder.

As *L* is travelled in time *t* with an ELP volumetric flow rate *Q*, the exact volume extruded along length *L* may be known, and thus the initial radius of the cylinder approximated. This should, however, be regarded only as an approximation, as the final diameter of the tube is also dependent upon the volume and concentration of GO, and the time for which the extruded ELP is left in the GO bath. The diffusion of each component occurs over time, growing the diameter at a rate previously reported.

To support the hypothesis that a negative velocity occurs when printhead movement velocity is greater than extrusion velocity, a print was attempted with the z-lift being greater than the nozzle ID. In this case, there is no initial anchoring of the extruded material. In this case, tube formation fails as the initial droplet is simply dragged with the nozzle, expanding radially to result in a single large sac as opposed to a tube.

Having determined printing parameters which yield successful tubular membrane formation, it was now explored how this system may be improved upon. Currently, the liquid-in-liquid extrusion setup required a bath of GO, the concentration of which is steadily depleted as more ELP is extruded into it. This steadily reduced the reliability with which robust membranes may be reliably formed over time. Additionally, this requires a large volume of GO compared to the relatively low volume of IK24 ELP solution and could be improved upon by reducing the required volume of GO. To counter both issues at once, a dual-extrusion setup was explored. Two possible manners of adopting this were

developed. In one, a side-by-side extrusion was developed while in the other, coaxial extrusion was used.

4.5 Dual Extrusion of GO-ELP

4.5.1 Side-by-side Extrusion

For a side-by-side extrusion system, a 3D printed nozzle adaptation was prepared. This adapter fits on the cartridges used in the extrusion printer and directs the flow from both cartridges towards each other. At the point of extrusion, both flows are introduced side-by-side. At this point, the ELP and the GO are introduced at the interface, and a membrane is formed. As the ELP is not injected into surrounding GO, it was predicted that this method would produce ribbons as opposed to a tubular membrane.

It was observed that, by extruding side-by-side, the formation of a ribbon-like membrane is possible (Figure 39). This membrane, however, was far less mechanically robust than observed in the liquid-in-liquid system, and was less reproducible than this system, yielding more variable widths and thicknesses. While a side-by-side system could still hold potential if the printing parameters are more fully optimised, perhaps using a syringe pump-like system as opposed to pneumatically driven extrusion, a coaxial system was subsequently investigated.

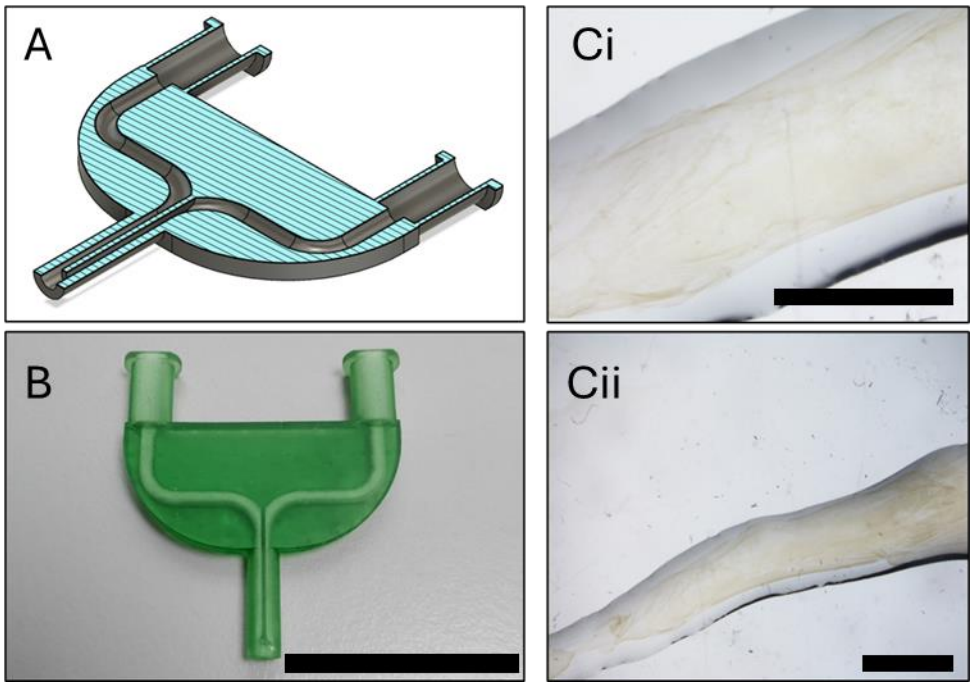

Figure 39: Side-by-side dual extrusion of GO and ELP to form an interfacial membrane. A) CAD cross-section of the dual extrusion system. B) 3D printed dual extrusion nozzle attachment for use on a Cellink INKredible+ extrusion printer. Scale = 3.5 mm. Ci&ii) Optical microscopy images of membranes formed by dual extrusion. Scale = 1 mm.

4.5.2 Coaxial Extrusion

To minimise the volume of GO used in this system, it was decided to switch to a coaxial extrusion system, where both ELP and GO are extruded simultaneously, with the GO forming a shell around the ELP. It was planned that membrane formation would occur immediately at the point of extrusion from the nozzle, with diffusion growth occurring during the lag phase between extrusion and deposition on the substrate below. Finally, it was theorised that a self-supporting tubular membrane would remain after extrusion. The thickness of the wall, too, was hypothesised to be limited in this system, owing to the drastic reduction in volume of GO available to react and grow the membrane.

4.5.2.1 Behaviour of GO under shear

A 28/22 coaxial nozzle was selected for use here, with exact the dimensions shown in Figure 41. Initially, it was planned that ELP would be extruded through the inner nozzle, while GO was extruded through the outer nozzle at an identical flow rate. Firstly, the way the imposition of shear would impact the fluid properties of the GO dispersion was investigated. GO is reported to be a

shear-thinning fluid,[8] and flow above a set Peclet number induces the dispersion of GO lamellae and alignment of GO flakes with flow.

The ordering of flakes in the GO dispersions at various concentrations was probed using polarised light microscopy (Figure 40). Below 0.3% w/v, no ordering of the GO flakes is observed, with an isotropic arrangement of flakes predicted based on previous literature correlating birefringence to GO crystalline ordering.[9] The difference in percentage weight by volume observed compared to previous literature may be attributed to a different flake size used here. In the isotropic phase, it may be predicted that individual GO flakes exist as single flakes in random orientation, and the material may be thought of as a viscoelastic liquid. At and above 0.3% w/v, some crystalline ordering of the GO is observed, and the material moves into a nematic phase, behaving as a liquid crystal. This ordering may arise as a result of the non-covalent interactions between GO sheets in close proximity, such as π-π interactions in the basal plane or hydrogen bonding between hydroxyl and carboxyl groups. These are important considerations for developing GO-based materials for processing. It is suggested, for example, that GO dispersions in the isotropic and nematic phases are unsuitable for printing 3D architectures, and may even struggle with 2D architectures.[9] The current fabrication method, however, overcomes these limitations by forming a more robust membrane immediately upon extrusion.

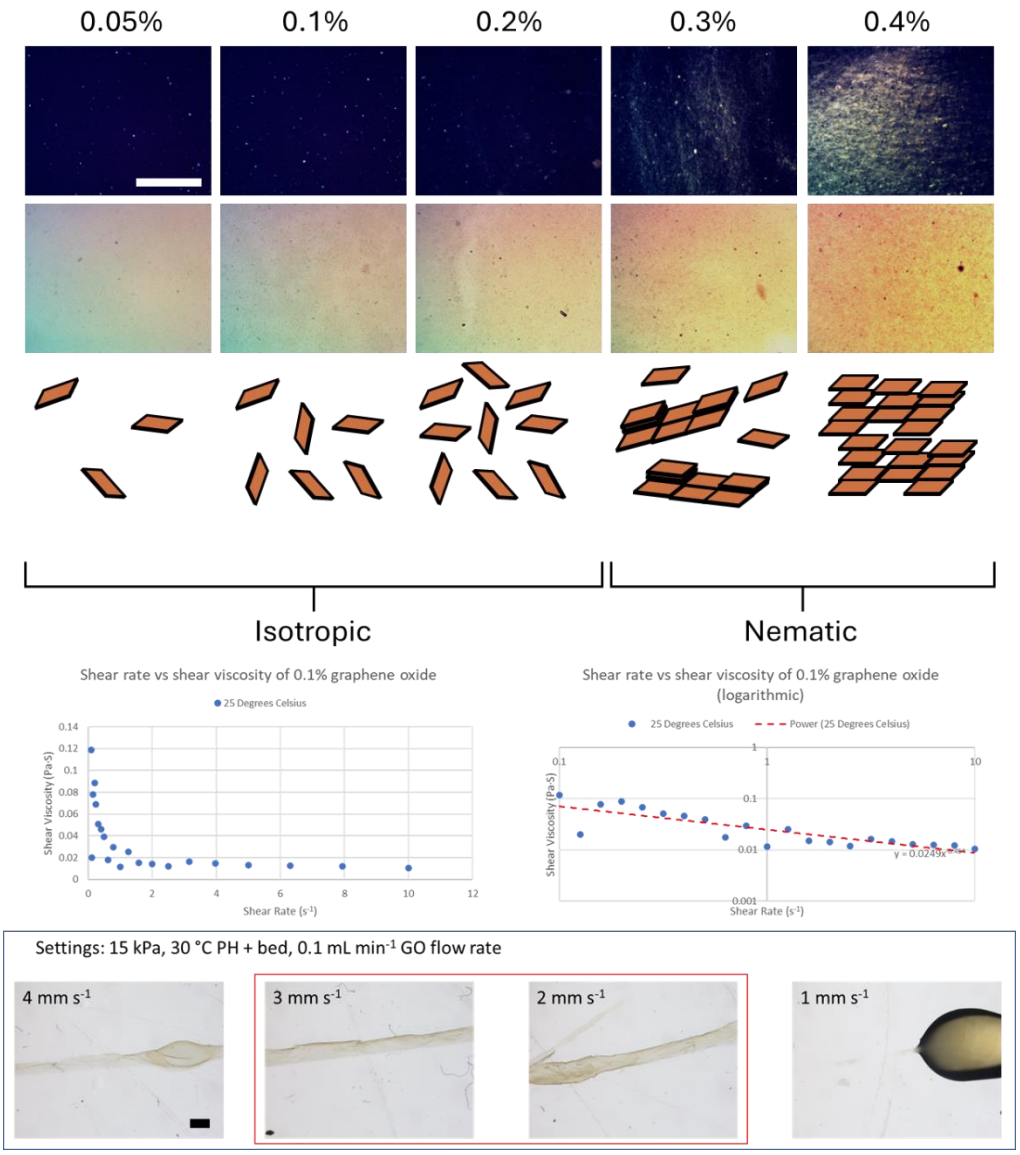

Figure 40: Characterisation of GO dispersions and subsequent membrane formation in coaxial printing. Upper: Polarised light (upper) and brightfield (lower) images of GO dispersions. The observation of birefringence at higher concentrations indicates the presence of crystalline ordering. Scale = 1 mm. All images same scale. Middle: Viscometric measurements of GO confirming shear thinning behaviour, and subsequent determination of the flow consistency index from the log-log graph. Lower: Impact of printhead movement speed on the formation of a membrane with homogenous diameter. Outside of an optimal range, membranes may be deposited as droplets (low velocity) or as a membrane with heterogenous widths along its length (high velocity). Scale = 1 mm, all images same scale.

Viscometric measurements confirmed the rapidly shear-thinning behaviour of a 0.1% GO dispersion at 25 °C (Figure 40). Graphene oxide and its properties in aqueous dispersion have been well documented, and its thixotropic behaviour is known. Here, at 0.1% GO w/v, it is predicted – based on previous literature studying the rheological properties of GO – that the GO will initially be present

as an isotropic dispersion. This leads to the lack of birefringence observed under polarised light microscopy (Figure 40).[9] Between 0.1-0.3% w/v, it is predicted that the GO dispersion will behave as a viscoelastic soft solid, with a viscosity suited to inkjet printing or spray deposition. However, as the GO is to immediately form a membrane upon extrusion, such predicted applications may not apply in this case.

Plotting the viscometry data as a log-log plot allows the determination of the non-Newtonian power law for this dispersion under these conditions:

$$\eta = K\dot{\gamma}^{n-1}$$

Equation 6: Non-Newtonian power law equation. Here, η = dynamic viscosity, K = flow consistency index, $\dot{\gamma}$ = shear rate, and n = power law constant.

The velocity of GO travelling through the outer nozzle was observed reach a maximum at 0.482 mm s^{-1}. Given the distance between the ⌀ of the inner nozzle and the ID of the outer nozzle is 0.025 mm, the shear rate experienced by the GO during extrusion may be given as:

$$\dot{\gamma} = \frac{v}{h} = \frac{0.000482}{0.000025} = 19.3\ s^{-1}$$

Equation 7: Calculation of shear rate during extrusion. Here, v = velocity (m s^{-1}) and h = distance between two parallel plates (m).

Knowing the shear rate experienced by the GO, the viscosity may be estimated as:

$$\eta = K\dot{\gamma}^{n-1} = 0.0249 \times 19.3^{-0.454} = 0.00650\ \text{Pa} \cdot \text{S}$$

Equation 8: Calculation of GO viscosity during extrusion using non-Newtonian power law.

Knowing the viscosity of the GO dispersion at the point of extrusion allows the calculation of its diffusivity constant, D_0, using manufacturer values for flake size:

$$D_0 = \frac{k_B T}{6\pi\eta r} = \frac{4.11 \times 10^{-21}}{6\pi \times 0.00650 \times (9 \times 10^{-7})} = 3.73 \times 10^{-14}\ \text{m}^2\text{s}^{-1}$$

Equation 9: Calculation of the diffusivity constant of GO during extrusion. Here, k_B = Boltzmann constant (J K^{-1}), T = temperature (K), η = dynamic viscosity (kg m^{-1} s^{-1}), and r = particle radius (m).

From this, the Péclet number may be obtained:

$$Pe = \frac{\dot{\gamma} a^2}{D_0} = \frac{19.28 \times (9 \times 10^{-7})^2}{3.73 \times 10^{-14}} = 419$$

Equation 10: Calculation of the Péclet number. Here, a is the average sheet radius (m).

As the Péclet number exceeds 1, it can be predicted that the effects of shear dominate the flow. Larger GO lamellae are dispersed under the imposition of shear in this case, resulting in individual flakes which likely align with the direction of flow. From these equations, it was predicted that membrane formation is far faster than in the liquid-in-liquid system, owing to the decreased viscosity of the shear-thinning GO dispersion. Furthermore, the resulting membrane may, possibly, be somewhat thinner than the liquid-in-liquid system, as individual flakes are diffusing to the interface rather than comparatively thicker lamellae.

4.5.2.2. Coaxial Constructs

Coaxial printing was initially performed directly onto a dry PDMS substrate, as opposed to printing into a liquid bath. Owing to the hydrophobicity of the PDMS, it was hoped that the contact angle of the aqueous materials would help with rounding of the membrane, aiding tube formation. Initial testing focussed on finding the correct printing parameters. Similarly with the liquid-in-liquid system, a range of successful parameters were found, outside of which either "blobbing" or "pinching" of the extruded material was observed (Figure 40), resulting in membrane failure.

Immediately, it was observed that the coaxially extruded membranes demonstrated reduced optical opacity when observed under a light microscope, compared to the liquid-in-liquid system (Figure 40). Due to the high optical opacity of GO dispersions, this would be indicative of a reduced volume of GO present on the final membrane. It was also observed, however, that it was not possible to form tubular membranes in this manner, as the membrane collapses under its own weight, leading to a flat "ribbon-like" structure. These ribbons are observed to be roughly 50 μm in thickness with a layered structure (Figure 41). The upper side of these ribbons appears morphologically similar to the GO-rich walls previously observed,[5] while the inner – observed on a cross-section –

appears to be more similar to an ELP-rich domain. Under polarised light microscopy, birefringence is observed, indicating a degree of anisotropy in the structure, perhaps because of the alignment of the GO under shear stress.

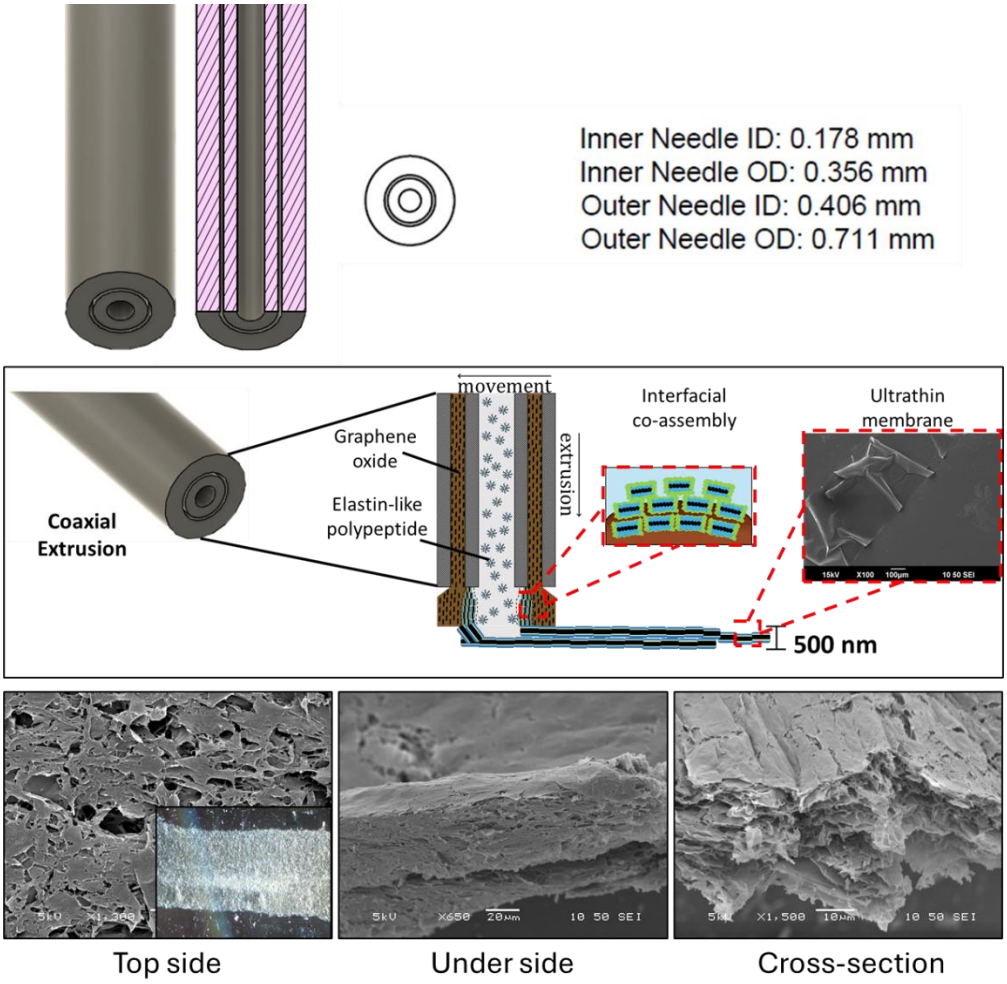

Figure 41: Coaxial GO-ELP extrusion. Upper: Schematic and measurements of a 28-22 stainless steel coaxial needle. Middle: Schematic of the coaxial extrusion process, with GO extruded through the outer nozzle and ELP extruded through the inner, leading to interfacial membrane formation at the point of extrusion and subsequent thin membrane formation. Lower: SEM micrographs of coaxially fabricated membranes demonstrating porosity (left and middle), anisotropy (inset) and a layered structure (right) as is observed with the liquid-in-liquid extrusion system.

The inability of the tube to support itself was hoped to be overcome by introducing some buoyancy. Here, coaxial extrusion was performed in a bath of ultrapure water heated to 30 °C. Here, however, it was observed that, while a membrane formed, it was incredibly thin and was destroyed by any attempt to handle and manipulate it. This did, however, indicate the possibility of fabricating ultrathin membranes, similar in thickness to that of native

membranes within biological systems. In nature, the basement membranes of endothelial tissues may reach as thin as 100 nm. Achieving such a structure artificially, which can subsequently support cell growth, would represent a useful technology for vascular tissue engineering and modelling.

To this end, the printhead movement speed was increased, and the z-lift decreased, to limit the amount of time available for the GO to diffuse to the interface and grow the membrane. In doing this, a decrease in ribbon thickness was observed when visualised with electron microscopy, and a reduction in thickness confirmed using ellipsometry (Figure 42). Ellipsometry was chosen as a quantitative technique here as SEM micrographs are unlikely to demonstrate a true thickness, especially at such low thicknesses here. The iridium coating used for SEM, for example, may misrepresent the true thickness of the membrane. Ellipsometry is a non-destructive, highly sensitive technique which may be used to measure film thickness. Other techniques, such as surface profilometry, were considered but would lack the sensitivity required to measure membranes of 100s of nanometres in thickness. The thickness was not observed to be perfectly uniform, but was observed the average at roughly 100-200 nm, and not exceed 283 nm. This membrane, however, was also unable to be handled or manipulated without being damaged.

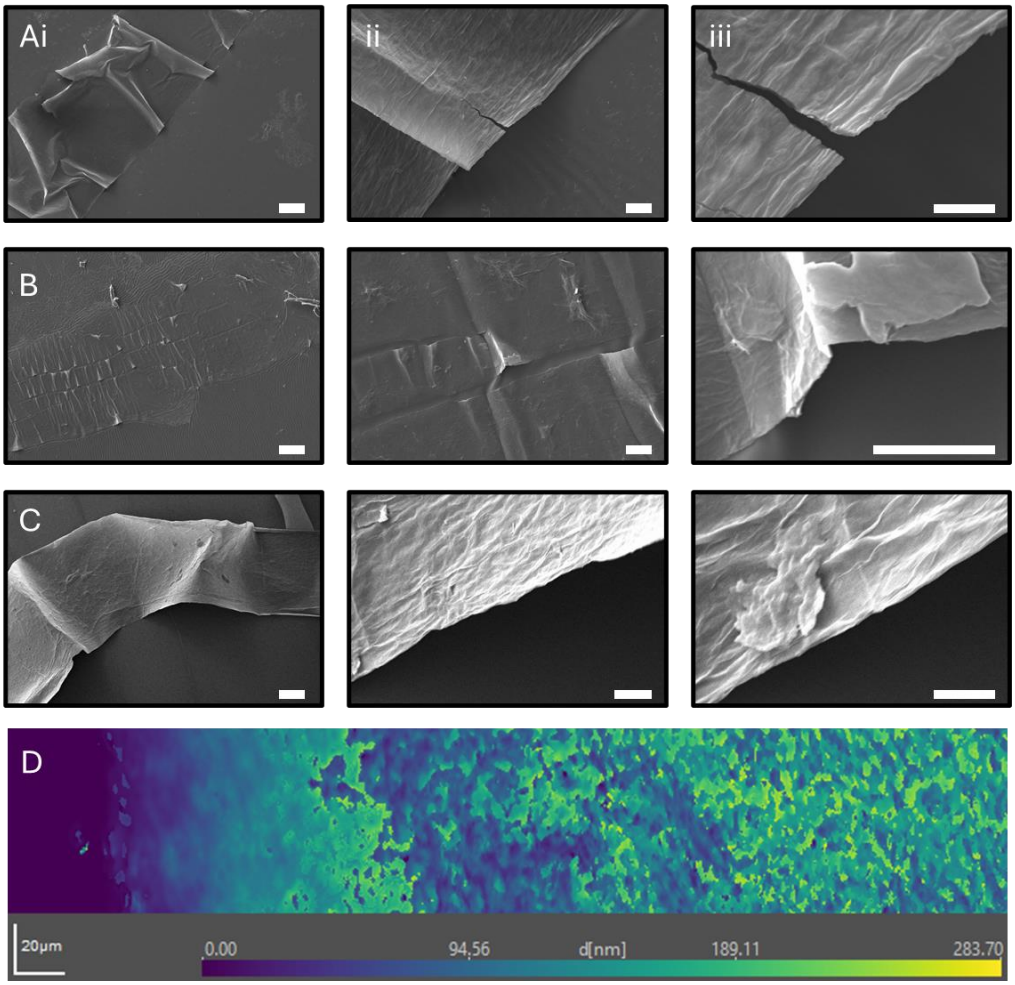

Figure 42: Ultrathin membranes formed through coaxial extrusion printing. A) Membranes formed using an ELP core and GO 0.4% w/v shell. B) Membranes formed using an ELP core and GO 0.05% w/v shell. C) Membranes formed using a GO 0.4% w/v core and ELP shell (inverted coaxial) Scale bars: i) 100 µm. ii) 10 µm. iii) 5 µm. D) Surface thickness map obtained from ellipsometry measurements with XY size scale and Z height colour scale inset.

Inverting the coaxial extrusion by extruding GO through the inner nozzle and ELP through the outer nozzle, also resulted in successful membrane formation (Figure 42). This membrane, too, was observed to result in a ribbon-like structure. This confirms that, regardless of the coaxial order, any tube formed is unable to support its own weight and collapses upon formation. To overcome this, extrusion was performed directly into a water bath, where it was hoped buoyancy would alleviate the issue of tube collapse. However, it was observed that, in this case, GO was washed away immediately upon extrusion, resulting in the formation of an ultrathin membrane which was subsequently destroyed by the fluid forces induced by printhead movement. Overall, these experiments confirm the ability to form ultrathin GO-ELP membranes but indicate the

necessity to improve its mechanical properties. To attempt expedite the outwards diffusion of the ELP, a triaxial system was attempted.

4.5.2.3. Triaxial Extrusion

A triaxial extrusion setup was developed wherein the central nozzle was extruded simply with an air flow, the second-most inner nozzle was extruded with ELP, and the outer nozzle was extruded with GO (Figure 43). When extruding directly upon a dry PDMS substrate, this construct was observed to collapse and form a flat membrane, as with the coaxial system. However, when suspended 2 mm above a water bath, a tubular structure was observed to form in the space between the nozzle and meniscus. Upon further extrusion, this tube was observed to grow in length. However, it was not possible to introduce lateral movement to direct the growth of or impose patterning upon this tube. The tube was observed to grow in an uncontrolled manner, curling at the top of the water bath, as it is not dense enough to sink as it grows. Additionally, the formation of large droplets along the length of the membrane was observed, and the extruded GO was observed to wet the nozzle, rather than extrude with the membrane. It was also observed that, under the same applied pressures and flow rates, the diameter, thickness, and shape of the tube would vary between replicates. Due to the poor reliability of this method, it was not immediately explored further. It may be said, however, that this method may hold promise for forming perfusable, tubular membranes with further optimisation.

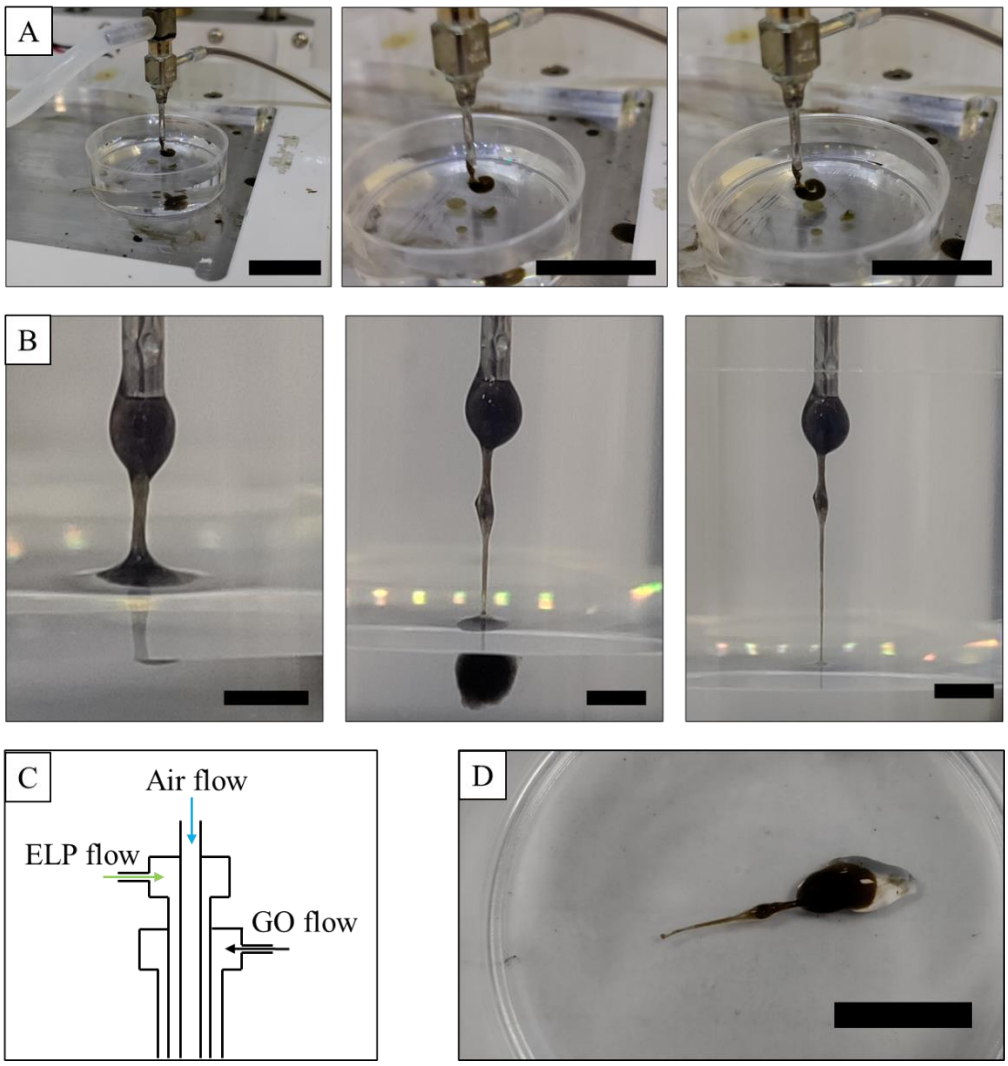

Figure 43: Triaxial GO-ELP extrusion. ***A)*** *Gradual formation of a tubular membrane upon extrusion into a water bath. The membrane is observed to be buoyant and form a curved structure in an uncontrolled manner. Scale = 16 mm.* ***B)*** *Extension of tubular membrane by dragging out of water bath. Scale = 1.5 mm.* ***C)*** *Schematic diagram of triaxial setup. Not to scale, for illustration purposes only.* ***D)*** *Final extruded membrane structure after removal from water bath and nozzle. Scale = 8 mm.*

Now understanding that it is possible to produce ultrathin ribbon-like membranes upon a dry hydrophobic substrate, with both GO-rich or ELP-rich faces, it was now investigated whether these materials can support cell growth. It has previously been observed that both the ELP-rich and GO-rich sides of these membranes may support human umbilical vein endothelial cell (hUVEC) proliferation, so it was determined that these cells should be used to confirm a translation of the tubular membranes' biological properties to these ribbon-like structures.

4.6 Endothelial Cell Culture

As these ribbon-like structures have demonstrated an ultrathin nature close to that of native basement membranes in biological systems, it was determined that their ability to support endothelial cell growth should be investigated. Basement membranes are ubiquitous in biology, supporting the correct structure and function of – for example – the brain, the lungs, the kidneys, and the eyes. Disruption, disorder, and disease of these membranes can lead to reduced organ function and failure. Additionally, there is a need to study the passage of ions, solutes, and biomolecules across these barriers in order to understand and develop drugs which may be delivered to, for example, the brain across the blood-brain barrier (BBB).

Currently, there exist few examples of artificial basement membranes which may support endothelial cell growth. Among these examples, rarely is the thickness of native basement membranes (<1 μm) achieved and those that do typically use highly synthetic materials or exist only in an experimental setup which inhibits handling or future implantation. Here, while direct handling remains an issue to be solved, the ability to produce ultrathin membranes using biological-based materials in ELPs has been demonstrated. It therefore must be demonstrated that these materials are able to support endothelial cell growth. For an in vitro model, hUVECs were chosen as a primary human model, bearing good relevance to the desired application. For BBB modelling, other cell types such as brain microvascular endothelial cells (BMECs) may be more relevant. For initial testing, however, hUVECs were deemed appropriate.

Here, 2 concentric circles were extruded into the base of a 12-well plate, washed gently 3x with PBS, and subsequently soaked in EGM-2 cell culture media containing 2% FBS for 24 hours. hUVECs (P10) were then seeded atop the preformed membranes at 137,000 cells per well. The cells were stained using CellTracker Green, which stains both live and dead cell membranes, for visualisation purposes (Experimental 4.8.11).

24 hours after seeding, it was observed that cells were present atop the membrane (Figure 44). These cells, however, had adopted a somewhat rounded morphology, indicating either poor adhesion or cell death. hUVECs typically

adopt a degree of anisotropy in healthy morphologies, with small projections at the apical tips. In the following 48 hours, the number of cells seen on the printed membrane was observed to decrease until, after 72 hours, no cells were observed on the face of the membrane. This was not entirely unexpected, as GO contains no cell adhesion motifs. It was hoped, however, that a media soak would adhere proteins to the surface of the GO which themselves have adhesion motifs, facilitating cell adhesion to the membrane. No such effect was observed. It may be the case that, in creating a flat membrane as opposed to a tubular membrane, curvature-sensing proteins in the hUVECs are not activated, and adhesion is inhibited as a result.

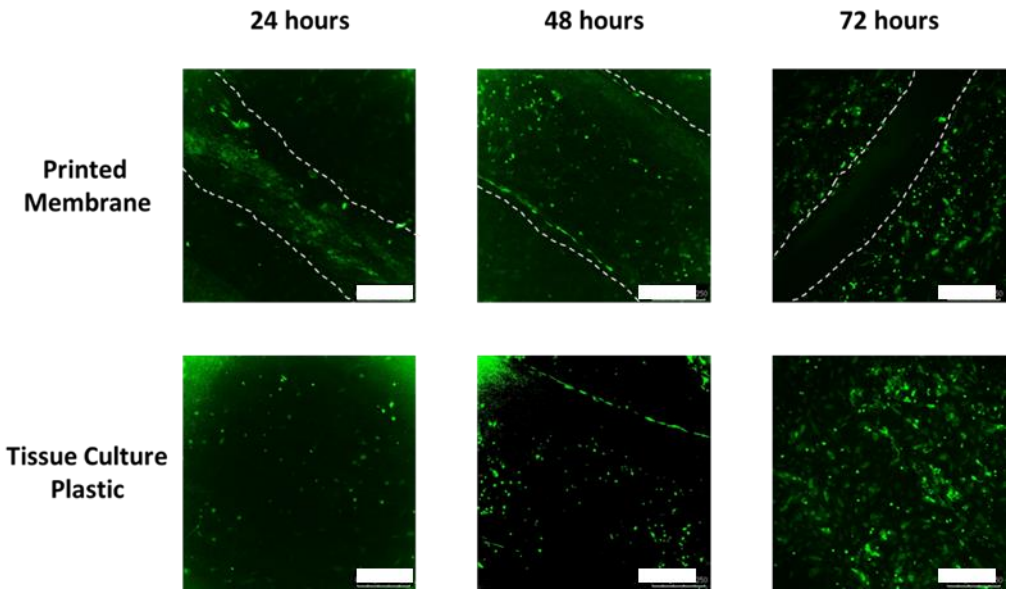

Figure 44: hUVEC culture on coaxially fabricated GO-ELP membranes. Cells were stained using CellTracker green and imaged every 24 hours for 3 days. A tissue culture plastic control was used to confirm normal cell behaviour. After 72 hours, cells are observed to be absent from the printed GO-ELP membrane, despite growing as normal on tissue culture plastic. Scale = 250 μm

It was observed, however, that on the curved edges of the membrane, hUVECs adhered and began to form a single-cell thick layer spanning the length of the membrane. There may be two reasons for such an effect. Firstly, as this is the edge of the ribbon, it may be the case that, upon collapse of the tube during formation, the ELP is exposed here. This may present a more favourable adhesion environment for hUVECs, however hUVECs have been demonstrated to adhere to both the ELP and GO side of the membrane.[5] However, the ELP

used here lacks adhesion motifs. Secondly, it may be that the curvature of the concentric circle may provide a physical cue for hUVECs to adhere and proliferate. hUVECs tend to form tubular structures when cultured in the presence of grooves,[10] and therefore providing physical cues for this to happen in the form of the concentric circles may result in their preferential adhesion to this curved surface.

It should also be discussed that the hUVECs used here were used at passage 10. This is typically too high of a passage number to use primary hUVECs, and their characteristic behaviours such as tube formation may be hindered as a result. A TCP control indicates that these cells are still able to adhere to and proliferate upon cell-adherent surfaces, but these processes may be hindered due to the age of the cells. hUVECs or other endothelial cells of a lower passage number were unavailable at the time of experiment.

There are other factors which may have impacted cell adhesion and proliferation atop the membrane. Firstly, some rounded morphologies are observed near the membrane after 72 hours of culture. While no quantitative measurement was performed, the rounding of hUVECs may be indicative of cell death and may indicate toxicity. However, as the GO-ELP membrane has previously been used to successfully culture hUVECs, it was assumed here that toxicity was not an issue. The rounding of cells, similarly to PAE_3, may likely be due to poor cell adhesion and proliferation. A high degree of rounding is also observed in the TCP sample, indicating a cell issue, as opposed to a material toxicity.

Should it indeed be the case that material curvature can overcome a lack of adhesion motifs and facilitate endothelial cell attachment and proliferation, a deviation from tubular membranes to a flat ribbon represents a move away from a functional material. While endothelial cells may indeed be cultured on flat surfaces, these surfaces typically present cell adhesion motifs, such as in the case of TCP. Therefore, should a structure of the thickness observed here be used as a functional material for endothelial cell growth, work must be conducted to maintain its shape as a hollow tube, with both an ELP and GO-rich wall. In doing this, curvature is naturally achieved, and it is predicted that endothelial cell adhesion would be improved.

4.7 Conclusions and Future Work

Initial work here attempted to develop a co-assembly system which incorporated a peptide-based material, utilising non-covalent interactions to achieve a hierarchical material. Several combinations were initially attempted, bringing together previous work which saw the co-assembly of an ELP or PA with GO to form a layered membrane, with attempts to co-assemble PAs with the ELP. It was observed that none of the attempted combinations were successful, and it was decided instead to improve upon the previously reported GO-ELP system.

Here, it has been demonstrated that, through precise control of the volume of GO available to react, an ultrathin membrane with a thickness in the range of 200 nm may be fabricated through coaxial extrusion printing. These membranes may be printed continuously on the centimetre length scale. However, these membranes lack several properties before they may be considered for tissue engineering or as basement membrane models.

Firstly, these membranes lack the ability to be handled. Any attempt to pick up the membrane results in its disintegration. It may be possible to deposit this membrane directly atop a surface on which it may be used, such as the base of a transwell plate for permeability measurements. However, the printing of the membrane requires drag from the printing substrate to prevent accumulation of extruded material around the tip of the nozzle. In doing this, a weak substrate such as the membrane of a transwell plate may well be damaged during the printing process.

Secondly, the membrane in its current form does not completely support endothelial cell growth. Cells seeded atop the membrane migrate away from it over the course of 72 hours and do not appear to adhere. This may be due to the lack of adhesion motifs present in the membrane constituents. Adhesion does, however, appear to be observed along the curved edges of the membrane, indicating some potential in this structure should it be more thoroughly optimised. It is possible that curvature of these membranes may aid with cell adhesion.

Beyond membrane formation, it may also be stated from this work that future work using extrusion printing should seek to employ a syringe pump-based system for the extrusion of low viscosity fluids, as opposed to a pneumatic device. The variance in flow rate observed between experiments on different days of experimentation indicate poor reliability of pneumatic devices when using low viscosity inks. A range, for example, of 30-200 kPa was required to initiate extrusion of GO through the outer nozzles, with no other parameters – including loading volume within the cartridge – changing. A syringe pump, however, would reliably extrude at a defined flow rate, facilitating more reproducible experiments.

There are possible pathways towards the successful application of this membrane. One such pathway of exploration may be the inclusion of more proteins which lend themselves to mechanical robustness. Native biological membranes, for example, consist of different types of collagens which improve their mechanical properties. Laminin, too, may be present which may act as a cell adhesion motif. By including these biomolecules, it may be possible to improve both the mechanical and biological properties of the membranes. However, doing so increases the complexity of design when preparing these molecules. As opposed to correctly balancing the reagents of a two-component system, introducing collagen and laminin would increase the possible permutations of weight ratios in different formulations.

To maintain a two-component system, it may be possible to introduce a scaffold to support the membrane after formation. This scaffold should ideally consist of a biologically compatible material which displays good elasticity and mechanical strength, so as to reinforce the structure of the GO-ELP membrane but not diminish its elastic properties. This scaffold could, ideally, be 3D printable, so that precise, defined architectures may be fabricated. The membrane would then be printed atop this scaffold, adhering through electrostatic forces, and so the scaffold should be hydrophilic in nature to facilitate this adsorption of the aqueous components. It is also envisioned that the GO-ELP membrane is formed directly within the pores of the scaffold, adhered by capillary or electrostatic forces to the walls. In doing this, the

membrane is divided into smaller sections, and less strain is placed on the membrane and transferred to the more robust scaffold.

It may be the case that the second methodology here is preferable, in that a porous scaffold is first soaked with GO before ELP is added. In this case, both an ELP-rich and GO-rich wall is formed, similar to the liquid-in-liquid extrusion method. Should this scaffold itself possess a curvature, this would present and ELP-rich wall with a defined curvature, which would likely improve cell adhesion and proliferation. Additionally, owing to the resolution of current 3D printers, it may be possible to produce scaffolds with nanoscale pores and thickness, facilitating the transfer of the ultrathin membrane to a structure which may be handled and manipulated without damaging the membrane. These scaffolds, too, could be designed to be tubular, representing a model of biological vasculature and possibly acting as permeability models for native basement membranes, such as modelling drug transport across the BBB.

4.8 Experimental

4.8.1 Co-assembling Peptide Systems

Peptide amphiphiles were synthesised in-house by solid-phase peptide synthesis. Successful synthesis and purity were confirmed by GCMS and HPLC. Credit is given to Dr. Bapan Pramanik for synthesis of PAs. PAs were dissolved in HEPES buffer at 2% w/v. PAE_3 was solubilised using NaOH (1.0 M) at 10 µL aliquots until pH 7.4 was achieved and the solution was transparent. PA solutions were used no later than 24 hours after preparation.

The IK24 ELP was synthesised by Technical Proteins Nanobiotechnology (Valladolid, Spain) through recombinant protein expression. ELP was stored at 4 °C until use. ELP solutions (2% w/v) were prepared in HEPES buffer at room temperature. Solutions were stored at -20 °C for prolonged storage ($\leq$ 2 months).

Graphene oxide (0.4% w/v, Merck, Catalogue No. 777676) was prepared by dilution in ultrapure water to the desired weight percentage. Brief sonication of dispersions was performed immediately before use.

4.8.2 PDMS Preparation

PDMS was prepared using Sylgard-184 elastomer base (Dowsil, USA) and crosslinker at a 10:1 mass ratio. Reagents were mixed together before being poured into a desired mould. The mixture was then incubated at 37 °C overnight to cure.

4.8.3 Uniaxial Extrusion

Extrusion printing was performed on an INKredible+ extrusion bioprinter (Cellink, Sweden) using a 30 G nozzle (Cellink, Catalogue No. KT0000002002). CAD files were designed using TinkerCAD (AutoDesk, USA) and sliced using Slic3r software available on the HeartWare bundle (Cellink). The gcode of sliced files was manually edited using a text editor.

3 mL of IK24 ELP (2% w/v) was added to a 3 cc cartridge (Cellink, Catalogue No. CSC010300102) and heated to 30 °C in the printhead. GO dispersion (0.1% w/v) was added to a 32 mm petri dish with a PDMS base, with sufficient GO to coat the base of the dish, and heated to 30 °C. Following printing, GO was aspirated through manual pipetting and simultaneously replaced with PBS, to maintain the tubular membrane.

4.8.4 Coaxial Extrusion

A 28-22 stainless steel coaxial nozzle (Ramé-Hart, USA) was utilised for coaxial printing. The printing setup was identical to uniaxial extrusion, except here instead of a GO bath, either a syringe was filled with a GO dispersion and attached to a syringe pump or a 3 cc cartridge was filled with GO and attached to printhead 2 of the INKredible+ bioprinter.

4.8.5 Triaxial Extrusion

For triaxial extrusion, a 26-20-17 stainless steel coaxial nozzle was adapted. Here, printhead 1 was loaded with ELP (2% w/v, 3 mL) and fed to the second nozzle. Printhead 2 fed air through the central nozzle, and an external syringe pump fed GO to the outer nozzle.

4.8.6 Scanning Electron Microscopy

Scanning electron microscopy was performed on a JEOL 7000F FEG SEM. Samples were prepared for SEM through sequential ethanol drying. Firstly,

samples were immersed in paraformaldehyde (4% w/v) for 20 minutes. Samples were then subjected to sequential ethanol drying at the following concentrations: 20, 50, 70, 80, 90, 96, and 100% v/v ethanol, with 2 washes for 3 minutes at each concentration. Following a 100% ethanol wash, samples were subjected to critical point drying and subsequent iridium coating (10 nm).

4.8.7 Optical Light Microscopy

Optical microscopy images were captured on an AmScope ME508 series light microscope and attached AmScope FMA050 adapter.

4.8.9 Polarised Light Microscopy

Polarised light microscopy images were captured on an AmScope ME508 series light microscope and attached AmScope FMA050 adapter.

4.8.10 Ellipsometry

Samples were prepared for ellipsometry through coaxial extrusion onto a PDMS substrate. Excess fluid was removed through wicking and the sample was not allowed to dry before measurements to prevent shrinking.

Ellipsometry was performed using an Accurion EP4 ellipsometer and data modelled on EP4Model software. Credit is given to Dr. Richard Cousins for performing Ellipsometry and modelling data.

4.8.11 Endothelial Cell Culture

hUVECs were sourced from the ATCC and used from passage 6-10. Cells were cultured using the EGM-2 BulletKit (Lonza, Catalogue Number CC-3162). Cells were cultured under standard conditions (37 °C, 5% CO_2) until 80% confluent at which time they were passaged and split at a 1:3 ratio. Media changes were performed once every 2 days.

For staining, CellTracker Green CMFDA (ThermoFisher, Catalogue Number C2925) was diluted 1:1000 in sterile PBS and mixed thoroughly. Media was then aspirated from culturing cells in a T25 flask and replaced with 1 mL staining solution. Cells were incubated at 37 °C for 30 minutes before being detached for seeding.

For seeding, cells were resuspended in 1 mL of media at the end of passaging. Cells were then seeded atop printed samples in a 12 well plate at a number of 137,000 cells per well.

4.8.12 Confocal Microscopy

Confocal microscopy was performed on a Leica SPE point-scanning microscope using a 488 nm laser. Images were obtained using the Leica LasX software.

4.9 Bibliography

1. Capito, R. M.; Azevedo, H. S.; Velichko, Y. S.; Mata, A.; Stupp, S. I., *Science* **2008,** *319* (5871), 1812-1816.

2. Barrett, D. W.; Okesola, B. O.; Costa, E.; Thrasivoulou, C.; Becker, D. L.; Mata, A.; Deprest, J. A.; David, A. L.; Chowdhury, T. T., *Prenat. Diagn.* **2021,** *41* (1), 89-99.

3. Hedegaard, C. L.; Collin, E. C.; Redondo-Gómez, C.; Nguyen, L. T. H.; Ng, K. W.; Castrejón-Pita, A. A.; Castrejón-Pita, J. R.; Mata, A., *Adv. Funct. Mater* **2018,** *28* (16), 1703716.

4. Majkowska, A.; Inostroza-Brito, K. E.; Gonzalez, M.; Redondo-Gómez, C.; Rice, A.; Rodriguez-Cabello, J. C.; Del Rio Hernandez, A. E.; Mata, A., *Biomacromolecules* **2023,** *24* (10), 4419-4429.

5. Wu, Y.; Okesola, B. O.; Xu, J.; Korotkin, I.; Berardo, A.; Corridori, I.; di Brocchetti, F. L. P.; Kanczler, J.; Feng, J.; Li, W.; Shi, Y.; Farafonov, V.; Wang, Y.; Thompson, R. F.; Titirici, M.-M.; Nerukh, D.; Karabasov, S.; Oreffo, R. O. C.; Carlos Rodriguez-Cabello, J.; Vozzi, G.; Azevedo, H. S.; Pugno, N. M.; Wang, W.; Mata, A., *Nat. Commun.* **2020,** *11* (1), 1182.

6. Wu, Y.; Fortunato, G. M.; Okesola, B. O.; Brocchetti, F. L. P. D.; Suntornnond, R.; Connelly, J.; De Maria, C.; Rodriguez-Cabello, J. C.; Vozzi, G.; Wang, W.; Mata, A., *Biofabrication* **2021,** *13* (3), 035027.

7. Luan, B.; Huynh, T.; Zhao, L.; Zhou, R., *ACS Nano* **2015,** *9* (1), 663-669.

8. Del Giudice, F.; Shen, A. Q., *Curr. Opin. Chem. Eng.* **2017,** *16*, 23-30.

9. Naficy, S.; Jalili, R.; Aboutalebi, S. H.; Gorkin Iii, R. A.; Konstantinov, K.; Innis, P. C.; Spinks, G. M.; Poulin, P.; Wallace, G. G., *Mater. Horiz.* **2014,** *1* (3), 326-331.

10. Jiang, W.; Yao, X.; Zhong, J.; Ouyang, Z.; Shen, J.; Qiu, Y.; Zeng, Y., *Mater. Today Bio.* **2024,** *26*, 101074.

5. Ultrathin Self-assembled Membranes for Endothelial Tissue Engineering

5.1 Introduction

Having determined that it is possible to engineer the GO-ELP system to yield membranes of a thickness within the range of native basement membranes in biological systems, it now remained to be demonstrated that these may be successfully applied to a tissue engineering or cell culture setting. These structures, determined by ellipsometry to be around 100 nm in thickness, are unable to support their own weight and form a robust tube as previously observed with more thick membranes.[1] Basement membranes in biological systems are not standalone structures; typically, they are synthesised in the presence of a supporting structure. The glomerular basement membrane in the kidney, for example, forms in the presence of epithelial podocytes and the vascular endothelium.[2] Furthermore, other thin structures in the body, such as lung alveoli, tend to exist as discrete units as opposed to a singular large structure. Using this alveolar structure as inspiration, it was proposed that a biocompatible support structure should be used to maintain the tubular shape of the ultrathin membranes.

Recent developments in the fabrication of microporous tubular structures made from melt-electrowritten (MEW) poly(caprolactone) (PCL) presented an excellent opportunity as scaffolds for ultrathin membrane formation.[3] These tubular structures have been shown to mimic the mechanical properties of human blood vessels, and may be fabricated on a biologically-relevant size scale.[4] A combination of VAMS and MEW has already been used to integrate the PCL tubes with GelMA to fabricate a thick, vascular-like structure with bifurcated tubes and the ability to support multi-cellular culture.[5] However, the GelMA structures were far thicker than the GO-ELP membranes fabricated in

the previous chapter, with a thickness of roughly 1 mm. It was decided that these PCL scaffolds would be ideal supports for the ultrathin GO-ELP, owing to the agreeable biocompatibility and mechanical properties of PCL.

5.2 Scope and Objectives

It was decided that a model should be developed which facilitated the use of these ultrathin membranes in a biomedical setting. Knowing that these membranes can support endothelial cell growth as self-supporting tubes,[6] it was believed that a similar application could be found with the ultrathin membranes. A distinct advantage being that a membrane of around 100 nm thick would be a closer mimic of native basement membranes upon which endothelial cells grow in vivo. By using a far thinner membrane as support for endothelial cell growth and vascular tissue engineering, it was hoped that diffusion of nutrients and the overall permeability of the membrane would be closer to that of native tissue.

Currently, however, the ultrathin membranes are difficult to handle and manipulate, making their integration into a tissue engineering application a great challenge. To overcome this, the use of a support structure – upon which the membrane may be formed – was hoped to be adopted to facilitate handling. Such a support structure should itself be robust enough to be handled but maintain a flexibility and softness that resembles vascular tissue. The membrane formation should not be impeded by the scaffold, and there should ideally be no scaffold blocking either face of the membrane. The membrane should be "draped" between pores present in the scaffold. Finally, the scaffold should have the capacity to be fabricated as a tube, so that a vascular structure may be formed.

Succinctly, the objectives for this chapter are to demonstrate the formation of the ultrathin GO-ELP membrane on a tubular scaffold, demonstrate the robustness of this construct through perfusion studies, and ultimately demonstrate the adhesion and survival of endothelial cells on the membrane. Achieving such would arguably provide a platform for future research in vascular tissue engineering, such as artificial blood-brain barriers or lung alveoli.

5.3 Fabrication of Ultrathin Membranes on Resin Scaffolds

Initial testing focussed on the ability to successfully fabricate the GO-ELP membrane within the pores of a larger structure. Several strategies were employed to investigate this. Initially, it was attempted to use the coaxial extrusion system to deposit the ultrathin membrane on the upper side of a porous structure. However, incomplete surface coverage, membrane breakage, and poor membrane formation were repeatedly observed when using previously optimised printing parameters, indicating the unsuitability of this methodology. As the coaxial extrusion system relies on the constant drag from the printing platform to continuously form the ultrathin membrane without ruptures or droplet formation on a hydrophobic surface, attempting to print atop a surface containing macroscopic pores is unlikely to yield successful membrane formation. Furthermore, this method would likely be unfeasible in a tubular structure and was not pursued any further. An immersion method was determined to be the most likely to yield successful membranes.

Understanding this, the ability to form the GO-ELP membrane within the pores of a larger structure was investigated. The overarching concept was viewed as similar to coaxial extrusion, wherein the volume of GO available for membrane formation is drastically reduced in comparison to a liquid-in-liquid system, therefore limiting the maximum thickness of the final membrane. This concept was confirmed on a larger scale using a surface fabricated using digital light processing (DLP) with a commercial photocurable resin. Despite the predicted hydrophobicity of the resin, it was observed that the aqueous GO dispersion may be suspended within the honeycomb-shaped pores by adherence to the walls (Figure 45A, Figure 45B). This suspension is not constant, however, and not all pores are covered owing to the hydrophobic nature of the resin preventing wetting. The addition of the ELP solution then results in the formation of the GO-ELP membrane within these pores. The GO dispersion is not displaced from the pores by the fluid forces of ELP addition, indicating that this concept may be successful on a smaller scale with pores of a lower volume.

SEM micrographs (Figure 45D) revealed that the surface of the membrane was topographically similar to the membranes formed in a liquid-in-liquid system, indicating that the mechanism of formation and final structure of the membrane

is unchanged. A somewhat porous nature is also observed, so it was believed that the membranes formed here should maintain properties in terms of permeability, a key parameter for biological membranes.

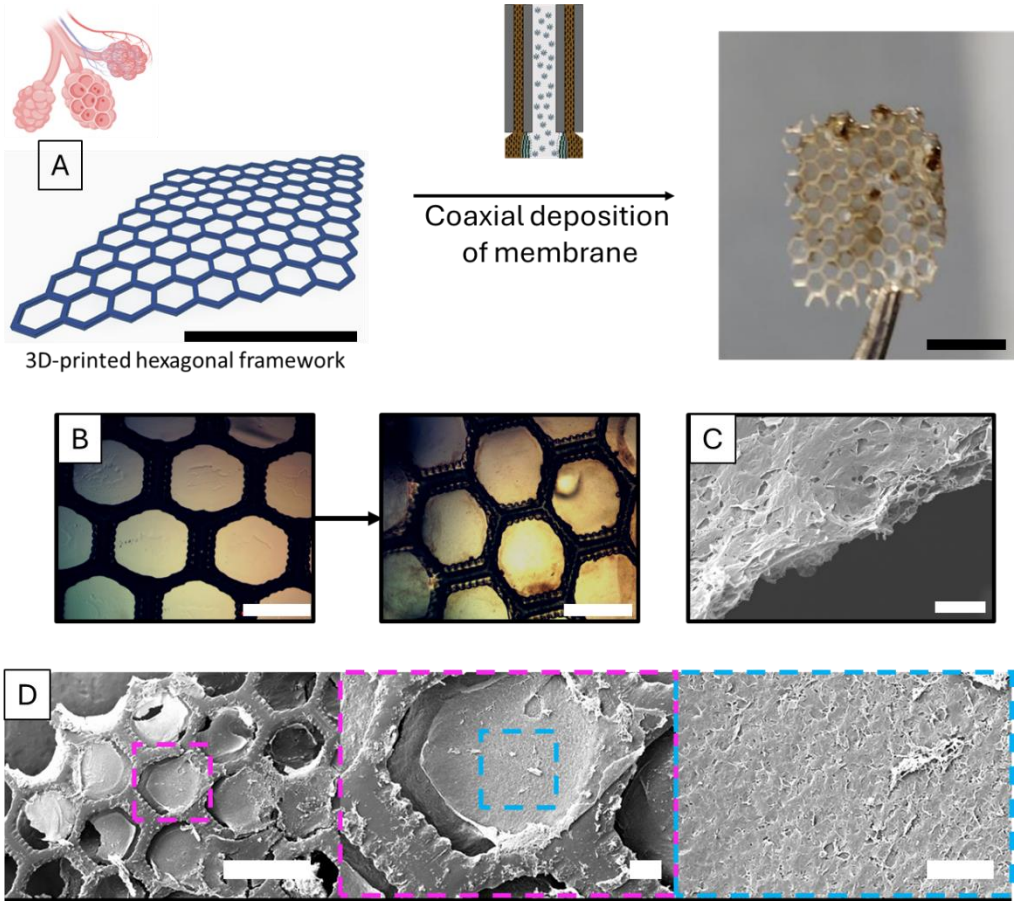

Figure 45: Formation of GO-ELP membranes on a 3D-printed support scaffold. ***A)*** *schematic of formation. A hexagonal scaffold is 3D printed using commercial resin in a DLP-based system. The GO-ELP membrane is then coaxially printed atop this scaffold and may now be handled. Scale = 5 mm.* ***B)*** *Optical microscope images of the hexagonal pores (left) before and (right) after membrane formation. Scale = 1 mm.* ***C)*** *SEM image of the membrane cross-section. Scale = 10 µm.* ***D)*** *SEM images of the membrane face confirming that the membrane is successfully formed in the pores of the scaffold. Scale (left to right): 500 µm, 100 µm, 50 µm*

The volume of each pore was found to be 0.0013 cm^3, with just 1 mm of thickness to contain the GO dispersion. This is a far greater thickness and volume than that which would be provided by the outer needle in the coaxial extrusion system, and this is reflected in the overall thickness of the observed membrane at roughly 5 µm (Figure 45C). While this is thicker than has been previously observed in liquid-in-liquid systems, this structure served as a good

proof-of-concept, indicating that it is indeed possible to form a co-assembled GO-ELP membrane within the pores of a support structure, indicating that preferable mechanical properties may be integrated with the bottom-up control of the membrane thickness. Using a support structure with a reduced overall thickness was, therefore, hoped to yield the ultrathin membranes observed in the coaxial extrusion system.

Moving forwards, it was not envisioned that commercial photopolymer resins would be a viable option for a biomedical implant. These resins typically contain free acrylates after curing and are likely to display cytotoxic behaviours as a result.[7] Removal of these monomers to a level at which cytotoxicity is not significantly observed is possible,[8] but the overall brittleness of many of these resins renders them unsuitable for vascular applications in pulsatile flow. On the other hand, biocompatible commercial resins with a greater elasticity are available and, with affordable commercial 3D printers advertising layer heights of 50 μm and pixel sizes of 18 μm, there is certainly scope for the future development of SLA scaffolds to act as supports for the GO-ELP membrane. Here, however, PCL scaffolds were chosen as their suitability for vascular tissue engineering has already been characterised,[9] and PCL is already an FDA-approved material for implantation.

5.4 Membrane Formation on MEW PCL Grids

5.4.1 Membrane Formation and Imaging

MEW PCL squares were then substituted in for the DLP resin scaffolds. Two structures were used, one consisting of 50 layers of pores with a 100 μm diameter and the other consisting of 15 layers of 50 μm diameter pores. Each layer consists of fibres of roughly 3 μm thickness, and these scaffolds therefore range from 150 to 45 μm thick. In both cases, it was observed that the hydrophobicity of the PCL scaffolds prevented complete wetting of the surface and sufficient filling of pores with GO. This is likely much more pronounced than on the DLP resin grid as the surface tension of the GO dispersion will likely prevent droplets entering the smaller hydrophobic pores – an effect less present in the larger pores of the DLP tubes. It was observed, however, that many pores were sufficiently filled with the GO dispersion for membrane formation to be

attempted. By adding ELP solution dropwise to one face of the scaffold, membrane formation may be initiated (Figure 46A).

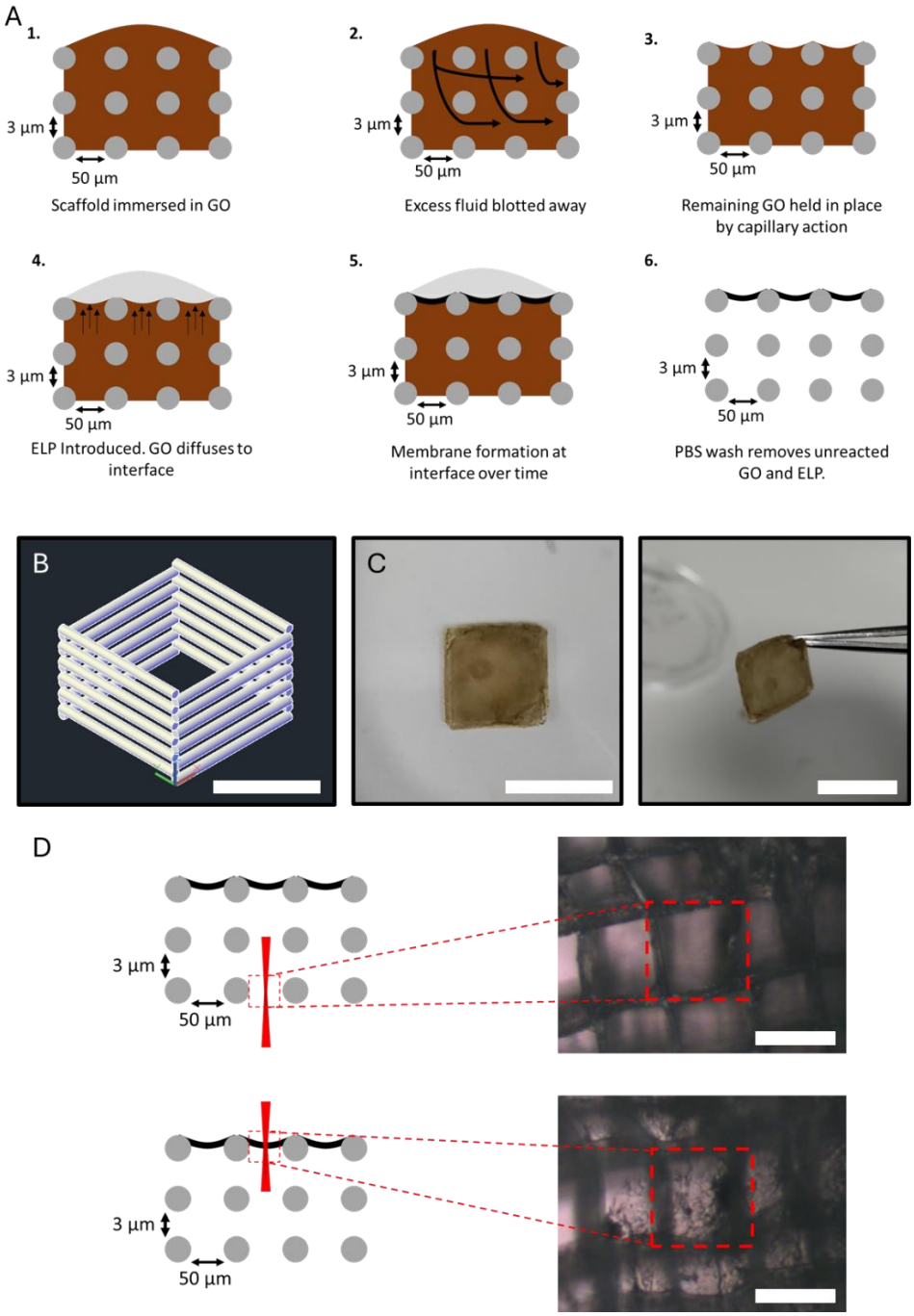

Figure 46: Formation of GO-ELP membrane in the pores of a PCL scaffold. ***A)*** *Schematic of the membrane fabrication method.* ***B)*** *CAD image of a single pore within the scaffold, with each rod representing a PCL fibre. Scale = 50 µm* ***C)*** *Camera images of the GO-ELP-PCL structure, demonstrating the ability to easily handle the scaffold using forceps. Scale = 1 cm.* ***D)*** *AFM images demonstrating the fabrication of the membrane on just the upper side of the scaffold. Scale = 50 µm.*

The GO-ELP-PCL construct fabricated in this way could be handled and manipulated with ease using forceps (Figure 46C). It was not destroyed by the application of reasonable force and displayed some degree of elasticity and flexibility. The mechanical properties of these MEW PCL scaffolds have previously been reported as roughly 0.5 MPa,[3] and it was not expected that the presence of the GO-ELP membrane would significantly impact these, as it alone is incredibly fragile. Immediately, the ability to handle the GO-ELP is a great improvement upon the standalone ultrathin membranes fabricated previously, which could not be moved without causing severe damage. This represents a step towards feasibility in biomedical application for the ultrathin membranes.

Further analysis of the fabricated structure by AFM imaging revealed that the membrane forms on a single face of the PCL scaffold, as opposed to spanning the entire depth of the structure (Figure 46D). This indicates that the thickness of the membrane is restricted here, as it is with coaxial printing, by the amount of GO present. The only volume of GO available to form the membrane is within the pores of the scaffold. For the scaffold with 50 μm pores, there is roughly 7.5 x 10^{-8} cm^3 volume per pore, severely restricting the amount of GO available to interact with ELP and limiting the membrane thickness. Additionally, the formation of a single, thin membrane on one face of the scaffold indicates that the mechanism of formation is relatively unchanged from that previously reported for the liquid-in-liquid system. That is, an initial barrier is formed at the interface between GO and ELP. Very little material diffuses across this barrier, but the diffusion of materials to the barrier triggers the growth of the membrane. This would also indicate that one side of the membrane is ELP-rich, while the other side is GO-rich.

SEM micrographs of the PCL scaffolds after treatment with GO-ELP, GO alone, and ELP alone (Figure 47) lend evidence to the theory that the membrane observed is a result of co-assembly between the ELP and GO, rather than simply being trapped GO dispersion or ELP solution within the pores. Here, a membrane with good coverage is only observed when ELP has been deposited atop a GO-filled scaffold. Some macroscopic holes are observed, but overall coverage is good.

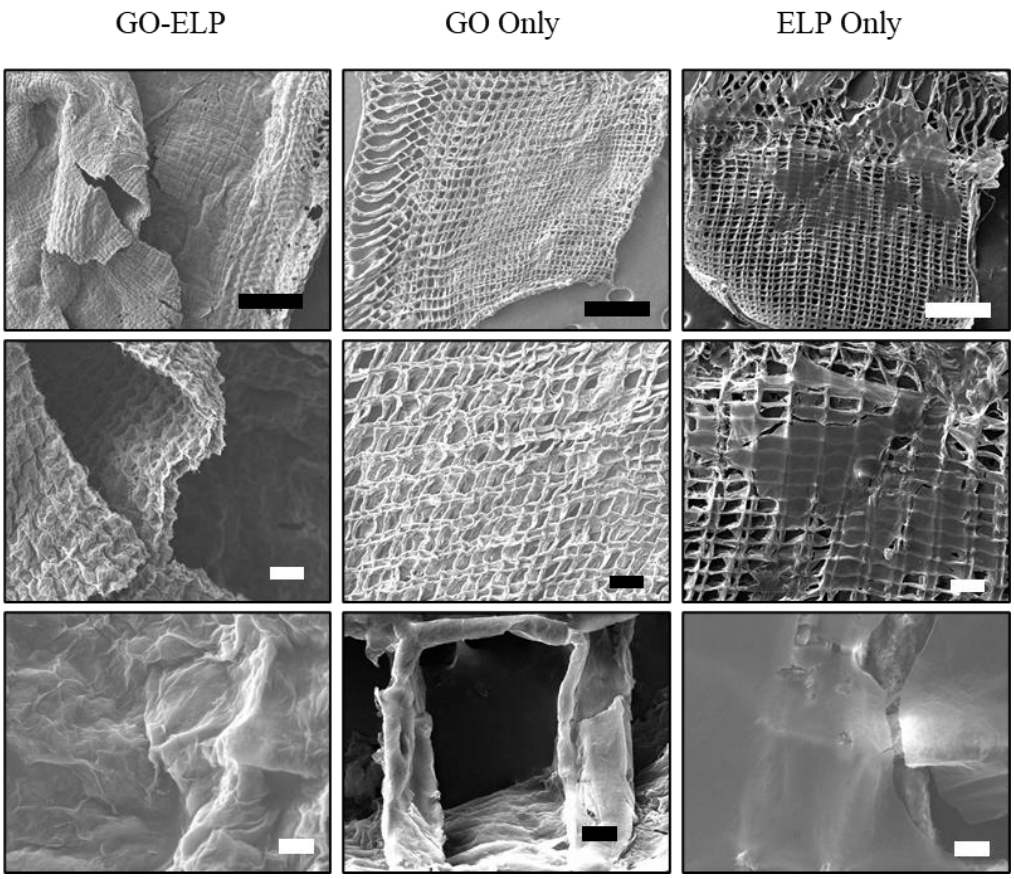

Figure 47: SEM Micrographs of PCL scaffolds (50 µm pores) after treatment with GO and ELP. Where GO and ELP are used together, a scaffold-spanning membrane is observed which coats the pores of the scaffold. In the case where only a single reagent is used, no scaffold-spanning membrane is observed. For GO only, coating of the PCL fibres is observed, but no membrane. Scale (top to bottom): 500 µm, 100 µm, 10 µm.

In the case where just GO is applied prior to imaging, no membrane formation is observed the pores of the scaffold remain uncovered and empty. Some coating of the PCL fibres is observed, and this may be due to the hydrophobic interactions of GO sheets with the PCL, causing slight aggregation on the fibres. Nonetheless, it is not possible here to cover the pores of the scaffolds using GO alone.

Interestingly, when ELP alone is applied before imaging, an incredibly thin membrane is observed across some of the pores, with some residue or evidence of membrane formation present in all pores – indicating that, at some point, this membrane may have covered all pores and was destroyed in the drying process. The presence of this membrane may possibly be explained as a result of paraformaldehyde (PFA) crosslinking.

In this system, ELP in its globular state in aqueous media is added to the PCL scaffold. Owing to the narrow pore width and hydrophobicity of the scaffold, both the aqueous media and the ELP are unable to enter the pores. A wicking step prior to SEM preparation removes almost all the aqueous media and ELP. This scaffold is then immersed in PFA and the remaining ELP is covalently crosslinked. This may occur through the amine present on the lysine side chain in the VPGKG pentapeptide, following known crosslinking mechanisms (Figure 48).[10] As there is no media or ELP in the pores of the scaffold, the resultant structure is a thin membrane across the surface of the PCL. While this process has inadvertently formed an ultrathin membrane, the use of PFA to crosslink the ELP would likely result in the presence of PFA when introducing biological material, which may negatively affect cell growth. However, should an ELP with, for example, an acrylate moiety be used and, instead of PFA, UV light was used to crosslink the polymers, it may be viable to produce crosslinked ultrathin membranes in this manner. Here, however, focus remained on the supramolecular, co-assembled GO-ELP system.

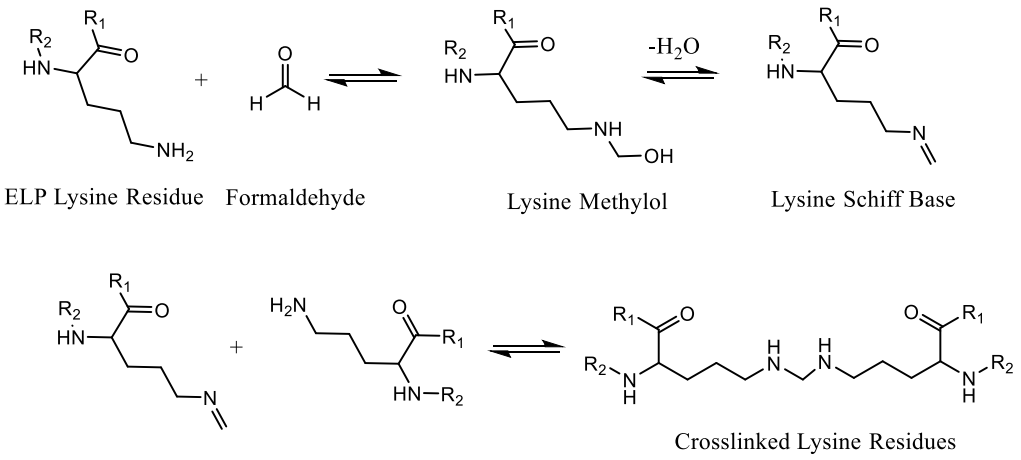

Figure 48: Proposed lysine residue crosslinking scheme. PFA reacts with the lysine side chain to yield a Schiff base, which then reacts with a second lysine to covalently crosslink the two residues.

5.4.2 Membrane Mechanical Characterisation

It was next sought to characterise the material properties of the GO-ELP membranes formed on the PCL scaffolds. AFM nanoindentation was used to probe surface roughness and the Young's modulus of the ELP-rich side of the membrane. These factors are important for biological applications, as surface roughness may lead to improved endothelial cell adhesion while Young's

modulus may indicate whether the membrane would be suitable to withstand blood flow.[11] As the GO-rich side of the membrane is not presented on an available surface, it was not possible to determine the surface roughness or Young's modulus of this side. Further to AFM nanoindentation, cross-sections of the membranes were also imaged using focussed electron gun (FEG) SEM to measure thickness.

Nanoscale investigation of the membrane by SEM and AFM revealed further information regarding its nature (Experimental 5.10.4). Surface roughness was seen to be dependent upon the concentration of GO used for membrane formation (Figure 49). In the case where 100 μm, there did not appear to be a direct correlation, although it may be the case that, in pores of this size, the membrane is too elastic to obtain a reliable measurement. Difficulty in obtaining any measurement at all was observed if the AFM tip was placed in the centre of the pore, and measurements were subsequently taken from the corner of pores to reduce any movement of the membrane. For 50 μm pores, there appears to be an increase in roughness as the GO concentration decreases. This may be because, with a lower GO concentration, there is less electrostatic attraction for the ELP and less ELP is present as a result. The roughness therefore closer reflects the natural roughness of GO. Indeed, this series appears to trend towards the reported Ra values of GO at 44 – 63 nm.[12] This control over surface roughness is an important factor for endothelial tissue engineering. It has been reported previously that hUVECs are sensitive to nanometre-scale roughness changes, and that an increase in surface roughness may lead to improved proliferation.[11]

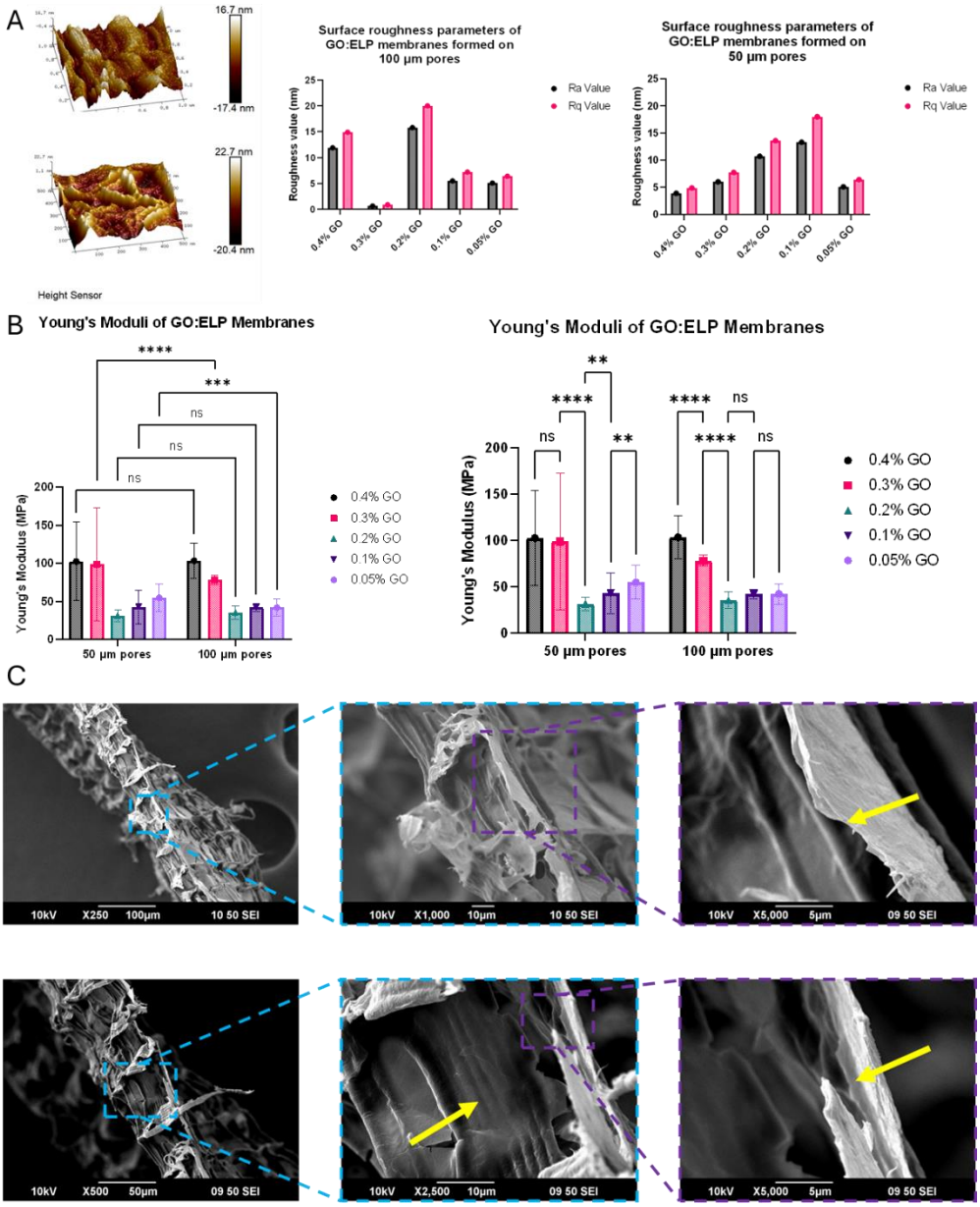

Figure 49: Characterisation of GO-ELP membranes formed in the pores of a PCL scaffold. ***A)*** *Surface roughness measurements and surface maps for GO-ELP membranes determined using atomic force microscopy (AFM) nanoindentation.* ***B)*** *Young's modulus of membranes determined using AFM nanoindentation. Statistical significance was determined using ordinary one-way ANOVA.* ***C)*** *Cross-sectional SEM images of the membrane formed within the scaffold. Sequential magnifications are shown to demonstrate the ultrathin membrane which forms across the opening of the pores in the scaffold, while also leaving a hollow pore underneath.*

Beyond cell culture, surface roughness plays an important role in blood rheology and haemodynamics in vivo.[13] Should these structures ever be implanted as acellular stents, for example, their effect on these should be known. Atypical blood flow may result in atherosclerosis and damage to the vessel wall.[14] It may be assumed that flow dynamics which damage arterial walls may

damage the GO-ELP membrane too, therefore making haemodynamics relevant here. These flow dynamics may also affect endothelial cell growth, with oscillatory shear stress, steady shear stress, and turbulent shear stress all affecting gene expression and cell morphology.[15] Control over the surface roughness by controlling the ratio of reactants in this system may lead to improved control over the haemodynamics and subsequent tissue engineering applications. Typically, however, surface roughness of native tissue ranges in the micrometre scale, so the nanometre Ra values observed here may be negligible.

The Young's modulus of each membrane also appears to be influenced by the concentration of GO used in its formation (Figure 49). In general, a greater GO concentration yields a harder membrane, although it is not a direct correlation. Modulus values are similar across pore sizes, indicating that it is most likely to be the GO concentration that affects this characteristic. This is likely because GO itself has a high Young's modulus, typically greater than 290 GPa,[16] so greater concentrations will increase the overall modulus. Elastin, for comparison, typically ranges from 0.2 – 1.1 MPa.[17] The overall values for Young's modulus were consistently greater than those reported for human femoral artery (12 MPa), internal mammary artery (8 MPa), and the saphenous vein (4.2 MPa), although far closer to these values than current stent materials Dacron (900 MPa) and Teflon (500 MPa).[18] This suggests that these GO-ELP membranes may be closer mimics of natural vascular tissue than current technologies. Furthermore, a slightly greater Young's modulus may be beneficial for cell growth, with previous studies demonstrating that an increase in Young's modulus on substrates for hUVEC culture results in more cell spreading and a less rounded morphology.[19]

SEM imaging also supports the hypothesis derived from AFM imaging that a membrane is observed to form on the face of the scaffold on which ELP is added, leaving behind a hollow space in the rest of the scaffold. The membrane remains "draped" over the pore (Figure 49). Importantly, this indicates that the ultrathin nature of the membrane reported in the coaxial system is maintained here, maintaining the physiologically relevant thickness of natural basement or elastic membranes. The layer-by-layer formation mechanism also appears to be

preserved in these structures, representing a good translation from the liquid-in-liquid system. To investigate further the molecular arrangement of the ELP and GO within membrane, XPS and ToF-SIMS depth profiling analyses were used.

5.4.3 Surface Chemistry of GO-ELP membranes

XPS depth profiling confirmed the presence of an ELP-rich side of the membrane. This was then quickly, although not immediately, lost as the membrane was probed deeper, indicating some mixing of the two components at the interface as opposed to the formation of an impermeable barrier (Figure 50). This profile was also indicated using ToF-SIMS, which revealed a decrease in the ratio of ELP deeper into the membrane (Experimental 5.10.6). Although any membrane draped over the pores of the scaffold appeared to have been destroyed in sample preparation, a gradual decrease in nitrogenous signals is observed on membrane formed on PCL fibres. Such data is in line with previously reported SANS data which predicted the presence of GO-ELP lamellar-like structures, wherein the ELP is interlinked around the edges of GO flakes within the membrane, with the flakes becoming more GO-rich towards the side where GO was added and more ELP-rich towards the side where ELP was added.[6]

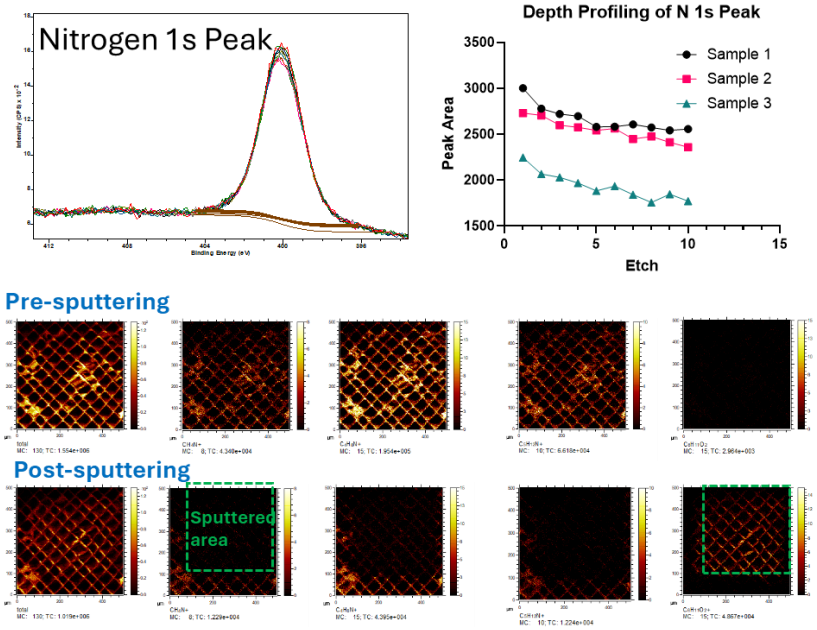

Figure 50: XPS (top) and ToF-SIMS (bottom) depth profiling of the GO-ELP membrane formed on PCL scaffolds. A gradient in nitrogen-containing compounds is observed deeper into the membrane, indicating intercalation of the ELP molecules with GO flakes.

For the XPS data, there is no source of the nitrogen 1s peak other than the ELP as neither GO nor PCL contain nitrogen. Similarly, none of the washing or dehydration steps introduce nitrogenous compounds. Therefore, it can be said that the nitrogen peak must be the ELP and therefore the decrease in peak area must correlate to a decrease in ELP concentration. The same is also true of the ToF-SIMS measurements, wherein nitrogenous signals must be present as a result of the ELP. There may be, however, nitrogenous compounds which occur during the degradation of PCL over time, such as carbodiimides. However, the degradation rate of PCL is incredibly slow, and it is unlikely that carbodiimides would be present in fresh, washed samples.

5.4.4 Plasma Surface Treatment of PCL

It now remained to improve the overall adherence of the GO and ELP to the PCL to improve pore coverage and overall membrane formation. As PCL is a hydrophobic polymer, it is likely that there is poor wetting of the pores and incomplete filling with GO. It was theorised that by making the PCL more hydrophilic it would significantly improve the wetting and pore filling, resulting in a more complete membrane. Surface modification with oxygen plasma was chosen, having previously been reported to improve the hydrophilicity, wettability, and cell adhesion in PCL constructs in comparison to, for example, argon or nitrogen plasma treatments.[20]

This treatment was observed to decrease the contact angle of GO dispersions on the PCL scaffold, with far greater spreading and pore filling predicted as a result (Figure 51B). Destruction of the nanofiber structure was also not observed, indicating the suitability of this processing. It was also possible to perform this treatment on tubular membranes. For the membrane formation, improved coverage of the scaffold was observed following the plasma treatment, indicating more reliable and robust membrane formation. Such a property is vital for the correct function of vascular structures, with holes resulting from incomplete membrane formation drastically reducing the viability of these structures.

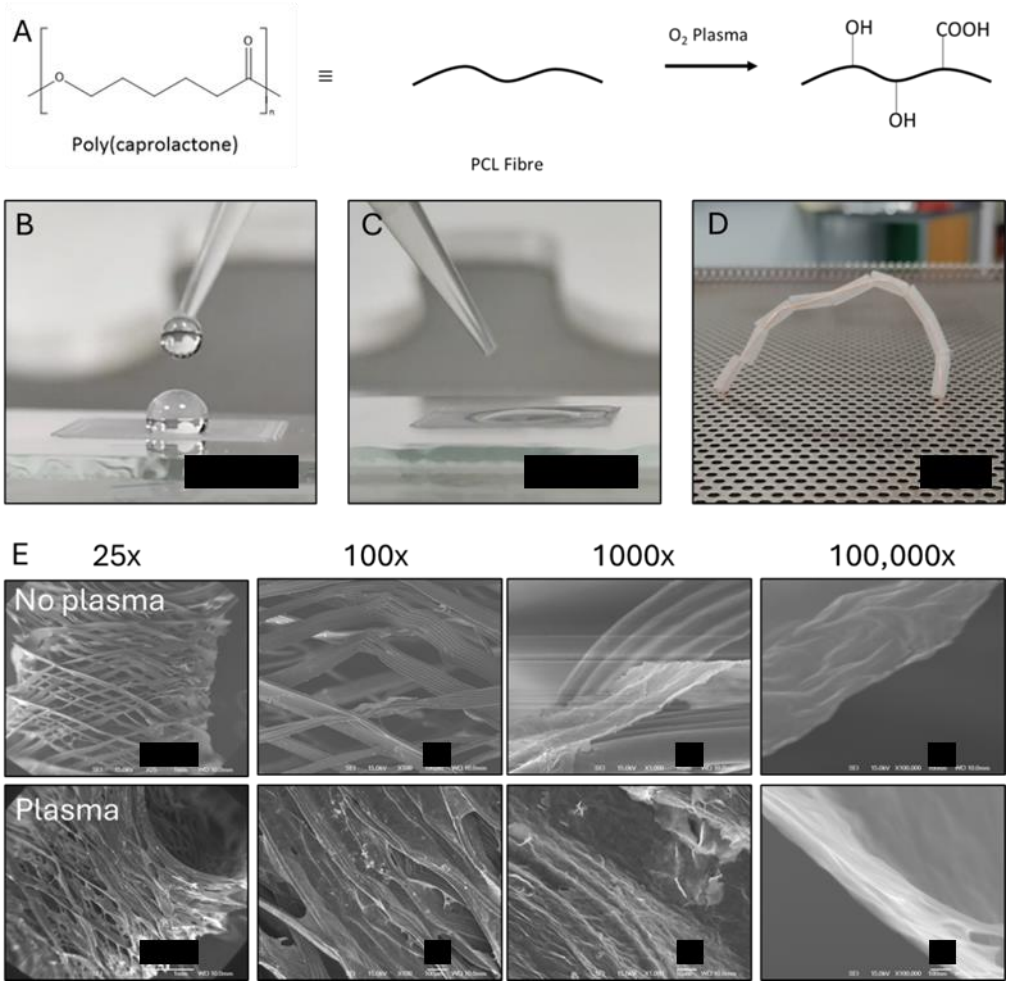

Figure 51: Plasma Treatment of PCL scaffolds. ***A)*** *General scheme of plasma surface treatment to introduce hydrophilicity to the polymer.* ***B)*** *Deposition of a water droplet atop untreated PCL. Scale = 5 mm.* ***C)*** *Deposition of a water droplet atop plasma treated PCL. Scale = 5 mm.* ***D)*** *method of plasma treating a batch of 10 tubular scaffolds by threading the lumen with copper wire which is linked to a grill. In the absence of an immobilisation technique, tubular scaffolds were lost or damaged during the etching process. Scale = 10 mm.* ***E)*** *SEM micrographs of GO-ELP membranes on PCL scaffolds either with or without plasma treatment demonstrating improved membrane formation following plasma treatment. Scales (left to right): 1 mm, 100 µm, 10 µm, 100 nm.*

Plasma treatment was observed to be vital for successful membrane formation in the case of tubular structures. Where no hydrophilic groups are present in the case of the untreated PCL, minimal pore coverage by the membrane is observed (Figure 51E). It may be the case that, as these membranes are formed under flow, there is insufficient outward diffusion of the GO dispersion to overcome the hydrophobic repulsion of the PCL, and no dispersion enters the pores. Some GO may coat the PCL fibres owing to the hydrophobic regions of GO, but the

bulk dispersion flows through the lumen of the tube without entering the pores. There is no wicking step here, as with the flat membranes, which may have forced the GO dispersion into the pores and facilitated membrane formation. Here, some thin membrane formation was observed, but only on the PCL fibres and not across the pores. In the case of plasma treated PCL, greater pore coverage by the GO-ELP membrane was observed (Figure 51E). Improved wetting will have facilitated entry of the GO dispersion into the pores. It also appears that the thickness of the membrane has not been impacted, further indicating the suitability of plasma treatment for the PCL scaffolds. The hydrophilicity was observed to last for several days in air before weakening, and lasted several weeks when stored in ethanol – a known effect of polar liquids on plasma-treated surfaces.[21]

Other possible treatments to improve the hydrophilicity of the PCL scaffolds may have been explored. For example, it is possible to soak PCL in a 5 M NaOH solution to induce hydrolysis and yield hydrophilic surface groups.[22] This method, however, does not appear to yield a water contact angle akin to O_2 plasma treatment. Furthermore, to achieve such an effect, PCL must be immersed in the NaOH for over 30 minutes. In doing this, severe degradation of the polymeric structure is observed, and over 50% of the mass of the polymer is lost within 2 weeks. Such an effect is not desirable when hoping to achieve long-term support of the GO-ELP membrane during cell growth.

The use of plasma treatment allowed for the development of novel methods of membrane formation, which may yield interesting properties or environments for cell growth. One possible line of enquiry which was explored was the development of dual-layer or "sandwich" membranes, wherein membrane formation is initiated simultaneously on both faces of the scaffold. It was theorised that this method would cause the GO to outwardly diffuse in two directions, forming two membranes with ELP-rich outer faces and GO-rich inner faces. These two membranes would form on the outer surfaces of the scaffold, leaving a separation between the two. Such a design may improve the mechanical properties of the overall system by forming two membranes instead of one and may improve cell growth by providing two ELP-rich faces for

adhesion. This possible method of formation was explored using both GO-soaked and ELP-soaked scaffolds (Figure 52A).

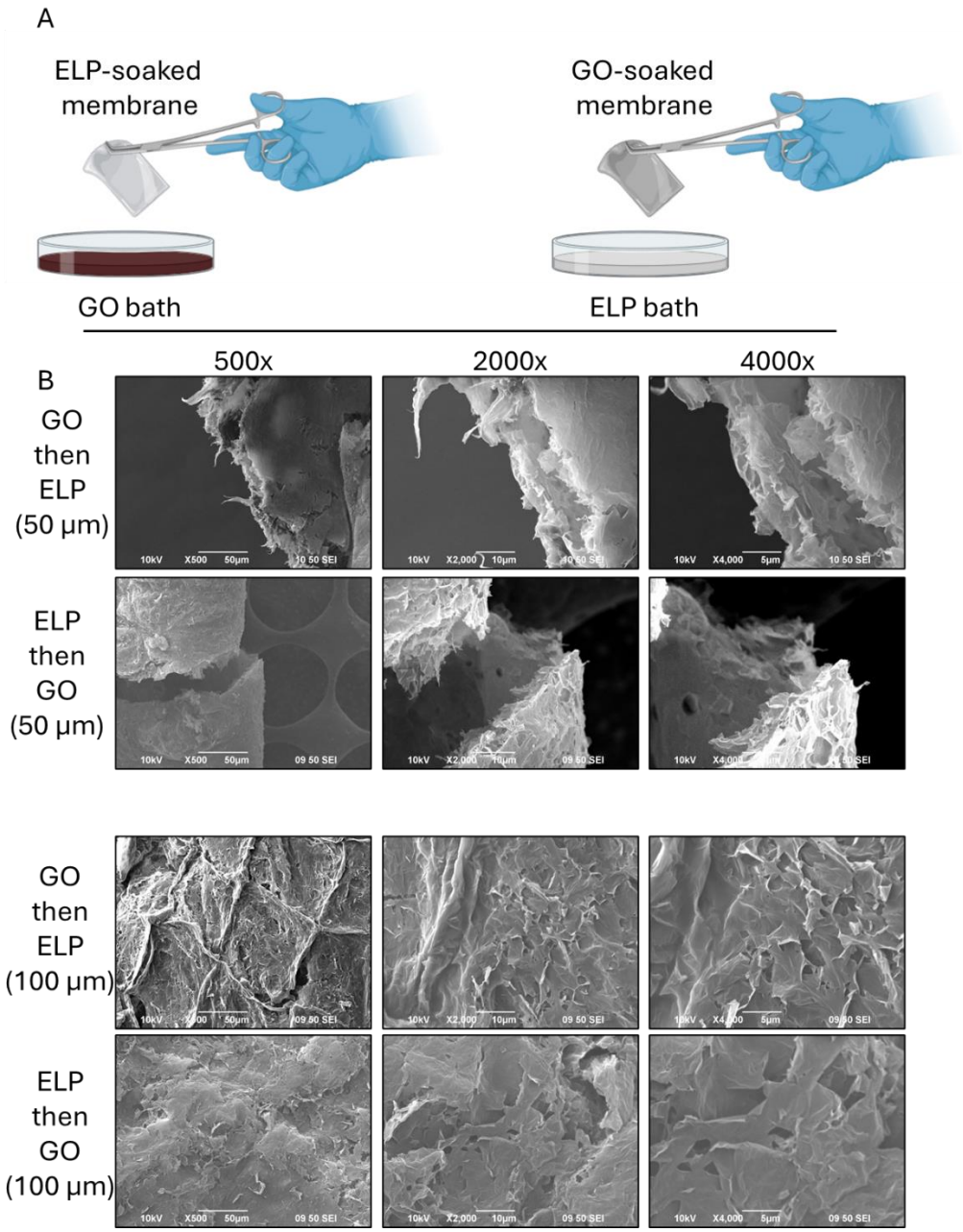

Figure 52: SEM micrographs of dual-layer membranes formed on PCL scaffolds by liquid immersion. ***A)*** *Simple schematic of methodology, wherein a PCL scaffold is soaked with either GO or ELP before being immersed into a bath of the other to initiate membrane formation.* ***B)*** *SEM Micrographs resulting from both orders of addition in both 50 and 100 µm PCL pores demonstrating improved membrane adherence to the PCL scaffold.*

Immediately, it is apparent that the control over the thickness of the membrane is lost in this method of membrane formation (Figure 52B). The sub-micron thickness observed in the coaxial system and in the controlled droplet addition

is lost here, and membranes in the order of 5-10 μm are observed. This is not unexpected, as the bath of either GO or ELP represents a largely uncontrolled volume available to diffuse to the interface between GO and ELP at the face of the scaffold, ultimately leading to a greater membrane thickness. While not necessarily a negative feature, it was not the aim of this experiment. Indeed, it may be possible to use these systems for endothelial cell culture as they maintained a flexible nature, and were not destroyed by handling, unlike membranes formed in the absence of the PCL scaffold. This still represents an improved method of membrane formation, as the membranes are far easier to handle without inducing significant damage. However, the loss of the ultrathin nature of the membranes indicates that this method of formation may not be suitable for producing close mimetics of biological basement membranes.

Where a scaffold of 50 μm pores is first soaked with GO before immersion in an ELP solution at 30 °C, good membrane formation may be observed on each side of the scaffold with what appears to be a separation between the two (Figure 52B). These membranes appear well adhered to the scaffold and uniform in thickness, indicating the potential to reliably form these membranes in repeat. The ability to form membranes in this manner is not unexpected, as it is not a drastic departure from previous methodology. In the case where the order of addition is reversed, and an ELP-soaked scaffold is immersed in a GO bath, however, a noticeable difference occurs. Here, the membrane is no longer adhered to the scaffold and is observed to be peeling away, leaving behind a bare scaffold. While confirming that a membrane is indeed formed on each face of the scaffold, this method of formation does not appear to offer any tangible benefit, as the detached membrane will likely be damaged by handling.

The detachment of the membrane from the scaffold here may be attributed to the poor adhesion between the ELP and the PCL (Figure 52B). Previously, it was demonstrated that a scaffold soaked only in GO would retain a layer of GO across all fibres in the depth of each pore. A scaffold soaked only in ELP, however, would result in a layer of ELP draped across the top of each pore with seemingly minimal remnant material adhered to the PCL fibres. This would mean that any membrane formed would not adhere to the scaffold and would be likely to detach, as was observed here. In the case of 100 μm pores, a detaching

membrane is again observed where the membrane is first soaked in ELP before immersion in GO, confirming the unsuitability of this method for membrane formation in PCL scaffolds.

It may have been possible to achieve a dual-layer, ultrathin membrane by first forming a membrane on one side, washing the scaffold, refilling the pores with GO, and then forming the membrane on the other side. In doing this, the volumes of GO and ELP are both controlled, and it is not possible for the membrane to grow in an uncontrolled manner. Successfully doing this would have achieved an ultrathin membrane on each face of the PCL scaffold, perhaps facilitating both endothelial and epithelial cell culture. However, there would have remained a gap the width of the scaffold between the two membranes, across which nutrient exchange may be limited, and overall limiting the importance of the membrane thickness.

Having now determined the optimal method for membrane formation using plasma treatment of flat scaffolds, it was now investigated whether endothelial cells could be cultured on the membranes. Primary human umbilical vein endothelial cells (hUVECs) were chosen as they represent a good model of vascularisation, and exhibit tube formation when cultured in vitro. These cells have also been demonstrated to adhere and proliferated on GO-ELP membranes. It was hoped that, should these cells adhere to the flat membranes, there would be a precedent for attempting to move to tubular membranes.

5.5 Endothelial Culture on Flat Membranes

Membranes were prepared as usual by soaking PCL scaffolds in GO, wicking excess fluid, and adding IK_{24} ELP dropwise to one face of the scaffold. These membranes were allowed to form for 5 minutes as 30 °C before being washed in PBS to remove any unreacted material. They were then placed in a non-tissue culture treated well for cell seeding. HUVECs stained with a fluorescent tracker were then seeded on the membranes and cell proliferation was monitored using fluorescence microscopy (Experimental 5.10.10).

HUVECs in a positive control of 2D tissue culture plastic were observed to proliferate as expected (Figure 53). From an initially rounded morphology immediately after seeding to a more elongated morphology with axial

protrusions at either end of the cell. This indicates that the cells are behaving as expected, and any change in morphology or proliferation would likely be due to the presence of the membrane and scaffold. For all samples where membrane is present, a non-treated well plate is used, therefore it was not expected for cells to adhere to and proliferate on the base of the well. All proliferation would therefore occur on the membrane or scaffold. Any non-adherent cells were expected to be removed with media changes.

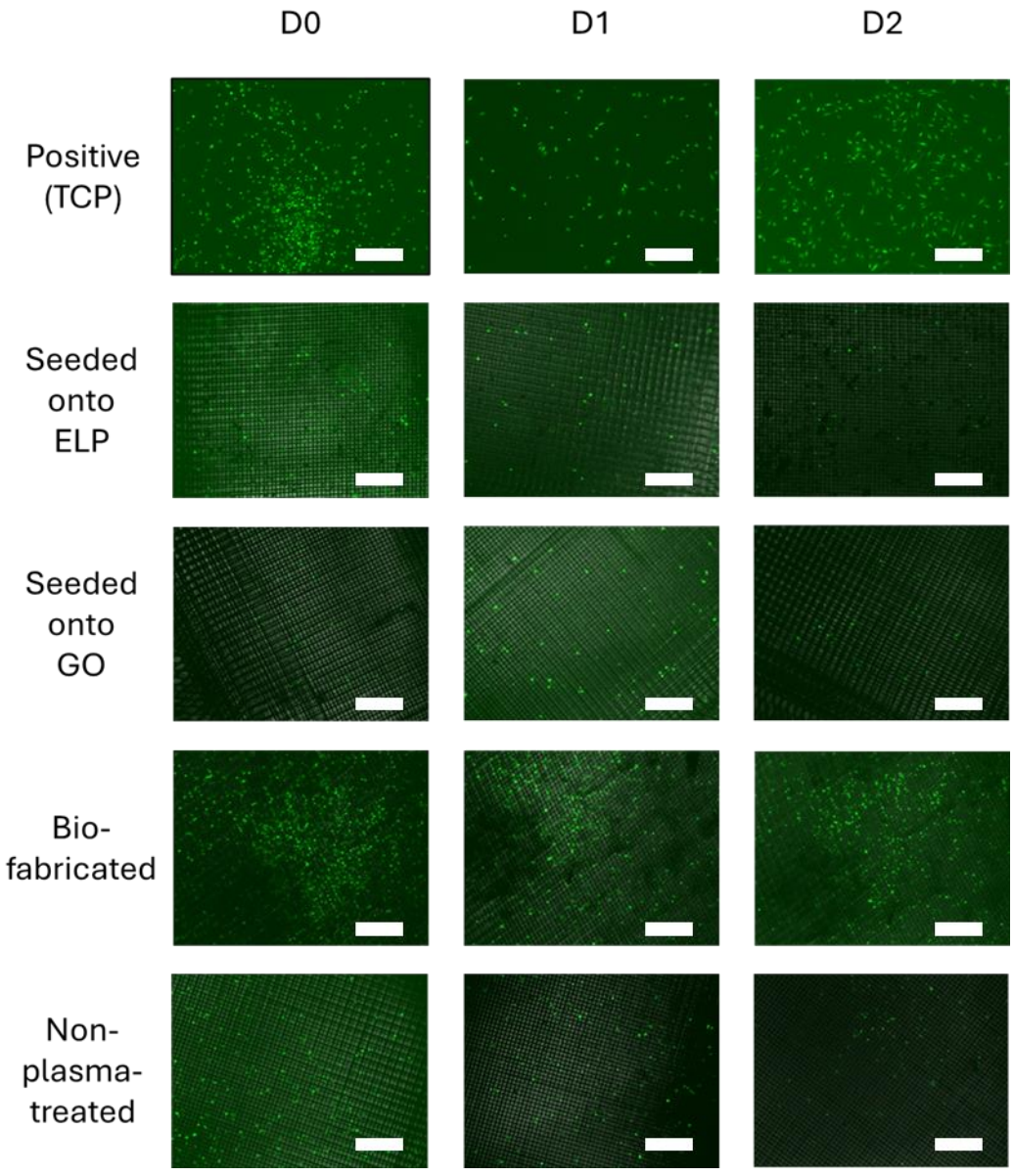

Figure 53: Fluorescence microscopy images of culture of hUVECs on flat membranes. Cells have been stained using CellTracker Green CMFDA, which stains both live and dead cells and is visible for up to 72 hours post-staining. Cells were not observed to proliferate in any of the samples, other than the positive (tissue culture plastic) control. Scale bar = 500 μm.

In both cases where cells were seeded onto the membrane – either the ELP-rich or GO-rich side – adhesion, proliferation, and morphological changes were minimal. It appears that, despite the presence of a plasma-treated scaffold beneath the membrane which may act as a cell adhesion mimic, the hUVECs – largely – were not able to adhere to the structure. Seeding density is not likely to be the issue, as cells were observed to proliferate in the positive control. It may be the case that cells do not adhere. This is, perhaps, not surprising as IK_{24} lacks any adhesion domains.

Previously, it has been observed that rat mesenchymal stem cells (rMSCs) poorly adhere to IK_{24} in comparison to other ELP sequences which contain an adhesion domain, such as the $HRGD_6$ ELP sequence, although adhesion to IK_{24} sequences in that study does not appear to be as low as is observed here.[23] Inserting an adhesion domain may have assisted in this case, but may also have impacted membrane formation as such alterations may reduce the binding constants (K_a) between ELP and GO. Furthermore, introduction of a cell adhesion sequence to the IK_{24} ELP would likely shift its thermal transition temperature away from the 30 °C currently observed. As the most robust GO-IK_{24} aggregates are formed at the transition temperature, as opposed to above or below it, shifting the T_t may result in biofabrication conditions which impose thermal stresses on cells, altering gene expression. It was also assumed that, owing to previous literature reporting cell adhesion to GO-IK_{24} membranes, cells would adhere in this case. Positively, as the functional groups deposited on PCL during plasma treatment may act as cell adhesion mimics, the lack of cell adhesion here appears to support the idea that membrane formation is more complete, and a greater surface area of the scaffold is covered by the membrane compared to non-plasma treated samples.

In the case of biofabricated samples, a greater number of cells was observed at all time points compared to seeded samples. Due to the apparent lack of adhesion, it may be speculated that the remaining cells are “encased” within the membrane which may act as a “blanket” – i.e., they are physically entrapped by the ELP as it forms a membrane with the GO, but they are not adhered to it. However, no change in morphology or aspect ratio is observed, indicating that, despite being encased within the membrane, the cells are not adhering or

proliferating. Positively, this data perhaps indicates that the GO-IK_{24} membranes at this thickness can support the weight of cells, indicating potential for this fabrication method should cell adhesion be achieved.

To remove the possibility of cytotoxicity being the cause of poor cell adhesion and proliferation, a cell viability study was performed on cells cultured in the presence of the GO-ELP-PCL scaffold. Should the scaffold prove toxic, the viability of the cells would decrease in comparison to a positive control. If the GO-ELP-PCL is non-toxic, then the lack of cells observed previously may be attributed to poor adhesion.

Using an MTS assay to assess the metabolic activity of cells cultured in contact with extract media of GO-ELP-PCL structures, no significant difference in terms of cell viability was observed, indicating non-toxicity (Figure 54). This was not entirely unexpected, as hUVECs have been cultured successfully on GO-ELP membranes before. However, here it has been observed that GO adheres to the PCL scaffold and may not be removed immediately by washing. Should this GO, which has not been incorporated into the GO-ELP membrane, be released from the structure into culture media, there is the possibility cellular uptake and cytotoxicity. Here, however, this does not appear to be a concern. The final amount of GO present on PCL fibres after washing is likely to be far below the concentration required to induce any cytotoxic effects.

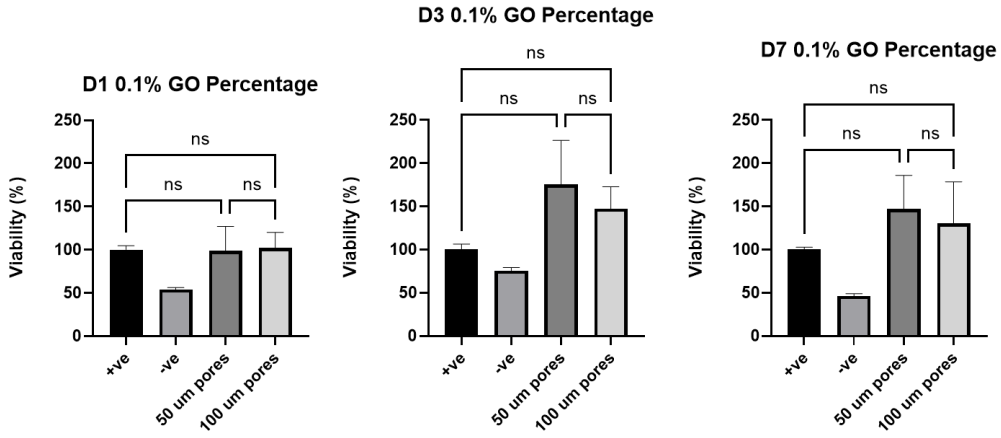

Figure 54: Cytotoxicity study of hUVECs cultured in the presence of GO-ELP-PCL scaffolds for 7 days. Viability is presented as a percentage compared to the positive control. Cytotoxicity was assessed using MTS cell viability kits and subsequent colorimetric assay. The constructs were not deemed to be cytotoxic as no significant difference was observed in cell viability compared to a positive control. Statistical significance assessed using ordinary one-way ANOVA ($p<0.05$).

The literature on GO cytotoxicity is conflicting, with some reports indicating that concentrations at or above 50 μg mL^{-1} of free GO may significantly reduce cell viability of hUVECs and A549 lung cells,[24, 25] while others are unable to find any significant effect. These studies also provide evidence of GO enhancing the proliferation of the LL-24 human fibroblast line following "biotransformation" through incubation in human serum. While here no evidence of GO cytotoxicity was found, it would be an interesting study to investigate whether GO presence altered the gene expression profiles of hUVECs cultured atop GO-ELP-PCL scaffolds. Here, however, as minimal proliferation is observed, such a study was not possible.

Regarding toxicity of other constituents, the potential toxicity of PCL alone was not focussed on here as it has FDA approval and was therefore considered non-toxic. Recent data has, however, indicated some acute toxicity in zebrafish embryo, with high toxicity observed when using biomedical grade PCL.[26] Here, it was theorised that the leaching of toxic additives may be responsible for some toxicity, as opposed to the PCL itself. The hydrolytic degradation of PCL may also cause the generation of nano/micro-plastics, which may enter cells leading to adverse effects and increased oxidative stress in vertebrates. A long-term toxicity study for these GO-ELP-PCL structures would be interesting to investigate whether the degradation products induce any adverse cell response in human cells.

Thirdly, the ELP was not expected to induce any cytotoxic effects. As a class of materials, ELPs are well studied and characterised, and their lack of cytotoxicity is known. Indeed, a complete set of biological tests has been completed for ELP materials to demonstrate their biocompatibility.[27] Within this, it has also been reported that no significant effect on blood clotting or haemolysis is observed, indicating the suitability of ELPs for vascular tissue engineering.

Overall, the cytotoxicity data indicate that induced cell death is an unlikely cause for the lack of cells observed on flat membranes, as the materials were not observed to be cytotoxic. A lack of cell adhesion, rather than cytotoxicity, is likely to be the chief cause of low cell counts. It was hoped that, by moving to a curved architecture, the hUVECs would be in a more favourable environment

and would be more likely to adhere to the surface of the membrane. A slight caveat to this data is the lack of a cell-free control. While none of the ELP, GO, or PCL are expected to be able to reduce the MTS to the soluble formazan, qualitative analysis of cell morphology at this point to would have been preferable to confirm viability. To do this, Live/Dead staining would have been performed and the number of both live and dead cells in all samples quantified. A live percentage greater than 70% would have confirmed non-toxicity.

5.6 Tubular Structures

5.6.1 Formation of GO-ELP Membrane in PCL Tubes

Knowing that the GO-ELP membrane may be reliably formed on plasma-treated PCL scaffolds, whilst maintaining the ultrathin nature, it was now explored if this may be translated to tubular constructs. Here, the droplet deposition method was slightly adapted for a tubular scaffold. A GO-soaked tubular scaffold was injected with ELP solution in the lumen, and the injected droplets adsorbed to and wetted the scaffold due to the plasma treatment-induced hydrophilicity. The lumen of the tube was filled with ELP and allowed to react for 5 minutes at 30 °C, followed by a PBS wash (Figure 55A). This methodology was observed to result in a membrane which represented a successful translation from square to tubular scaffolds. The ultrathin nature of the membrane was maintained, while the membrane was observed to form only on the inner wall of the tubular scaffold. Complete coverage of the pores was observed in plasma treated tubes, while poor or complete loss of membrane formation was seen in non-plasma treated tubes, confirming the importance of continuing this step in future works.

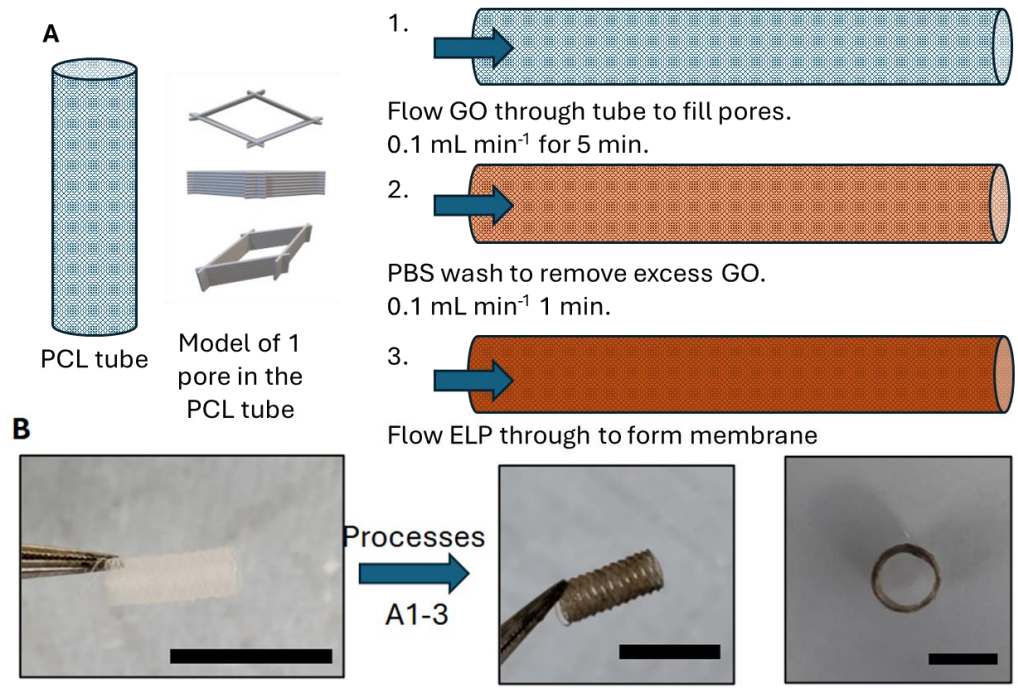

Figure 55: Formation of GO-ELP Membranes in PCL Tubes. ***A1-3)*** *Schematic of membrane formation. PCL pores are filled with GO dispersion, after which ELP is added under flow. The membrane forms at the interface of the two fluids.* ***B1-3)*** *Camera images of tubular scaffold before and after membrane formation. Scale (left and middle): 6 mm, (right) 3 mm.*

The formation and growth of the membrane was not assumed to be dissimilar to that observed in the liquid-in-liquid system. The application of flow to GO in the first step may cause the dissociation of large clusters into individual flakes, but it is likely that this process is reversed once the dispersion fills the pores and flow is arrested. The PBS wash potentially acts as a replacement to the wicking step performed on flat membranes, removing excess GO dispersion and washing the lumen to ensure membrane formation happens closely to the tube walls. It was observed that, without the PBS wash, membrane formation and GO aggregation was observed to occur in a fashion which partially blocked the tube lumen. The removal of excess GO was therefore deemed vital in this process.

Finally, applying ELP to GO under flow was not expected to significantly impact membrane formation if performed under gentle conditions. A flow of a too high velocity may damage the membrane in the early stages of formation and restrict the time in which the membrane may form. It was observed that a volumetric flow rate of 0.1 cm^3 min^{-1} resulted in successful membrane

formation. At this flow rate, the ELP can successfully diffuse to the wall of the tube and intercalate with the GO flakes, and any mass transport limitations do not appear to negatively impact the membrane formation process. It may be the case that the overall thickness of the final membrane could also be tuned using different flow rates, as this would alter the amount of ELP which diffuses to the tube walls and is involved in membrane formation. However, increased shear at greater flow rates may damage the membrane, reducing its overall integrity.

SEM micrographs revealed that the thickness of the final membrane was retained from both the coaxial fabrication method and the formation of membranes on flat PCL scaffolds. Under high magnification, a thickness of around 100 nm is observed at the membrane cross-section (Figure 56). Furthermore, it may be observed that this structure is layered, with distinct lamellar regions running parallel to the membrane. This indicates that the mechanism of formation is unchanged from the liquid-in-liquid system, confirming good translation from that method to this.

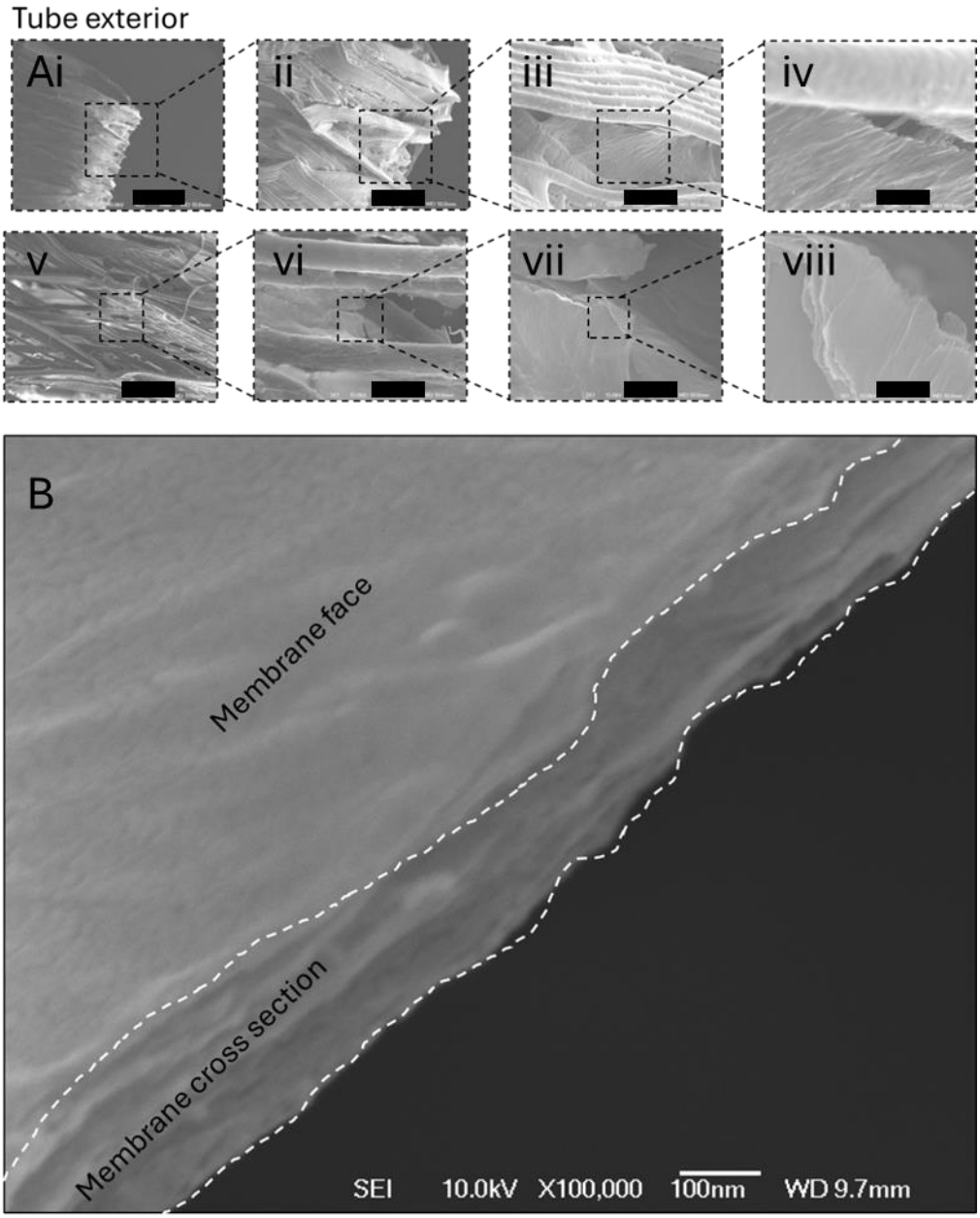

Figure 56: SEM Micrographs of Ultrathin Membrane Formed on PCL Tubes. Ai-viii: Micrographs showing the membrane viewed from the exterior of the tube. Sequential magnification demonstrates the location of the membrane within the tube and highlights the ultrathin nature of the membrane. Scales: Ai = 1 mm, ii, iii = 200 µm, iv = 10 µm, v = 200 µm, vi = 20 µm, vii = 5 µm, viii = 1 µm. B: cross-sectional image of the ultrathin membrane formed in the pores of a PCL tubular scaffold. The cross-section is highlighted and a layered structure is observed.

It was then investigated whether the membrane formation process could be automated for high-throughput fabrication. A simple flow system consisting of a syringe pump, tubing, and Luer adapters was set up (Figure 57A). It was possible to semi-automate the formation of the membrane on the tube, requiring

only the manual changing of syringes. This indicates that the bare PCL scaffold may be implanted within a microfluidic device and the membrane may then be fabricated in situ, removing the possibility of damaging the membrane during an implantation step, or allowing for a fully sterile manufacturing process.

5.6.2 Perfusion and Permeability of Tubular Membranes

With the vascular membrane now connected to a flow system, the ability of the membrane to withstand flow at a range of velocities was tested. It was observed that the ability of the membrane to withstand flow was dependent upon the concentration of GO used in its formation (Figure 57B). At lower concentrations (0.1%, 0.2% w/v), complete removal of membrane after flow was observed. In the case of 0.4% w/v GO, however, the membrane was observed to remain present after a flow of 50 mL/min was passed through for 30 seconds. The concentration of ELP used (1% and 2% w/v) was not observed to impact the robustness of the membrane. This is likely due to the GO contributing more to the overall mechanical properties of the membrane, such as the observed Young's moduli. While not exactly the same as the shear (storage) modulus, the Young's modulus may indicate the membrane's ability to resist and survive the shear applied by flow. Greater Young's modulus may therefore indicate greater robustness of the membrane in flow. Indeed, the 0.4% GO membranes which survived under flow were previously measured to have the greatest Young's modulus. This is also likely to have an impact on other important parameters, such as the burst pressure of the membrane. It would have been interesting to quantify the plasticity of this membrane and its ability to deform and regain its shape. However, doing so would be incredibly difficult owing to the weak mechanical properties of the membrane. Fortunately, no breakage of the membrane was observed upon mechanical manipulation including axial stretching and compression, bending, torsion, and folding, indicating suitability.

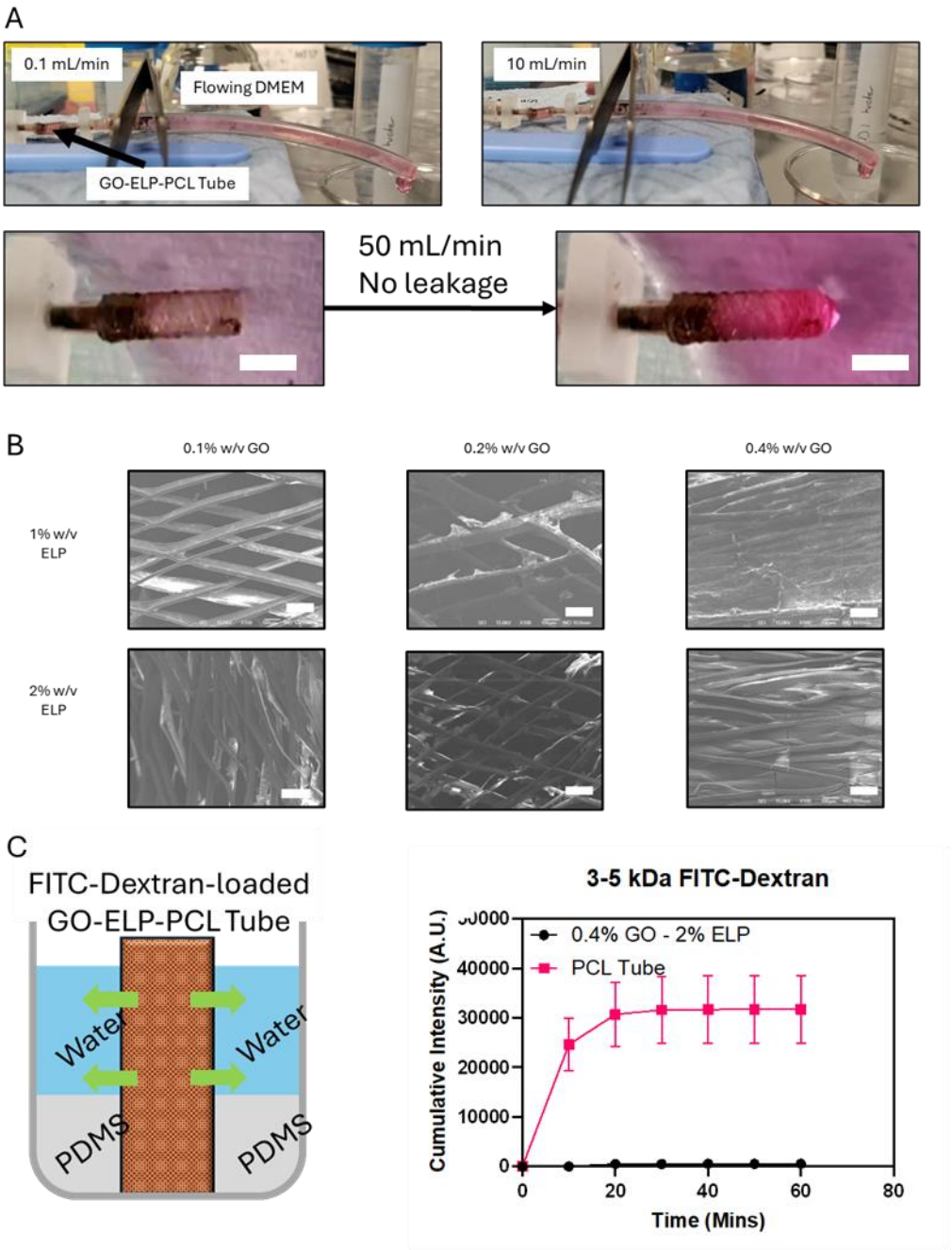

Figure 57: Perfusion and permeability of GOELP membranes in tubular structures. ***A)*** *Camera images of the perfusion of cell culture media (DMEM) through tubes. Flow was observed up to 50 mL/min without leakage from the walls of the tubes. Scale = 3 mm* ***B)*** *SEM micrographs of the inner walls of tubes after perfusion at 50 mL/min for 30 seconds at a range of different GO and ELP concentrations. Scale = 100 µm.* ***C)*** *Diffusion of FITC-Dextran through the membrane without flow, compared to a bare tube.*

The permeability of the membrane to solutes was then investigated using FITC-labelled dextran with a mW range of 3-5 kDa (Figure 57C) (Experimental 5.10.9). Molecules around this mW are of biological relevance in vascular

models, especially in the case of the blood-brain barrier (BBB). Extravasation of dextrans of 4 kDa and above is indicative of BBB disruption, allowing the entrance of neurotoxins such as thrombin to enter the brain.[28] Here, GO-ELP membranes were formed in PCL tubes, half of which were embedded in PDMS to maintain the tube in an upright orientation with one end sealed. The tubes were then filled with a solution containing FITC-dextran, and PBS was added to the well plate in which the tube was held. It was ensured that the meniscus of the added FITC-dextran or PBS did not rise above the top of the tube.

It was observed that, after 60 minutes of residence time within the tube, very little FITC-dextran had passed across the membrane, indicating that these ultrathin membranes are largely impermeable to molecules above this size. Comparatively, the PCL tube with no membrane present offered minimal resistance to the outwards diffusion of FITC-dextran, with equilibrium being reached within 20 minutes of residence time. These data are somewhat in line with those previously reported for thicker GO-ELP membranes, wherein the permeability of membranes tends towards 0 for 20 kDa FITC-dextran and sodium fluorescein with increasing GO % w/v, up to 0.15%. It follows, therefore, that permeability would be far lower when using 0.4% GO, despite the drastic reduction in thickness (<1 μm here compared to roughly 50 μm in the previous study). Importantly, these data indicate that these ultrathin membranes may be fabricated without sacrificing vital physical properties observed in previous studies.

Further to this study, it would have been interesting to repeat using a range of FITC-dextran molecular weights, and also with the FITC sodium salt. While serving to improve the robustness of the data, these measurements would also help to accurately ascertain the molecular weight cutoff point of these membranes. Other molecular weights may act as substitutes for ion, solute, and protein diffusion across the membrane. Currently, it may be said that molecules above 3 kDa may not pass through these membranes.

5.7 Cell Culture on Tubular Ultrathin Membranes

Having determined that fluid may be perfused through the tubular membranes up to a rate of 50 mL min^{-1}, that the membrane is of good integrity, and is

impermeable to solutes above 3 kDa in mW, it was now decided that the ability of endothelial cells to adhere and survive on the walls of the membrane should be investigated. To this end, hUVECs were again employed as a close model of human vascular systems. Here, hUVECs were either seeded on the inner walls of pre-formed GO-ELP tubular membranes, or they were mixed with an ELP solution and subsequently flowed into a PCL tube soaked with GO (biofabricated) (Experimental 5.10.10). In both cases, 0.4% GO was used, as this was previously determined to yield membranes which were the most robust in the presence of fluid flow in the lumen of the membrane.

After 3 days, good spreading of cells was observed in the seeded samples, with a slightly elongated morphology of cells observed in a somewhat random orientation (Figure 58). This indicates good adhesion to the membrane, allowing cells to proliferate and spread in this case. The random elongation of cells is typical of hUVECs grown on a 2D surface in the absence of flow. It may be possible to induce alignment of these cells, as is observed in nature, by conducting culture under flow conditions. The spatial patterning of endothelial cells is important in biological systems for effective blood flow and nutrient uptake and should therefore be a target for future tubular models of endothelial cell growth. In this case, too, it may have been the case that applying an optimal shear stress to the hUVECs in culture could have improved their proliferation and survival across the entire tube, as has been previously reported.[29] Nonetheless, it was promising to observe adhesion of cells to the membrane after 3 days of culture, indicating that, given further optimisation of the cell culture conditions, it may be possible to achieve long-term culture and tissue growth. Currently, after 7 days, the number of live cells had visibly decreased – the lack of dead cells perhaps attributable to detachment and washing – and the observed morphologies were somewhat more rounded, indicating sub-optimal culture conditions.

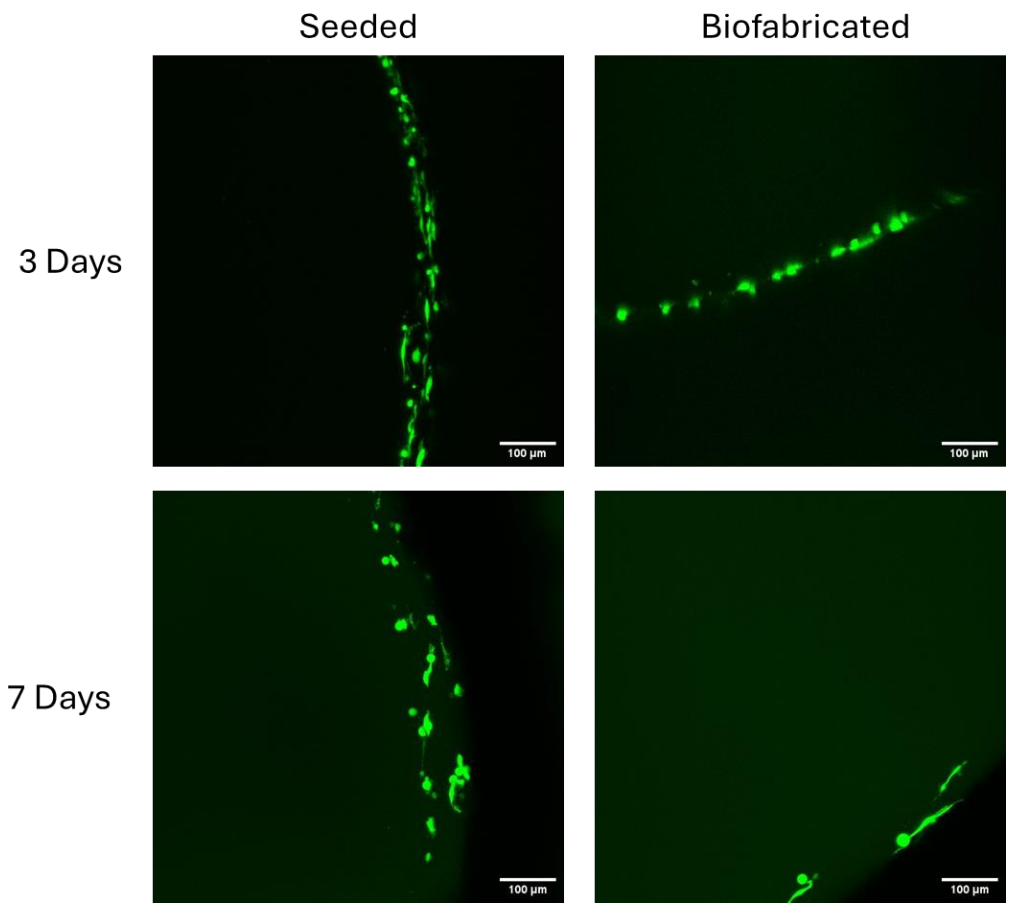

Figure 58: Cross-section views of culture of hUVECs on tubular GOELP membranes. hUVECs were either seeded (left) on the inner wall of GO-ELP membranes formed on PCL scaffolds or biofabricated (right) by mixing the cell suspension with the ELP solution and flowing through a GO-soaked PCL scaffold. Cells were cultured for 7 days and observed using Live/Dead staining.

In the case of biofabricated membranes, wherein cells had been mixed with the ELP solution, fewer cells were observed after 3 days compared to the seeded sample (Figure 58). The cells which were observed had a more rounded morphology. It may be the case that, during the formation of the membrane, the ELP diffuses towards the GO at the interface between the two materials due to electrostatic attraction. This electrostatic attraction may not be present between the cell membrane and the GO flakes, meaning cells do not diffuse to the membrane and, largely, flow through the lumen and exit the tube. The few cells which do remain may have been in the tube after flow was arrested, allowing them to adhere to the membrane. The ultimate seeding density may therefore be too low to support cell proliferation. This is observed after 7 days, where very few cells remain. The live cells which do remain, however, appear to have an

elongated morphology, indicating that there is the possibility to also support long-term endothelial cell growth on these membranes.

Unavoidably, the cells in the biofabricated samples were subjected to greater shear than the seeded samples. It has previously been reported that the application of shear during the seeding process negatively impacts cell adhesion and proliferation, with the effect becoming more pronounced at greater shear rates.[30] The shear rate experienced by the cells in this system, where a volumetric flow rate of 0.1 mL min^{-1} is applied to a tube of a diameter of 3 mm, was calculated to be 0.63 s^{-1}. While this is an incredibly low shear rate – around two orders of magnitude lower than the lowest reported in vivo blood shear rate – it is possible that cell adhesion may be improved by imposing a slower flow rate. Such an alteration would likely require temperature controls to ensure the ELP is maintained at 30 °C during the membrane formation.

It was also investigated whether different membrane formation techniques could have an impact on the adhesion and proliferation of cells. Here, hUVECs were seeded on the inner wall of tubes formed through the standard method (Figure 55), and tubes which were formed using a dual immersion method (Figure 52). It was observed that a greater number of live cells were present 7 days after seeding in tubes formed through the standard method, while tubes formed through the dual-immersion method were almost completely without live cells (Figure 59).

Cells were present on the dual-immersion membranes after 3 days, but these were observed to be rounded, indicating cell death. Indeed, it appears these cells detached from the membrane by day 7. In doing this, it appeared to be suggested that the ultrathin membranes – when fully optimised – have the potential to perform better in terms of cell adhesion and proliferation than thicker membranes. Further data and replicates would be required to confirm this. This may be because the ultrathin membrane still provides some access to the charge-based affinity between the plasma-treated PCL and the cell membranes, whereas this is not experienced by the cell through the thicker membranes. Such an affinity may be analogous to the growth of the membrane itself, where charge-

based attractions cause the lateral movement of molecules towards the membrane interface.

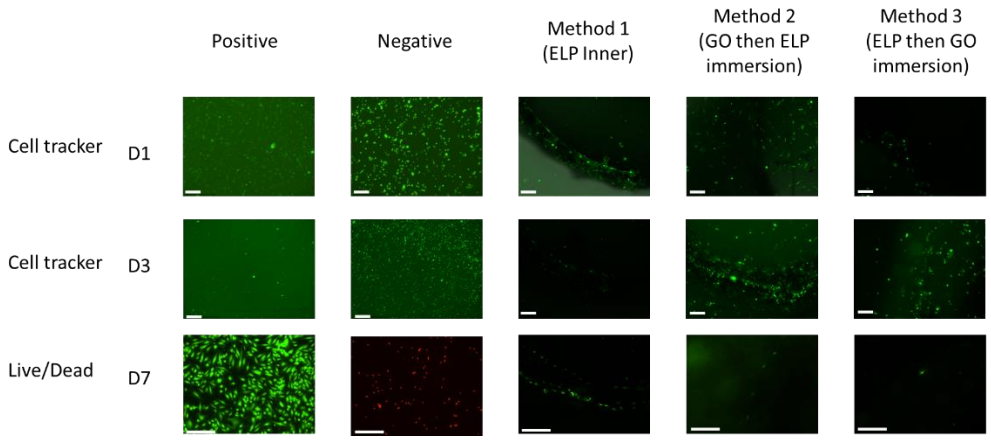

Figure 59: hUVEC culture on tubular membranes formed with different methods in PCL scaffolds. Cells were first stained using CellTracker Green and observed using a confocal microscope for 72 hours. After 7 days, cells were stained using Live/Dead staining kits and imaged using confocal microscopy. Cells were observed to adhere for the greatest time using Method 1, where ELP is flowed through a GO-soaked tubular PCL scaffold. Scale = 100 μm.

Interestingly, by simply altering the shape of the substrate upon which the cells were cultured from flat to curved membranes, cell adhesion was observed to improve, along with a more promising cell aspect ratio. No alterations were made in the formulation of the GO-ELP compared to the flat membranes in which no adhesion was observed. It may therefore be possible that the architecture of the scaffold upon which the cells are seeded has an impact upon cell adhesion. The curvature, κ, of our membranes may be defined as the reciprocal of the radius (1.5 mm):

$$\kappa = \frac{1}{r}$$

Equation 11: Curvature of a circle. The curvature is denoted by κ while r is the radius of the circle.

Yielding a curvature of 0.667 mm^{-1}. A concave architecture would force adhesion points closer together in 3-dimensional space, making them more abundant for a single cell to adhere to. There does exist in endothelial cells elastin-binding domains,[31] such as the integrin $\alpha_V\beta_3$ which binds to the carboxy terminus of human tropoelastin,[32] and a curved architecture may aid in adhesion in this way. Indeed, it has previously been reported that cell adhesion to curved

surfaces is molecularly distinct to adhesion upon flat surfaces, involving membrane curvature sensing proteins such as FCHo2.[33] Therefore, by introducing curvature, a different molecular mechanism for adhesion may be activated, improving cell adhesion in this case. Such a mechanism would also explain previous successes in achieving cell adhesion on tubular membranes while attachment was not possible on flat membranes. In future, it would be interesting to observe how altering only the curvature, κ, of our tubes may impact cell adhesion.

Furthermore, there is evidence that elastin-derived peptide sequences may improve the angiogenic behaviour of endothelial cells. In vivo, elastin peptides are generated through elastolysis, indicating tissue damage. The presence of elastin peptides may cause the upregulation of membrane-type metalloproteinases – key contributors to angiogenesis – by binding to the elastin binding protein (EBP) expressed in cells.[34] The presence of substrate curvature may sterically present ELP sequences in a manner which makes them more accessible compared to a flat substrate, resulting in improved adhesion and proliferation. Such an effect would also explain the more elongated morphology of the hUVECs on the curved surface. Further study into the effect of curvature and IK_{24}-hUVEC interactions should be carried out to confirm this hypothesis.

5.8 Conclusions

Here, it has been observed that ultrathin membranes formed through the co-assembly of the IK24 ELP and GO flakes may be supported using a precisely manufactured PCL scaffold. By using O_2 plasma treatment to yield a hydrophilic surface, these scaffolds may be reliably soaked with the GO dispersion. Flowing the ELP solution through the lumen of these scaffolds yields the formation of a membrane at the interface of GO and ELP situated on the inner wall of the scaffold. In doing this, the volume of GO dispersion available to form a membrane is limited, and the ultrathin nature of the membranes observed in a coaxial system is maintained. This thickness may be reduced to as low as 100 nm, within the range of biological basement membranes such as the blood-brain barrier.

It was established that the membrane here is formed in the same hierarchical manner as in previous GO-ELP publications, yielding both an ELP-rich and GO-rich side on the inner and outer respectively. Mechanically, the Young's modulus of this membrane determined by AFM is closer to vascular tissue than current vascular replacements which are commercially available. The membrane can survive the application of shear stress in the form of flow, up to 50 mL min^{-1}, and is impermeable to molecules above 3 kDa. All these factors indicate the suitability of this material to tissue engineering applications.

It was observed that the membranes may support endothelial cells culture – namely hUVECs – in static culture conditions for a minimum of 3 days. After this point, there is currently an observable decrease in the number of cells present on the membrane, indicating poor proliferation and detachment over time. Nonetheless, the survival of some cells for up to 7 days indicates that there is potential for this membrane to be further optimised and act as a platform for long-term endothelial cells growth and possibly vascular modelling. It is hoped that, in the future, these membranes may be used in BBB-on-a-chip technologies for modelling drug delivery, neurodegenerative diseases, and brain injury. Further still, should these membranes prove to be accurate recreations of human vasculature, they may be used as models for all vascular tissue.

5.9 Future Work

The work here has demonstrated that it is possible to achieve ultrathin membranes using a supramolecular co-assembly system. These membranes may be integrated into a flow system and may be able to act as in vitro vascular models. However, a current limiting factor to their impact is the minimal cell adhesion observed in this case. Should a vascular tissue engineering outcome be desired, then future work should focus on overcoming this drawback.

In order to do this, there are several possible avenues of exploration. Firstly, the inclusion of integrin-binding adhesion motifs into the IK_{24} ELP sequence may be attempted. This, however, is likely to alter the T_t of the ELP, and care should be taken to ensure this remains within an amiable range for biofabrication. In addition, alteration of the sequence would likely impact the binding affinity

between the ELP and GO, potentially compromising the membrane integrity and limiting its resistance to flow.

It may, instead, be preferable to incorporate further proteins of the native basement membrane into these GO-ELP membranes, such as collagen, fibronectin, and perlecan. These proteins are capable of binding to cell membrane proteins and may aid in cell adhesion. Furthermore, their presence may help to improve the mechanical and biological properties of the membranes. Collagen, for example, may hydrogen bond to the peripheral carboxyl groups of GO to form a self-assembled structure,[35] and could therefore be integrated into a purely supramolecular GO-ELP-collagen membrane. IK_{24} assembles on the basal plane of the GO, while collagen assembles on the peripheral carboxyl groups, indicating that these co-assembly mechanisms may not compete against or inhibit each other. Beyond being simply cell adhesive, these biomolecules may be cell instructive, improving endothelial cell proliferation and overall angiogenesis.

Beyond the biomolecular portion of the membrane, different GO chemistries could be explored, such as different degrees of oxidation or surface modifications to improve outer wall cell adhesion or ELP binding affinity. It has already been observed in previous studies that altering the size of the GO flakes may impact the membrane formation. If the binding affinity were to be improved, it may be feasible to alter the ELP sequence to include a cell adhesion motif without compromising the integrity of the membrane. Ultimately, this would represent full optimisation of the system.

Should cell adhesion be improved by these or other methods, the next step for this technology should be its integration into biomedical devices or vascular tissue engineering. A simple next step would be the integration into an organ-on-a-chip device, with the membrane acting as a vascular mimic for, for example, drug screening for entry into the brain and representing a move away from animal models. Secondly, should the long-term safety and efficacy of the GO-ELP-PCL be demonstrated, it may be viable to use as a vascular implant, perhaps first acting as an autologous scaffold for angiogenesis of a patient's own cells before implantation.

Should a BBB-model be desired, work should also be conducted using brain microvascular endothelial cells (hBMECs), as opposed to umbilical vein endothelial cells. The cells which line the BBB are highly specialised and behave differently to non-brain endothelial cells. For example, brain endothelial cells resist elongation under flow.[36] It may be the case that, for future experiments, switching to hBMECs may yield more applicable data for brain vasculature applications.

5.10 Experimental

5.10.1 3D Printing of Resin Scaffolds

Hexagonal resin scaffolds were printed on an AnyCubic Photon Mono 4K (AnyCubic, Shenzen, China) with AnyCubic Clear Resin using manufacturer-recommended settings. CAD files were designed using AutoDesk AutoCAD (student version) and sliced using AnyCubic Photon Workshop.

5.10.2 MEW PCL Scaffolds

PCL scaffolds were kindly provided by the FMZ Group at the University of Würzburg, Germany.

5.10.3 Scanning Electron Microscopy

Samples were prepared for SEM imaging first by immersion in 4% PFA solution for 20 minutes. Samples were then subjected to sequential drying in ethanol by 3-minute immersion periods in 20, 50, 70, 80, 90, 96, and 100% ethanol. Ethanol was then removed using CO_2 critical point drying on a Leica CPD300 critical point dryer (Leica, Wetzlar, Germany), except for PCL-containing samples which were allowed to air-dry. Finally, samples were coated with a 10 nm layer of iridium using a Quorum Q300T sputter coater (Quorum, Lewes, England). Images were obtained using a JEOL 7000F FEG-SEM (JEOL, Tokyo, Japan) and exported in .tif format with corresponding metadata.

5.10.4 Atomic Force Microscopy

AFM imaging and nanoindentation were performed using a Bruker Dimension Icon AFM (Bruker, Massachusetts, USA). Nanoindentation and surface mapping were performed using an RTESPA-150 cantilever with the instrument

in Tapping Mode. Surface maps were taken over 500x500 nm regions near the corners of each pore. Surface roughness and maps were processed and imaged using NanoScope Analysis software V1.9. Young's Modulus was derived from nanoindentation force curves using an in-house Excel Macro. A minimum of 200 force curves were obtained from each 500x500 nm region.

5.10.5 X-ray Photoelectron Spectroscopy

Samples for XPS were prepared as for SEM imaging without iridium coating. XPS depth profiling was performed on a ThermoFisher K-Alpha X-ray Photoelectron Spectrometer system (ThermoFisher, Massachusetts, USA).

5.10.6 Time-of-Flight Single-ion Mass Spectrometry

Samples for ToF-SIMS were prepared as for SEM imaging without iridium coating. ToF-SIMS depth profiling was performed using an IONTOF ToF-SIMS 5 (IONTOF GmbH, Münster, Germany) with a Bi^{3+} LMIG primary beam 25 keV, Ar GCIB 10 keV at 7.5 nA. Images were taken in delayed extraction mode with a 500x500 µm field of view at 512x512 pixels, while an area of 400x400 µm was sputtered for 160 s with a dose of $7.48x10^{12}$ ions cm^{-2}.

5.10.7 Plasma Treatment

PCL scaffolds were treated with 100% O_2 plasma for 120 s using an RF-generator 13.56 MHz, 300 W and LF-generator 40 kHz (Diener electronic GmbH, Ebhausen, Germany) All scaffolds were stored in 100% ethanol after treatment until use to prevent loss of hydrophilicity.

5.10.8 Membrane Formation in PCL scaffolds

For static membrane formation, plasma-treated PCL scaffolds were first immersed in a bath of an aqueous GO dispersion (0.05-0.4% w/v, 30 °C) for 5 minutes, after which the scaffold was removed and excess fluid wicked gently away with an absorbent material. An aqueous solution of IK24 ELP (2% w/v, 30 °C, 20 µL) was then added dropwise to one face of the scaffold and incubated for 5 minutes at 30 °C. Membranes were then washed 3x in PBS before further use. Prior to cell culture experiments, membranes were also soaked in FBS overnight.

For membrane formation in flow, plasma-treated tubular PCL scaffolds were adjoined to a male-to-male tubing adapter, which was then attached to PVC tubing. The tubing was attached to a Cole Parmer Masterflex syringe pump (Cole Parmer, Illinois, USA) and mounted syringe. An aqueous GO dispersion (0.05-0.4% w/v, 30 °C) was then injected at a rate of 0.1 mL/min for 5 minutes, with the presence of an air bubble at the back to ensure flow was not arrested while GO still filled the tube. The process was then repeated with PBS and then with an aqueous solution of IK24 ELP (2% w/v, 30 °C). Tubular membranes were then washed 3x with PBS.

5.10.9 Membrane Permeability Measurements

Plasma-treated tubular PCL scaffolds were placed upright in the wells of a 48-well plate. PDMS was prepared by mixing Sylgard-184 elastomer (Dow Corning, Michigan, USA) with the Sylgard-184 crosslinking agent at a 10:1 weight ratio. 100 µL of PDMS was then injected into the base of the well while holding the PCL scaffold in place. Once settled, the PDMS was allowed to cure overnight at 37 °C. Membrane was then formed on the inner wall of the tubular scaffolds using the static membrane formation method. A solution of FITC-dextran (3-5 kDa, 30 µL, 25 mg/mL) was then injected into the tube, after which PBS (400 µL) was added to the well outside of the tube. The PBS was transferred to a separate well for measurements before being returned to the same well. Fluorescence measurements were taken using a Tecan Infinite 200 plate reader (Tecan, Männedorf, Switzerland). A FITC-dextran calibration curve was created to allow accurate concentration determinations.

5.10.10 Cell culture and seeding

Primary HUVECs were cultured using the EGM-2 Endothelial Cell Growth Medium BulletKit (Lonza, Basel, Switzerland). Cells were cultured at 37 °C, 5% CO_2. Cells were passaged at 80% confluency and re-seeded at a 1:3 ratio in T25 flasks. Cells were never used above P7 and never re-frozen after initial thawing to prevent cryo-damage. Mycoplasma-free certification was obtained from the supplier before beginning cell work.

For culture on flat membranes, cells were resuspended in enough media to achieve 1,000,000 cells cm^{-3} and seeded at a density of 30,000 cells cm^{-2} atop

membranes. Cells were then allowed to adhere at 37 °C for 1 hour before each well was filled with EGM-2 media. Media was changed every 2 days.

For culture in tubular membranes, cells were resuspended at 1,000,000 cells cm^{-3} and transferred to a 1 mL syringe mounted on a syringe pump. In the case of biofabricated samples, a 4% w/v ELP solution was prepared in EGM-2 media, which was then mixed in a 1:1 volume ratio with a 2,000,000 cells cm^{-3} suspension, yielding a 2% ELP solution loaded with 1,000,000 cells cm^{-3}. Tubes, having a diameter of 3 mm and a length of 8 mm, have a surface area of 0.75 cm^2. Each tube was placed horizontally on the base of a well plate and 5,625 cells were injected along the inside of the tube. These cells were allowed to adhere for 1 hour, before the tube was rolled 90 ° and a further 5,625 cells were injected along the length. This process was repeated a further two times, to ensure as much of the inner wall of the tube was coated with cell suspension as possible and to achieve a final cell concentration of 30,000 cells cm^{-2}. 1 hour after the final addition, the wells were filled with EGM-2 media.

5.10.11 Cell staining and imaging

HUVECs were stained using CellTracker Green CMFDA (Invitrogen, Massachusetts, USA) prepared as per provided protocol. Briefly, the stain was diluted 1:1000 in PBS without Ca^{2+} or Mg^{2+}. At 80% confluency, media was removed from hUVECs cultured in a T25 flask and the flask was rinsed with PBS. 1 mL of staining solution was then added to the cells and incubated at 37 °C, 5% CO_2 for 30 mins.

5.10.12 Cytotoxicity Testing

HUVECs were seeded at 30,000 cells cm^{-2} in a 96 well plate and cultured for 24 hours to allow adherence. After this, a GO-ELP-PCL scaffold was placed in each well and media was replaced every 2 days. A negative control was performed using DMSO to induce cell death, while the positive control is cells cultured as normal in the absence of GO-ELP-PCL. Cell viability was measured using a 3-(4,5-dimethylthiazol-2-yl)-5-(3-carboxymethoxyphenyl)-2-(4-sulfophenyl)-2H-tetrazolium (MTS) assay. Cells were incubated for the same length of time (3 hours) with MTS at each time point before the media was removed to a separate well plate and absorbance was measured at 490 nm. By

removing the media to a separate well, this ensured no interference from the GO-ELP-PCL scaffolds in the measured absorbance.

5.10.13 Graphing and Statistical Analysis

All graphing of data and determinations of statistical significance were performed using GraphPad Prism 10.

5.11 Bibliography

1. Wu, Y.; Fortunato, G. M.; Okesola, B. O.; Brocchetti, F. L. P. D.; Suntornnond, R.; Connelly, J.; De Maria, C.; Rodriguez-Cabello, J. C.; Vozzi, G.; Wang, W.; Mata, A., *Biofabrication* **2021,** *13* (3), 035027.
2. Abrahamson, D. R.; Hudson, B. G.; Stroganova, L.; Borza, D. B.; St John, P. L., *J. Am. Soc. Nephrol.* **2009,** *20* (7), 1471-9.
3. Pien, N.; Bartolf-Kopp, M.; Parmentier, L.; Delaey, J.; De Vos, L.; Mantovani, D.; Van Vlierberghe, S.; Dubruel, P.; Jungst, T., *Macromol. Mater. Eng.* **2022,** *307* (7), 2200097.
4. Bartolf-Kopp, M.; de Silva, L.; Rosenberg, A. J. W. P.; Groll, J.; Gawlitta, D.; Jungst, T., *Adv. Funct. Mater* **2024,** *n/a* (n/a), 2311797.
5. Größbacher, G.; Bartolf-Kopp, M.; Gergely, C.; Bernal, P. N.; Florczak, S.; de Ruijter, M.; Rodriguez, N. G.; Groll, J.; Malda, J.; Jungst, T.; Levato, R., *Adv. Mater.* **2023,** *35* (32), 2300756.
6. Wu, Y.; Okesola, B. O.; Xu, J.; Korotkin, I.; Berardo, A.; Corridori, I.; di Brocchetti, F. L. P.; Kanczler, J.; Feng, J.; Li, W.; Shi, Y.; Farafonov, V.; Wang, Y.; Thompson, R. F.; Titirici, M.-M.; Nerukh, D.; Karabasov, S.; Oreffo, R. O. C.; Carlos Rodriguez-Cabello, J.; Vozzi, G.; Azevedo, H. S.; Pugno, N. M.; Wang, W.; Mata, A., *Nat. Commun.* **2020,** *11* (1), 1182.
7. Wulff, J.; Schweikl, H.; Rosentritt, M., *J. Dent.* **2022,** *120*, 104097.
8. Brooks, A. K.; Yadavalli, V. K., *J. Appl. Polym. Sci.* **2025,** *142* (9), e56545.
9. Zhao, F.; Sun, J.; Xue, W.; Wang, F.; King, M. W.; Yu, C.; Jiao, Y.; Sun, K.; Wang, L., *Bioact Mater* **2021,** *6* (9), 2969-2982.
10. Hoffman, E. A.; Frey, B. L.; Smith, L. M.; Auble, D. T., *J Biol Chem* **2015,** *290* (44), 26404-11.
11. Chung, T.-W.; Liu, D.-Z.; Wang, S.-Y.; Wang, S.-S., *Biomaterials* **2003,** *24* (25), 4655-4661.
12. Ho, C.-Y.; Wang, H.-W., *Appl. Surf. Sci.* **2015,** *357*, 147-154.
13. Owen, D. G.; Schenkel, T.; Shepherd, D. E. T.; Espino, D. M., *J R Soc Interface* **2020,** *17* (169), 20200327.
14. Malek, A. M.; Alper, S. L.; Izumo, S., *Jama* **1999,** *282* (21), 2035-42.
15. Malek, A.; Izumo, S., *Am. J. Physiol. Cell Physiol.* **1992,** *263* (2), C389-C396.
16. Liu, L.; Zhang, J.; Zhao, J.; Liu, F., *Nanoscale* **2012,** *4* (19), 5910-5916.
17. Muiznieks, L. D.; Keeley, F. W., *Biochim. Biophys. Acta, Mol. Basis Dis.* **2013,** *1832* (7), 866-875.
18. Camasão, D. B.; Mantovani, D., *Mater. Today Bio.* **2021,** *10*, 100106.

19. Jalali, S.; Tafazzoli-Shadpour, M.; Haghighipour, N.; Omidvar, R.; Safshekan, F., *Cell Commun. Adhes.* **2015,** *22* (2-6), 79-89.
20. Ivanova, A. A.; Syromotina, D. S.; Shkarina, Svetlana N.; Shkarin, R.; Cecilia, A.; Weinhardt, V.; Baumbach, T.; Saveleva, M. S.; Gorin, D. A.; Douglas, T. E. L.; Parakhonskiy, B. V.; Skirtach, A. G.; Cools, P.; De Geyter, N.; Morent, R.; Oehr, C.; Surmeneva, M. A.; Surmenev, R. A., *RSC Adv.* **2018,** *8* (68), 39106-39114.
21. Bormashenko, E.; Chaniel, G.; Grynyov, R., *Appl. Surf. Sci.* **2013,** *273*, 549-553.
22. Zhou, Z. X.; Chen, Y. R.; Zhang, J. Y.; Jiang, D.; Yuan, F. Z.; Mao, Z. M.; Yang, F.; Jiang, W. B.; Wang, X.; Yu, J. K., *Front Pharmacol* **2020,** *11*, 471.
23. Punet, X.; Mauchauffé, R.; Rodríguez-Cabello, J. C.; Alonso, M.; Engel, E.; Mateos-Timoneda, M. A., *Regen Biomater* **2015,** *2* (3), 167-75.
24. Dabrowski, B.; Zuchowska, A.; Kasprzak, A.; Zukowska, G. Z.; Brzozka, Z., *Chem Biol Interact* **2023,** *376*, 110444.
25. Dabrowski, B.; Ulanowicz, G.; Brzozka, Z.; Zuchowska, A., *Environ Toxicol Pharmacol* **2024,** *110*, 104541.
26. James, B. D.; Medvedev, A. V.; Makarov, S. S.; Nelson, R. K.; Reddy, C. M.; Hahn, M. E., *ACS Biomater. Sci. Eng.* **2024,** *10* (8), 5237-5251.
27. Urry, D. W.; Parker, T. M.; Reid, M. C.; Gowda, D. C., *J. Bioact. Compat. Polym.* **1991,** *6* (3), 263-282.
28. Hoffmann, A.; Bredno, J.; Wendland, M.; Derugin, N.; Ohara, P.; Wintermark, M., *Transl Stroke Res* **2011,** *2* (1), 106-11.
29. Ballermann, B. J.; Dardik, A.; Eng, E.; Liu, A., *Kidney Int.* **1998,** *54*, S100-S108.
30. Pritchard, W. F.; Davies, P. F.; Derafshi, Z.; Polacek, D. C.; Tsao, R.; Dull, R. O.; Jones, S. A.; Giddens, D. P., *J. Biomech.* **1995,** *28* (12), 1459-1469.
31. Heilshorn, S. C.; DiZio, K. A.; Welsh, E. R.; Tirrell, D. A., *Biomaterials* **2003,** *24* (23), 4245-4252.
32. Wilson, B. D.; Gibson, C. C.; Sorensen, L. K.; Guilhermier, M. Y.; Clinger, M.; Kelley, L. L.; Shiu, Y. T.; Li, D. Y., *Ann Biomed Eng* **2011,** *39* (1), 337-46.
33. Zhang, W.; Lu, C. H.; Nakamoto, M. L.; Tsai, C. T.; Roy, A. R.; Lee, C. E.; Yang, Y.; Jahed, Z.; Li, X.; Cui, B., *Nat Cell Biol* **2023,** *25* (10), 1453-1464.
34. Robinet, A.; Fahem, A.; Cauchard, J. H.; Huet, E.; Vincent, L.; Lorimier, S.; Antonicelli, F.; Soria, C.; Crepin, M.; Hornebeck, W.; Bellon, G., *J Cell Sci* **2005,** *118* (Pt 2), 343-56.
35. Girão, A. F.; Gonçalves, G.; Bhangra, K. S.; Phillips, J. B.; Knowles, J.; Irurueta, G.; Singh, M. K.; Bdkin, I.; Completo, A.; Marques, P. A. A. P., *RSC Adv.* **2016,** *6* (54), 49039-49051.
36. Ye, M.; Sanchez, H. M.; Hultz, M.; Yang, Z.; Bogorad, M.; Wong, A. D.; Searson, P. C., *Sci. Rep.* **2014,** *4* (1), 4681.

6. Conclusions and Outlook

The ubiquity of self-assembly in biological systems enables the genesis, development, and growth of living systems. Non-covalent interactions drive the formation of cell membranes, the folding of proteins, and the structure of DNA. On a macroscopic scale, the fundamentals of biological self-assembly allow nature to flourish, observed in the adherence of geckoes to surfaces and the flocking of birds. Given this ubiquity, it was argued that integrating the fundamentals of biological self-assembly into biomedicine, and more specifically biomaterials, would facilitate a more seamless development of tissue engineering constructs. By exploiting and controlling non-covalent interactions, it is possible to design materials with myriad biological properties, capable of interacting with and guiding the growth of cells and tissues.

In this thesis, it was presented that peptide-based materials offer a unique opportunity to exploit, manipulate, and control non-covalent interactions on the atomic scale. Beyond directly controlling biological properties, these interactions also affect the material itself, impacting its stiffness and surface roughness as examples. These too, have a knock-on effect on the encapsulated cells. This is a degree of control which is unmatched when compared to other biomaterials, and it was believed that this thesis would contribute to the growing body of work concerning the use of supramolecular biomaterials for tissue engineering. In addition, it was argued that these materials may be integrated with additive manufacturing, yielding the combination of bottom-up and top-down control for precision design of the nano, micro, and macroscale properties of the resulting material.

Initially, PAs were targeted as self-assembling biomaterials for use as 3D printable hydrogels. Taking inspiration from previous works, a heparin-based system was integrated with PAE_3 to yield a system which may have its fibres unidirectionally aligned. Birefringence was observed in this system under polarised light microscopy. With this system, the capacity of heparin to bind multiple active factors was exploited by introducing SCS, with the goal of introducing the paracrine effect to these gels for the development of cell-free

therapies. The heparin-mimetic PA was observed to demonstrate similar binding kinetics to heparin. As the neurotrophic capacity of the SCS is already known, a neural application was suggested for this system. Indeed, a heparin-mimetic PA loaded with SCS was observed to increase the length of neurite outgrowths in the SH-SY5Y cell line, indicating a positive neurotrophic effect. The extent to which this effect was observed also appears to be dependent upon the ratio of bioactive-to-filler PA.

Following confirmation that this system may be beneficial in a neurological setting, attempts were made to 3D print this system. Extrusion printing was first attempted, although the viscosity of the system was initially too low for use on the current printing setup – a syringe-pump based system is recommended for future PA printing. Increasing the viscosity using glycerol improved the printability, but affects the gelation mechanism and rate of the PA. It is possible, however, that this system could be developed further for biofabrication should a lower volume extrusion printer be introduced.

Light-based printing was then attempted using a photoacid generator to lower the pH and trigger the assembly of PAE_3. This system was not observed to successfully induce gelation in a useful timeframe for additive manufacturing, although the possibility remains that a photoacid-PA system could be 3D printed, as bulk gelation of a PA with a photoacid has been previously demonstrated.

Through integrating the PA with a polymer gel, it becomes possible to 3D print the system using light-based techniques and subsequently trigger PA gelation within the printed structure. This was demonstrated to be possible using gelatin norbornene/gelatin thiol and was successfully printed on a two-photon polymerisation printer. This was then combined with the paracrine effect, and a beneficial neurotrophic effect was again suggested by the increased neurite outgrowth observed.

The 3D printing of this system indicates broader applicability of PAs within light-based printing. The efficacy of the PA was not lost, indicating that other amino acid sequences – and therefore other bioactivities – could be printed in this manner. 2PP requires minimal volume, so is effective for printing PA

hydrogels. With the existence of 2PP-active photoacid generators, it may even be possible to print a purely supramolecular system in this manner. These systems would likely function as designed implants for a desired biological effect.

It was then attempted to introduce a degree of hierarchy to this system by introducing another molecule which may co-assemble with the PA. However, the molecules tried here – an ELP and GO – did not yield any functional material. These two materials together, however, co-assemble to yield an interfacial membrane which may support endothelial cell growth. This system may also be biofabricated in an extrusion system, and so it was decided to attempt to optimise this.

It was observed that, by limiting the volume of GO available to react, an ultrathin membrane could be fabricated using a coaxial extrusion method. This membrane was observed to be of a thickness within the range of native basement membranes, such as this in the blood-brain barrier or the glomerulus. It was suggested that this membrane may be used as an artificial basement membrane, recapitulating the true thickness in a manner not yet observed elsewhere.

This membrane, however, could not support its own weight, and collapsed into a flat ribbon upon removal from an aqueous environment. By introducing a porous support scaffold made from melt-electrowritten PCL, it was possible to form the ultrathin membrane within the pores and fabricate a self-supporting tubular structure. Cell adhesion to this structure was observed up to 7 days after seeding, but proliferation was poor. These data suggest some promise for these membranes, but further optimisation of the culture conditions and perhaps membrane composition is required.

Given the potential to recapitulate the blood-brain barrier, a neurological application of these membranes may also be suggested. In this case, a heparin-based PA could also be re-introduced, as heparin protects the glycocalyx of the BBB from damage. Perhaps as a dual system, the paracrine effect could also be integrated into these membranes, should the HMPA be introduced, perhaps in the case of ischemic stroke where a breakdown of the BBB is observed, and

where the paracrine effect of SCS has been demonstrated to have a beneficial effect.

Summarily, it has here been demonstrated that self-assembling systems may be integrated into biofabrication techniques, and their beneficial properties appear to translate well into these technologies. This indicates the potential for future large-scale, personalised fabrication of 3D-printed, bioactive scaffolds with a range of potential applications. Binding and release of multiple active factors provide the heparin-based system with a multitude of possible applications yet unexplored, while artificial vasculature fabricated using the GO-ELP-PCL system may be used as either implantable therapies or as models for drug delivery. The integration of biofabrication with supramolecules, therefore, presents itself as an opportunity for the development of future biomedical applications, offering unmatched versatility at all scales to deliver the unmet need of tissue and organ repair and replacement.